UNIVERSITY OF Southampton

University of Southampton Research Repository
ePrints Soton

Copyright © and Moral Rights for this thesis are retained by the author and/or other copyright owners. A copy can be downloaded for personal non-commercial research or study, without prior permission or charge. This thesis cannot be reproduced or quoted extensively from without first obtaining permission in writing from the copyright holder/s. The content must not be changed in any way or sold commercially in any format or medium without the formal permission of the copyright holders.

When referring to this work, full bibliographic details including the author, title, awarding institution and date of the thesis must be given e.g.

AUTHOR (year of submission) "Full thesis title", University of Southampton, name of the University School or Department, PhD Thesis, pagination

http://eprints.soton.ac.uk

UNIVERSITY OF SOUTHAMPTON

FACULTY OF NATURAL AND ENVIRONMENTAL SCIENCES

School of Chemistry

Characterisation of Bimetallic Alloy and Core-Shell Electrocatalysts

by

Anna MacDonald Wise

Thesis for the degree of Doctor of Philosophy

May 2012

UNIVERSITY OF SOUTHAMPTON

ABSTRACT

FACULTY OF NATURAL AND ENVIRONMENTAL SCIENCES
SCHOOL OF CHEMISTRY

Doctor of Philosophy

CHARACTERISATION OF BIMETALLIC ALLOY AND CORE-SHELL ELECTROCATALYSTS

by Anna MacDonald Wise

Core-shell electrocatalysts are of interest for the oxygen reduction reaction in proton exchange membrane fuel cells as enhancements in activity have been reported compared to the traditionally-used Pt/C electrocatalysts. To fully understand the origin of the activity of these samples, and how the structure changes in the electrochemical environment, full in situ structural characterisation is required. The aim of this work was to develop and apply in situ synchrotron based X-ray characterisation techniques (EXAFS, WAXS, SAXS and ASAXS) to study a set of well-defined Pd-core, Pt-shell electrocatalysts with 0.5, 1, 2 and 4 monolayers (ML) of Pt, with the primary motivation of determining the advantages and limitations of each technique when applied to materials of this nature.

Measurements were conducted in and ex situ to study the effect of Pt-shell thickness on the structure of the nanoparticles and the response to applied electrode potential. Catalyst electrodes subjected to accelerated ageing tests were also characterised to investigate the mechanisms of degradation responsible for an observed loss in electrochemical surface area, with the dominant mechanism found being dissolution for the core-shell catalysts with ≤ 2 ML shell and coalescence (Ostwald ripening) for the 4 ML.

EXAFS was found to be the most useful of the four techniques owing to the detailed structural information obtainable and the relative ease of data collection. The SAXS data provided information not obtained from the EXAFS, and combined with electrochemical measurements, enabled determination of the mechanisms of degradation. WAXS provided complementary information to the EXAFS. Attempts to fit the ASAXS data with a simplistic model were unsuccessful, thus, without the application of more complex theoretical models, little additional information could be obtained from this technique.

TABLE OF CONTENTS

DECLARATION OF AUTHORSHIP

I, Anna MacDonald Wise, declare that the thesis entitled

Characterisation of Bimetallic Alloy and Core-Shell Electrocatalysts

and the work presented in it are my own and has been generated by me as the result of my own original research.

I confirm that:

1. This work was done wholly or mainly while in candidature for a research degree at this University;

2. Where any part of this thesis has previously been submitted for a degree or any other qualification at this University or any other institution, this has been clearly stated;

3. Where I have consulted the published work of others, this is always clearly attributed;

4. Where I have quoted from the work of others, the source is always given. With the exception of such quotations, this thesis is entirely my own work;

5. I have acknowledged all main sources of help;

6. Where the thesis is based on work done by myself jointly with others, I have made clear exactly what was done by others and what I have contributed myself;

7. Parts of this work have been published as:

A.E. Russell, B. Tessier, A. Wise, A. Rose, S.W. Price, P.W. Richardson, S. Ball, B. Theobald, D. Thompsett, E.M. Crabb, *ECS Transactions*, **2011**, 41, 55-67.

Signed: ……..

Date: ……..

ACKNOWLEDGEMENTS

Firstly I would like to thank my supervisor, Andrea Russell, for her continuous support, encouragement and enthusiasm throughout the course of this PhD. I would also like to thank Sarah Ball, Jonathan Sharman and Dave Thompsett for their valuable advice and useful discussions.

Brian Theobald, Beatrice Tessier, Elvis Christian, Maria Campos and Greg Peace are also due thanks for their help with catalyst synthesis and electrochemical characterisation, and I would like to acknowledge the whole of the ECP group at Johnson Matthey for being so welcoming and for sparking my initial interest in fuel cell research. Thanks also go to the JMTC analytical department, and to Haibo E, University of Oxford, for HRTEM images.

Patrick Hendra is owed a special thank you for his help in the design of and for building the in situ cell, including the many iterations before the design was optimised, without which much of the work contained within this thesis would not have been possible.

Over the course of this PhD I have been fortunate to have worked at a large number of different facilities with many interesting people. I would like to thank all of the beamline scientists who have helped with the data collection presented in this work, in particular Ulla Vainio, HASYLAB, and Michael Toney, SSRL, for their advice and help with analysis.

The frequent trips to synchrotrons for data collection would not have been possible without the support of the other members of the Russell research group. I would like to thank Steve Price, Jon Speed, Gael Chouchelamane, and Laura Calvillo Lamana for giving up their time to help with the measurements. Special thanks go to Pete Richardson who was with me for most of my trips and was invaluable for the success of the project, both in terms of the data collection itself and for his company, making the whole experience many times more enjoyable. In addition to their help with data collection, I would also like to thank the members of the group mentioned above and Katie Blaney, Prabalini Kannan and Rosie Baker for welcoming me to Southampton and making my time here so enjoyable. Rob Johnson also deserves a special mention for his friendship and support over the time I have been here.

I would also like to thank all of my friends for understanding my frequent disappearances off the radar and for all of the good times in between. An enormous thank you goes to Jack who has kept a smile on my face every day and made my time in Southampton very happy. Finally, to Mum, Dad, Sally, Ewan and Isobel - I couldn't have done this without you, all my love and thanks, Anna.

LIST OF ABBREVIATIONS

a.u.	arbitrary unit
acac	acetylacetone
AgBeh	silver behenate
ASAXS	anomalous small-angle X-ray scattering
BF	bright field
CCD	charge-coupled device
CSR	controlled surface reaction
CV	cyclic voltammogram
DFT	density functional theory
ECA	electrochemical surface area
EDX	energy dispersive X-ray
EPMA	electron probe micro-analyser
EPSA	electrochemical Pt surface area
EXAFS	extended X-ray absorption fine structure
FCC	face centred cubic
FWHM	full width at half maximum
GDL	gas diffusion layer
GPES	general purpose electrochemistry software
HAADF	high angle annular dark field
HRTEM	high resolution transmission electron microscopy
ICP-ES	inductively coupled plasma emission spectroscopy
MEA	membrane electrode assembly
ML	monolayer
MMS	mercury mercurous sulphate
MSD	mean-square displacement
OCV	open-circuit voltage
ORR	oxygen reduction reaction
PEMFC	proton exchange membrane fuel cell
PSF	partial structure factor
PTFE	polytetrafluoroethylene
RDE	rotating disk electrode
RHE	reversible hydrogen electrode
SAXS	small-angle X-ray scattering

STEM	scanning transmission electron microscopy
TEM	transmission electron microscopy
UPD	underpotential deposition
WAXS	wide-angle X-ray scattering
XANES	X-ray absorption near-edge spectroscopy
XAS	X-ray absorption spectroscopy
XRD	X-ray diffraction

CHAPTER ONE: INTRODUCTION

1 Aim

The aim of this thesis was to develop and apply in situ synchrotron radiation based X-ray techniques to the study of Pt-core, Pd-shell carbon-supported nanoparticle electrocatalysts for the oxygen reduction reaction (ORR) in proton exchange membrane fuel cells (PEMFCs), investigating the effect of Pt shell thickness on the activity and stability of these materials in the electrochemical environment. A combination of techniques was used to assess the benefits of employing several different methods to characterise the structure of these materials, and to determine the advantages and limitations of each technique in the study of systems of this nature.

2 Motivations

2.1 X-Ray Characterisation Techniques

The synchrotron radiation based X-ray techniques used in this study were extended X-ray absorption fine structure spectroscopy (EXAFS), wide-angle X-ray scattering (WAXS), small-angle X-ray scattering (SAXS) and anomalous small-angle X-ray scattering (ASAXS). Synchrotron radiation provides a bright, tuneable source of X-rays which is important for EXAFS and ASAXS as these techniques rely on energy-dependent variations in X-ray absorption and scattering processes. The high intensity X-ray beam produced by synchrotron radiation, along with the ability to use a shorter, more penetrating wavelength, is also advantageous for SAXS and WAXS as it facilitates in situ measurements which can be conducted over a much shorter timescale than with laboratory-based instrumentation.[1],[2]

2.1.1 Extended X-Ray Absorption Fine Structure Spectroscopy

EXAFS is an element-specific technique used to determine the local coordination structure around an atom on a per atom average basis, in terms of the identity of, number of and distance to the neighbouring atoms. The theory of EXAFS is described in detail in Chapter Three. EXAFS has been shown to be a valuable technique for the study of monometallic and bimetallic electrocatalysts, both due to the level of structural information which can be obtained and the ability to conduct these measurements in situ.[3]

Imai *et al*. used a combination of EXAFS and synchrotron X-ray diffraction (XRD) to study the growth of oxide on Pt nanoparticles at potentials up to 1.4 V vs. RHE (reversible hydrogen electrode), allowing the mechanism of the formation of a few monolayers of oxide on the surface to be deduced.[4] Another illustration of the use of in situ EXAFS in the study of monometallic electrocatalysts is the work carried out by Mukerjee *et al*., who investigated the effect of particle size on the specific activity to ORR of Pt nanoparticles with diameters ranging from 2.5 to 9 nm.[5]

Examples of the use of EXAFS to study bimetallic alloys include the work on the effect of composition on the structure of PtRu alloys by Wiltshire *et al.* where well-mixed/alloyed particles with some surface enrichment of Pt were detected using EXAFS and XRD, with the increase in the proportion of Ru being seen to cause a contraction the Pt-Pt bond length.[6] The surface segregation of a set of Ru modified Pt/C electrocatalysts was studied by Rose *et al*., who were able to detect alloying and dealloying of the Ru as a function of applied electrode potential, thus highlighting the sensitivity of EXAFS to the distribution of metals within a particle when data is collected from the perspective of both elements.[7] Mukerjee *et al*. used in situ EXAFS to investigate the structure of a series of Pt_3M alloys (M = Cr, Mn, Fe, Co, Ni), relating the structural and electronic effects of alloying Pt on the activity to oxygen reduction.[8]

More recently, in situ EXAFS has been used to investigate the underpotential deposition (UPD) of Cu on carbon-supported Au nanoparticles, which is the first step of core-shell nanoparticle synthesis using the UPD method.[9] An IrNi core-shell system for ORR has also been studied by Sasaki *et al*., who used in situ EXAFS to confirm the formation of Ir shells on IrNi alloy cores, with the Ir shell protecting the Ni from dissolution in 1 M $HClO_4$ at potentials up to 1.11 V vs. RHE.[10] Wells *et al*. used ex situ EXAFS to investigate the effect of shell thickness on a series of Pd-core, Pt-shell and Pt-core, Pd-shell electrocatalysts, correlating the structure with activity to ORR and stability.[11]

Whilst EXAFS is well developed in terms of its use to characterise fuel cell electrocatalysts in situ, its application to the study of the structure of core-shell electrocatalysts as a function of applied electrode potential and shell thickness is relatively limited. The aim within this work is to utilise the known strengths of EXAFS to determine the local coordination structure and to develop a further understanding of the sensitivity of the technique to the effects of shell thickness on the response to electrode potential and electrochemical ageing of Pd-core, Pt-shell materials.

2.1.2 Wide-Angle X-Ray Scattering

WAXS is analogous to powder X-ray diffraction and is used to determine the nature of the crystal structure of the catalyst nanoparticles in terms of the lattice parameter, the crystallite size and the different phases present in the crystalline regions of the catalyst nanoparticles, which typically consist of both amorphous and crystalline regions.

Ex situ WAXS (or XRD) is used routinely to characterise as-prepared electrocatalysts, both to determine the crystalline nature of monometallic nanoparticles and the degree of alloying of bimetallic nanoparticles.[12],[13] The analysis of WAXS data to obtain the lattice parameter and the crystallite size is discussed in Chapter Three. Vegard's law is often employed in the study of alloys, drawing a correlation between the lattice parameter and the atomic composition to assess the presence of a solid solution.[14] However, Vegard's law is only approximately valid in the study of bimetallic materials where the monometallic bulk lattice parameters of each element in the system are close in value, as in the Pt-Pd system studied here.[15] More detailed analysis of WAXS data by line profile fitting such as Rietveld analysis can provide further information about the crystalline phases present in the particle.[16]

Some examples of the use of in situ WAXS combined with EXAFS to study the effect of applied electrode potential on the structure of catalyst nanoparticles are given in Section 2.1.1. WAXS has also been used to investigate Pd hydride formation in carbon-supported Pd nanoparticles, both under a hydrogen atmosphere and in the electrochemical environment as a function of applied potential.[17],[18] WAXS has also been used in situ to study the formation of bimetallic nanoparticles as demonstrated by Strasser *et al*.,[19] who also used surface XRD to investigate the electrochemical dealloying of PtCu at the surface of PtCu alloy nanoparticles.[20] Synchrotron radiation WAXS has been employed in the study of the stability of Pt_3CO/C nanoparticles subjected to testing under real PEMFC conditions.[21]

The aim of the WAXS measurements conducted as a part of this thesis project was to determine the sensitivity of the technique to the effect of Pt shell thickness on the response of the core-shell electrocatalysts to applied electrode potential and to the structural changes resulting from electrochemical ageing, assessing the level of information that can be obtained for these materials and any advantages that WAXS displays both independently from and in combination with the other techniques investigated.

2.1.3 Small-Angle X-Ray Scattering

SAXS is used to provide information about the size and/or shape and the polydispersity of a sample, which is complementary to that obtained using transmission electron microscopy (TEM). The theory of SAXS is discussed in Chapter Five. The added advantages of SAXS are that the average structure of the whole of the sample in the irradiated area is investigated, rather than from a relatively small number of particles, and that measurements can be conducted in situ.[22]

Stevens *et al*. demonstrated the validity of SAXS for determining the size distribution of carbon-supported Pt nanoparticles using laboratory-based instrumentation.[23] Several studies have also been reported comparing the particle size distributions of electrocatalyst nanoparticles determined using SAXS, WAXS and TEM, with generally good agreement between the techniques observed.[24],[25],[26]

There has been limited use of in situ SAXS in the investigation of the structure of Pt and Pt alloy nanoparticles. Wang *et al*. studied the changes in the size distribution of Pt/C nanoparticles as a function of temperature, detecting a growth in the particle size with increased temperature, which, combined with XRD measurements, allowed a step-wise growth mechanism to be deduced.[27] Smith *et al*. investigated the effect of cycling the applied electrode potential on the particle size distribution, with increases and decreases in the particle size observed during each potential cycle and an overall increase in Pt/C particle size detected.[28] Figure 1 shows the change in particle size observed by Smith *et al*. during potential cycling between 0.4 and 1.4 V vs. RHE.

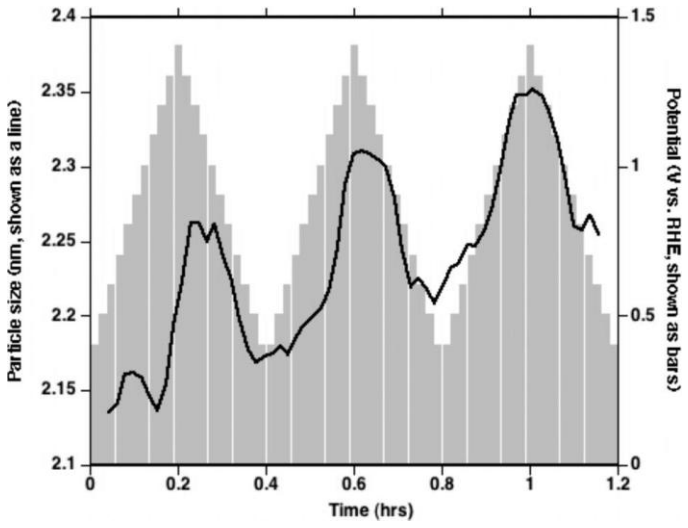

Figure 1: Change in particle size of Pt/C nanoparticles as a function of applied electrode potential in 0.1 M $HClO_4$.[28]

This thesis project aims to apply the use of in situ SAXS to bimetallic systems, studying the particle size distribution of the Pd-core, Pt-shell electrocatalysts as a function of electrode potential and following electrochemical ageing.

2.1.4 Anomalous Small-Angle X-Ray Scattering

ASAXS provides element specificity to SAXS, enabling the structure of an elemental region to be deduced, with the theory described in more detail in Chapter Five. As with SAXS, the use of ASAXS in the study of electrocatalyst nanoparticles has been fairly limited, due in part to the complexity of the data analysis. A review of the use of ASAXS in materials science by Goerigk *et al*. illustrates some examples.[29]

Several studies on Pt nanoparticles have been conducted, both in and ex situ by Haubold *et al*., illustrating the advantages of this technique over SAXS in terms of the accurate isolation of the scattering from the Pt nanoparticles from that of the carbon support. The in situ investigations include the study of Pt nanoparticle formation,[30] and the effect of applied electrode potential on the structure of the particles, allowing the growth of oxide shells at a potential of 1.1 V vs. Ag/AgCl to be inferred.[31] In situ ASAXS has also been successfully applied to the study of Au and Pd carbon-supported catalysts, highlighting the potential of this technique in the study of fuel cell electrocatalysts.[32],[33],[34]

For bimetallic systems, ASAXS has been used to investigate the distribution of the metallic elements within the nanoparticle, as shown by Yu *et al*. who were able to infer a pseudo core-shell structure in dealloyed PtCu nanoparticles.[35] Haas *et al*. used ex situ ASAXS to deduce the formation of Se clusters on Ru nanoparticles, rather than the intended core-shell structure, thus illustrating the sensitivity of ASAXS to the structure of the elemental regions within the system.[36]

The previous ASAXS studies described demonstrate the power of this technique in determining the distribution of elements within a nanoparticle. The aim in this work is to use ASAXS to investigate the structure of the Pd-core, Pt-shell nanoparticles in terms of the level of coverage of the core by the shell, developing the analysis of this technique for core-shell electrocatalysts, and to study the effect of electrochemical ageing on the retention of the core-shell structure.

2.2 Proton Exchange Membrane Fuel Cells

2.2.1 General Principles

Proton exchange membrane fuel cells (PEMFCs) have been the topic of substantial research over recent years due to their potential as an alternative, 'greener' source of power to traditional sources such as the internal combustion engine in applications such as automotive transport. A fuel cell is an electrochemical device in which the chemical energy of a reaction between a fuel and an oxidant is converted directly into electrical energy. The fuel is oxidised at the anode and electrons travel around an external circuit to the cathode. The oxidant is simultaneously reduced at the cathode and the reaction is balanced by diffusion of ions through the electrolyte. The flow of electrons from the anode to the cathode is a direct current which can then be used to power an application, with the cell operating continuously as long as reactants are supplied.[37] There are several different types of fuel cell, defined by the fuel and/or electrolyte.

PEMFCs combine H_2, either as pure gas or from reformate, and O_2, either pure or from air, to generate electricity, typically operating at temperatures of around 80 °C, with the operating temperature usually being determined by the choice of membrane material. The H_2 is oxidised to protons at the anode which then pass through the electronically insulating proton exchange membrane to the cathode, where they react with the reduced O_2 to form water. The reactions at the anode and the cathode are catalysed by electrocatalysts such as Pt nanoparticles supported on carbon. A key advantage of this system is that the only by-products of the complete reaction are water and heat. The equations for the reactions occurring at the anode and cathode, and the overall cell reaction are given in Equation 2.1 - Equation 2.3 respectively.

Anode: $2H_2 \longrightarrow 4H^+ + 4e^-$ $E^0 = 0.00$ V vs. RHE Equation 2.1

Cathode: $O_2 + 4H^+ + 4e^- \longrightarrow 2H_2O$ $E^0 = 1.23$ V vs. RHE Equation 2.2

Overall: $2H_2 + O_2 \longrightarrow 2H_2O$ $E^0 = 1.23$ V vs. RHE Equation 2.3

2.2.2 Fuel cell components

Figure 2 shows a schematic diagram of the membrane electrode assembly (MEA), which is the core component of a PEMFC.

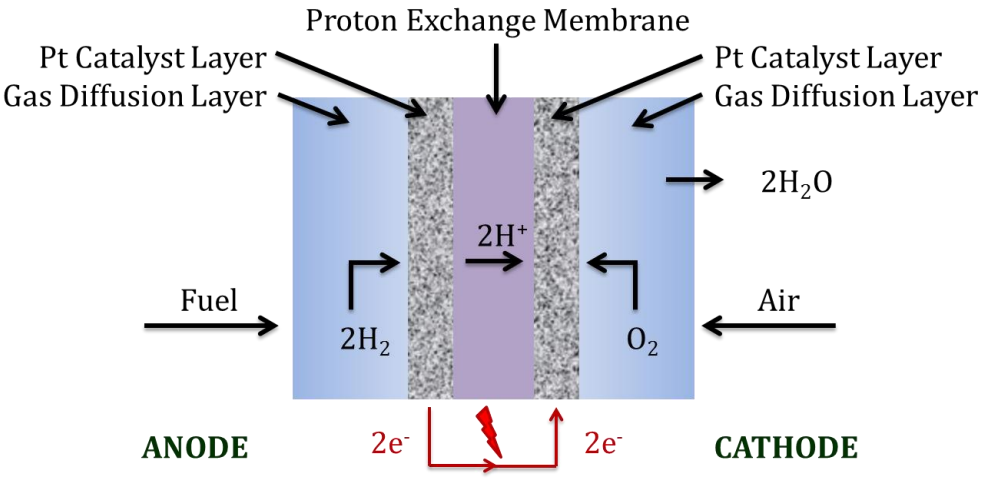

Figure 2: Schematic diagram of a PEMFC membrane electrode assembly.

As can be seen from Figure 2, the anode and cathode consist of a gas diffusion layer (GDL) and a catalyst layer. The GDL is electronically conductive and allows both the flow of gas to the catalyst layer and the removal of waste products and unused fuel from the system. Carbon fibre paper such as Toray (Toray Industries Inc.) is often used as the gas diffusion layer. The catalyst layer typically consists of metal nanoparticles supported on carbon, the details of which will be discussed later on in relation to the oxygen reduction reaction.

The proton exchange membrane, also referred to as the polymer electrolyte membrane, needs to be conductive to protons but electronically insulating in order to force the electrons around the external circuit. In addition to this the membrane needs to be chemically stable and prevent crossover of fuel from the anode to cathode and vice versa.

A commonly used membrane is the perfluorinated membrane Nafion (Dupont), which consists of a polytetrafluoroethylene (PTFE) backbone with sulphonic acid (HSO_3) side chains (structure shown in Figure 3). PTFE is strongly hydrophobic and the strong F-C bonds mean that the polymer is chemically stable. As HSO_3 is ionically bonded, this results in the formation of hydrophilic clusters of SO_3^- and H^+ ions within the hydrophobic structure. These clusters can then absorb water, causing the membrane to swell. When the membrane is fully hydrated, the H^+ ions are weakly attracted to the SO_3^- ions and so are

free to migrate through the hydrated regions of the membrane, thus enabling the transport of protons from the anode to the cathode.

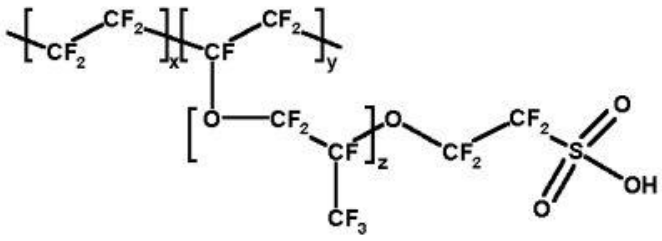

Figure 3: Structure of Nafion

2.2.3 Performance Losses

As shown in Equation 2.3, the theoretical cell voltage of the PEM fuel cell is 1.23 V. In practice, the voltage obtained from the cell is significantly lower than this owing to losses arising from the activation of the catalysts, mass transport effects and resistance. Figure 4 illustrates the effect of these losses on the observed cell performance as a function of current density.

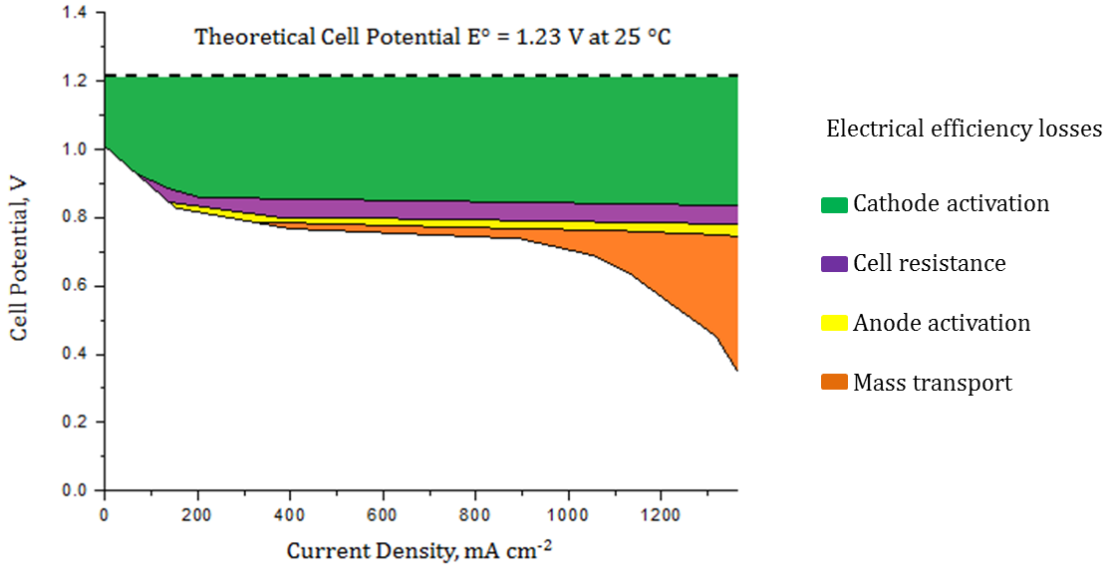

Figure 4: Illustration of the losses observed in a PEMFC as a function of the current density.

It can clearly be seen in Figure 4 that a significant cause of the reduced cell performance compared to the theoretical cell voltage is the activation of the cathode catalyst, which arises from the slow kinetics of the oxygen reduction reaction (ORR).

2.3 Core-Shell Electrocatalysts

The slow kinetics of the ORR represent a major challenge in the commercialisation of PEMFCs. Pt nanoparticles supported on carbon have been traditionally used as ORR electrocatalysts, however, the high cost of Pt is another cause for concern in terms of the commercial viability of these systems. As a result of this, strategies for reducing the Pt loading and/or improving the activity of the catalysts for ORR have been the subject of significant research in recent years.[38]

Hammer *et al*. have demonstrated a link between the d-band centre of the metal, which is correlated with the O_2 dissociative adsorption energy, and the activity towards the ORR using DFT calculations on (111) metal surfaces.[39],[40] The surface structure and, therefore the centre of the d-band, can be tuned by alloying with another metal due to lattice strain and the ligand effects which result from the electronic interaction between the two metals.[41],[42] Modifications in the d-band centre of Pt were also seen as a result of a structure consisting of a Pt monolayer deposited on another transition metal, essentially simulating a core-shell structure.[43],[44] The activity of electrocatalysts as a function of the calculated d-band centre is typically shown as a volcano plot. Figure 5 shows the volcano plot obtained for the ORR activity of a series of Pt monolayers deposited on different metal substrates.[43]

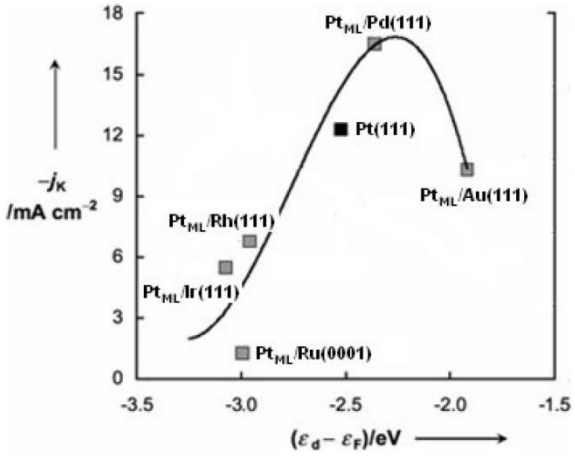

Figure 5: Kinetic current densities at 0.8 V for O_2 reduction in 0.1 M $HClO_4$ on Pt monolayers supported on different crystal surfaces as a function of the calculated d-band ε_d centre relative to the Fermi level ε_F. Adopted from [43].

As can be seen from Figure 5 the Pt_{ML}/Pd(111) shows the highest activity of the systems investigated and also shows an improvement in activity compared to the pure Pt(111) surface, demonstrating the potential activity benefits of a Pd-core, Pt-shell system. A core-

shell system, if catalytically active as the data shown in Figure 5 implies, would also be beneficial in terms of the cost of the electrocatalysts as a large reduction in the Pt loading could be achieved, thus providing a possible solution to the issues hindering the commercial viability of PEMFCs in terms of the cathode catalyst.

Owing to the potential activity and cost benefits demonstrated above, Pd-core, Pt-shell nanoparticles have since been the topic of several studies by Adzic *et al*., with activity benefits being reported.[45],[46],[47] As the activity of electrocatalysts is strongly correlated to the structure, due to the lattice strain and ligand effects mentioned above, a full understanding of the structure of these catalysts is required to understand the effect of Pt shell thickness on the activity to ORR.

B. Tessier and P. Wells studied the synthesis of Pd-core, Pt-shell catalysts using a controlled surface reaction (CSR) developed by Crabb *et al*.[48],[49],[50],[51],[52] The reaction was successfully employed to deposit a chosen number of monolayers of Pt onto Pd-cores with different diameters, thus affording a series of core-shell catalysts with different shell thicknesses. The presence of a core-shell structure was confirmed using HRTEM for the samples prepared by B. Tessier with a 3 nm core diameter, an example of which is shown for the Pt_{2ML}/Pd/C sample in Figure 6, with the brighter Pt shell clearly visible around the darker Pd core.[48]

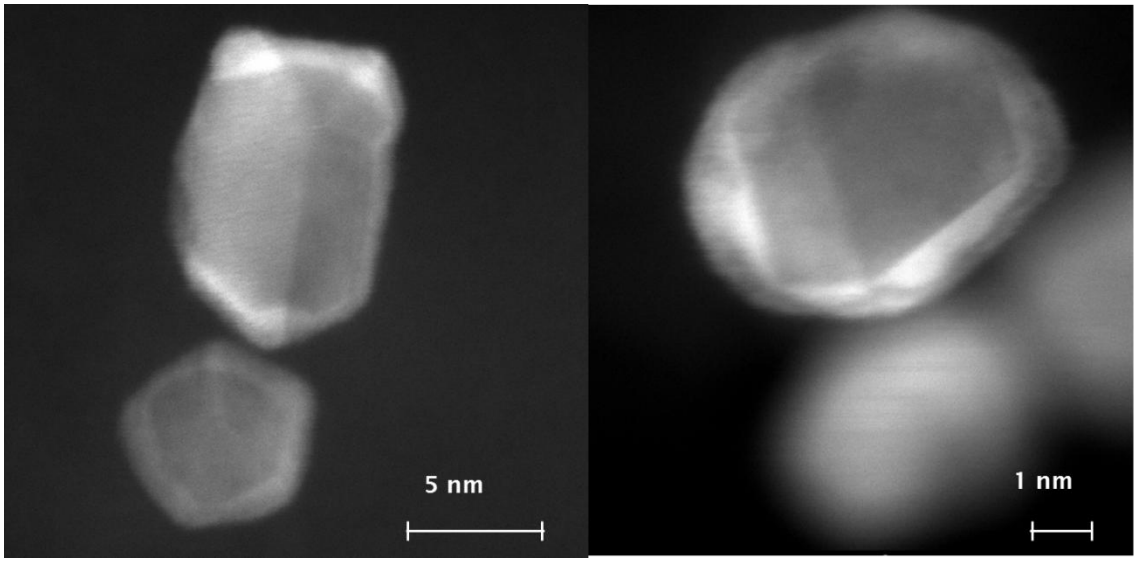

Figure 6: HRTEM images of a Pt_{2ML}/Pd/C core-shell electrocatalyst prepared using the CSR.[48]

The controlled synthesis of these materials makes them ideal samples to investigate both the limitations of the X-ray characterisation techniques described in Section 2.1 and the effect of Pt-shell thickness on the activity for ORR.

The stability of these core-shell systems is not well understood, and losses in the electrochemical surface area (ECA) have been observed following accelerated electrochemical ageing methods by Sasaki *et al*. and in the thesis work of B. Tessier.[53],[48] In addition to the loss of ECA, Sasaki *et al*. also reported the presence of a band of Pd deposited in the membrane following the accelerated ageing test, determined by using TEM on a cross-section of the MEA. The loss of ECA seen in these samples was lower than that for Pt/C nanoparticles and so protection of the Pt by the Pd core was inferred.[53]

S. Ball also investigated the stability of the Pt_{2ML}/Pd/C catalyst used in this work and also observed a loss of ECA. EPMA analysis of the aged MEA showed a band of Pd deposited in the centre of the membrane and a band of Pt/Pd deposited at the cathode-membrane interface.[54] The EPMA image is shown in Figure 7.

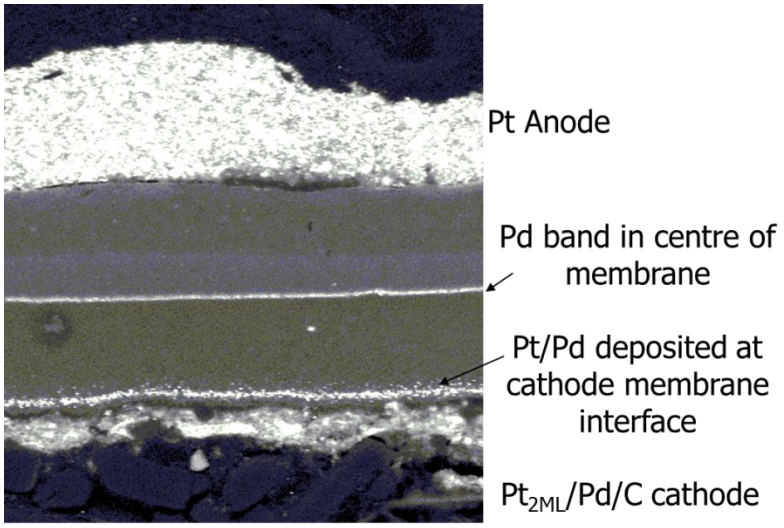

Figure 7: EPMA image of Pt_{2ML}/Pd/C containing MEA following accelerated ageing.[54]

These studies of the stability of Pd-core, Pt-shell electrocatalysts show that a loss of ECA occurs following accelerated ageing tests and a loss of Pd and Pt from the catalyst. To fully understand the mechanisms of degradation behind these losses, more in depth structural characterisation is required and this was the focus of much of the work presented in this thesis.

3 Thesis Structure

The structure of this thesis is set out as follows:

- Chapter Two describes the synthesis of the Pd-core, Pt-shell electrocatalysts and their initial characterisation using laboratory-based techniques. The theory of the electrochemistry used throughout this work is also introduced. The last part of this chapter describes the development of the in situ electrochemical cell used in the synchrotron based X-ray studies that follow.

- Chapter Three introduces the theory of EXAFS and WAXS and reports the results of the in situ characterisation of the fresh catalysts using these methods.

- Chapter Four investigates the effect of electrochemical ageing on the electrochemical characteristics of the Pd-core, Pt-shell catalysts and reports the changes in the structure following potential cycling determined from in situ EXAFS and WAXS.

- Chapter Five focusses on the characterisation of both the fresh and cycled catalyst electrodes using in situ SAXS and ex situ ASAXS.

- Chapter Six concludes the findings in this work, drawing together the structural information obtained from each technique and discusses the advantages and limitations of each of the methods used.

References

[1] R. D. Marco, J.-P. Veder, *TrAC, Trends Anal. Chem.* **2010**, *29*, 528-537.
[2] J. P. Simon, *J. Appl. Crystallogr.* **2007**, *40*, S1-S9.
[3] A. E. Russell, A. Rose, *Chem. Rev.* **2004**, *104*, 4613-4635.
[4] H. Imai, K. Izumi, M. Matsumoto, Y. Kubo, K. Kato, Y. Imai, *J. Am. Chem. Soc.* **2009**, *131*, 6293-6300.
[5] S. Mukerjee, J. McBreen, *J. Electroanal. Chem.* **1998**, *448*, 163-171.
[6] R. J. K. Wiltshire, C. R. King, A. Rose, P. P. Wells, H. Davies, M. P. Hogarth, D. Thompsett, B. Theobald, F. W. Mosselmans, M. Roberts, A. E. Russell, *Phys. Chem. Chem. Phys.* **2009**, *11*, 2305-2313.
[7] A. Rose, E. M. Crabb, Y. D. Qian, M. K. Ravikumar, P. P. Wells, R. J. K. Wiltshire, J. Yao, R. Bilsborrow, F. Mosselmans, A. E. Russell, *Electrochim. Acta* **2007**, *52*, 5556-5564.
[8] S. Mukerjee, S. Srinivasan, M. P. Soriaga, J. McBreen, *J. Electrochem. Soc.* **1995**, *142*, 1409-1422.

[9] S. W. T. Price, J. D. Speed, P. Kaman, A. E. Russell, *J. Am. Chem. Soc.* **2011**, *133*, 19448-19458.
[10] K. Sasaki, K. A. Kuttiyiel, L. Barrio, D. Su, A. I. Frenkel, N. Marinkovic, D. Mahajan, R. R. Adzic, *J. Phys. Chem. C* **2011**, *115*, 9894-9902.
[11] P. P. Wells, E. M. Crabb, C. R. King, R. Wiltshire, B. Billsborrow, D. Thompsett, A. E. Russell, *Phys. Chem. Chem. Phys.* **2009**, *11*, 5773-5781.
[12] T. Hyde, *Platinum Met. Rev.* **2008**, *52*, 129-130.
[13] S. Alayoglu, P. Zavalij, B. Eichhorn, Q. Wang, A. I. Frenkel, P. Chupas, *ACS Nano* **2009**, *3*, 3127-3137.
[14] A. Guinier, D. L. Dexter, *X-Ray Studies of Materials*, Interscience Publishers, New York, **1963**.
[15] X. Li, S. S. S. Fang, J. Teo, Y. L. Foo, A. Borgna, M. Lin, Z. Zhong, *ACS Catal.* **2012**, *2*, 360-369.
[16] H. Rietveld, *J. Appl. Crystallogr.* **1969**, *2*, 65-71.
[17] N. K. Nag, *J. Phys. Chem. B* **2001**, *105*, 5945-5949.
[18] A. Rose, S. Maniguet, R. J. Mathew, C. Slater, J. Yao, A. E. Russell, *Phys. Chem. Chem. Phys.* **2003**, *5*, 3220.
[19] M. Oezaslan, F. Hasche, P. Strasser, *Chem. Mater.* **2011**, *23*, 2159-2165.
[20] R. Z. Yang, P. Strasser, M. F. Toney, *J. Phys. Chem. C* **2011**, *115*, 9074-9080.
[21] F. Maillard, L. Dubau, J. Durst, M. Chatenet, J. André, E. Rossinot, *Electrochem. Commun.* **2010**, *12*, 1161-1164.
[22] H. Schnablegger, Y. Singh, *A Practical Guide to SAXS*, Anton Paar GmbH, Graz, **2006**.
[23] D. A. Stevens, S. Zhang, Z. Chen, J. R. Dahn, *Carbon* **2003**, *41*, 2769-2777.
[24] H. Borchert, E. V. Shevehenko, A. Robert, I. Mekis, A. Kornowski, G. Grubel, H. Weller, *Langmuir* **2005**, *21*, 1931-1936.
[25] V. Goertz, N. Dingenouts, H. Nirschl, *Part. Part. Syst. Charact.* **2009**, *26*, 17-24.
[26] T. Rieker, A. Hanprasopwattana, A. Datye, P. Hubbard, *Langmuir* **1999**, *15*, 638-641.
[27] W. Wang, X. Chen, Q. Cai, G. Mo, L. S. Jiang, K. Zhang, Z. J. Chen, Z. H. Wu, W. Pan, *Eur. Phys. J. B* **2008**, *65*, 57-64.
[28] M. C. Smith, J. A. Gilbert, J. R. Mawdsley, S. Seifert, D. J. Myers, *J. Am. Chem. Soc.* **2008**, *130*, 8112-+.
[29] G. Goerigk, H. G. Haubold, O. Lyon, J. P. Simon, *J. Appl. Crystallogr.* **2003**, *36*, 425-429.
[30] H. G. Haubold, T. Vad, N. Waldofner, H. Bonnemann, *J. Appl. Crystallogr.* **2003**, *36*, 617-620.
[31] H. G. Haubold, X. H. Wang, G. Goerigk, W. Schilling, *J. Appl. Crystallogr.* **1997**, *30*, 653-658.
[32] A. Benedetti, S. Polizzi, P. Riello, F. Pinna, G. Goerigk, *J. Catal.* **1997**, *171*, 345-348.
[33] A. Benedetti, L. Bertoldo, P. Canton, G. Goerigk, F. Pinna, P. Riello, S. Polizzi, *Catal. Today* **1999**, *49*, 485-489.
[34] S. Polizzi, P. Riello, G. Goerigk, A. Benedetti, *J. Synchrotron Radiat.* **2002**, *9*, 65-70.
[35] C. F. Yu, S. Koh, J. E. Leisch, M. F. Toney, P. Strasser, *Faraday Discuss.* **2008**, *140*, 283-296.
[36] S. Haas, G. Zehl, I. Dorbandt, I. Manke, P. Bogdanoff, S. Fiechter, A. Hoell, *J. Phys. Chem. C* **2010**, *114*, 22375-22384.
[37] J. Larminie, A. Dicks, *Fuel Cell Systems Explained*, Second ed., Wiley, Chichester, **2003**.
[38] H. A. Gasteiger, S. S. Kocha, B. Sompalli, F. T. Wagner, *Appl. Catal., B* **2005**, *56*, 9-35.
[39] B. Hammer, J. K. Norskov, *Surface Science* **1995**, *343*, 211-220.
[40] B. Hammer, J. K. Norskov, in *Advances in Catalysis, Vol 45: Impact of Surface Science on Catalysis* (Eds.: B. C. Gates, H. Knozinger), Elsevier Academic Press Inc, San Diego, **2000**, pp. 71-129.
[41] N. M. Markovic, P. N. Ross, *Surf. Sci. Rep.* **2002**, *45*, 121-229.

[42] J. Greeley, I. E. L. Stephens, A. S. Bondarenko, T. P. Johansson, H. A. Hansen, T. F. Jaramillo, J. Rossmeisl, I. Chorkendorff, J. K. Norskov, *Nat. Chem.* **2009**, *1*, 552-556.
[43] J. L. Zhang, M. B. Vukmirovic, Y. Xu, M. Mavrikakis, R. R. Adzic, *Angew. Chem., Int. Edit.* **2005**, *44*, 2132-2135.
[44] A. U. Nilekar, M. Mavrikakis, *Surf. Sci.* **2008**, *602*, L89-L94.
[45] R. R. Adzic, J. Zhang, K. Sasaki, M. B. Vukmirovic, M. Shao, J. X. Wang, A. U. Nilekar, M. Mavrikakis, J. A. Valerio, F. Uribe, *Top. Catal.* **2007**, *46*, 249-262.
[46] J. Zhang, M. B. Vukmirovic, K. Sasaki, F. Uribe, R. R. Adzic, *J. Serb. Chem. Soc.* **2005**, *70*, 513-525.
[47] J. Zhang, Y. Mo, M. B. Vukmirovic, R. Klie, K. Sasaki, R. R. Adzic, *J. Phys. Chem. B* **2004**, *108*, 10955-10964.
[48] B. C. Tessier, *PhD Thesis: Preparation, Characterisation and Evaluation of Core-Shell Electrocatalysts for PEMFCs*, University of Southampton, **2009**.
[49] P. Wells, *PhD Thesis: Controlled Suface Modification of Supported Platinum Group Metal Catalysts*, **2007**.
[50] E. M. Crabb, M. K. Ravikumar, *Electrochim. Acta* **2001**, *46*, 1033-1041.
[51] E. M. Crabb, M. K. Ravikumar, Y. Qian, A. E. Russell, S. Maniguet, J. Yao, D. Thompsett, M. Hurford, S. C. Ball, *Electrochem. Solid State Lett.* **2002**, *5*, A5-A9.
[52] E. M. Crabb, M. K. Ravikumar, D. Thompsett, M. Hurford, A. Rose, A. E. Russell, *Phys. Chem. Chem. Phys.* **2004**, *6*, 1792-1798.
[53] K. Sasaki, H. Naohara, Y. Cai, Y. M. Choi, P. Liu, M. B. Vukmirovic, J. X. Wang, R. R. Adzic, *Angew. Chem., Int. Edit.* **2010**, *49*, 8602-8607.
[54] S. C. Ball, *World J. Eng.* **2010**, *19*, 87.

CHAPTER TWO: CATALYSTS AND THEIR CHARACTERISATION

This chapter details the synthesis of the Pd-core, Pt-shell electrocatalysts used throughout this work and the initial structural characterisation carried out on them. The electrochemical techniques employed in this project are also introduced, with the theoretical and experimental aspects being described, along with the development of the in situ cell used for the X-ray characterisation methods detailed in Chapters Three to Five.

1 Reagents

Table 1 gives details of the reagents and materials used in this work, along with their respective suppliers.

Table 1: List of reagents and materials used with their respective suppliers

Material/Reagent	**Supplier**
High surface area carbon	Johnson Matthey
$Pd(NO_3)_2$	Johnson Matthey
NaOH	Aldrich
$C_5H_8O_2$	Fluka Chemika
K_2PtCl_4	Johnson Matthey
KOH	Alfa Aesar
$Pt(acac)_2$	Johnson Matthey
Toluene	Sigma-Aldrich
Teflonated carbon paper	Toray
40 wt% Pt/C	Johnson Matthey Technology Centre
Aqueous Nafion solution (10.85% solids)	Johnson Matthey Technology Centre
H_2SO_4	Fisher Scientific
H_2	BOC
N_2	BOC
CO	BOC

2 Catalyst Preparation

$Pt_{0.5ML}$/Pd/C, Pt_{1ML}/Pd/C, Pt_{2ML}/Pd/C, Pt_{4ML}/Pd/C (Pd-core, Pt-shell) and Pt/Pd/C (alloy) electrocatalysts were synthesised by the controlled surface reaction (CSR) mentioned in Chapter One using a $Pt(acac)_2$ precursor.[1] The details of each stage of the synthesis are given in the following sections.

2.1 Preparation of Pd/C Core

40 g of the 20 wt% Pd/C core material was prepared via the precipitation and deposition of Pd onto the carbon support followed by a hydrogen reduction step. A carbon slurry was first prepared by dispersing 34 g of the carbon support (6 wt% H_2O, determined by thermogravimetric analysis) in 4 L of demineralised water using a Silverson mixer at 50 Hz for 30 minutes. In the meantime, 56.5 g $Pd(NO_3)_2$ (14.2 wt% Pd) was diluted to 400 mL in demineralised water. The carbon slurry was then transferred to the 10 L reaction vessel equipped with a paddle stirrer and diluted further with demineralised water. The Pd solution was added slowly over a period of two hours to the stirred slurry using a peristaltic pump, with an autotitrator being used to add 1 M NaOH simultaneously whilst maintaining pH 7. Following the addition of the reactants to the slurry, the mixture was stirred for 90 minutes at room temperature. The product was filtered off and washed repeatedly with demineralised water until the conductivity of the filtrate measured less than 10 μS, thus indicating that most of the sodium and nitrate ions had been removed from the catalyst. The resulting $Pd(OH)_2$/C was dried overnight in air at 105 °C then sieved (1.70 mm then 0.15 mm mesh), before being reduced to Pd/C in 5% H_2/N_2 at 200 °C for 2 hours with the aim of obtaining a particle size of around 3 nm. The particle size was subsequently determined using transmission electron microscopy (TEM) and is reported in Section 3.3.

2.1.1 CO Chemisorption

CO chemisorption measurements were used to determine the dispersion (*D*) of the Pd, with dispersion defined as the proportion of surface atoms with respect to the total number of atoms. The measurements were conducted using an automated chemisorption instrument at Johnson Matthey Technology Centre. Around 25 mg of the Pd/C was placed in a glass u-tube which was then connected to the gas inlet and outlet ports of the instrument. The catalyst was reduced under hydrogen at 50 °C for 30 minutes then allowed to cool. Carbon monoxide was flowed through the sample, with the amount of CO leaving the cell monitored until no change was seen, meaning that the reduced metal

surface was therefore saturated with CO. The mass of the sample used and the number of moles of CO adsorbed were recorded by the instrument, thus allowing the dispersion to be calculated using Equation 2.1:

$$D\ (\%) = \frac{\left(\frac{n\mathrm{CO}}{\mathrm{mass}_{\ \mathrm{sample}}}\right)}{\left(\frac{\mathrm{wt\%\ Metal}}{MM\ (\mathrm{Metal})}\right)}$$

Equation 2.1

Where *n*CO is the number of moles of CO adsorbed in mol, $\mathrm{mass}_{\mathrm{sample}}$ is the mass of the sample used in g, wt% Metal is the metal loading on the carbon support (determined by ICP-ES analysis as described in Section 3.1) and *MM* (Metal) is the molar mass of the metal in the catalyst. Equation 2.1 assumes 1:1 metal-CO bonding whereas for Pd the average chemisorption stoichiometry is 2:1, therefore, the calculated dispersion needed to be doubled.[2] The measurement was carried out several times and an average dispersion of 50% was obtained.

2.2 Preparation of $Pt(acac)_2$

To prepare the $Pt(acac)_2$, 26.4 g K_2PtCl_4 was dissolved in 650 mL demineralised water in a 3-neck round bottomed flask and purged with N_2. The conjugate base acetylacetonate ($C_5H_7O_2^-$) was formed by mixing 93.8 mL acetylacetone ($C_5H_8O_2$) with 187.5 mL 1 M KOH and added to the red Pt solution. The reaction mixture was refluxed until the colour changed to yellow then cooled down under N_2. The resulting yellow solid was filtered off and dried overnight in a vacuum oven at 40 °C. This was all carried out in a glove box to avoid sensitisation to the Pt salt. The product was purified by Soxhlet extraction, using toluene as the solvent. The toluene was removed by rotary evaporation following completion of the extraction.

2.3 Controlled Surface Reaction

The experimental set-up used for the controlled surface reaction (CSR) is shown in Figure 2.1. 2 g of Pd/C was added to the 5-necked round-bottomed flask. The flask was fitted with a dropper for the addition of the $Pt(acac)_2$ solution, a condenser to reduce the loss of solvent, a temperature probe and a gas inlet tube. The flask was purged with N_2 for 30 minutes after which the gas was switched to H_2 and the catalyst was reduced at 200 °C for 30 minutes then left to cool.

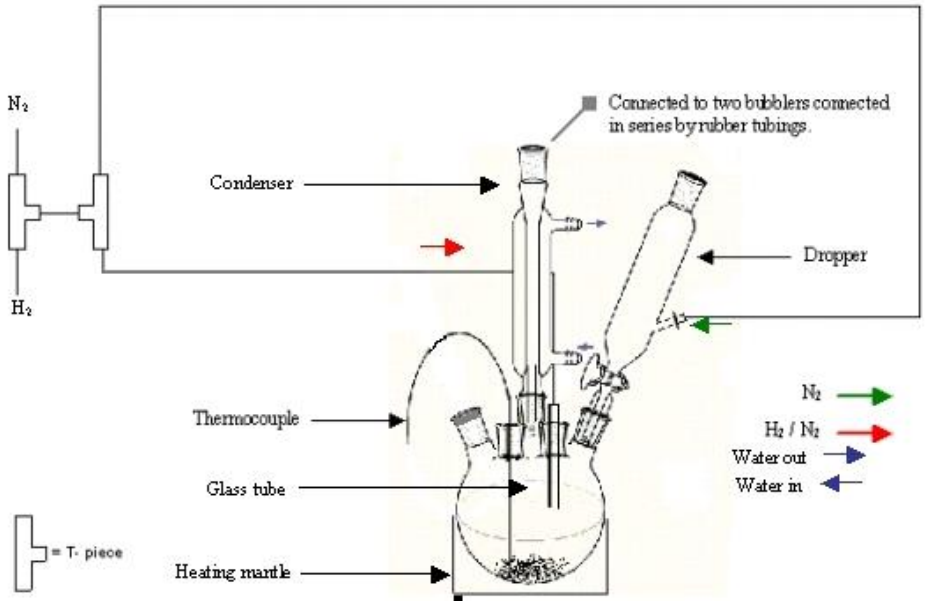

Figure 2.1: Diagram of the equipment set-up used for the controlled surface reaction

The required amount of $Pt(acac)_2$ to achieve the desired coverage on the Pd core catalyst was dissolved in toluene and added to the dropper, where it was purged with N_2 for 30 minutes. The mass of $Pt(acac)_2$ needed was calculated based on the dispersion of Pd to give the required number of monolayers as shown in Equation 2.2

$$\text{Mass Precursor} = \frac{\text{wt\% Pd} \times \text{mass Pd/C} \times D \times x \times \text{RMM Pt(acac)}_2}{\text{RMM Pd}}$$

Equation 2.2

Where wt% Pd is the Pd loading of the catalyst, D is the dispersion of Pd and x is the number of monolayers.

The $Pt(acac)_2$ solution was added to the flask while flowing H_2 and the temperature was raised to 90 °C. The reaction mixture was then stirred at 90 °C under H_2 for 6 hours after which the gas was switched back to N_2 and the vessel allowed to cool. The catalyst was filtered off, washed with toluene and dried in a fume cupboard overnight. To remove any adsorbed organic species, the catalysts were heat-treated at 140 °C in 5% H_2/N_2 for 90 minutes. The catalyst was then passivated after cooling by gradually increasing the concentration of air in the N_2 flow to prevent self-ignition of the catalyst upon full exposure to air. The Pt/Pd/C alloy was prepared from a Pt_{2ML}/Pd/C catalyst which was subsequently heat-treated at 863 °C.

3 Characterisation

Initial characterisation using ICP-ES, powder XRD and TEM with EDX was carried out on the prepared electrocatalysts to determine the metal assay, crystallinity, particle size and elemental distribution at the Johnson Matthey Technology Centre by members of the analytical group as indicated below. High-resolution TEM (HRTEM) was also performed by Haibo E (Oxford University).

3.1 Inductively Coupled Plasma Emission Spectroscopy (ICP-ES)

ICP-ES is used to determine the concentration of a particular element in a sample. The sample is decomposed using intense heat generated by the ICP source into a cloud containing free atoms and ions. The excited atoms then return to their ground state, emitting light at a wavelength characteristic of the element. The intensity of the emission is then used to determine the concentration. The ICP-ES analysis was carried out by Godson Nnorom-Junior.

Table 2 compares the theoretical composition of the Pt/Pd/C catalysts with the yield composition as determined by ICP-ES analysis. It can be seen that the wt% Pt yield is slightly lower in each case than the theoretical wt%, however the agreement is fairly good and indicates successful deposition.

Table 2: ICP-ES elemental analysis of Pt/Pd/C catalysts

	Theoretical Composition / wt%		Yield Composition / wt%	
Catalyst	Pt	Pd	Pt	Pd
$Pt_{0.5ML}$/Pd/C	8.4	17.9	8.1	17.9
Pt_{1ML}/Pd/C	17.1	16.3	16.3	16.1
Pt_{2ML}/Pd/C	27.5	14.2	26.4	14.2
Pt_{4ML}/Pd/C	41.9	11.4	38.9	11.2
Pt/Pd/C	28.3	14.1	27.6	14.8

3.2 Powder X-Ray Diffraction

Powder X-ray diffraction (XRD) was used to identify the metallic phases within the catalyst particles and to determine the average crystallite size of the particles. The analysis was carried out using a Bruker AXS D8 diffractometer with a Ni filtered Cu K_α X-ray source. The metallic phases were identified by comparison of the diffraction patterns with known standards, in this case Pt and Pd. Rietveld analysis was carried out using Topas 4 and Bruker-AVS software to determine the crystallite size and lattice parameters, with the presence of amorphous material being determined by comparison of the intensity with that of reference samples. The theory behind XRD will be discussed in detail in Chapter Three. The data collection and analysis was carried out by Hoi Jobson and James McNaught.

The XRD patterns obtained for all samples are shown below in Figures 3.1 to 3.3. A broad diffraction peak is seen in all samples at $2\theta \approx 25°$ which is due to the carbon support. All samples showed poor crystallinity due to the small size of the particles. The metallic phase identification of the Pd/C core material (Figure 3.1) indicated that the predominant phase identified was very poorly crystalline cubic palladium with no evidence of any additional crystalline phases. The diffraction pattern from the Pt/Pd/C alloy (Figure 3.2) showed a poorly crystalline Pt/Pd alloy phase which was intermediate in lattice parameters between Pt and Pd, thus indicating a relatively well-mixed alloy.

The diffraction patterns of the core-shell samples are shown in Figure 3.3, with zoomed in patterns focused on the (220), (311) and (222) peaks shown Figure 3.4. The 0.5 ML and 1 ML core-shell samples both showed a major amount of poorly crystalline cubic Pd and amorphous material with no indication of any other crystalline phases, showing that the addition of this amount of Pt has not had an effect on the crystallinity of the sample. The diffraction pattern of Pt_{2ML}/Pd/C showed a major amount of a poorly crystalline phase which was shifted very subtly to lower 2θ from the cubic palladium reference along with amorphous material. A further shift to lower 2θ was observed in the diffraction pattern of the Pt_{4ML}/Pd/C sample which can be seen more clearly in Figure 3.4. These shifts may be due to some alloying between the Pt and Pd at the interface between the core and the shell or to a Pt phase distorted by the Pd core.

Comparison of the diffraction patterns of the core-shell samples (Figure 3.3) with that of the Pt/Pd/C alloy (Figure 3.2) suggests that the core-shell samples do indeed contain two

separate phases, one of poorly crystalline Pd and an amorphous phase presumed to contain the Pt, rather than the clearly mixed Pt/Pd phase seen in the alloy.

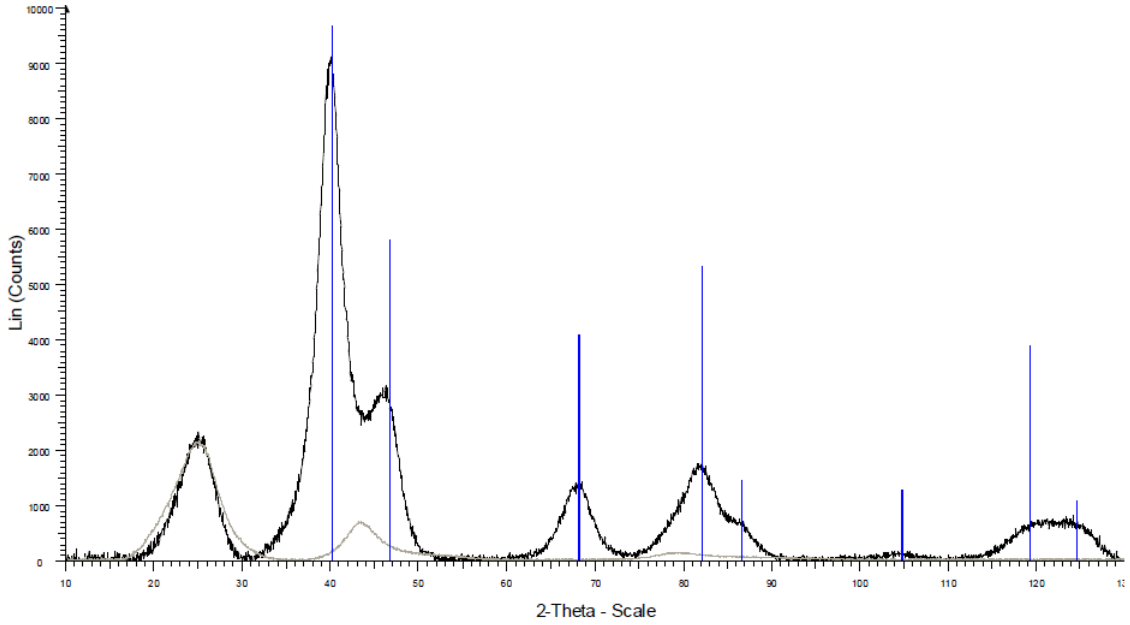

Figure 3.1: XRD Pattern of 20 wt% Pd/C core material (black line) compared with the XRD pattern of the carbon support (grey line) and the cubic Pd reference (PDF No. 00-046-1043) (|)

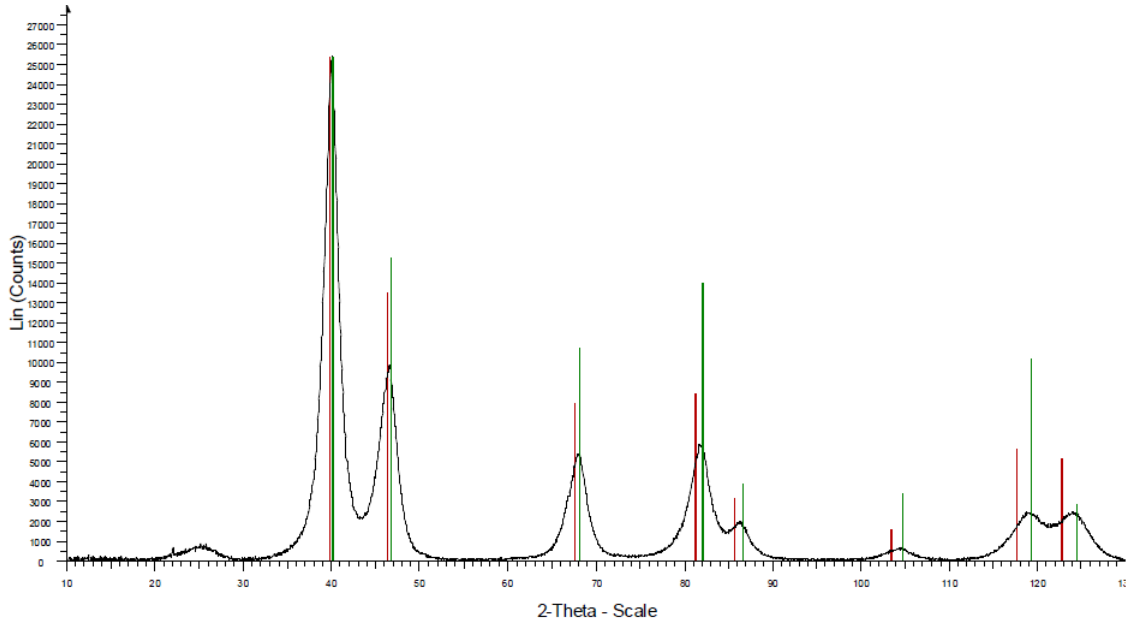

Figure 3.2: XRD Pattern of Pt/Pd/C alloy (black line) compared with the cubic Pd reference (PDF No. 00-046-1043) (|) and the cubic Pt reference (PDF No. 00-004-0802) (|)

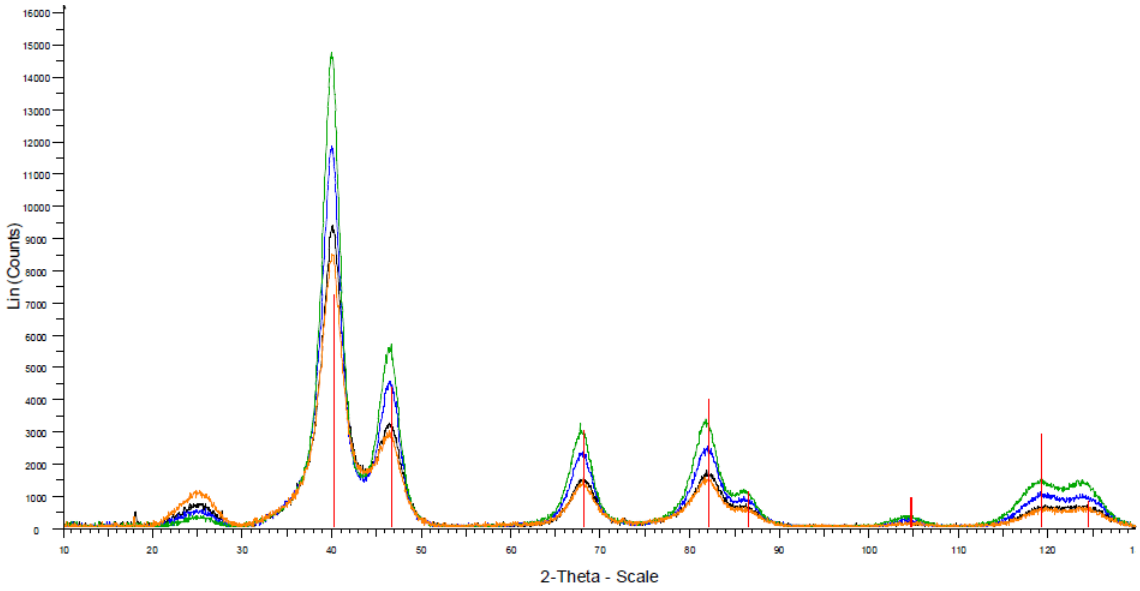

Figure 3.3: XRD Patterns of $Pt_{0.5ML}$/Pd/C (orange line), Pt_{1ML}/Pd/C (black line), Pt_{2ML}/Pd/C (blue line) and Pt_{4ML}/Pd/C (green line) compared with the cubic Pd reference (PDF No. 00-046-1043) (|)

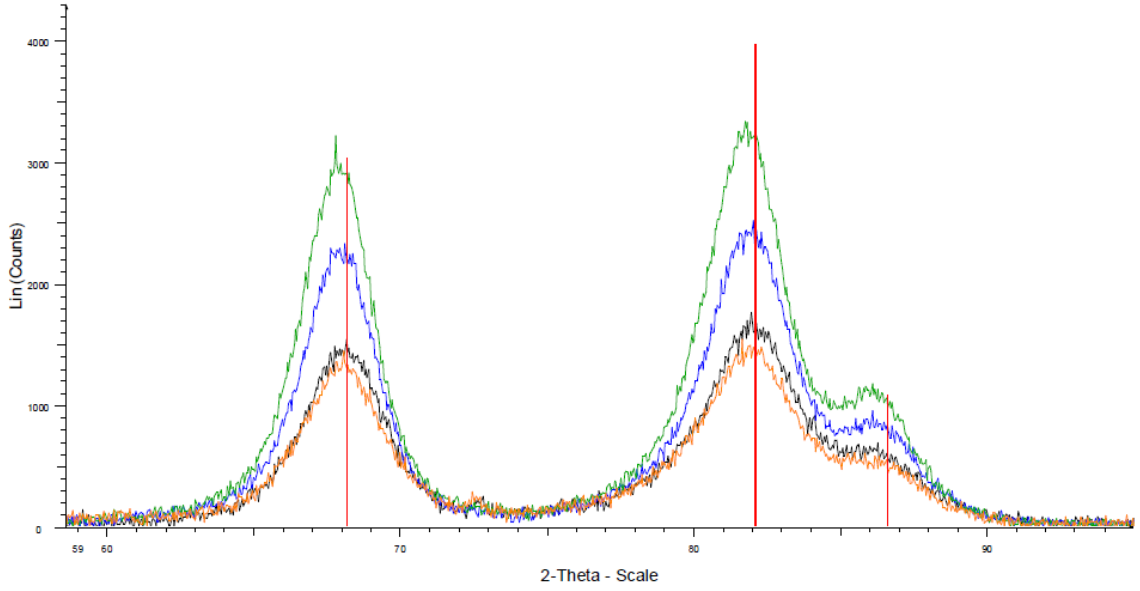

Figure 3.4: XRD Patterns shown in Figure 3.3 zoomed in on (l-r) the (220), (311) and (222) peaks of $Pt_{0.5ML}$/Pd/C (orange line), Pt_{1ML}/Pd/C (black line), Pt_{2ML}/Pd/C (blue line) and Pt_{4ML}/Pd/C (green line) compared with the cubic Pd reference (PDF No. 00-046-1043) (|)

Rietveld analysis was carried out on all samples with the crystalline size and lattice parameters obtained given in Table 3. Due to the poor crystallinity of the samples, in particular the Pd/C core material, the calculated values can only really be regarded as estimates of the particle sizes.

Table 3: Crystallite size and lattice parameters obtained by Rietveld analysis

Catalyst	XRD Crystallite Size / nm	Lattice Parameter (a = b = c) / Å
Pd/C	~ 1.6	3.899 ± 0.001
$Pt_{0.5ML}Pd/C$	2.60 ± 0.06	3.8958 ± 0.0006
$Pt_{1ML}Pd/C$	2.30 ± 0.07	3.8896 ± 0.0007
$Pt_{2ML}Pd/C$	2.54 ± 0.05	3.8969 ± 0.0005
$Pt_{4ML}Pd/C$	2.63 ± 0.05	3.9038 ± 0.0004
Pt/Pd/C Alloy	3.13 ± 0.04	3.9018 ± 0.0004
Pt Reference	n/a	3.92310
Pd Reference	n/a	3.89019

3.3 Transmission Electron Microscopy and Energy Dispersive X-Ray Spectroscopy

Transmission electron microscopy (TEM) was used to determine the particle size of the electrocatalysts and their dispersion on the carbon support, with energy dispersive X-ray (EDX) spectroscopy being used to determine the distribution of the Pt and Pd over a region within the sample. In TEM, a high energy beam of electrons is focused on a thin sample, with the electrons transmitted through the sample being detected by a fluorescent screen to give a 2D projection of the size and shape of the sample. This mode of detection is known as bright field (BF). The particle size distribution is then determined by analysing the particles seen in several images. In EDX, X-rays emitted by the sample due to the bombardment by the electron beam are detected, allowing for elemental analysis. The electron beam can be scanned across the sample to give a line profile of the distribution of elements.

To prepare the samples for analysis the catalyst was ground between two glass slides and dusted onto a holey carbon coated Cu TEM grid. A Tecnai F20 Transmission Electron Microscope operated with a voltage of 200 kV was used. The measurements and analysis were carried out by Steve Spratt and Don Ozkaya.

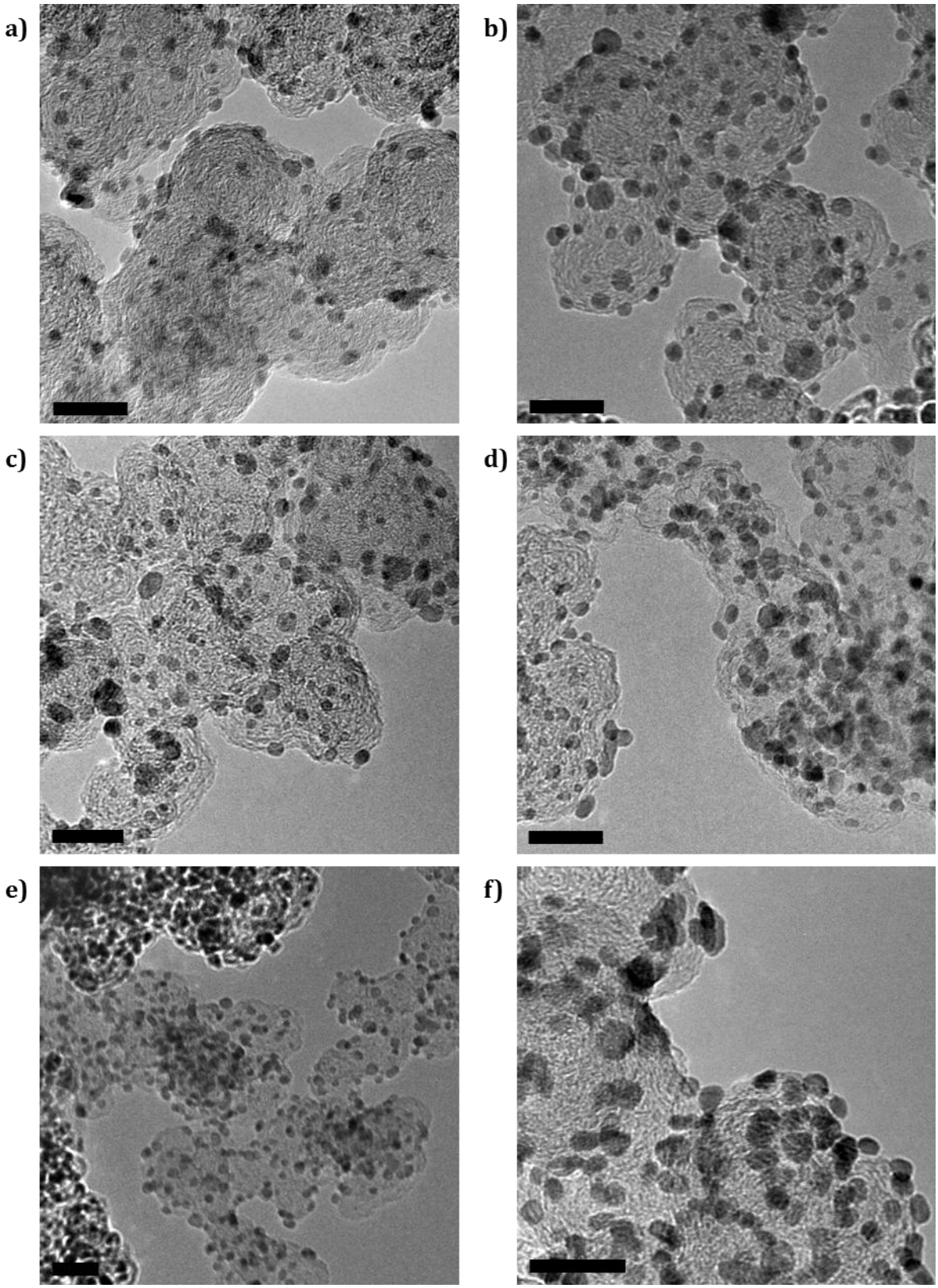

Figure 3.5: TEM micrographs of Pd/C core material (a), Pt/Pd/C alloy (b), $Pt_{0.5ML}$/Pd/C (c), Pt_{1ML}/Pd/C (d), Pt_{2ML}/Pd/C (e) and Pt_{4ML}/Pd/C (f), where the scale bar represents 20 nm.

Figure 3.5 shows the bright field TEM micrographs obtained of the Pd/C core, Pt/Pd/C alloy and $Pt_{0.5ML}$/Pd/C, Pt_{1ML}/Pd/C, Pt_{2ML}/Pd/C and Pt_{4ML}/Pd/C core-shell materials. It can be seen that in all cases the metal nanoparticles are well dispersed on the carbon support. Particle size analysis was carried out on the micrographs shown, with the particle sizes obtained given in Table 4. There are large differences in the particle sizes determined by TEM and the crystallite sizes calculated from XRD, in particular for the Pd/C core material, due to the low crystallinity of the nanoparticles. An increase in particle size is seen with increasing Pt coverage from one to four monolayers for the Pt/Pd/C catalysts, however, the particle sizes of Pd/C and $Pt_{0.5ML}$/Pd/C are larger than that of Pt_{1ML}/Pd/C and Pt_{2ML}/Pd/C. A possible explanation for this is that the coverage of the Pd/C material by a complete Pt monolayer causes a contraction of the Pd lattice for the Pt_{1ML}/Pd/C sample as seen in Table 3.

Table 4: Mean particle size obtained from TEM

Catalyst	TEM Mean Particle Size / nm (σ)	Number of Observed Particles
Pd/C	3.80 (2.12)	733
$Pt_{0.5ML}$Pd/C	3.70 (1.35)	166
Pt_{1ML}Pd/C	3.04 (1.57)	83
Pt_{2ML}Pd/C	3.63 (1.37)	95
Pt_{4ML}Pd/C	4.32 (1.32)	166
Pt/Pd/C	3.80 (1.46)	98

Figure 3.6 shows the EDX analysis of the Pt_{1ML}/Pd/C sample. From the line profile it can be seen that the Pt and Pd are present in the same regions of the sample area investigated, showing that the Pt and Pd exist in the same particles rather than as separate particles of Pt and Pd. This was the case for all Pt/Pd/C samples.

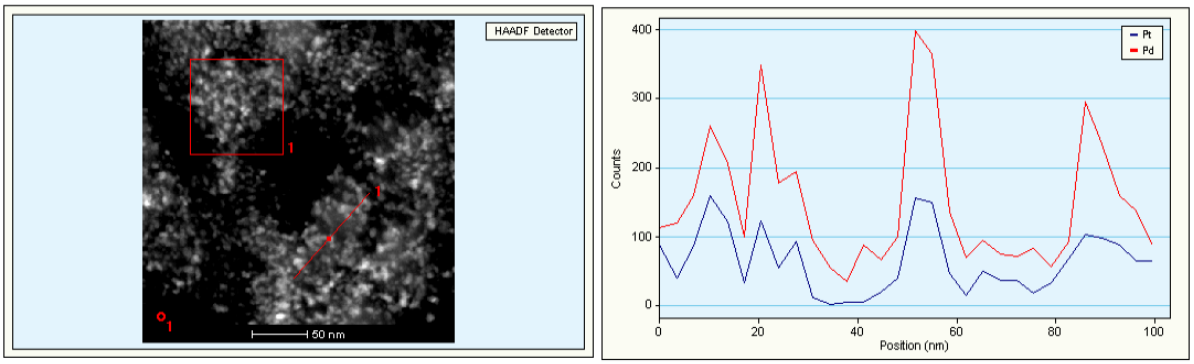

Figure 3.6: Transmission Electron Micrograph and the corresponding EDX Line Profile of $Pt_{1ML}/Pd/C$

3.4 High Resolution Transmission Electron Microscopy

Another detection mode used in TEM is the high angle annular dark field mode (HAADF), which detects the backscattered electrons and is based on a Z^2 contrast mechanism, enabling the distribution of different elements to be detected. Combining HAADF detection with a scanning transmission electron microscopy (STEM) probe allows for higher spatial resolution (up to 0.1 nm) due to the finely focused high energy electron beam used in STEM. At this level the resolution is limited by spherical aberration which is caused by the microscope lenses focusing electrons from the sides of the lens to a different point compared to the electrons scattered from the centre of the lens. This can be corrected for by using non-spherical lenses in a system known as aberration corrected TEM, enabling spatial resolution of distances below 0.1 nm.

High resolution TEM micrographs were recorded in HAADF detection mode by Haibo E at the Department of Materials, University of Oxford, using an aberration-corrected STEM instrument. Figure 3.7 shows HRTEM images of the $Pt_{2ML}/Pd/C$ catalyst. Some variation in the particle size can be seen but most of the particles are of a similar size and shape. The brighter atoms seen around the top of the particle in image B of Figure 3.7 can be attributed to a Pt shell, which was confirmed by EDX point analysis. EDX line analysis showed a higher presence of Pt around the edges of all the particles investigated, indicative of a core-shell structure.

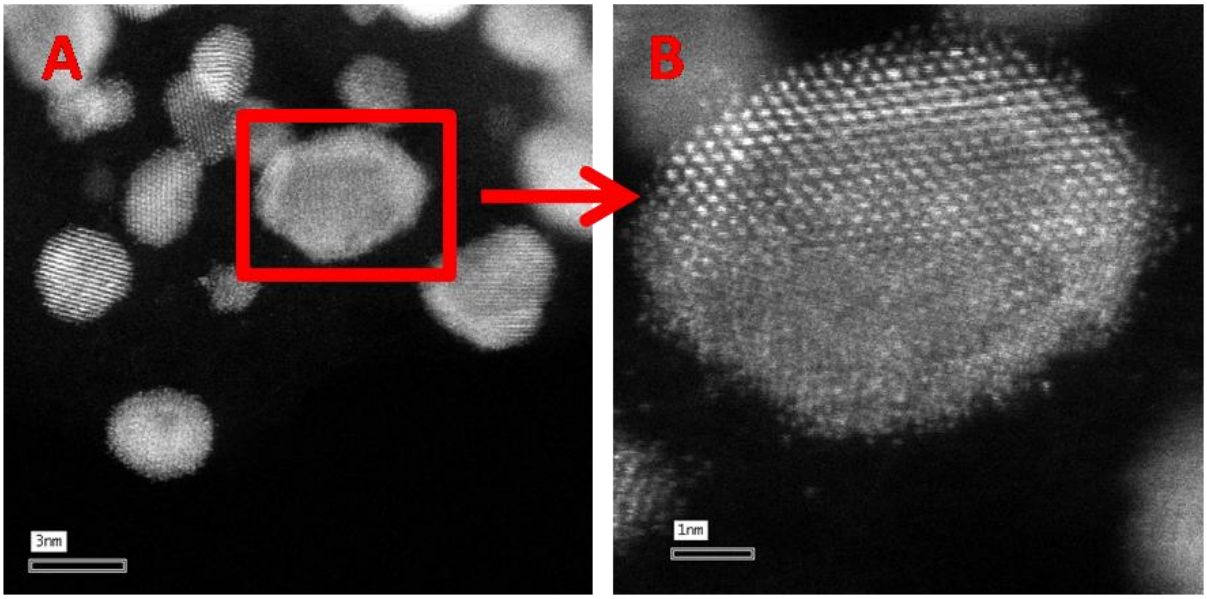

Figure 3.7: HRTEM images of $Pt_{2ML}/Pd/C$

4 Electrochemical techniques

4.1 General Theory

The electrochemical characterisation of fuel cell electrocatalysts is of key importance for determining their effective catalytic surface area and stability. Two techniques commonly employed for this purpose are cyclic voltammetry (CV) and CO oxidation voltammetry.

Cyclic voltammetry is carried out by sweeping the potential, E, of the working electrode from E_1 to E_2 and back to E_1 at a constant sweep rate, repeating these cycles as necessary. The potential is controlled between the working electrode and the reference electrode and the current is measured between the counter electrode and working electrode. The current is recorded as a function of potential, providing information about the redox processes occurring at the electrode.[3]

The heterogeneous reactions of fuel cells can be studied using cyclic voltammetry by focusing on adsorbed species on the surface of the electrode to gain information about the number, type and reactivity of the available catalytic sites. Figure 4.1 shows a typical cyclic voltammogram (CV) of a Pt/C electrode. The CV can be divided into three separate regions as shown, where region A is the hydrogen region, region B is the double layer region and region C is the oxide region.

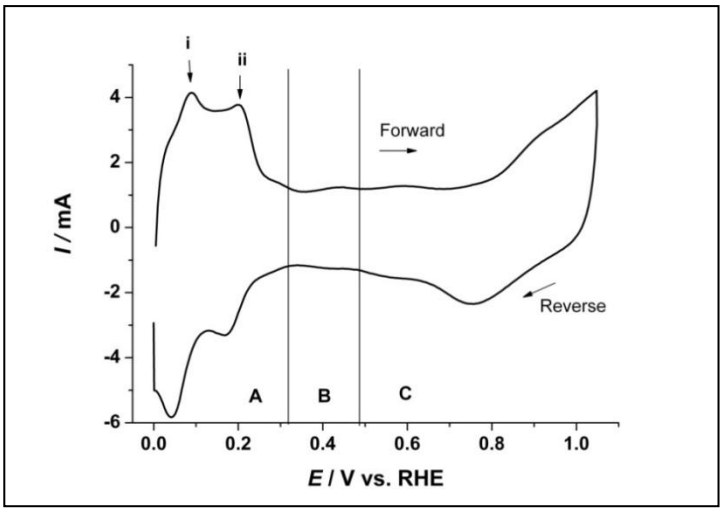

Figure 4.1: Typical cyclic voltammogram of a Pt/C electrode

The hydrogen region corresponds to the adsorption and desorption of hydrogen atoms during the reverse and forward scans respectively, as shown in Equation 4.1. The two peaks seen on each scan correspond to two different adsorption sites with different strengths of adsorption, where i represents the more weakly bound hydrogen atoms which require a lower overpotential for desorption.

$$Pt + H^+ + e^- \leftrightarrow Pt\text{-}H_{ads}$$

Equation 4.1

The area of the hydrogen adsorption peak can be used to calculate the Pt area of the electrode as hydrogen adsorbs to form a complete monolayer. This electrochemical Pt surface area (EPSA) can then be normalised with respect to the Pt loading to give an electrochemical surface area (ECA) and enable the direct comparison of different electrocaytalysts. These calculations are shown in Equation 4.2 and Equation 4.3, where the charge density = 210 μC cm^{-2} and n is the number of electrons involved in the process.

$$\text{EPSA } (cm^2_{Pt}) = \frac{\text{Charge (C)}}{n \times \text{Charge density (C } cm^{-2}) \times \text{ Electrode Area } (cm^2)}$$

Equation 4.2

$$\text{ECA } (m^2_{Pt}\ g^{-1}_{Pt}) = \frac{\text{EPSA } (cm^2_{Pt})}{\text{Loading } (mg_{Pt} cm^{-2}) \times 10}$$

Equation 4.3

The current response observed in the double layer region is due to the double layer charging of the catalyst and carbon support, with no chemical processes taking place.

In the oxide region, the peak seen in the forward scan can be attributed to the formation of an oxide layer via Pt-OH_{ads} → Pt-O_{ads} → Pt-O_{2ads} with increasing overpotential, eventually leading to the onset of oxygen evolution at approximately 1.23 V vs. RHE. The peak seen at 0.75 V vs. RHE on the reverse scan in Figure 4.1 is the oxide removal peak. Integration of the oxide growth and oxide removal peaks shows that not all of the oxide is removed, which, along with the relatively high overpotential required to remove the oxide, points to some of the oxide growth being irreversible on the timescale of the potential sweep. It is thought that the oxygen enters the bulk of the Pt via a place exchange mechanism, resulting in a build-up of sub-surface oxygen which alters the Pt structure.[4] This sub-surface oxygen is removed more slowly.

Another method used to determine the ECA of a catalyst is CO oxidation voltammetry. CO has a high affinity for Pt and will adsorb onto the surface to form a monolayer. Figure 4.2 shows an example of cyclic voltammograms recorded of a Pt/C electrode with a monolayer of CO adsorbed onto the surface. The large peak seen at 0.85 V vs. RHE in the first scan arises from the oxidation of CO to CO_2, thus removing the CO from the catalyst surface and resulting in a Pt CV in the second scan.

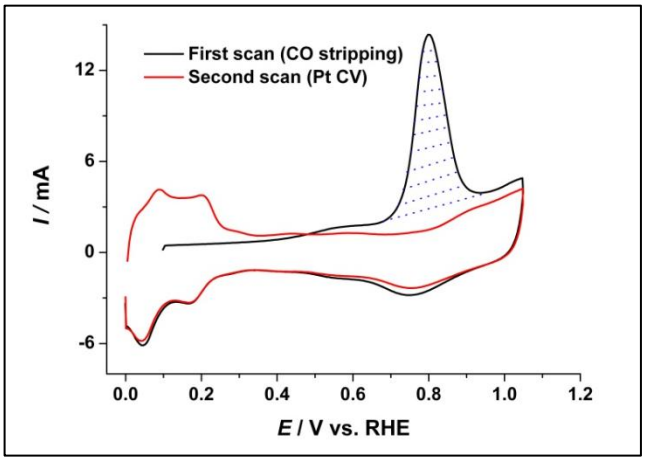

Figure 4.2: Example of CO oxidation voltammetry of a Pt/C electrode

The oxidation of CO to CO_2 is a two electron process as shown in Equation 4.4.[5]

$$Pt\text{-}CO_{ads} + H_2O \rightarrow Pt + CO_2 + 2H^+ + 2e^-$$

Equation 4.4

Integration of the CO oxidation peak can be used to calculate the ECA using Equation 4.2 and Equation 4.3 as detailed for the hydride adsorption peak area. The position of the CO oxidation peak can also give information about the CO tolerance of the catalyst, as the overpotential required to oxidise CO is directly related to the relative ease of oxidation. The strong adsorption of CO onto Pt is a problem in fuel cells as it results in the blocking of catalyst sites and thus a reduction in activity. CO tolerance is of particular concern in reformate-fed PEMFCs.

4.2 Experimental Aspects

4.2.1 Preparation of Electrodes

Catalyst electrodes were prepared by brush-coating a catalyst-ionomer ink onto teflonated carbon paper to give an electrode of a desired Pt loading. The ink was prepared by sonication and homogenisation of a mixture of the catalyst powder, aqueous Nafion solution and demineralised water, with the volume of Nafion used calculated to give a loading of 80% wrt. carbon and the water added as necessary to obtain an ink of a suitable viscosity. Thin layers of ink were painted onto the carbon paper, drying the electrode and rotating it 90° between coats to ensure an even distribution of ink on the electrode. Once the desired loading had been reached the electrode was hot-pressed at 180 °C to bind the ink to the carbon paper. Before electrochemical testing, the electrodes were hydrated by boiling in demineralised water.

4.2.2 Electrochemical Cell Configuration

The electrochemical measurements were conducted in a half-cell using a three-electrode configuration as described in Section 4.1. For this work a mercury mercurous sulphate (MMS) reference electrode was used (0.69 V vs. RHE), connected to the cell via a Luggin capillary, with a Pt gauze counter electrode. The working electrode consisted of the painted button electrode (typically 1 cm diameter) held in place using a either a gold or a platinum wire. The electrode potential was controlled using an Autolab PGSTAT30 potentiostat.

4.2.3 Electrochemical Methods

The electrochemical cell was filled with 1 M H_2SO_4 (~100 mL) and purged with N_2 for 20 minutes to deaerate the electrolyte, after which the N_2 flow was maintained over the electrolyte to prevent air entering the system while avoiding the bubbles disrupting the electrochemical measurements. Measurements were conducted either at room temperature or at 80 °C to emulate the working conditions of a fuel cell, with temperature control achieved via a circulating water bath connected to the jacketed cell. Cyclic voltammograms were typically recorded between 0.02 and 1.00 V vs. RHE with a sweep rate of 10 mV s^{-1}. CO oxidation voltammetry measurements were carried out by holding the potential at 0.15 V vs. RHE, while purging first with CO for 15 minutes to adsorb CO onto the electrocatalyst surface, then with N_2 for 30 minutes to remove any excess CO from the solution. The potential was then swept cyclically from 0.15 to 1.00 to 0.02 V vs. RHE for three cycles with a sweep rate of 10 mV s^{-1}.

4.2.4 Electrochemical Data

Examples of the cyclic voltammograms (CVs) and CO oxidation CVs of $Pt_{0.5ML}$/Pd/C, Pt_{1ML}/Pd/C, Pt_{2ML}/Pd/C, Pt_{4ML}/Pd/C and Pt/Pd/C are shown in Figure 4.3 and Figure 4.4 to illustrate the data obtained, with a more detailed discussion of the electrochemical characteristics of the samples given in Chapter Four. It can be seen from the CVs in Figure 4.3 that the hydrogen region is not well defined in any of the prepared catalysts, however the peak on the reverse scan at 0.1 V vs. RHE of the 1, 2 and 4 monolayer catalysts corresponds with the peak seen in the CV of Pt, suggesting a Pt-like surface. Figure 4.4 shows a shift in the CO oxidation peak position for the 0.5, 1 and 4 Pt monolayer catalysts to lower potentials more characteristic of a Pt-only catalyst as the amount of Pt is increased. The CO oxidation peak of the Pt_{2ML}Pd/C catalyst is recorded at a higher potential than would be expected given the trend seen with the increasing shell thickness for 0.5, 1 and 4 Pt monolayers. In all cases the CO oxidation peak is at a significantly lower potential than for the Pd/C material.

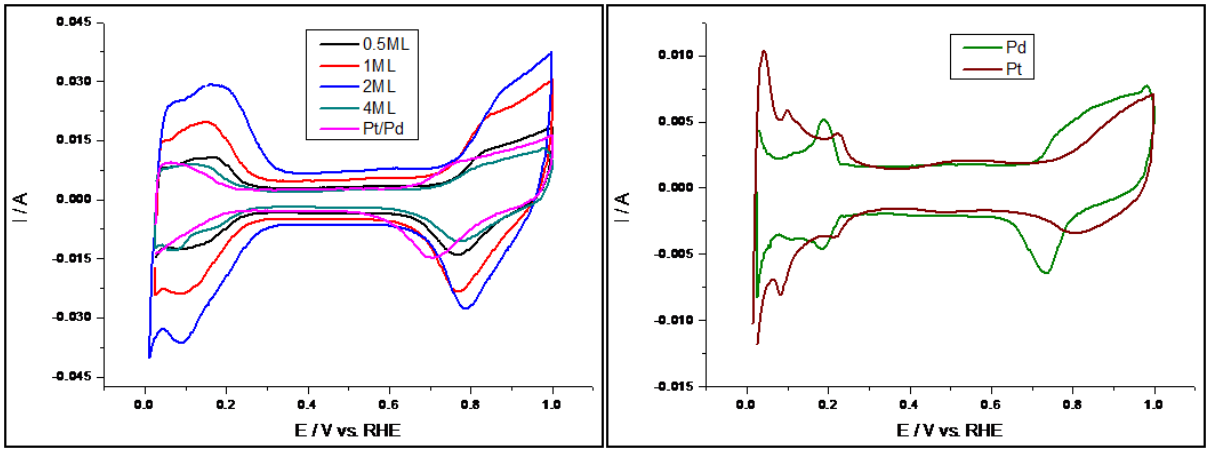

Figure 4.3: Cyclic voltammograms of Pt/Pd/C catalysts (left) compared with Pt and Pd (right), 80 °C, 1 M H_2SO_4, 10 mVs^{-1}.

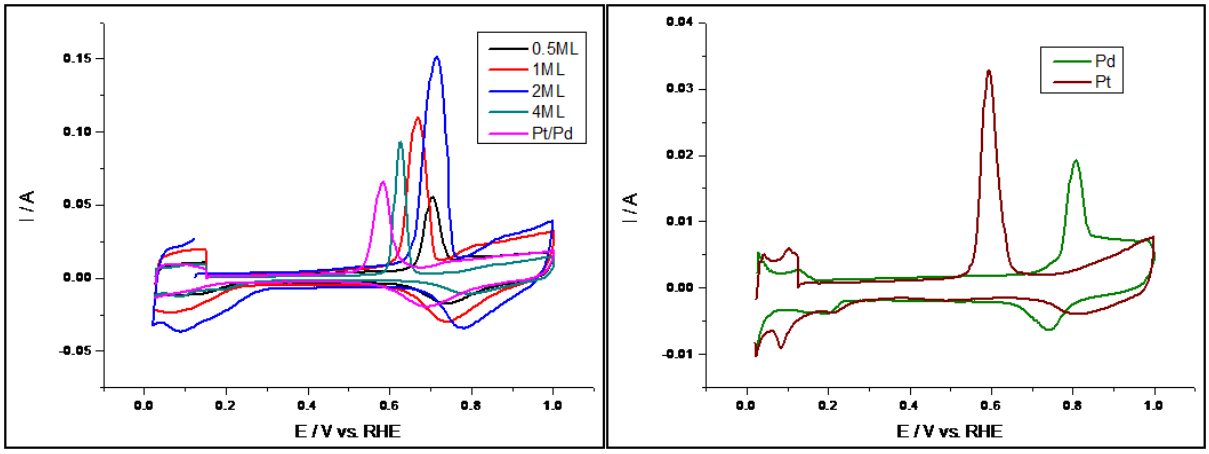

Figure 4.4: CO oxidation voltammograms of Pt/Pd/C catalysts (left) compared with Pt and Pd (right), 80 °C, 1 M H_2SO_4, 10 mVs^{-1}.

5 Cell for in situ Measurements

A key aspect of the work carried out in this study was the development of an electrochemical cell compatible with the X-ray characterisation techniques described in Chapters Three to Five. The cell was designed with the help of Patrick Hendra who also built the cell.

For in situ X-ray characterisation using EXAFS, WAXS, SAXS and ASAXS, the cell needed:

- To be transparent to X-rays
- Have a short X-ray path length
- Display good electrochemistry
- To be leak tight
- To have the versatility to be mounted in different beamline configurations

The cell design was based on the cells previously used within the research group for in situ EXAFS measurement,[6] however, for SAXS a smaller X-ray path length through the cell was required to minimise the scattering from the electrolyte. Adjustments were made based on the cell used by Haubold *et al*. for in situ SAXS measurements to give an X-ray path length through the cell of 2-3 mm.[7] Figure 5.1 shows the final cell design.

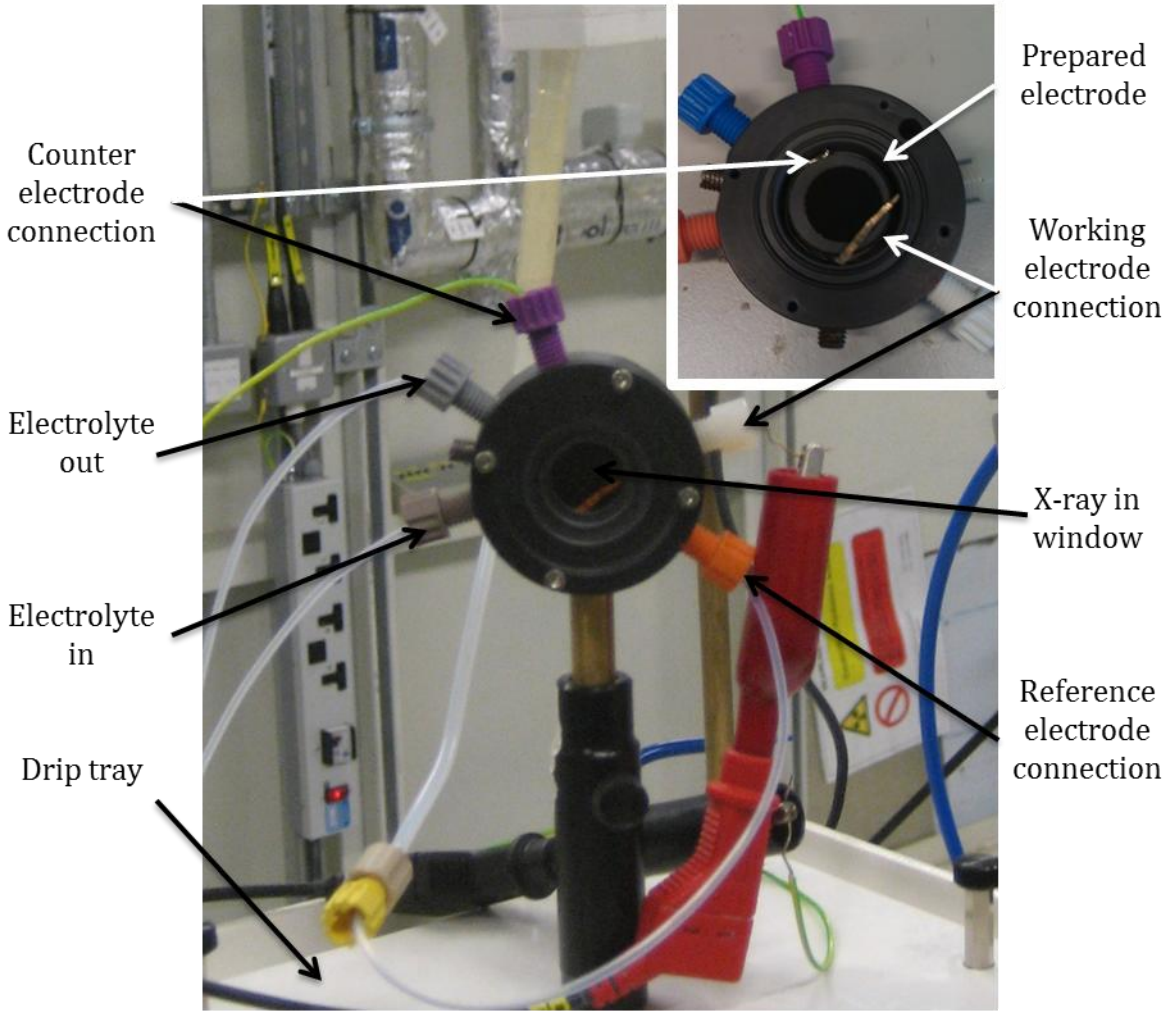

Figure 5.1: In situ cell developed for X-ray characterisation methods.

The body of the cell was machined from 40% glass-filled polyphenylene sulphide with Kapton sheet used for the X-ray windows. The working electrode was contacted with a flattened 0.5 mm diameter gold wire. The counter electrode consisted of a Pt wire located in the recess behind the working electrode and the reference electrode (in all cases a mercury mercurous sulphate reference electrode) was connected via a salt bridge. A peristaltic pump (Masterflex C/L 77120-62) was used to introduce the electrolyte into the cell, with relatively rapid solution changeover possible. Figure 5.2 illustrates the quality of the cyclic voltammograms obtained using the in situ cell.

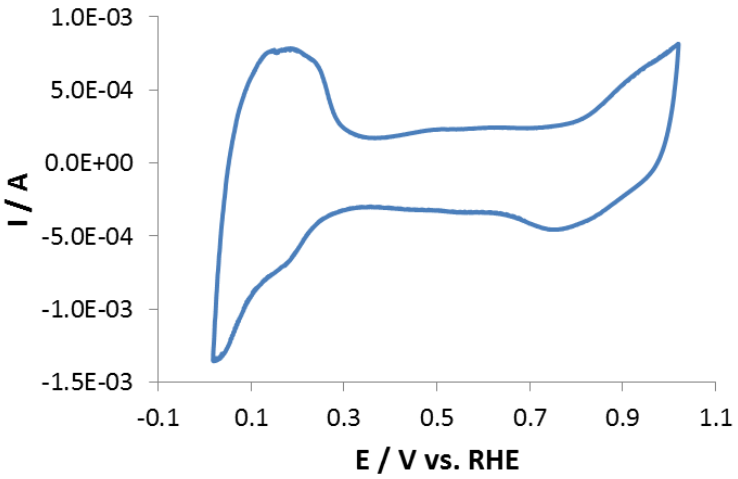

Figure 5.2: Cyclic voltammogram recorded with a scan rate of 5 mV s^{-1} in 1 M H_2SO_4 of a 40 wt% Pt/C catalyst electrode.

The CV shown in Figure 5.2 was recorded using a scan rate of 5 mV s^{-1}. At higher scan rates, IR drop (cell resistance) was seen in the CVs due to the thin layer of the electrolyte. As a result of this the cell could not be used reliably for in situ cycling measurements but proved to be stable for steady state potential holds. The cell was therefore used to investigate the changes in the electrode structure by holding the potential at a fixed value. The potentials used in this study were:

- 0.50 V vs. RHE to determine the structure of the catalyst when no redox processes were occurring
- 0.05 V vs. RHE to study the effect of hydrogen adsorption
- 0.00 V vs. RHE to study the effect of hydrogen absorption
- 1.00 V vs. RHE to investigate the effect of oxide growth.

Conclusions

The characterisation of the prepared electrocatalysts discussed in this chapter is indicative of the successful synthesis of well dispersed Pd-core, Pt-shell materials. The metal assays obtained from the ICP-ES analysis show good correlation with the theoretical wt% showing that the deposition of Pt was effective. The presence of the cubic Pd phase for the core-shell materials combined with the absence of any other distinct crystalline phases suggests that the Pd core remained relatively unperturbed by the deposition of Pt, unlike for the alloy, which displayed a well-mixed Pt/Pd phase. EDX line analysis provided evidence that Pt and Pd were present in the same particles, with TEM micrographs

showing that the metal nanoparticles were evenly dispersed over the carbon support. HRTEM micrographs confirm the increased presence of Pt around the edge of the particles and the electrochemical responses were indicative of a Pt surface.

References

[1] B. C. Tessier, A. E. Russell, B. R. Theobald, D. Thompsett, *ECS Trans.* **2009**, *16*, 1-11.
[2] P. Canton, G. Fagherazzi, M. Battagliarin, F. Menegazzo, F. Pinna, N. Pernicone, *Langmuir* **2002**, *18*, 6530-6535.
[3] P. T. Kissinger, W. R. Heineman, *J. Chem. Educ.* **1983**, *60*, 702-706.
[4] P. A. Christensen, A. Hamnett, *Techniques and Mechanisms in Electrochemistry*, First ed., Chapman and Hall, Oxford, **1994**.
[5] F. Maillard, E. R. Savinova, U. Stimming, *J. Electroanal. Chem.* **2007**, *599*, 221-232.
[6] S. Maniguet, R. J. Mathew, A. E. Russell, *J. Phys. Chem. B* **2000**, *104*, 1998-2004.
[7] H. G. Haubold, X. H. Wang, H. Jungbluth, G. Goerigk, W. Schilling, *J. Mol. Struct.* **1996**, *383*, 283-289.

CHAPTER THREE: CHARACTERISATION OF FRESH CATALYSTS USING EXAFS AND WAXS

Chapter One introduced the need for structural characterisation of core-shell electrocatalysts. The synthesis and initial characterisation of Pd-core, Pt-shell catalysts, along with the development of the electrochemical cell used for in situ X-ray measurements, were detailed in Chapter Two. This chapter describes the theoretical and experimental aspects of extended X-ray absorption fine structure (EXAFS) spectroscopy and wide-angle X-ray scattering (WAXS) and the results obtained from the study of the fresh catalysts, both in and ex situ. The chapter is divided into two main sections focussing separately on EXAFS and WAXS.

Some of this work has been published elsewhere.[1]

1 Extended X-Ray Absorption Fine Structure (EXAFS) Spectroscopy

1.1 Introduction to EXAFS

Extended X-ray absorption fine structure (EXAFS) spectroscopy is a regime of X-ray absorption spectroscopy (XAS) used to determine the average local structure of an element within a material in terms of the bond distances to neighbouring atoms and the identity and average number of those neighbouring atoms. XAS arises from the absorption of monochromatic X-rays by an element at a characteristic energy known as an absorption edge, first observed by de Broglie in 1913.[2] Fine structure oscillations in the X-ray absorption coefficient beyond the absorption edge were then observed in the 1920's by Fricke *et al.*,[3] with the first theory of EXAFS published by Kronig in 1932.[4] There was then little development until the 1970's when, aided by the advent of the bright, tunable X-rays from synchrotron radiation, the modern theory was developed by Sayers *et al*., who solved the application of the Fourier transform to the EXAFS equation.[5] Further improvements to the approximations used in the calculation of scattering contributions were made in subsequent years, resulting in the theory used today.[6]

EXAFS is a versatile technique and, as long-range order is not required within the material, it can be applied to the study of many systems. The main requirement of the sample being

studied is that the absorption edge (discussed in detail in Section 1.1.2) of the element of interest is within the accessible energy range of the instrument, typically 2 – 35 keV. It is important to note that EXAFS is a per atom average technique, containing contributions from all of the structural environments of the element being investigated within the irradiated area.

EXAFS has been widely used in the investigation of metal nanoparticles, both ex situ to study as-prepared materials and in situ to study nanoparticle formation and monitor the effects of temperature, absorbates and electrode potential.[7]

1.1.1 Theory of EXAFS

X-rays are absorbed as they pass through a sample according to Beer's Law, with the probability of absorption determined by μ, the absorption coefficient, as shown in Equation 1.1:

$$I_t = I_0 e^{-\mu x}$$

Equation 1.1

Where I_0 is the incident intensity of the X-rays, I_t is the transmitted intensity, and x is the sample thickness. In general, μ decreases smoothly with increasing X-ray energy ($h\upsilon$), resulting in the X-rays becoming more penetrative, however, when the energy reaches the binding energy (E_b) of a core electron a sharp rise in absorption occurs, known as the photoelectric effect.[8] This is due to the transfer of the X-ray energy to the core electron, resulting in its excited state and ejection into continuum above the Fermi level, leaving one of the core electron levels empty. The excited electron is known as a photoelectron, with energy E_k as shown in Equation 1.2, and the empty electron level is referred to as a core hole.

$$E_k = h\upsilon - E_b$$

Equation 1.2

The absorption edges are named as K, L_1, L_2, L_3 etc. based on the principle quantum number of the shell from which the photoelectron was ejected. The K absorption edge corresponds to the excitation of an electron in the 1s orbital, while the L edges relate to excitation from the 2s, $2p_{1/2}$ and $2p_{3/2}$ as shown in Figure 1.1.

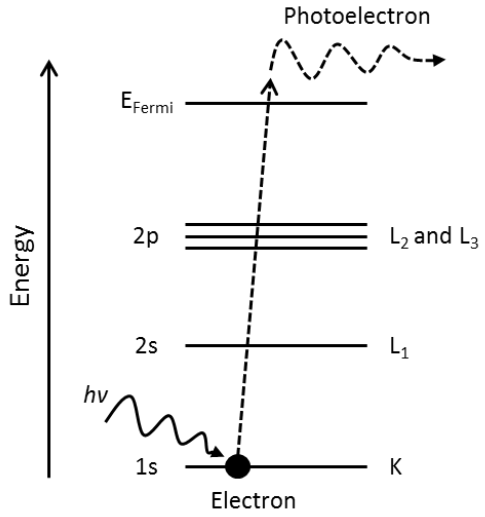

Figure 1.1: Schematic diagram of the photoelectric effect depicting the excitation of a 1s electron by X-ray energy to continuum, giving rise to a K absorption edge.

The ejected photoelectron can be considered as a spherical wave, with a wave vector k, related to the energy of the X-ray photon as shown in Equation 1.3, where E_0 is the zero point energy, usually defined by the maximum of the first derivative of the absorption edge, and m_e is the mass of an electron.

$$k = \sqrt{\left(\frac{8\pi^2 m_e}{h^2}\right)(h\upsilon - E_0)}$$

Equation 1.3

The absorption coefficient is proportional to the probability of a transition according to Fermi's 'Golden Rule':[6]

$$\mu \propto \sum_f \left|\langle \varphi_f | p.A(r) | \varphi_i \rangle\right|^2 \delta(E_f - E_i - \hbar\upsilon)$$

Equation 1.4

$$\varphi_f = \varphi_{outgoing} + \varphi_{backscattered}$$

Equation 1.5

Where φ_i and φ_f represent the initial and final states, p is the momentum operator, and $A(r)$ is the vector potential of the incident electromagnetic field with the final state wave function dependent on both the outgoing and backscattered waves. This is because the outgoing photoelectron wave is backscattered off surrounding atoms, resulting in constructive and destructive interference which gives rise to the oscillations seen in the absorption spectrum. The absorption can be defined in terms of the wave vector k as follows:

$$\chi(k) = \frac{\mu_{tot}(k) - \mu_0(k)}{\mu_0(k)}$$

Equation 1.6

Where $\mu_{tot}(k)$ is the total absorption, $\mu_0(k)$ is the background absorption, and $\chi(k)$ is the EXAFS signal extracted from the absorption spectrum. An example of an XAS spectrum is shown in Figure 1.2, highlighting the effects of the backscattering of the photoelectron wave.

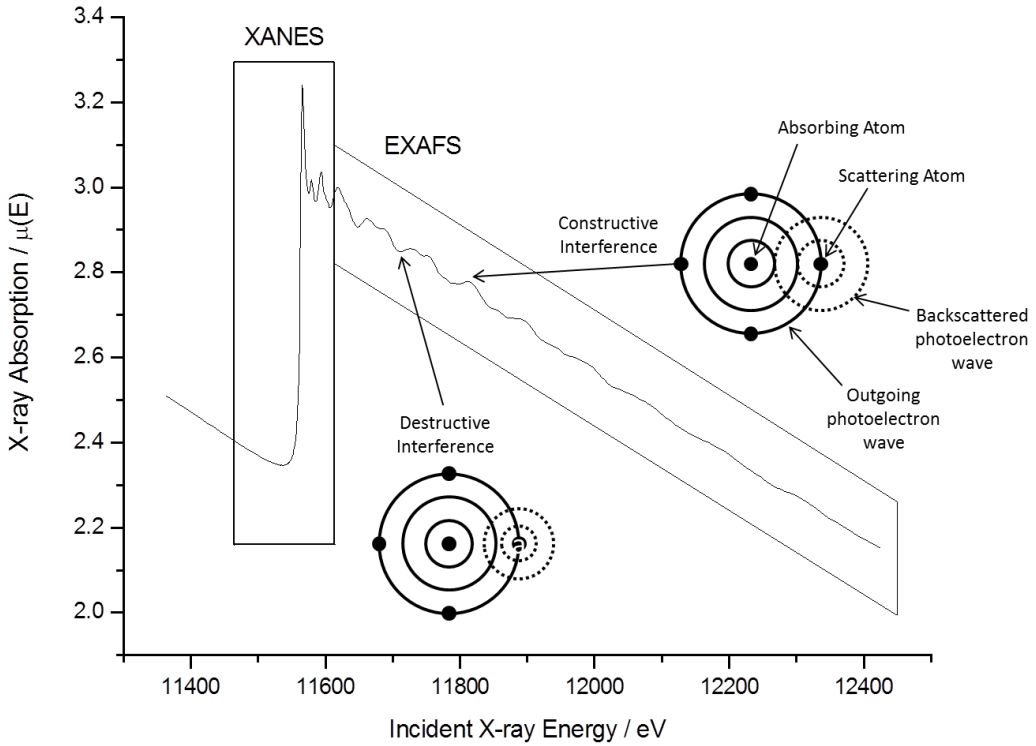

Figure 1.2: XAS spectrum of a Pt foil recorded at the Pt L_3 edge; indicating the XANES and EXAFS regions of the spectrum and illustrating the constructive and destructive interference caused by the backscattered photoelectron wave with the corresponding effects on $\mu(E)$.

The XAS spectrum is divided into two regions – X-ray Absorption near-edge spectroscopy (XANES) and extended X-ray absorption fine structure (EXAFS), as shown in Figure 1.2.

XANES includes the pre-edge region, where the energy of the incident X-rays is lower than that of the binding energy, and extends to 100-200 eV above the absorption edge. The XANES region contains information about the density of the available electronic states, with the shape of the absorption edge related to the coordination chemistry and oxidation state of the absorbing atom. The position of the absorption edge is also affected by the oxidation state of the absorber, with higher oxidation states resulting in a shift of a few electronvolts to higher energy. XANES analysis is complicated by multiple scattering and multiple photon absorption effects and there is currently no simple analytical description which makes quantitative interpretation of the data difficult. Typically XANES is used as a fingerprint to identify phases, with linear combination fitting based on spectra of model compounds being used to determine the ratios of valence states.

The EXAFS region extends from the absorption edge up to around 1000 eV above the edge, with the oscillations in the spectrum containing structural information about the local environment of the absorbing atom. Single scattering by the nearest neighbours dominates the signal, with each atom at the same radial distance from the absorber contributing to the same part of the EXAFS signal. The EXAFS equation enables the quantitative interpretation of the EXAFS spectrum, allowing the number of, identity of, and distance to neighbouring atoms to be determined.

1.1.1.1 The EXAFS Equation

The EXAFS equation can be written as the sum of the contributions from all of the photoelectron scattering paths:[9]

$$\chi(k) = \sum_i \chi_i(k)$$

Equation 1.7

Each scattering path can be defined as:

$$\chi_i = \frac{(N_i S_0^2) F_{eff_i}(k)}{kR_i^2} \sin[2kR_i + \varphi_i(k)]\, e^{-2\sigma_i^2 k^2}\, e^{\frac{-2R_i}{\lambda(k)}}$$

Equation 1.8

with

$$R_i = R_{0i} + \Delta R_i$$

Equation 1.9

and

$$k = \sqrt{\frac{2m_e(E - E_0 + \Delta E_0)}{\hbar}}$$

Equation 1.10

The terms of Equation 1.7 - Equation 1.10 are described below in relation to single scattering paths, where the subscript *i* indicates that the value can be different for each scattering path (also referred to as a shell):[10]

($N_i S_0^2$): N_i represents the coordination number within a particular shell. S_0^2 is the amplitude reduction factor which allows for the slight relaxation of the remaining electrons around the core hole. The value is typically between 0.7 and 1.0 and varies with different elements, but can generally be applied to all paths originating from the same element at the same edge.[11]

$F_{effi}(k)$: $F_{effi}(k)$ is the effective scattering amplitude and incorporates the element specificity into the EXAFS equation. It is the atomic scattering factor used in X-ray diffraction and is dependent on the number of electrons in the scattering atom.[12]

***k*:** the excess kinetic energy of the photoelectron in wavenumber, derived from the incident X-ray energy using Equation 1.10.

R_i: denotes the half path length of the photoelectron which equates to the distance between the absorbing and scattering atoms, with R_{0i} being the theoretical path length which is modified by ΔR_i. The $1/R_i^2$ dependence should be noted, showing the decrease in the contribution to the EXAFS signal from shells of atoms at increased distances from the absorber.

$\sin[2kR_i + \varphi_i(k)]$: φ_i is the phase shift caused by the interaction of the photoelectron with the nuclei of the scattering atom and absorbing atoms, resulting in a loss of energy. This term accounts for the oscillations in the EXAFS, showing the dependency of the phase on the distance and identity of the atoms involved.

$e^{-2\sigma_i^2 k^2}$**:** σ_i^2 is known as the Debye Waller factor and is the mean-square displacement of the bond length between the absorbing and scattering atoms. It describes the structural disorder and thermal motion in the system.

$e^{\frac{-2R_i}{\lambda(k)}}$ **:** λ is the mean free path of the photoelectron which has a finite lifetime due to the decay in energy from inelastic scattering. This results in the EXAFS signal being dominated by the scattering contributions from atoms up to around 10 Å from the absorber, making it a local structure probe.

ΔE_i**:** Written in Equation 1.10 as ΔE_0, this is a shift energy applied to the theoretical calculation to align it with the measured data.

$F_{effi}(k)$, $\varphi_i(k)$ and $\lambda(k)$ are calculated theoretically using a computer program such as FEFF 6.0[6], with the parameters N_i, S_0^2, ΔR_i, σ^2 and ΔE_i being determined by modelling the data to provide the local average structure. The practicalities of the data analysis are described in Section 1.2.5.

1.2 Experimental Aspects

1.2.1 Experiment Geometry

An EXAFS measurement is the measurement of the dependence of μ on the incident X-ray energy, meaning that the absorption of X-rays with increasing energy by a sample needs to be detected. The simplest method of measuring this absorption is to monitor the number of incident X-rays before (I_0) and after (I_t) they pass through the sample – this acquisition mode is known as transmission. Rearranging Equation 1.1 then gives the absorption as follows:

$$\mu x = \ln\left(\frac{I_0}{I_t}\right)$$

Equation 1.11

For dilute samples, where the signal-to-noise ratio will be poor, fluorescence detection can be used. X-ray fluorescence occurs due to the decay of the excited atomic state. An electron from a higher energy orbital relaxes to fill the core hole, emitting an X-ray at a well-defined energy characteristic of the element. The probability of emission is directly

proportional to the absorption probability, allowing μ to be determined by monitoring the intensity of a fluorescence line as shown in Equation 1.12.

$$\mu \propto \frac{I_f}{I_0}$$

Equation 1.12

Fluorescence is emitted isotropically but to minimise scattering the detector (commonly a solid state detector) is normally placed at 90° to the incident beam with the sample positioned at 45°. Figure 1.3 shows the configuration of the experiment.

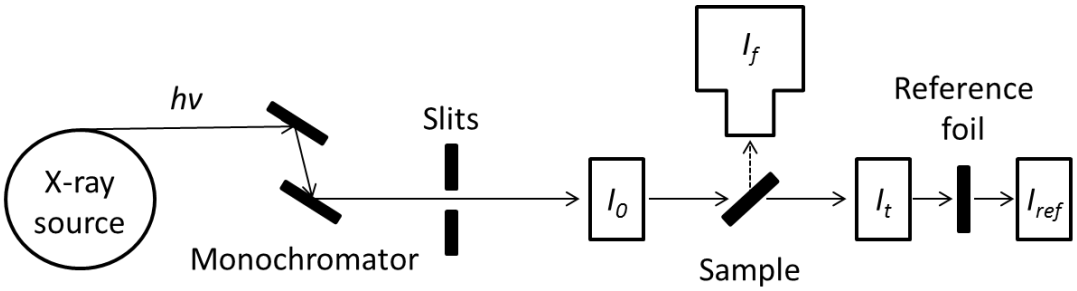

Figure 1.3: Schematic diagram of the EXAFS experiment configuration.

The monochromator is used to define the incident X-ray energy and typically consists of a pair of perfect, parallel silicon crystals which determine the energy by selecting the angle, θ, based on Bragg diffraction:

$$n\lambda = n\frac{hc}{E} = 2d\sin\theta$$

Equation 1.13

It is necessary to remove the higher harmonics from the beam before it reaches the sample. This can be achieved by detuning the crystals or by use of a harmonic rejection mirror. The method of harmonic rejection employed by each beamline used for data collection in this work is given in Section 1.2.2. The slits are used to define the beam size and to block unwanted X-rays.

A reference sample, in this work a foil of either Pt or Pd, is typically recorded to calibrate the X-ray energy. Where possible reference data is also collected simultaneously with the

sample measurement to check the stability of the monochromator by the inclusion of a third ionisation chamber shown in Figure 1.3 as I_{ref}.

1.2.2 Beamlines

Several different beamlines at various synchrotron facilities were used to collect the data reported in this chapter. The specifications of the beamlines are detailed briefly here.

X23A2, NSLS, Brookhaven National Laboratory, USA[13]**:** X23A2 has an energy range of 4.9 – 30 keV from a bending magnet source. A Si(311) monochromator was used with a single bounce harmonic rejection mirror. The beamline scientist was Bruce Ravel.

BM26A (DUBBLE), European Synchrotron Radiation Facility (ESRF), France[14]**:** BM26A is supplied by a bending magnet source and has an energy range of 4 – 32 keV. The monochromator used contained Si(311) crystals. Higher harmonics were removed by two harmonic rejection mirrors, using a Si coating at the Pt L_3 edge and Pt coating at the Pd K edge. Fluorescence was detected using a 9-element monolithic Ge detector. The beamline was also set up to collect SAXS and WAXS data simultaneously with the in situ EXAFS. Due to calibration issues this was not successful and the SAXS and WAXS data collected will be omitted from this work. The beamline scientists were Sergey Nikitenko and Miguel Silveira.

X1, HASYLAB, Deutsches Elektronen-Synchrotron (DESY), Germany[15]**:** Beamline X1 has a large energy range of 6 – 80 keV from a bending magnet source. Si(311) crystals were again used in the monochromator and harmonic rejection was achieved by detuning to 65%. A 7 pixel HPGe detector was used for fluorescence detection. The beamline scientists were Edmund Welter and Adam Webb.

B18, Diamond Light Source, UK[16]**:** B18 has an energy range of 2 – 35 keV, with X-rays supplied by a bending magnet source. The monochromator was used with a set of Si(311) crystals. Higher harmonics were rejected using Cr coated mirrors at the Pt L_3 edge and Pt coated mirrors at the Pd K edge. A 9 element Ge detector was used for fluorescence detection. The beamline scientist was Silvia Ramos.

1.2.3 Ex situ Measurements

Ex situ EXAFS measurements were carried out in transmission mode under a hydrogen atmosphere at the Pt L_3 and Pd K edges on beamline X23A2, NSLS, by Stephen Price and Gael Chouchelamane. The samples were prepared as pellets by mixing the ground sample with boron nitride (BN) to form a homogenous mixture, and then compressed using a purpose-built pellet press. This ensured that there were no pinholes in the samples which would distort the amplitude of $\chi(k)$.[17] The concentration of the element within the sample is of importance for EXAFS transmission measurements – too little and the signal-to-noise ratio would be too poor, too much and all of the X-rays would be absorbed. The amount of sample required was therefore calculated based on the mass absorption coefficient, μ_ρ, of the element being considered:

$$mass = \frac{(\mu x)(sample\ area)}{\mu_\rho}$$

Equation 1.14

Ideally, the absorption edge step (μx) of the element being studied should be between 0.3 and 1. However, absorption by other elements present in the material also needs to be considered and the total absorption of the sample should not exceed 2.5. The mass absorption coefficients calculated by McMaster *et al.* were used to determine the appropriate mass of the sample in this study.[18]

The gas treatment cell shown in Figure 1.4 was used to conduct the EXAFS measurements under a H_2 atmosphere. The pellet was loaded into the cell and the cell purged with pure hydrogen for 30 minutes in a fume hood, with the exhaust gas being diluted to <2.5% with nitrogen. The taps were then closed and the cell transferred to the experimental hutch. Following the EXAFS measurement the cell was purged with nitrogen for 20 minutes to remove hydrogen before allowing air into the cell.

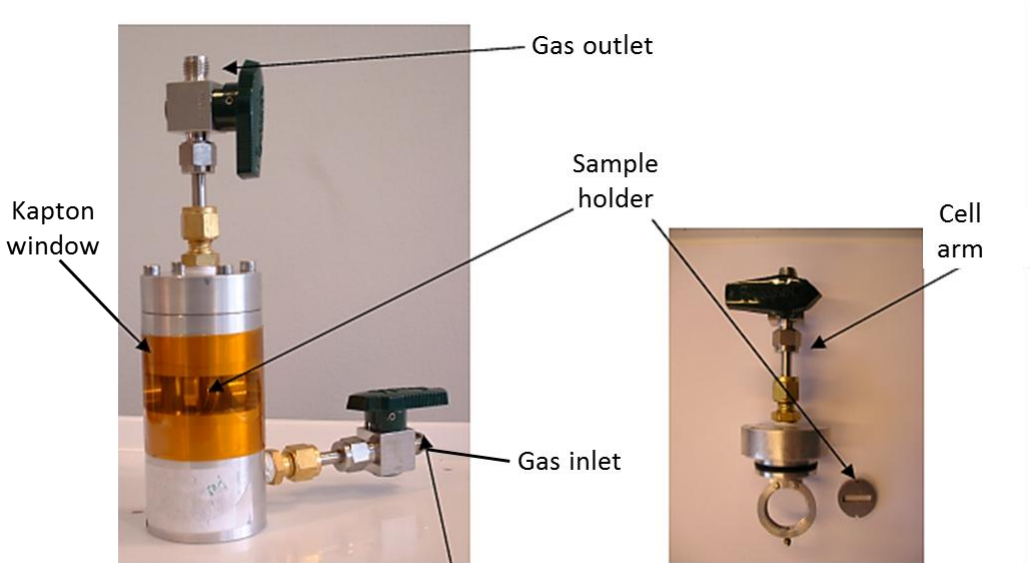

Figure 1.4: Gas cell used for ex situ EXAFS measurements.

1.2.4 In situ Measurements

In situ EXAFS measurements were carried out using the in situ electrochemical cell described in Chapter Two. Several beamlines were used for this study, with Table 1.1 showing the data collected and experimental team at each beamline.

Table 1.1: Details of the data collected and experimental team at each beamline.

Beamline	Sample	Absorption Edge	Experimental Team
BM26A, ESRF	Pd/C core material	Pd K	Peter Richardson, Andrea Russell, Anna Wise
	Pt_{1ML}/Pd/C	Pt L_3 & Pd K	
X1, HASYLAB	40 wt% Pt/C	Pt L_3	Laura Calvillo Lamana, Peter Richardson, Anna Wise
	Pt/Pd/C Alloy	Pt L_3 & Pd K	
	Pt_{2ML}/Pd/C		
	Pt_{4ML}/Pd/C	Pt L_3	
B18, Diamond	$Pt_{0.5ML}$/Pd/C	Pt L_3 & Pd K	Laura Calvillo Lamana, Peter Richardson, Andrea Russell, Anna Wise
	Pt_{4ML}/Pd/C	Pd K	

Catalyst electrodes were prepared as detailed in Chapter Two, Section 4.2.1. Before being loaded into the in situ cell, the electrodes were hydrated by boiling in demineralised

water. 0.5 M H_2SO_4 (~ 50 mL) was purged with N_2 for 15 minutes to deoxygenate the electrolyte prior to being introduced into the cell via the peristaltic pump. Once the loaded cell was filled and connected to the potentiostat, three cyclic voltammograms (CVs) were collected between 1.00 V and 0.05 V vs. RHE, starting the scan at OCV with a scan rate of 50 mV s^{-1}, to ensure the electrode was fully wetted and that contact was complete. Three further CVs were then recorded with a scan rate of 10 mV s^{-1} to ensure the electrode was stable and to determine the potentials of the regions of interest. The experiment then proceeded as follows:

- Potential set manually to 0.50 V vs. RHE (this involved gradually moving the potential from OCV to the desired potential)
- EXAFS scans collected
- Potential reduced manually to 0.05 V vs. RHE
- EXAFS scans collected
- Potential reduced manually to 0.00 V vs. RHE
- EXAFS scans collected
- CVs (10 mV s^{-1}) recorded from 0.00 V to 1.00 V vs. RHE to remove absorbed hydrogen from the sample and check the state of the catalyst has not been permanently altered
- Potential manually moved to 1.00 V vs. RHE
- EXAFS scans collected
- CVs (10 mV s^{-1}) were then recorded between 1.00 V and 0.05 V vs. RHE to check the final state of the electrode.

The only variation to this procedure was in the case of the Pd/C and Pt_{1ML}/Pd/C samples, where potentials of 0.07 V and 0.52 V were used instead of 0.05 V and 0.50 V respectively. In all experiments a mercury mercurous sulphate (MMS) reference electrode was used, with the electrodes connected to a μAutolab III potentiostat controlled by General Purpose Electrochemistry Software (GPES, Metrohm Ltd.). EXAFS data was collected in fluorescence mode, with an acquisition time of approx. 30 minutes per scan depending on the beamline used. Typically 2-3 EXAFS scans were recorded per potential to improve the signal-to-noise ratio and check that the sample was not changing throughout the measurement. Due to the geometry of the in situ cell it was not possible to measure reference foil data simultaneously with the sample data. To ensure that the monochromator remained stable throughout the measurements, reference foils were

recorded periodically. Figure 1.5 shows the experimental set-up on beamline B18, Diamond, which was typical of all experiments.

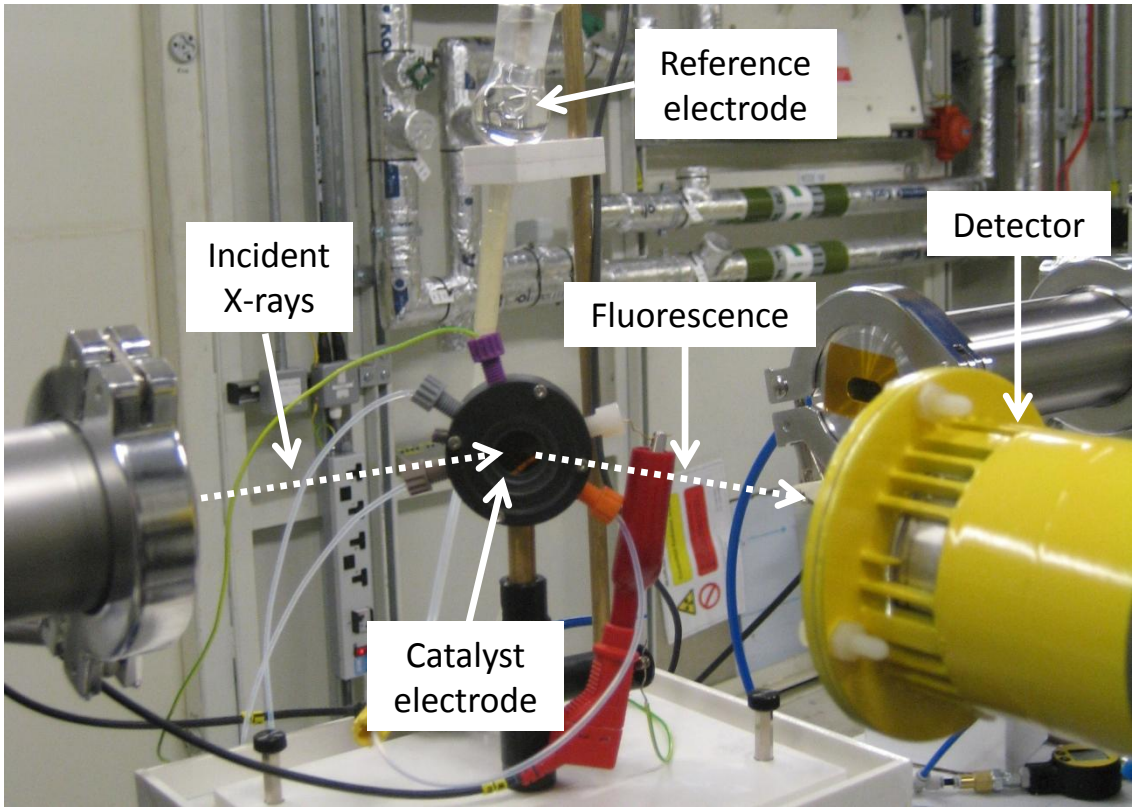

Figure 1.5: In situ EXAFS set-up on beamline B18, Diamond.

1.2.5 Data Analysis

Data was processed and analysed using ATHENA and ARTEMIS respectively, parts of the IFEFFIT software suite.[19],[20]

The raw data was imported into ATHENA as $\mu(E)$ by preprocessing the signals from the relevant detectors in the import menu. The data then needed to be calibrated, normalised, background subtracted and converted from E to k.

Calibration was carried out using the reference foil data collected as part of the sample measurements. The first derivative of the absorption edge of the reference was set to the tabulated absorption energy[18] to calibrate the energy scale. The same shift in energy was then applied to the sample data. The absorption edge energy (referred to earlier as the zero point energy), E_0, of the sample was then determined from the first derivative of the sample data.

There were two aspects to the data normalisation: a pre-edge function and a post-edge function. The pre-edge function is a line regressed to the data in the pre-edge region and extrapolated out to the maximum energy used in the measurement. It is then subtracted from $\mu(E)$. The post-edge function is a quadratic polynomial which should be set to pass evenly through the middle of the oscillations in the data. The difference between the pre-edge and post-edge functions at the absorption edge is then normalised to give an edge step of 1. This allows the data from different experiments at the same edge to be directly compared.

Background subtraction is needed to remove the contribution to the total absorption from the absorption by a single atom, $\mu_0(E)$. $\mu_0(E)$ is approximated by a spline fitted to the data using the AUTOBK algorithm present in ATHENA.[21] The spline removes the low frequency components of $\mu_0(E)$, passing through the nodes of the EXAFS data without following the oscillations.

The data can then be converted from E to k space using:

$$k = \sqrt{\frac{2m_e(E - E_0)}{\hbar}}$$

Equation 1.15

The resulting $\chi(k)$ plot can be weighted to amplify the signal at higher k. As k is normalised to the absorption edge energy, data recorded at different absorption edges can now be directly compared. The Fourier transform of the k data, known as R space, is then used for fitting the data in ARTEMIS using the FEFF 6.0 code.[6] Figure 1.6 shows the processing of a Pt foil data set using the steps detailed above.

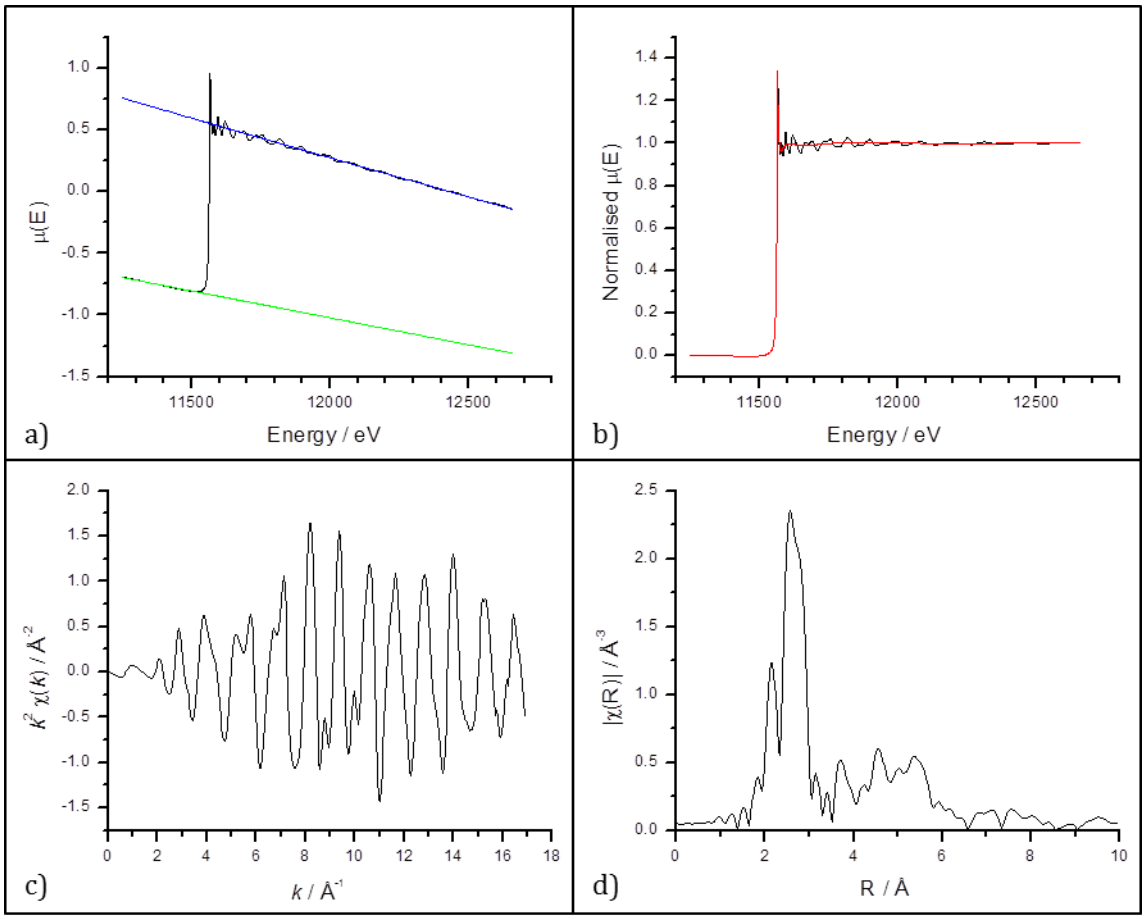

Figure 1.6: Processing Pt foil EXAFS data: a) $\mu(E)$ data (black), showing the pre-edge (green) and post-edge (blue) functions; b) Normalised $\mu(E)$ data (black) with the background spline (red); c) k^2 weighted $\chi(k)$ data; d) Fourier transform of the k space data.

The processed data is transferred to ARTEMIS where fitting is carried out by comparison of theoretical calculations with the data, with the fit refined by a non-linear least squares minimisation. In ARTEMIS the goodness-of-fit can be assessed using the reduced χ^2 (χ_υ^2) and the *R*-factor. The reduced χ^2 is a statistical parameter used to compare different fitting models and is defined as:

$$\chi_\upsilon^2 = \frac{\chi^2}{\upsilon}$$

Equation 1.16

where

$$\chi^2 = \frac{N_{idp}}{\varepsilon N_{data}} \sum_{i=min}^{max} \left[\mathrm{Re}\left(\chi_d(r_i) - \chi_t(r_i)\right)^2 + \mathrm{Im}\left(\chi_d(r_i) - \chi_t(r_i)\right)^2 \right]$$

Equation 1.17

and

$$\upsilon = N_{idp} - N_{var}$$

Equation 1.18

N_{idp}, N_{data} and N_{var} are the number of independent points in the model fit, the number of data points and the number of variables respectively, ε is the measurement uncertainty, χ_d is the EXAFS data and χ_t is the theoretical fit to the data.

The value typically reported as an assessment of the fit is the *R*-factor, R_f. R_f represents the mean square misfit between the data and the fit for both the real and imaginary parts of the Fourier transform (Equation 1.19). R_f values below 0.03 generally indicate a good fit.

$$R_f = \frac{\sum_{i=min}^{max}\left[\mathrm{Re}\left(\chi_d(r_i) - \chi_t(r_i)\right)^2 + \mathrm{Im}\left(\chi_d(r_i) - \chi_t(r_i)\right)^2\right]}{\sum_{i=min}^{max}\left[\mathrm{Re}\left(\chi_d(r_i)\right)^2 + \mathrm{Im}\left(\chi_d(r_i)\right)^2\right]}$$

Equation 1.19

All data was imported and processed as described above. Where multiple scans were recorded for each measurement the individual scans were processed in the same way then merged together. Fits were carried out using a *k* range of 3 – 13 $Å^{-1}$ and an R range of 1.4 – 3.2 Å (a range of 1.2 – 3.2 Å was used when oxygen neighbours were present), with multiple *k* weightings of 1, 2 and 3. The FEFF input used in these fits was an fcc cluster of a 1:1 Pt/Pd alloy, using a lattice parameter of 3.9018 Å taken from the XRD analysis of the Pt/Pd/C alloy detailed in Chapter Two, Section 3.2, resulting in a R_{0i} value for all metal-metal bonds of 2.759 Å. Where oxygen neighbours were present the alloy input file was doped with O in the first shell, resulting in a metal-O R_{0i} value of 1.951 Å. The S_0^2 value was determined for each edge at each beamline by fitting the reference foil data using the same data range as for the sample data.

The remaining parameters to be determined were the coordination number, N_i; ΔR_{0i} to calculate R_i; the mean squared displacement (MSD) of the bond, σ_i^2; and the shift in energy required to align the fit to the data, ΔE_0. To minimise the number of variables the following restraints were applied to the fits for each data set:

- ΔE_0: set to be the same for all paths for each edge measurement
- ΔR_{0i} and σ_i^2: set to be the same for the Pd-Pt and Pt-Pd interactions, with the data from both absorption edges being fitted simultaneously for each measurement.[22]

1.3 Results

1.3.1 Ex situ EXAFS

The ex situ EXAFS data with the corresponding fits are shown in Figure 1.7 - Figure 1.11, with the fit parameters obtained given in Table 1.2 - Table 1.6. It can be seen that the data recorded was of good quality, with very little noise at higher *k*. This resulted in good fits being obtained, as shown by the graphical agreement with the data and the low *R*-factor, R_f.

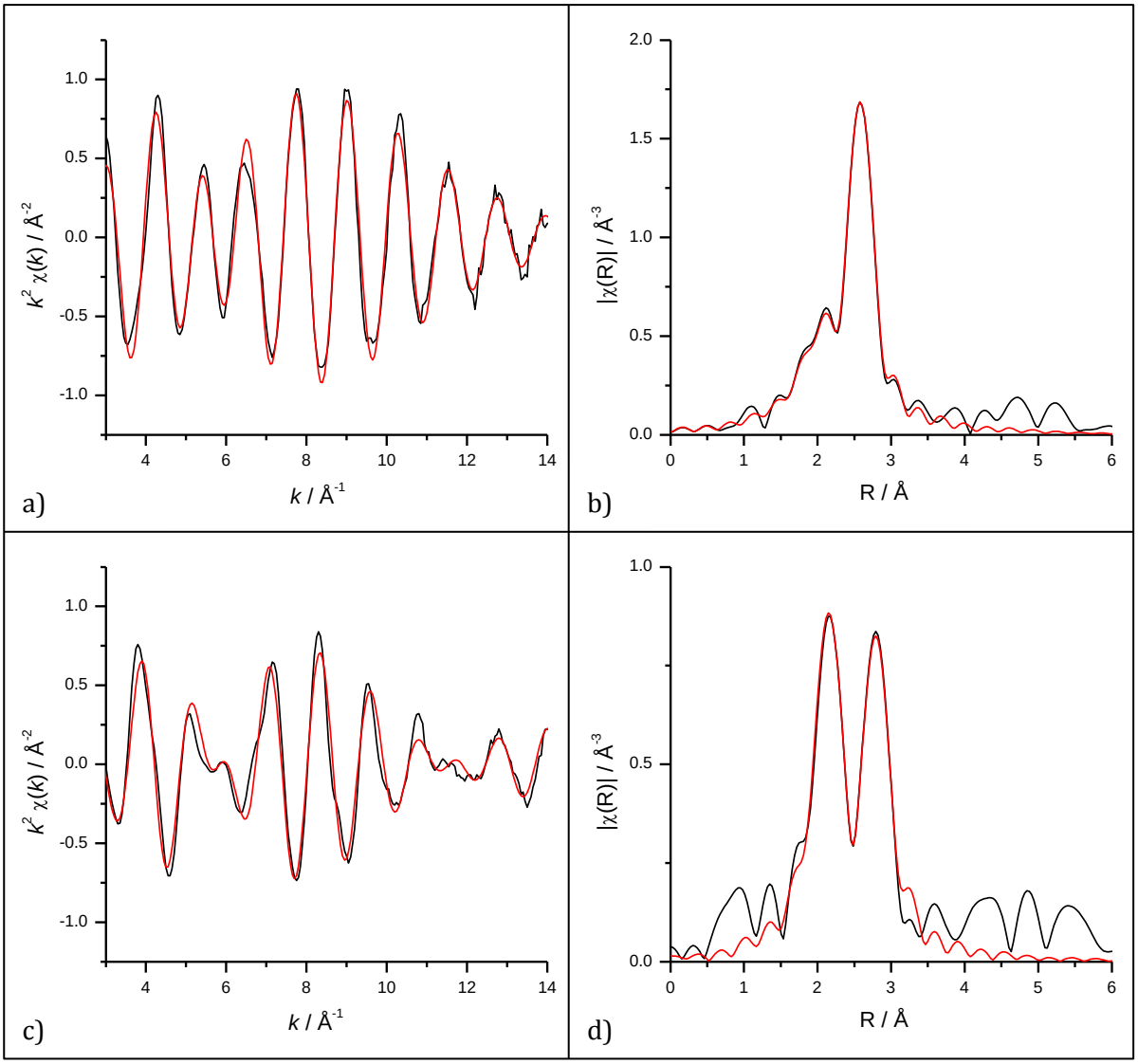

Figure 1.7: k^2 weighted experimental data (black) and fit (red) with the corresponding Fourier transform for $Pt_{0.5ML}/Pd/C$ recorded at the Pd K (a-b) and Pt L_3 (c-d) edges under H_2.

Table 1.2: Structural parameters obtained for $Pt_{0.5ML}/Pd/C$ from fitting EXAFS data acquired under H_2. (N.B. first element in the neighbour pair indicates absorption edge of data)

Neighbour	N	R / Å	σ^2 / Å^2	ΔE_0 / eV	R_f
Pd-Pd	9.07 ± 1.03	2.799 ± 0.008	0.0076 ± 0.0007	-1.91 ± 0.71	0.0043
Pd-Pt	1.75 ± 0.85	2.750 ± 0.005	0.0054 ± 0.0006		
Pt-Pd	3.66 ± 0.44			4.99 ± 0.41	
Pt-Pt	5.88 ± 0.64	2.750 ± 0.005	0.0054 ± 0.0006		

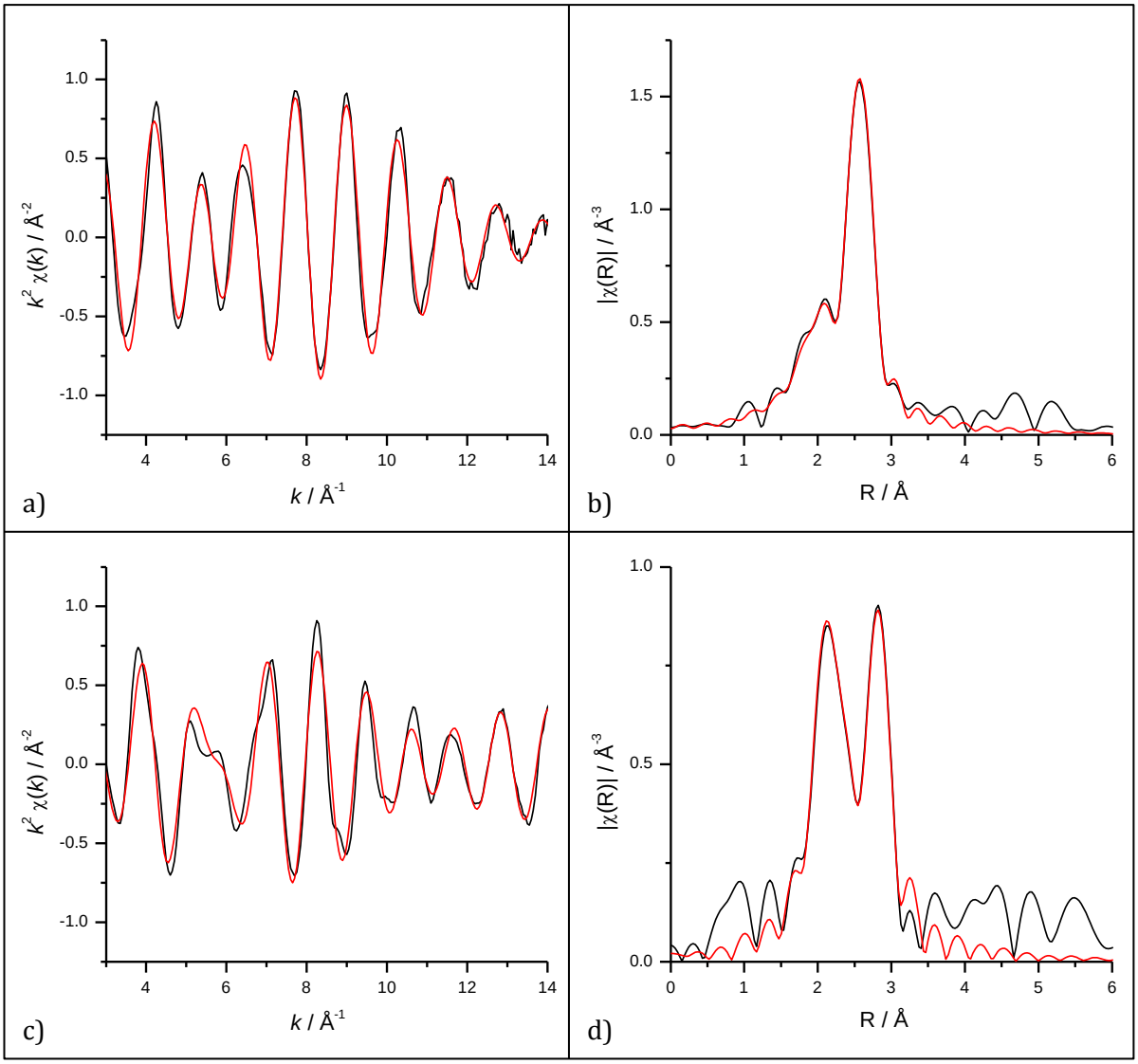

Figure 1.8: k^2 weighted experimental data (black) and fit (red) with the corresponding Fourier transform for $Pt_{1ML}/Pd/C$ recorded at the Pd K (a-b) and Pt L_3 (c-d) edges under H_2.

Table 1.3: Structural parameters obtained for $Pt_{1ML}/Pd/C$ from fitting EXAFS data acquired under H_2. (N.B. first element in the neighbour pair indicates absorption edge of data)

Neighbour	N	R / Å	σ^2 / Å^2	ΔE_0 / eV	R_f
Pd-Pd	8.30 ± 0.92	2.792 ± 0.007	0.0074 ± 0.0007	-4.11 ± 0.63	0.0034
Pd-Pt	2.22 ± 0.71	2.751 ± 0.006	0.0047 ± 0.0007		
Pt-Pd	2.43 ± 0.34			5.16 ± 0.38	
Pt-Pt	7.36 ± 0.70	2.752 ± 0.004	0.0053 ± 0.0004		

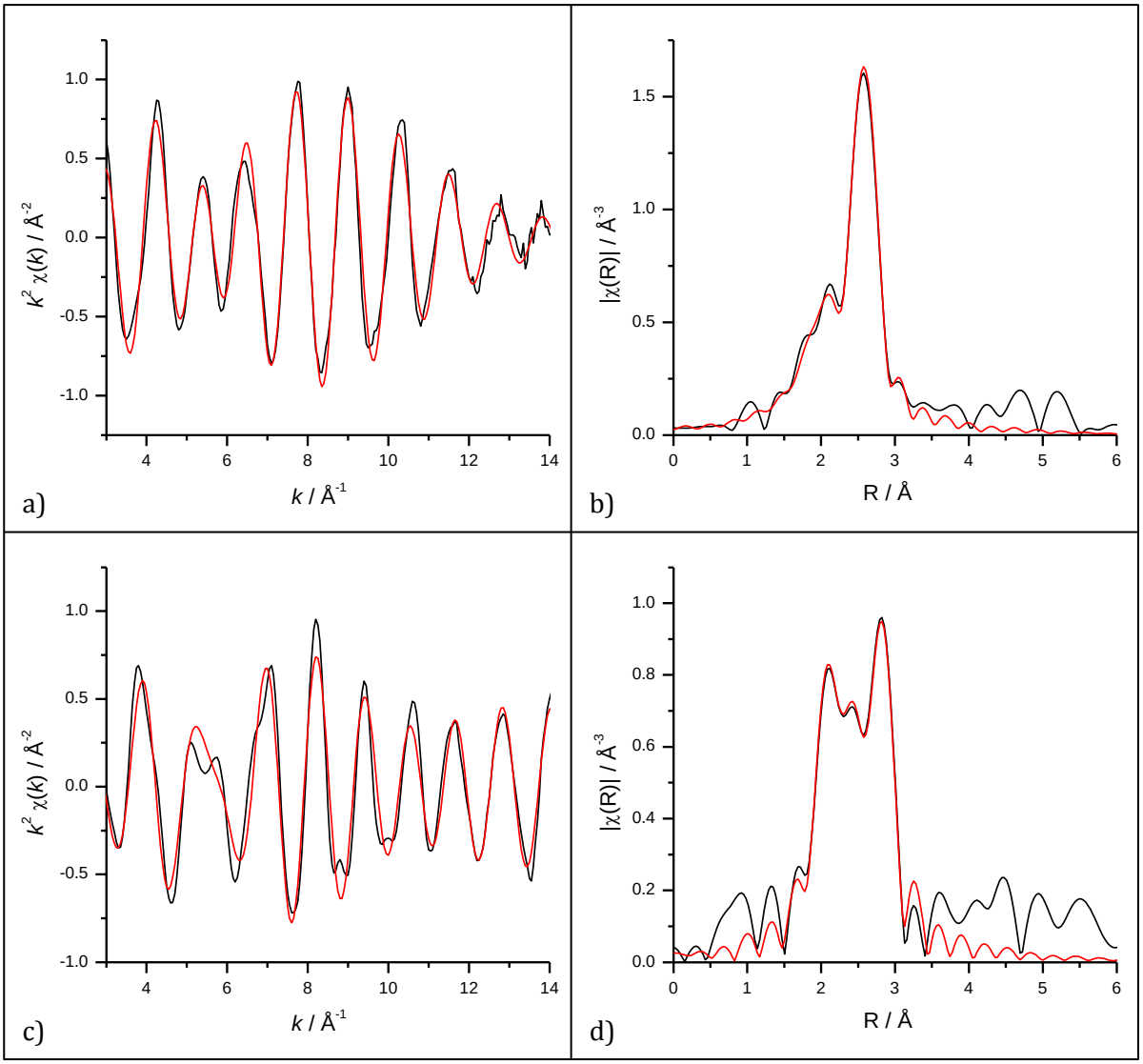

Figure 1.9: k^2 weighted experimental data (black) and fit (red) with the corresponding Fourier transform for Pt_{2ML}/Pd/C recorded at the Pd K (a-b) and Pt L_3 (c-d) edges under H_2.

Table 1.4: Structural parameters obtained for Pt_{2ML}/Pd/C from fitting EXAFS data acquired under H_2. (N.B. first element in the neighbour pair indicates absorption edge of data)

Neighbour	N	R / Å	σ^2 / Å^2	ΔE_0 / eV	R_f
Pd-Pd	8.05 ± 1.02	2.792 ± 0.008	0.0070 ± 0.0008	-3.38 ± 0.72	0.0040
Pd-Pt	2.42 ± 0.79	2.752 ± 0.007	0.0041 ± 0.0009		
Pt-Pd	1.53 ± 0.27			4.92 ± 0.37	
Pt-Pt	8.15 ± 0.74	2.756 ± 0.003	0.0052 ± 0.0003		

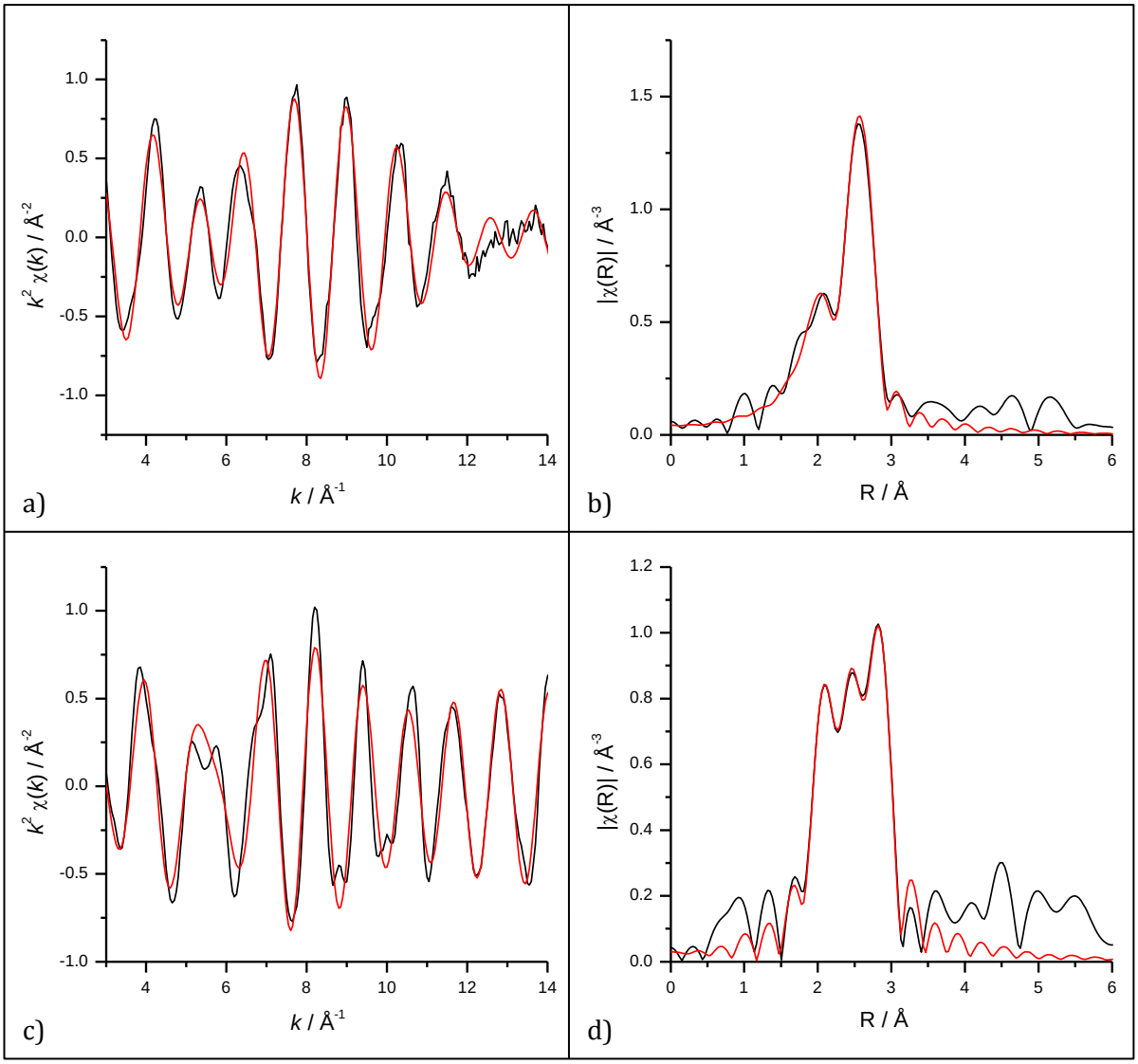

Figure 1.10: k^2 weighted experimental data (black) and fit (red) with the corresponding Fourier transform for Pt_{4ML}/Pd/C recorded at the Pd K (a-b) and Pt L_3 (c-d) edges under H_2.

Table 1.5: Structural parameters obtained for Pt_{4ML}/Pd/C from fitting EXAFS data acquired under H_2. (N.B. first element in the neighbour pair indicates absorption edge of data)

Neighbour	N	R / Å	σ^2 / Å^2	ΔE_0 / eV	R_f
Pd-Pd	6.49 ± 1.14	2.775 ± 0.010	0.0060 ± 0.0012	-6.41 ± 0.90	0.0063
Pd-Pt	2.97 ± 0.88	2.751 ± 0.007	0.0030 ± 0.0010		
Pt-Pd	1.05 ± 0.21			6.25 ± 0.33	
Pt-Pt	8.58 ± 0.75	2.757 ± 0.003	0.0050 ± 0.0003		

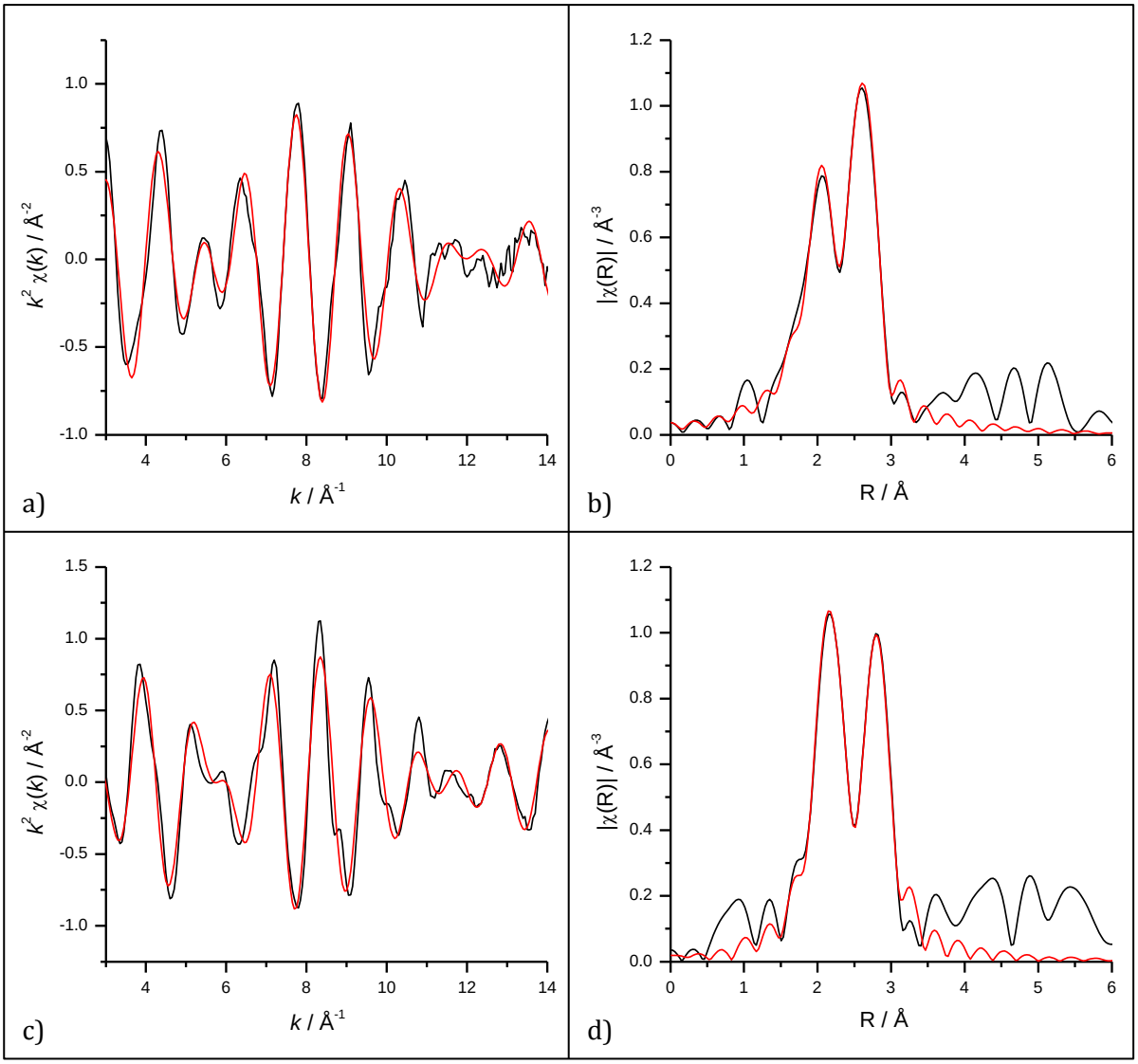

Figure 1.11: k^2 weighted experimental data (black) and fit (red) with the corresponding Fourier transform for Pt/Pd/C Alloy recorded at the Pd K (a-b) and Pt L_3 (c-d) edges under H_2.

Table 1.6: Structural parameters obtained for Pt/Pd/C Alloy from fitting EXAFS data acquired under H_2. (N.B. first element in the neighbour pair indicates absorption edge of data)

Neighbour	N	R / Å	σ^2 / Å^2	ΔE_0 / eV	R_f
Pd-Pd	4.39 ± 0.71	2.751 ± 0.006	0.0043 ± 0.0010	-3.78 ± 0.59	0.0048
Pd-Pt	5.09 ± 0.73	2.745 ± 0.004	0.0039 ± 0.0005		
Pt-Pd	3.38 ± 0.36			5.85 ± 0.31	
Pt-Pt	6.84 ± 0.64	2.745 ± 0.003	0.0045 ± 0.0004		

Considering first the Fourier transforms of the data (plots b and d in Figure 1.7 - Figure 1.11), it can be seen that the Pd data (b) remains relatively unchanged with increasing Pt shell thickness for the core-shell samples. However, a marked difference is seen in the data of the Pt/Pd/C alloy, with a sharp increase in the peak at ~2 Å which may be attributed to the Pd-Pt interaction. On the other hand, the Fourier transforms of the Pt data (d) show significant changes in the Pt environment with increasing shell thickness, whereas the alloy data resembles that of the $Pt_{0.5ML}$/Pd/C sample. Figure 1.12 compares the bond lengths and coordination numbers of the different interactions in the samples.

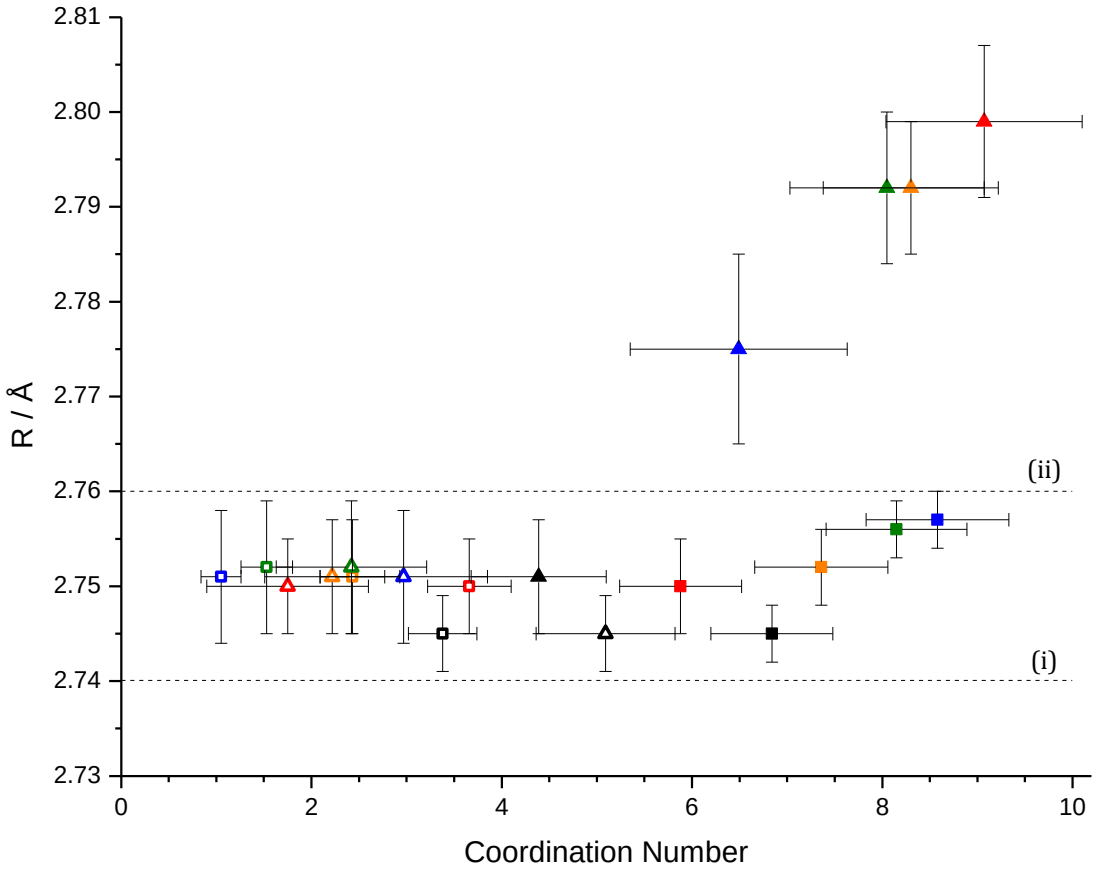

Figure 1.12: Comparison of the bond lengths and coordination numbers, with their respective errors, of the Pd-Pd (▲), Pd-Pt (△), Pt-Pt (■) and Pt-Pd (□) interactions for $Pt_{0.5ML}$/Pd/C (red), Pt_{1ML}/Pd/C (orange), Pt_{2ML}/Pd/C (green), Pt_{4ML}/Pd/C (blue) and the Pt/Pd/C Alloy (black). Representative Pd-Pd (i) and Pt-Pt (ii) bond lengths taken from Pd/C and Pt/C pellet data[23] are also shown (---).

The following observations can be made regarding the coordination numbers of the different interactions in the core-shell samples:

- **Pd-Pd:** decreases with increasing Pt shell thickness
- **Pt-Pt:** increases with increasing shell thickness

- **Pd-Pt and Pt-Pd:** The number of the mixed metal interactions are significantly lower than the number of Pd-Pd and Pt-Pt interactions, with a general increase in Pd-Pt interactions and decrease in Pt-Pd interactions with increasing Pt shell thickness.

The segregation in the number of M_1-M_1 and M_1-M_2 (where M_1 = Pd or Pt and M_2 = Pt or Pd respectively) coordination numbers is indicative of two separate elemental phases.[24] This is highlighted by the difference seen between the core-shell samples and the Pt/Pd/C alloy, which has the same elemental composition as the Pt_{2ML}/Pd/C, with the alloy displaying a much narrower distribution in the coordination numbers of the different interactions. The increase in the Pd-Pt interactions with increasing shell thickness indicates that the thinner shells may not have provided complete coverage of the core.

Comparison of the Pt-Pt bond lengths obtained for the core-shell samples shows an increase with increasing shell thickness from midway between the values obtained for Pd/C and Pt/C nanoparticles for the 0.5 ML sample to a value of 2.757 Å for the 4 ML sample which is significantly closer to that of the Pt/C at 2.76 Å. The bond length obtained for the alloy was lower than that obtained for the core-shell samples, but again lies between the values for Pd/C and Pt/C. The increase in Pt-Pt bond length with increasing shell thickness adds further weight to the assumption that two elemental phases are present in the sample.

The first thing to note regarding the Pd-Pd bond lengths for the core-shell samples is that they are much higher than the values obtained for both Pd/C and Pt/C nanoparticles. This is due to the well-known absorption of hydrogen into the Pd-core, forming a palladium hydride phase and causing expansion of the Pd lattice.[25] A clear effect of shell thickness can again be seen, with the 4 ML sample showing a much shorter bond length than the 0.5 ML sample. This is due to the restriction of the expansion in the Pd caused by hydrogen absorption by the thicker coverage of platinum. The alloy sample displays a slightly higher Pd-Pd bond length than the Pd/C value, suggesting that some hydrogen is absorbed, albeit to a much lesser extent than in the core-shell samples.

The M_1-M_2 interactions show little variation in the bond length between the core-shell samples and are mid-way between the Pd/C and Pt/C values (note that the values of Pd-Pt and Pt-Pd are the same per sample owing to the restriction on parameters applied in the fitting).

The other parameter of structural interest is the mean squared displacement (MSD), σ^2. The MSD remains relatively unchanged throughout the core-shell samples for the Pt-Pt interactions; however, a decrease is seen in the MSD of the Pd-Pd and M_1-M_2 bonds with increasing shell thickness. The MSD is increased with increasing structural disorder arising from variations in the sample environment. In the 0.5 ML sample, the largest Pd-Pd bond length is seen which, coupled with the expected surface environment of some of the Pd atoms, will increase the Pd-Pd MSD, also affecting the disorder in the mixed metal bond. These effects are reduced with increasing shell thickness, thus accounting for the decrease in the MSD.

1.3.2 In Situ EXAFS

The in situ EXAFS data and fits are shown in Figure 1.13 - Figure 1.19, with the corresponding fit parameters obtained given in Table 1.7 - Table 1.13. The quality of the data is slightly worse than that obtained for the pellets due to the difference in sample preparation (pressed pellet vs. painted electrode), and the fact that the in situ data was collected in fluorescence mode with much more dilute samples. This varied depending on the beamline used; in particular the data obtained for the Pd/C core material and the Pt_{1ML}/Pd/C sample on beamline BM26A at the ESRF is noticeably worse in terms of noise at higher *k*. This is partly due to the beamline being configured to collect SAXS and WAXS data simultaneously with the EXAFS, with compromises being made in the attempt to conduct the three techniques in parallel.

As in the ex situ data, an amplitude reduction factor had to be determined to obtain the coordination numbers. Whilst the values from the reference foils could again be used, the data was recorded in transmission and so would not account for the effect of the fluorescence detector on the S_0^2.[26] To allow the data at different potentials to be compared, the amplitude reduction factor for each set of beamline data was estimated based on the foil data to obtain coordination numbers for the data recorded at 0.05 V comparable to those of the pellets. The errors were propagated to allow for the estimation, resulting in the relatively large error values seen for the coordination. The coordination numbers did not change significantly between 0.00 V and 0.50 V, showing that within the error of the measurement the distribution of the elements within the particle remained stable at these potentials. The effect of oxygen neighbours on the coordination will be discussed in more detail later.

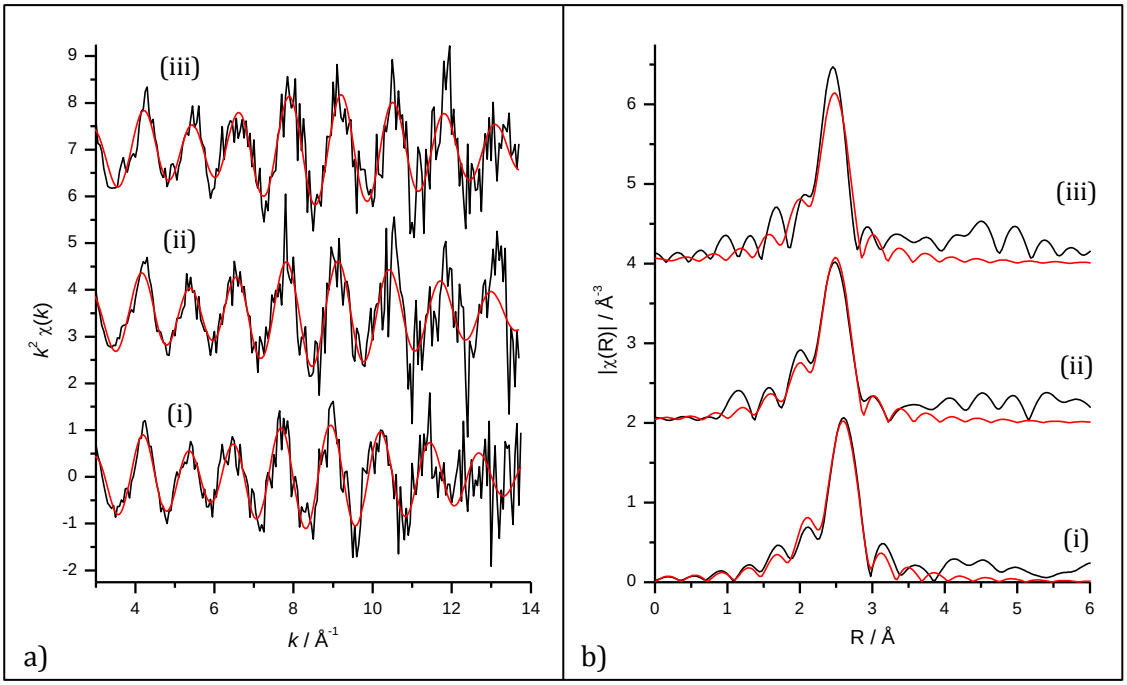

Figure 1.13: k^2 weighted experimental data (black) and fit (red) with the corresponding Fourier transform for the Pd/C core material. Data was recorded in situ at the Pd K edge, holding the potential at 0.0 V (i), 0.07 V (ii), and 0.52 V (iii) vs. RHE in 0.5 M H_2SO_4.

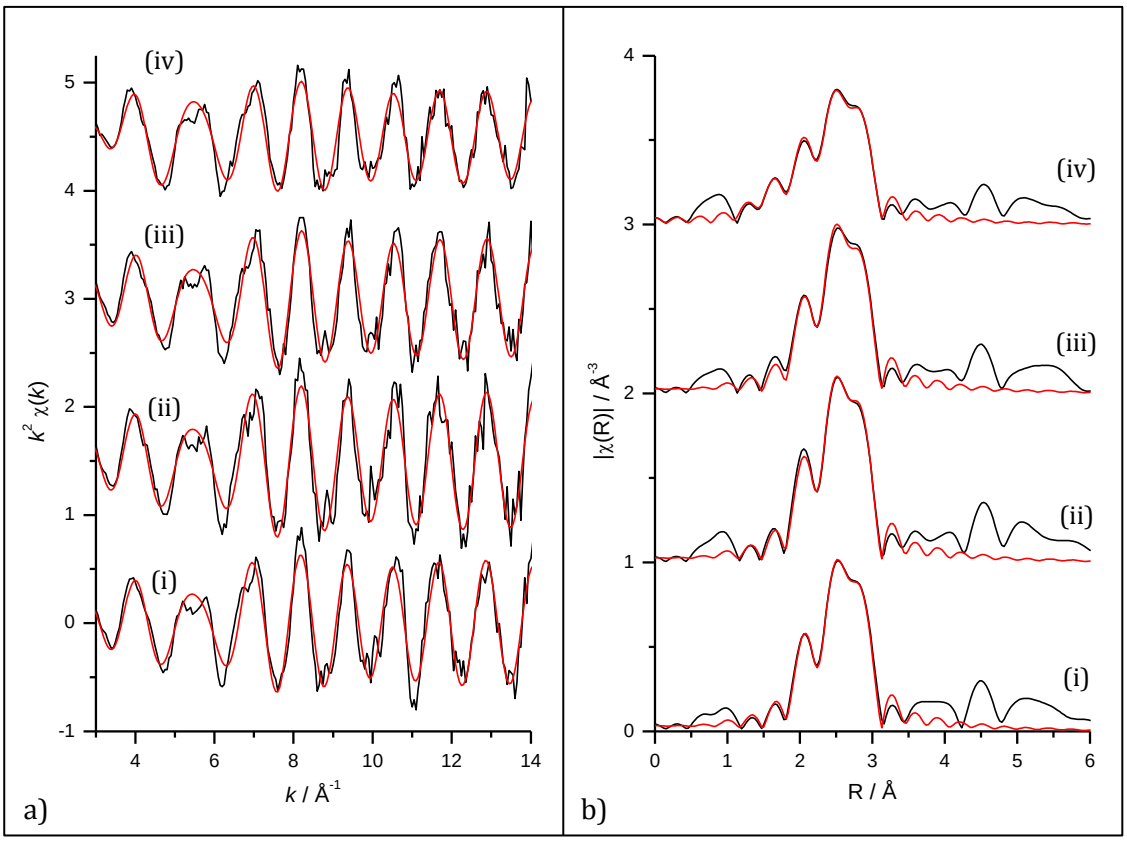

Figure 1.14: k^2 weighted experimental data (black) and fit (red) with the corresponding Fourier transform for 40 wt% Pt/C. Data was recorded in situ at the Pt L_3 edge, holding the potential at 0.0 V (i), 0.05 V (ii), 0.50 V (iii) and 1.00 V (iv) vs. RHE in 0.5 M H_2SO_4.

Table 1.7: Structural parameters obtained for the Pd/C core material from fitting in situ EXAFS data acquired under potential control in 0.5 M H_2SO_4 at the Pd K absorption edge.

Potential	Neighbour	N	R / Å	σ^2 / Å^2	ΔE_0 / eV	R_f
0.00 V vs. RHE	Pd-Pd	10.76 ± 1.88	2.828 ± 0.006	0.0066 ± 0.0008	-1.77 ± 0.79	0.0201
0.07 V vs. RHE	Pd-Pd	10.47 ± 1.72	2.760 ± 0.005	0.0066 ± 0.0007	-6.72 ± 0.71	0.0147
0.52 V vs. RHE	Pd-Pd	9.58 ± 1.50	2.741 ± 0.004	0.0058 ± 0.0006	-6.07 ± 0.62	0.0092

Table 1.8: Structural parameters obtained for 40 wt% Pt/C from fitting in situ EXAFS data acquired under potential control in 0.5 M H_2SO_4 at the Pt L_3 absorption edge.

Potential	Neighbour	N	R / Å	σ^2 / Å^2	ΔE_0 / eV	R_f
0.00 V vs. RHE	Pt-Pt	9.44 ± 1.66	2.760 ± 0.002	0.0049 ± 0.0003	7.67 ± 0.40	0.0041
0.05 V vs. RHE	Pt-Pt	10.35 ± 1.81	2.756 ± 0.002	0.0049 ± 0.0002	7.42 ± 0.36	0.0048
0.50 V vs. RHE	Pt-Pt	9.61 ± 1.73	2.754 ± 0.003	0.0051 ± 0.0004	7.85 ± 0.52	0.0066
1.00 V vs. RHE	Pt-Pt	8.67 ± 1.51	2.758 ± 0.002	0.0056 ± 0.0002	8.14 ± 0.39	0.0016
	Pt-O	1.04 ± 0.33	2.016 ± 0.013	0.0105 ± 0.0047		

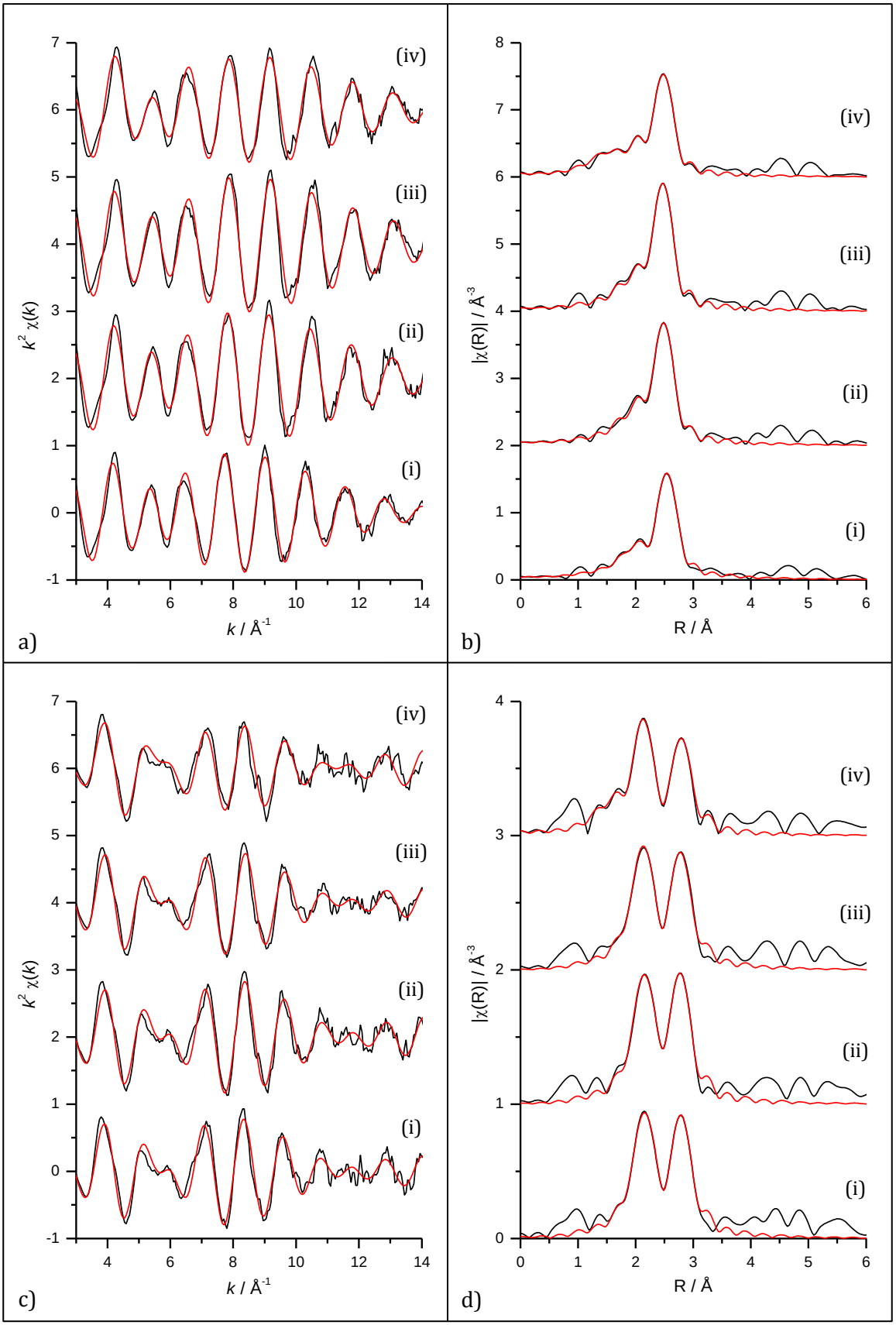

Figure 1.15: k^2 weighted experimental data (black) and fit (red) with the corresponding Fourier transform for $Pt_{0.5ML}/Pd/C$. Data was recorded in situ at the Pd K (a-b) and Pt L_3 (c-d) edges, holding the potential at 0.0 V (i), 0.05 V (ii), 0.50 V (iii) and 1.00 V (iv) vs. RHE in 0.5 M H_2SO_4.

Table 1.9: Structural parameters obtained for $Pt_{0.5ML}$/Pd/C from fitting in situ EXAFS data acquired under potential control in 0.5 M H_2SO_4. (N.B. first element in the neighbour pair indicates absorption edge of data)

Potential	Neighbour	N	R / Å	σ^2 / Å^2	ΔE_0 / eV	R_f
0.00 V vs. RHE	Pd-Pd	8.31 ± 1.12	2.785 ± 0.004	0.0074 ± 0.0004	-5.52 ± 0.35	0.0035
	Pd-Pt	1.89 ± 0.48	2.750 ± 0.006	0.0054 ± 0.0008		
	Pt-Pd	3.90 ± 0.66			5.02 ± 0.54	
	Pt-Pt	6.62 ± 1.07	2.747 ± 0.006	0.0055 ± 0.0008		
0.05 V vs. RHE	Pd-Pd	8.10 ± 1.11	2.750 ± 0.003	0.0060 ± 0.0004	-6.36 ± 0.35	0.0051
	Pd-Pt	1.81 ± 0.50	2.744 ± 0.007	0.0049 ± 0.0010		
	Pt-Pd	3.99 ± 0.75			5.22 ± 0.66	
	Pt-Pt	5.95 ± 1.09	2.740 ± 0.007	0.0045 ± 0.0010		
0.50 V vs. RHE	Pd-Pd	8.26 ± 1.10	2.741 ± 0.003	0.0062 ± 0.0003	-6.32 ± 0.29	0.0044
	Pd-Pt	1.43 ± 0.44	2.733 ± 0.007	0.0057 ± 0.0009		
	Pt-Pd	3.95 ± 0.69			4.85 ± 0.57	
	Pt-Pt	6.48 ± 1.07	2.733 ± 0.006	0.0056 ± 0.0008		
1.00 V vs. RHE	Pd-Pd	6.40 ± 0.88	2.745 ± 0.003	0.0059 ± 0.0004	-5.56 ± 0.37	0.0039
	Pd-O	1.25 ± 0.42	1.995 ± 0.014	0.0082 ± 0.0046		
	Pd-Pt	1.14 ± 0.37	2.732 ± 0.008	0.0043 ± 0.0010		
	Pt-Pd	2.81 ± 0.56			5.18 ± 0.77	
	Pt-O	0.80 ± 0.30	1.948 ± 0.027	0.0102 ± 0.0039 *		
	Pt-Pt	5.58 ± 1.04	2.737 ± 0.007	0.0049 ± 0.0010		

* Restraint applied to σ^2 for Pt-O interaction to keep value positive within error

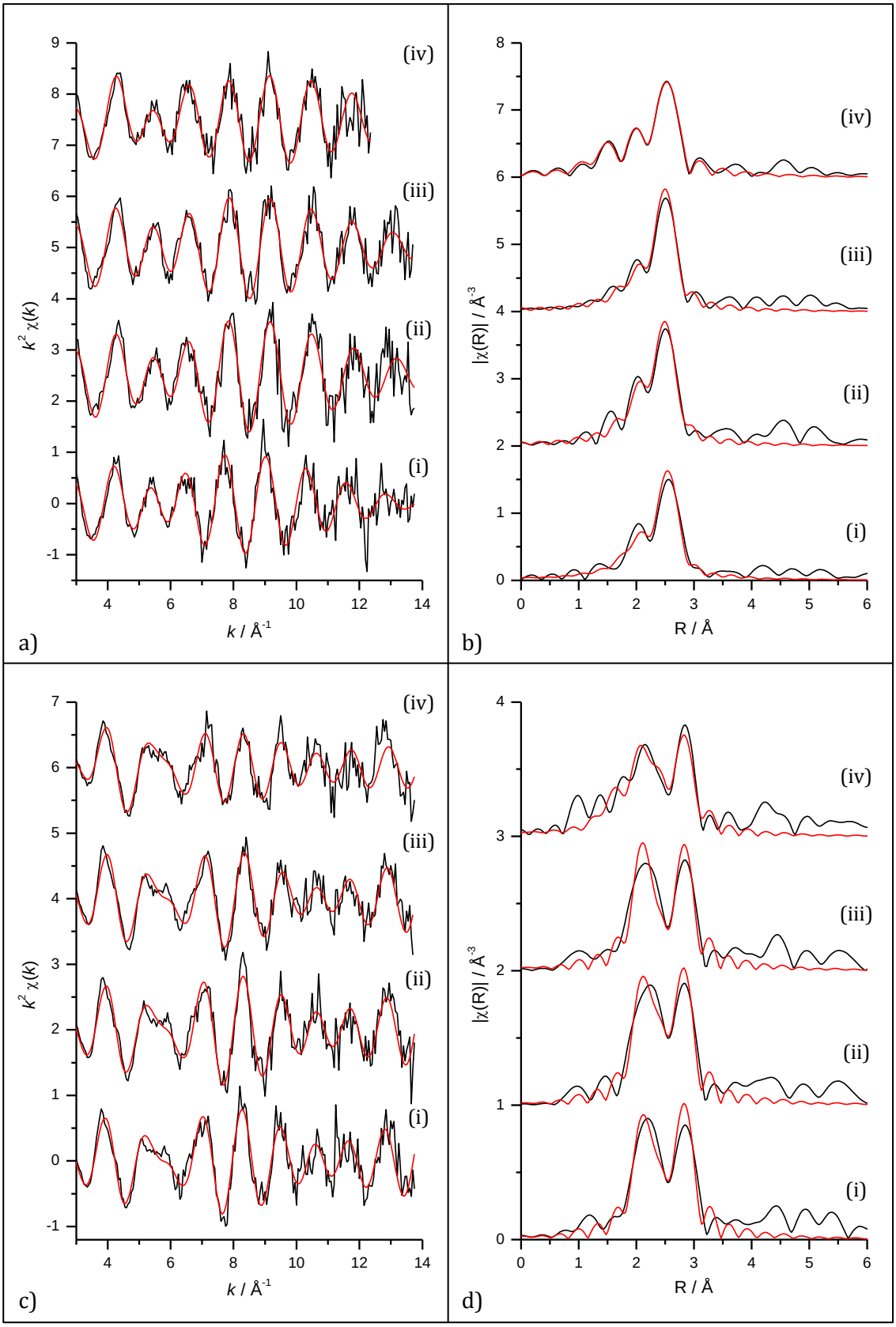

Figure 1.16: k^2 weighted experimental data (black) and fit (red) with the corresponding Fourier transform for $Pt_{1ML}/Pd/C$. Data was recorded in situ at the Pd K (a-b) and Pt L_3 (c-d) edges, holding the potential at 0.0 V (i), 0.075 V (ii), 0.525 V (iii) and 1.00 V (iv) vs. RHE in 0.5 M H_2SO_4.

Table 1.10: Structural parameters obtained for Pt_{1ML}/Pd/C from fitting in situ EXAFS data acquired under potential control in 0.5 M H_2SO_4. (N.B. first element in the neighbour pair indicates absorption edge of data)

Potential	Neighbour	N	R / Å	σ^2 / Å^2	ΔE_0 / eV	R_f
0.00 V vs. RHE	Pd-Pd	7.50 ± 1.48	2.777 ± 0.009	0.0058 ± 0.0010	-4.99 ± 0.85	0.0167
	Pd-Pt	2.92 ± 1.11	2.754 ± 0.009	0.0042 ± 0.0013		
	Pt-Pd	2.78 ± 0.66			5.86 ± 0.70	
	Pt-Pt	7.15 ± 1.19	2.758 ± 0.006	0.0041 ± 0.0007		
0.07 V vs. RHE	Pd-Pd	7.56 ± 1.26	2.742 ± 0.005	0.0046 ± 0.0007	-4.61 ± 0.57	0.0096
	Pd-Pt	2.92 ± 0.81	2.741 ± 0.008	0.0033 ± 0.0011		
	Pt-Pd	2.28 ± 0.52			6.10 ± 0.61	
	Pt-Pt	7.77 ± 1.20	2.745 ± 0.005	0.0042 ± 0.0006		
0.52 V vs. RHE	Pd-Pd	8.49 ± 1.36	2.749 ± 0.006	0.0062 ± 0.0007	-4.64 ± 0.57	0.0077
	Pd-Pt	1.33 ± 0.73	2.730 ± 0.008	0.0044 ± 0.0010		
	Pt-Pd	2.74 ± 0.57			6.53 ± 0.55	
	Pt-Pt	7.08 ± 1.07	2.741 ± 0.005	0.0044 ± 0.0005		
1.00 V vs. RHE	Pd-Pd	6.77 ± 1.49	2.756 ± 0.010	0.0055 ± 0.0013	-5.56 ± 0.37	
	Pd-O	1.18 ± 0.55	1.983 ± 0.032	0.0046 ± 0.0034 *		
	Pd-Pt	1.71 ± 1.68	2.749 ± 0.033	0.0078 ± 0.0050		
	Pt-Pd	2.58 ± 1.27			5.18 ± 0.77	
	Pt-O	0.94 ± 0.38	1.999 ± 0.034	0.0079 ± 0.0035 *		
	Pt-Pt	6.11 ± 1.71	2.745 ± 0.017	0.0056 ± 0.0022		

* Restraint applied to σ^2 for Pt-O interaction to keep value positive within error

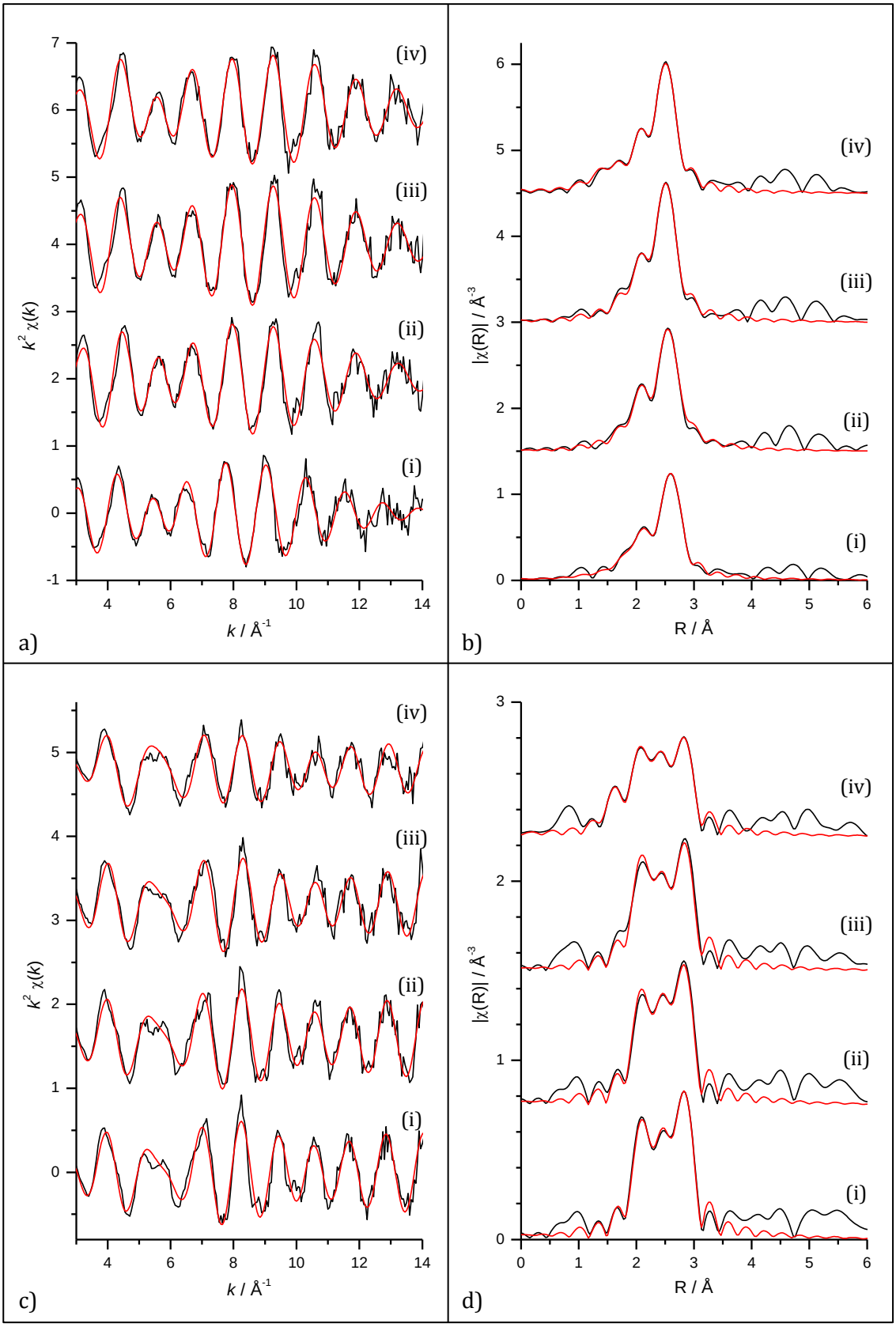

Figure 1.17: k^2 weighted experimental data (black) and fit (red) with the corresponding Fourier transform for $Pt_{2ML}/Pd/C$. Data was recorded in situ at the Pd K (a-b) and Pt L_3 (c-d) edges, holding the potential at 0.0 V (i), 0.05 V (ii), 0.50 V (iii) and 1.00 V (iv) vs. RHE in 0.5 M H_2SO_4.

Table 1.11: Structural parameters obtained for Pt_{2ML}/Pd/C from fitting in situ EXAFS data acquired under potential control in 0.5 M H_2SO_4. (N.B. first element in the neighbour pair indicates absorption edge of data)

Potential	Neighbour	N	R / Å	σ^2 / Å^2	ΔE_0 / eV	R_f
0.00 V vs. RHE	Pd-Pd	6.91 ± 1.23	2.786 ± 0.005	0.0060 ± 0.0005	-1.37 ± 0.44	0.0032
	Pd-Pt	3.30 ± 0.74	2.756 ± 0.006	0.0045 ± 0.0008		
	Pt-Pd	1.91 ± 0.41			6.86 ± 0.35	
	Pt-Pt	8.32 ± 1.47	2.758 ± 0.003	0.0044 ± 0.0003		
0.05 V vs. RHE	Pd-Pd	7.89 ± 1.41	2.743 ± 0.004	0.0055 ± 0.0006	1.94 ± 0.43	0.0059
	Pd-Pt	2.11 ± 0.66	2.743 ± 0.009	0.0036 ± 0.0014		
	Pt-Pd	1.51 ± 0.44			6.95 ± 0.58	
	Pt-Pt	8.27 ± 1.56	2.749 ± 0.004	0.0045 ± 0.0007		
0.50 V vs. RHE	Pd-Pd	8.03 ± 1.41	2.736 ± 0.004	0.0051 ± 0.0005	-0.58 ± 0.41	0.0076
	Pd-Pt	2.19 ± 0.68	2.733 ± 0.010	0.0041 ± 0.0014		
	Pt-Pd	1.64 ± 0.49			7.57 ± 0.60	
	Pt-Pt	8.42 ± 1.61	2.744 ± 0.005	0.0050 ± 0.0006		
1.00 V vs. RHE	Pd-Pd	7.09 ± 1.22	2.737 ± 0.003	0.0049 ± 0.0004	-0.42 ± 0.37	0.0021
	Pd-O	0.94 ± 0.25	1.972 ± 0.016	0.0050 ± 0.0018 *		
	Pd-Pt	2.02 ± 0.58	2.731 ± 0.009	0.0044 ± 0.0014		
	Pt-Pd	1.05 ± 0.31			7.16 ± 0.57	
	Pt-O	0.63 ± 0.17	1.990 ± 0.014	0.0030 ± 0.0018 *		
	Pt-Pt	7.15 ± 1.33	2.741 ± 0.004	0.0055 ± 0.0006		

* Restraint applied to σ^2 for Pd-O and Pt-O interactions to keep values positive within error

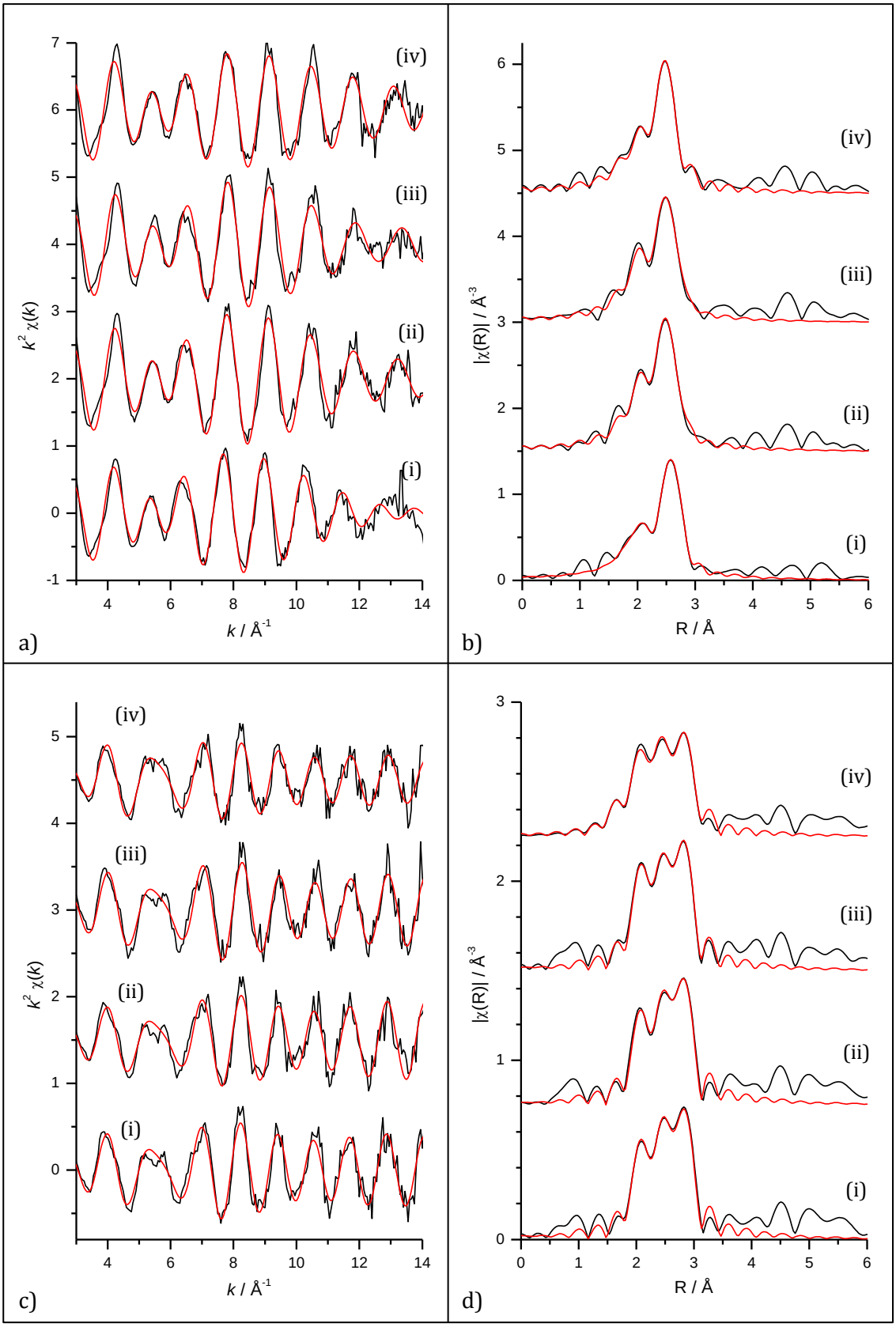

Figure 1.18: k^2 weighted experimental data (black) and fit (red) with the corresponding Fourier transform for $Pt_{4ML}/Pd/C$. Data was recorded in situ at the Pd K (a-b) and Pt L_3 (c-d) edges, holding the potential at 0.0 V (i), 0.05 V (ii), 0.50 V (iii) and 1.00 V (iv) vs. RHE in 0.5 M H_2SO_4.

Table 1.12: Structural parameters obtained for Pt_{4ML}/Pd/C from fitting in situ EXAFS data acquired under potential control in 0.5 M H_2SO_4. (N.B. first element in the neighbour pair indicates absorption edge of data)

Potential	Neighbour	N	R / Å	σ^2 / Å^2	ΔE_0 / eV	R_f
0.00 V vs. RHE	Pd-Pd	6.40 ± 0.93	2.785 ± 0.006	0.0064 ± 0.0007	-5.29 ± 0.48	0.0061
	Pd-Pt	3.94 ± 0.79	2.758 ± 0.007	0.0051 ± 0.0011		
	Pt-Pd	1.10 ± 0.45			7.42 ± 0.74	
	Pt-Pt	8.27 ± 1.70	2.757 ± 0.005	0.0050 ± 0.0008		
0.05 V vs. RHE	Pd-Pd	6.28 ± 0.92	2.745 ± 0.005	0.0044 ± 0.0006	-6.10 ± 0.52	0.0070
	Pd-Pt	3.63 ± 0.84	2.747 ± 0.008	0.0039 ± 0.0012		
	Pt-Pd	0.97 ± 0.44			7.23 ± 0.93	
	Pt-Pt	7.19 ± 1.60	2.751 ± 0.006	0.0043 ± 0.0009		
0.50 V vs. RHE	Pd-Pd	6.39 ± 0.95	2.736 ± 0.004	0.0049 ± 0.0006	-6.03 ± 0.53	0.0072
	Pd-Pt	3.17 ± 0.77	2.738 ± 0.010	0.0034 ± 0.0012		
	Pt-Pd	1.04 ± 0.40			7.58 ± 0.81	
	Pt-Pt	8.28 ± 1.73	2.745 ± 0.005	0.0049 ± 0.0008		
1.00 V vs. RHE	Pd-Pd	6.46 ± 0.93	2.746 ± 0.004	0.0055 ± 0.0006	-6.72 ± 0.52	0.0045
	Pd-O	-	-	-		
	Pd-Pt	4.10 ± 1.22	2.753 ± 0.013	0.0083 ± 0.0026		
	Pt-Pd	1.29 ± 0.63			7.63 ± 0.92	
	Pt-O	0.41 ± 0.26	2.017 ± 0.051	0.0055 ± 0.0030 *		
	Pt-Pt	7.88 ± 1.70	2.749 ± 0.007	0.0062 ± 0.0009		

* Restraint applied to σ^2 for Pt-O interaction to keep value positive within error

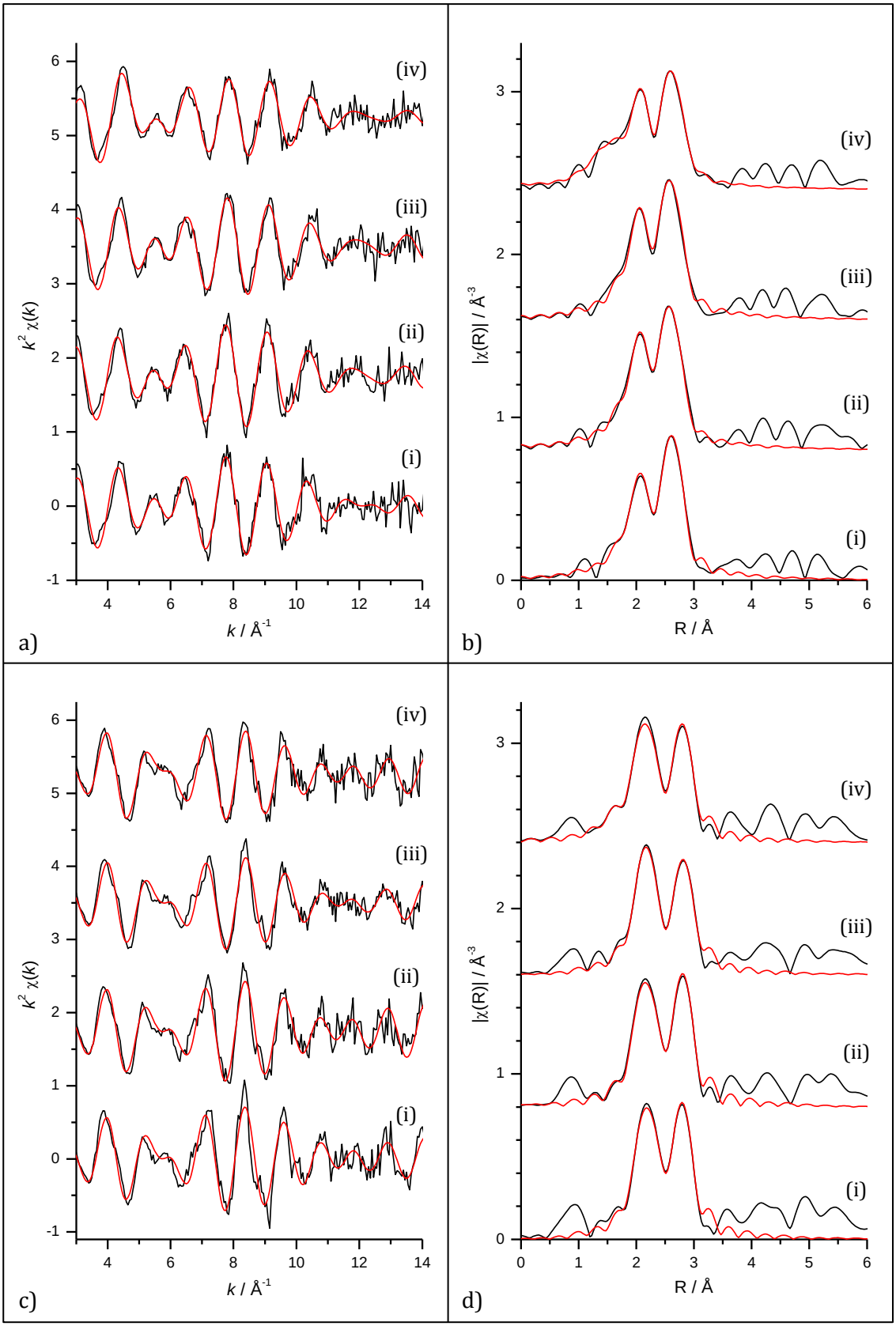

Figure 1.19: k^2 weighted experimental data (black) and fit (red) with the corresponding Fourier transform for Pt/Pd/C Alloy. Data was recorded in situ at the Pd K (a-b) and Pt L_3 (c-d) edges, holding the potential at 0.0 V (i), 0.05 V (ii), 0.50 V (iii) and 1.00 V (iv) vs. RHE in 0.5 M H_2SO_4.

Table 1.13: Structural parameters obtained for Pt/Pd/C Alloy from fitting in situ EXAFS data acquired under potential control in 0.5 M H_2SO_4. (N.B. first element in the neighbour pair indicates absorption edge of data)

Potential	Neighbour	N	R / Å	σ^2 / Å^2	ΔE_0 / eV	R_f
0.00 V vs. RHE	Pd-Pd	4.84 ± 0.92	2.756 ± 0.005	0.0047 ± 0.0007	-2.49 ± 0.45	0.0059
	Pd-Pt	4.90 ± 0.94	2.749 ± 0.004	0.0040 ± 0.0006		
	Pt-Pd	3.76 ± 0.73			6.91 ± 0.44	
	Pt-Pt	7.16 ± 1.36	2.743 ± 0.004	0.0042 ± 0.0006		
0.05 V vs. RHE	Pd-Pd	4.66 ± 0.83	2.745 ± 0.004	0.0040 ± 0.0005	-4.00 ± 0.36	0.0043
	Pd-Pt	5.79 ± 1.04	2.743 ± 0.004	0.0045 ± 0.0005		
	Pt-Pd	3.96 ± 0.75			6.79 ± 0.41	
	Pt-Pt	6.81 ± 1.30	2.741 ± 0.004	0.0039 ± 0.0006		
0.50 V vs. RHE	Pd-Pd	4.92 ± 0.95	2.741 ± 0.005	0.0045 ± 0.0008	-2.81 ± 0.49	0.0077
	Pd-Pt	4.81 ± 0.96	2.740 ± 0.005	0.0041 ± 0.0006		
	Pt-Pd	3.54 ± 0.71			7.33 ± 0.48	
	Pt-Pt	7.05 ± 1.37	2.741 ± 0.005	0.0047 ± 0.0007		
1.00 V vs. RHE	Pd-Pd	3.82 ± 0.75	2.740 ± 0.006	0.0045 ± 0.0008	0.04 ± 0.57	0.0059
	Pd-O	1.33 ± 0.36	1.974 ± 0.018	0.0102 ± 0.0021 *		
	Pd-Pt	4.57 ± 0.94	2.736 ± 0.006	0.0049 ± 0.0008		
	Pt-Pd	3.60 ± 0.77			6.82 ± 0.69	
	Pt-O	0.57 ± 0.34	1.978 ± 0.047	0.0105 ± 0.0054 *		
	Pt-Pt	7.04 ± 1.53	2.734 ± 0.007	0.0048 ± 0.0010		

* Restraint applied to σ^2 for Pd-O and Pt-O interactions to keep values positive within error

As seen in the pellet data, the shape of the Fourier transforms changes with increasing shell thickness. In addition to this, a shift in the peak positions for the Pd K edge data at 0.00 V to higher R compared to the data at other potentials is observed (plots b(i)). This is due to the lattice expansion caused by hydrogen absorption. An increase in the amplitude at low R is also visible in the data recorded at 1.00 V at both edges (plots b(iv) and d(iv)), which can be attributed to the presence of oxygen neighbours. This discussion will focus firstly on the effect of reducing the potential from the double layer to the hydrogen region, and then on the effect of oxide growth at 1.00 V.

The variation in bond length with the reduction of the electrode potential from 0.50 V to 0.00 V is shown in Figure 1.20.

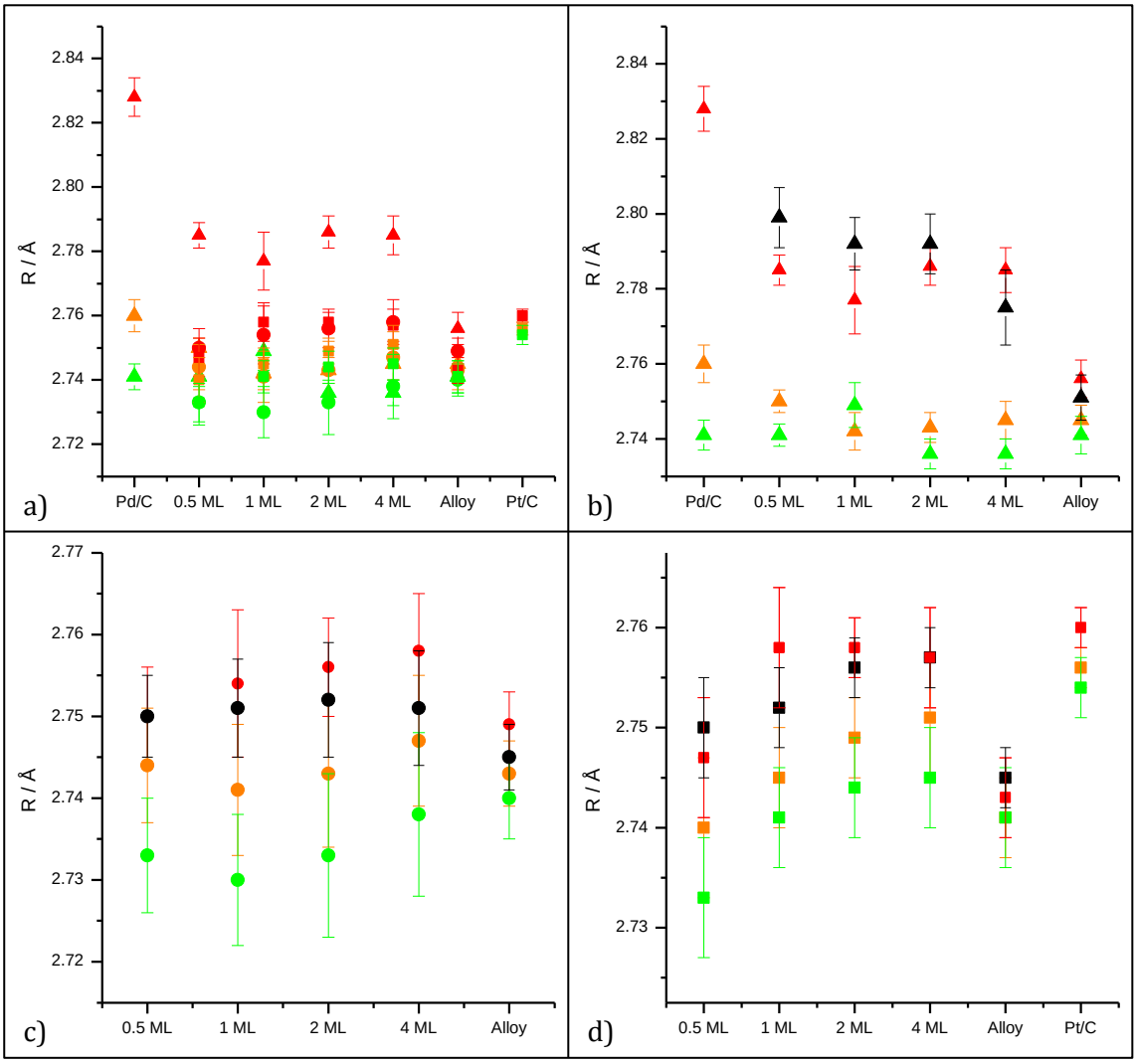

Figure 1.20: Comparison across the samples of the Pd-Pd (▲), Pd-Pt (●) and Pt-Pt (■) bond lengths at 0.00 V (red), 0.05 V (orange) and 0.50 V (green). All interactions are shown in (a), with (b) – (d) focusing on the Pd-Pd, Pd-Pt and Pt-Pt bonds respectively. Ex situ data (black) is included in plots (b) – (d) for reference.

Overall an increase in the bond lengths can be seen with the decrease in potential, most noticeably with the decrease from 0.05 V to 0.00 V, which can be attributed to the absorption of hydrogen into the palladium. This has an effect on the lengths of all of the bonds in the system showing that the nanoparticle as a whole is being perturbed. The alloy shows much less variation in bond length than the core-shell materials, particularly noticeable is the reduction in the perturbation due to hydrogen absorption, again adding evidence to the core-shell samples consisting of separate elemental phases. A slight increase in the Pt-Pt bond of the Pt/C catalyst is seen with the reduction in potential, showing that it is not immune to the presence of hydrogen.

The increase in Pd-Pd bond length due to hydrogen absorption is much larger in the Pd/C core material than when Pt is present, demonstrating that even half a monolayer of Pt on the surface is sufficient to restrict the lattice expansion. The effect of shell thickness on the expansion is not obvious, although it is interesting to note that the ex situ data recorded under a hydrogen atmosphere appears to display a longer Pd-Pd bond length than the electrochemically induced absorption for the 0.5, 1 and 2 monolayer samples. The Pd-Pd bond lengths for the 0.5, 2 and 4 ML samples at 0.00 V are very similar, suggesting perhaps a limit to the hydride formation in these samples at this potential.

Figure 1.21 compares the bond lengths and coordination numbers of the interactions at 0.50 V and 1.00 V, including the Pd-O and Pt-O neighbours. Fitting the data at 1.00 V proved more difficult than the data recorded at lower potentials. This is partially due to the reduction in the signal at higher *k*, due to the presence of oxygen neighbours which dominate the signal at lower *k*, resulting in noisier data. The other difficulty was the large number of parameters being fitted to what was essentially the first coordination shell of the absorber. The presence of three different neighbours at a similar distance means that the data needs to be of a high quality in order for the fitting procedure to accurately separate the contributions from each one. Correspondingly, in some cases, a restraint was applied to the MSD of the metal-oxygen interactions to keep it positive within error. The restraint applies a penalty to the data if the value is outside a user-defined range. In all instances the implementation of the restraint did not alter the values of the other parameters.

The large error bars obtained as a result of the difficulties in fitting the oxide data can clearly be seen in Figure 1.21, making it difficult to draw any significant conclusions from the data. The metal-metal bond lengths remain similar to the values obtained at 0.50 V for

the 0.5 ML, 2 ML and alloy samples, whereas increases are seen in the values for the 1 and 4 ML samples. A slight increase in the Pt-Pt bond length is seen for the Pt/C catalyst. In terms of the metal-oxygen bond lengths, the errors obtained were larger than those for the metal-metal bonds which could be attributed to a range of oxygen species present at a variety of sites. In general an increase in $R_{Pt\text{-}O}$ and a decrease in $R_{Pd\text{-}O}$ is seen with increasing shell thickness.

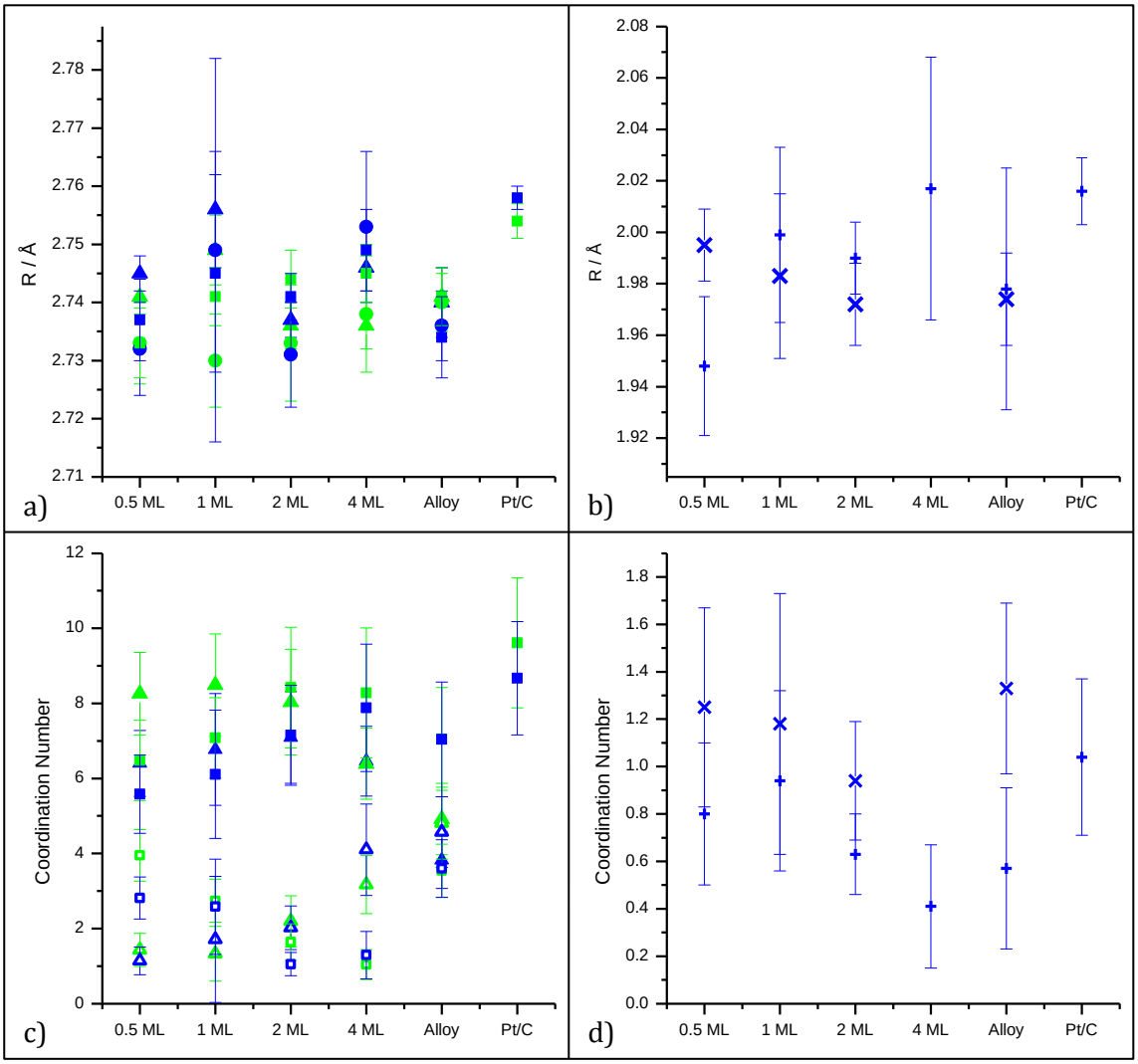

Figure 1.21: Comparison across the samples of the Pd-Pd (▲), Pd-Pt (●), Pt-Pt (■), Pd-O (✕) and Pt-O (✚) bond lengths (a & b) and Pd-Pd (▲), Pd-Pt (△), Pt-Pd (□), Pt-Pt (■), Pd-O (✕) and Pt-O (✚) coordination numbers (c & d) at 0.50 V (green) and 1.00 V (blue).

A decrease in the coordination numbers of all of the metal-metal bonds is seen with the presence of oxygen, showing that the formation of the metal-oxygen species is altering both the Pd core and the Pt shell. The number of metal-oxygen interactions decreases with increasing shell thickness. In the case of Pt, this can be attributed to a bulk averaging effect; with more Pt present the effect of the addition of oxygen to the structure is

diminished. The Pd environment is altered less by the addition of further Pt shells, meaning that the decrease in $N_{Pd\text{-}O}$ can be deemed a 'real' effect, showing that less of the Pd is accessible to oxygen with increasing shell thickness. It was not possible to fit Pd-O neighbours for the Pt_{4ML}/Pd/C sample. However, this doesn't mean that none were present, rather that the contribution to the average structure by any oxygen neighbours was too small to be resolved in the fitting process.

1.4 Conclusions

The combination of in and ex situ EXAFS has shown:

- Two separate elemental environments are present in the core-shell samples.
- The addition of further shells of Pt results in an increase in $R_{Pt\text{-}Pt}$ and a reduction in the lattice expansion due to the absorption of hydrogen from a hydrogen atmosphere.
- The electrochemically induced hydrogen absorption is significantly lower for the bimetallic samples than for the Pd/C core material, even when only 0.5 ML of Pt is present.
- Hydrogen absorption has an effect on all of the bond lengths in the core-shell materials, showing that the Pt is perturbed by the expansion in the Pd lattice.
- Large errors were associated with the parameters obtained from fitting the data at 1.00 V, however, there appeared to be a decrease in the Pd-O and an increase in the Pt-O bond lengths with increasing shell thickness.
- The number of Pd-O interactions decreases with increasing shell thickness, showing that more complete coverage of the Pd has been achieved by the Pt.

These findings are consistent of a structure with a Pd core surrounded by Pt. The presence of Pd-O neighbours suggests that coverage of the core is not complete with 0.5 to 2 ML thickness, although the inability to fit Pd-O neighbours does not prove that none are present in the Pt_{4ML}/Pd/C.

2 Wide-Angle X-Ray Scattering (WAXS)

2.1 Introduction to WAXS

Wide-angle X-ray scattering refers to the scattering, or diffraction, of X-rays by electrons to angles above 3° 2θ, where 2θ is the angle between the incident beam and the scattered signal. It is an X-ray diffraction technique (XRD) synonymous with the powder XRD described in Chapter Two, although the term WAXS is often applied to measurements made using synchrotron radiation of samples with a limited degree of crystallinty, and so is used to describe this work.

As seen by the powder XRD data shown in Chapter Two, these measurements can be conducted successfully using a laboratory-based diffractometer. However, there are several advantages to using synchrotron radiation. The high brilliance collimated X-rays produced at a synchrotron beamline result in a monochromatic beam with a much greater intensity than that available from a laboratory X-ray source, thus allowing weak diffraction peaks to be detected. X-rays of a higher energy, and therefore shorter wavelength, can also be used which gives higher resolution and allows greater penetration of the sample, facilitating in situ measurements. The high intensity beam also means that much shorter collection times are required.[27]

2.1.1 Theory of WAXS

X-rays interact with the atoms in a sample via absorption, elastic scattering and inelastic scattering processes. X-ray diffraction techniques such as WAXS are concerned with the elastic scattering of X-rays.

When X-rays are scattered by a material, spherical waves are emitted from each atom. In elastic scattering these waves are coherent, causing constructive and destructive interference which produces a scattering pattern on the detector. This pattern is a Fourier transform of the structure of the sample, therefore the larger the angle between the incident beam and the scattered X-rays, the smaller the structure being detected.

In a crystal structure, the atoms in the lattice form a periodic array of coherent scatterers. When constructive interference from these atoms occurs, the diffracted X-rays result in a bright spot of intensity on the detector, known as a reflection, related to specific lattice planes. These reflections are named by the Miller indices, (*hkl*), of the reflecting plane. For this to happen, the diffraction must satisfy Bragg's Law:

$$n\lambda = 2d_{hkl} \sin \theta_{hkl}$$

Equation 2.1

Where λ is the wavelength of the incident X-rays, n is an integer known as the order of the reflection, d_{hkl} is the spacing between two (hkl) lattice planes, and θ_{hkl} is the angle between the incident X-rays and the reflecting lattice plane.[28] A schematic representation of Bragg's Law is shown in Figure 2.1.

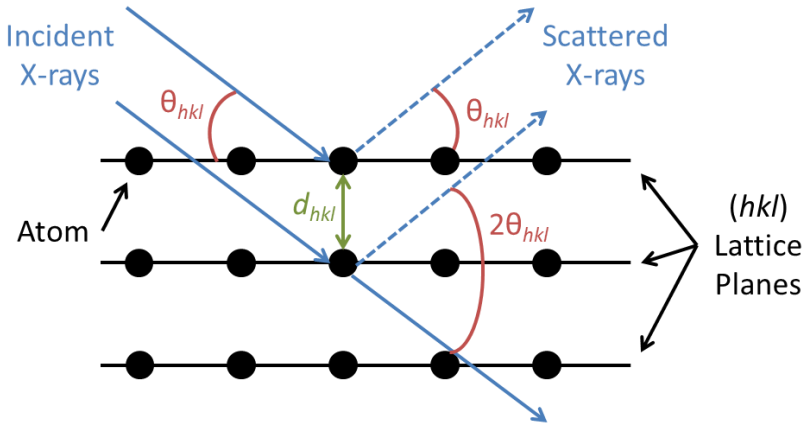

Figure 2.1: Illustration of Bragg's Law

If the sample being studied is made up of many randomly orientated crystals, as in powder XRD and WAXS, the Bragg diffraction results in concentric cones of radiation, resulting in circles of intensity on the detector known as a Debye-Scherrer rings (Figure 2.2).[29]

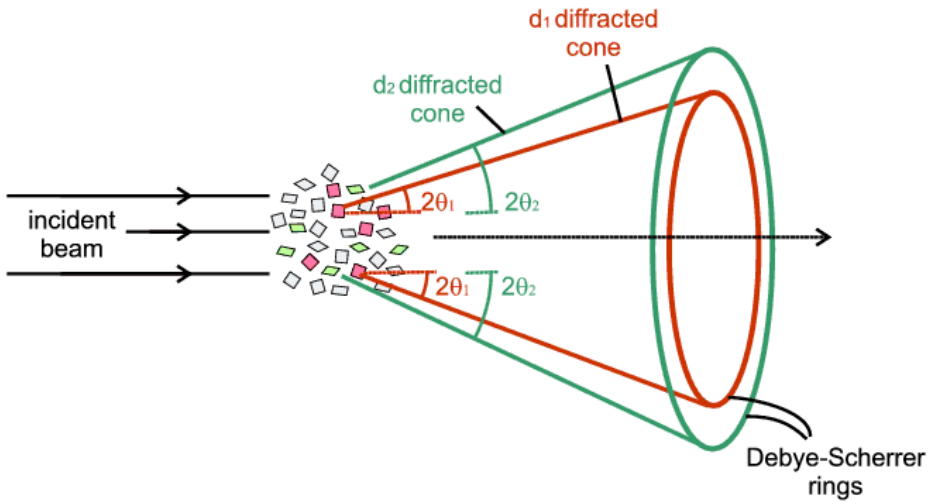

Figure 2.2: Depiction of the diffraction of X-rays by randomly orientated crystals.[30]

The 2D pattern obtained is typically azimuthally averaged and integrated to give a plot of the intensity as a function of 2θ, with the peaks, known as Bragg peaks, corresponding to the reflections from the crystal lattice planes:

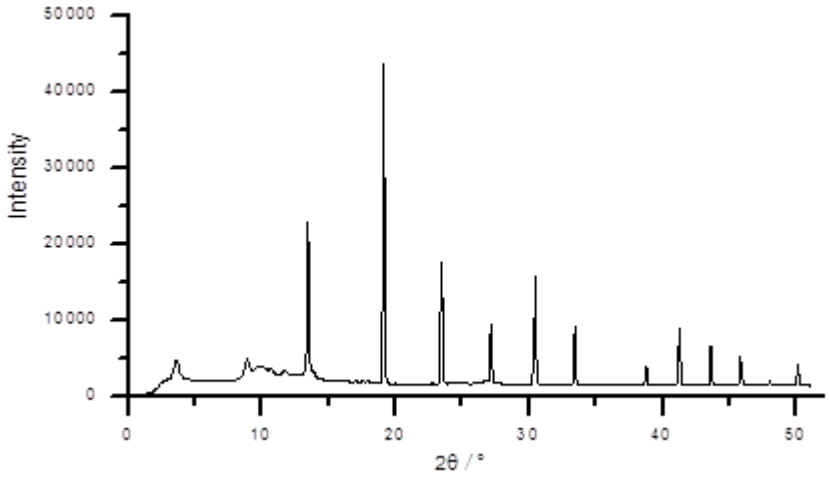

Figure 2.3: Azimuthally averaged WAXS pattern of LaB_6.

The Miller indices (*hkl*) specify the points at which a plane in the crystal intercepts the axis of the unit cell with dimensions *a*,*b*,*c*. In a face centered cubic (fcc) system, such as in the crystal structures of Pt and Pd studied here, $a = b = c$ and the lattice parameter of the unit cell is *a*. The interplanar spacing, d_{hkl}, is used to derive the lattice parameter of the unit cell using the following relationship:

$$d_{hkl} = \frac{a}{\sqrt{h^2 + k^2 + l^2}}$$

Equation 2.2

Combining Equation 2.1 and Equation 2.2 enables the determination of the lattice parameter from the 2θ position of the Bragg peaks:[31]

$$\sin^2 \theta_{hkl} = \frac{\lambda^2}{4a^2}(h^2 + k^2 + l^2)$$

Equation 2.3

In the powder XRD data shown in Chapter Two, the crystallite size was reported along with the lattice parameter, *a*. This was determined from the Scherrer formula given in Equation 2.4, where *L* is the crystallite size, $B_{2\theta}$ is the FWHM of the peak in radians, λ is the

wavelength of the incident X-rays and θ_{max} is the position of the maximum of the Bragg peak.[32]

$$L = \frac{0.9\lambda}{B_{2\theta} \cos \theta_{max}}$$

Equation 2.4

The ability to determine the crystallite size from the width of the Bragg peak arises from the broadening seen in the peak with decreasing crystallite size for crystals below 1 μm. However, broadening of the peak also results from instrumental broadening and strain in the lattice caused by distortions and dislocations, the effects of which need to be separated from the size-related broadening for crystallite size to be determined with any accuracy.[33]

Owing to the dependence of WAXS on the presence of a crystalline structure, long-range order is required within the sample being investigated. In the case of metal nanoparticles such as those studied here, the structure typically consists of a combination of crystalline and amorphous regions. Thus it should be noted that WAXS can be used to obtain information on the crystalline fraction of the particle or sample only, rather than the particle as a whole.

2.2 Experimental Aspects

2.2.1 Data Collection

WAXS data was collected in situ using the electrochemical cell described in Chapter Two on beamline 11-3, Stanford Synchrotron Radiation Lightsource, using a wavelength of 0.9760 Å and a sample-to-detector distance of ca. 150 mm. Beamline 11-3 has a multipole wiggler source and a side-deflecting Si(311) monochromator resulting in a fixed wavelength.[34] The measurements were conducted by Peter Richardson, Andrea Russell and Anna Wise and the beamline scientists were Michael Toney and Sumohan Misra.

Prior to measuring any catalyst samples, a LaB_6 reference sample was placed in the catalyst electrode position in the in situ cell and WAXS data collected. This was to calibrate the sample-to-detector distance to allow accurate determination of the position of the Bragg peaks and, therefore, the lattice parameter of the catalyst samples.[35]

As with the in situ EXAFS measurements detailed in Section 1.2.4 of this chapter, the prepared catalyst electrodes were hydrated by boiling in demineralised water before being loaded into the in situ cell. N_2-purged 0.5 M H_2SO_4 was then introduced into the cell using the peristaltic pump and the electrodes were connected to the μAutolab III potentiostat, again using a MMS reference electrode to determine the potential. The cell was mounted on the beamline parallel to the MAR345 image plate detector so that the incident beam entered through the rear window of the cell, with the diffracted X-rays leaving the cell through the front window as shown in Figure 2.4. A beamstop was used to protect the detector from the high intensity direct beam passing through the sample.

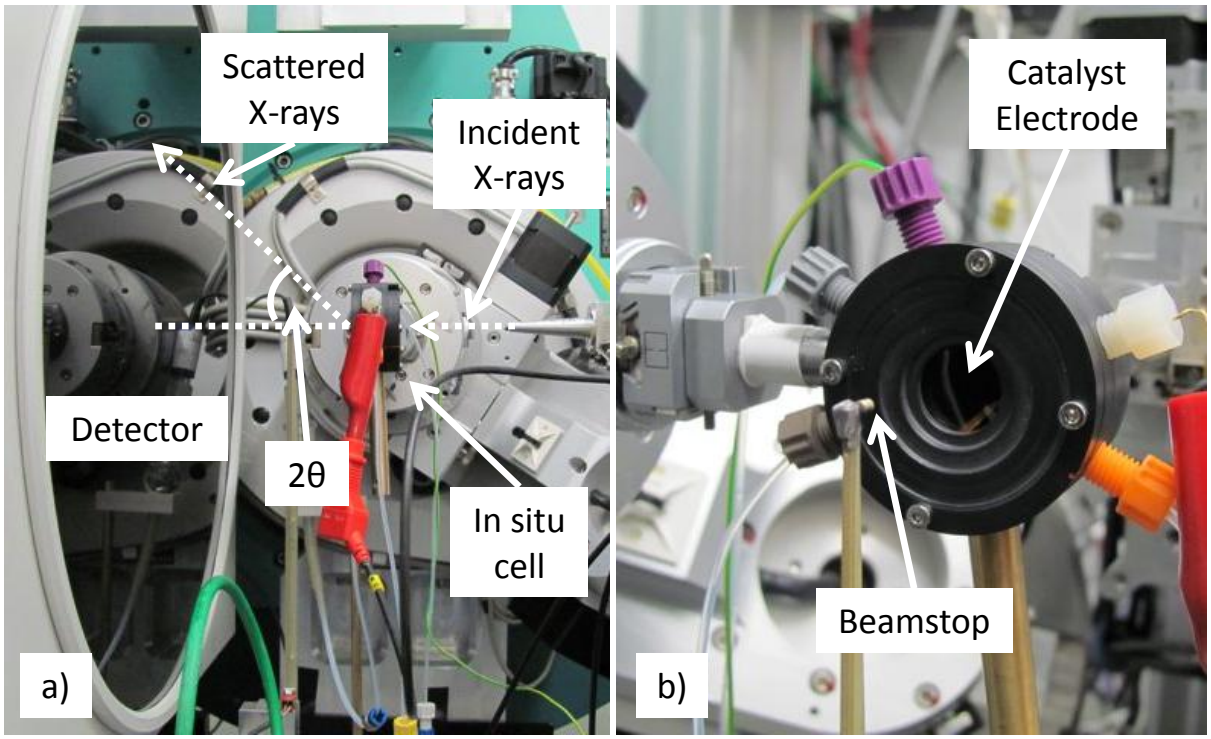

Figure 2.4: Experimental set-up on beamline 11-3, showing the cell in parallel with the detector (a) and a close-up of the front of the cell (b).

The WAXS measurements were collected over a total of 6 minutes divided into several exposures, dependent on the maximum intensity recorded, to keep below the saturation limit of the detector. The shorter collection time compared to EXAFS meant that it was possible to repeat the measurements obtained in the double layer region to check for alterations in the structure following the potential holds at 0.00 V and 1.00 V, and to check for time-dependent changes at 1.00 V. WAXS data was collected for each catalyst sample as follows:

- First WAXS collection at OCV
- Three CVs at 50 mV s^{-1} were recorded between 1.00 V and 0.07 V, starting at OCV, followed by three CVs at 10 mV s^{-1}
- WAXS data collected, holding the potential at 0.50 V vs. RHE
- WAXS data collected, holding the potential at 0.07 V vs. RHE
- WAXS data collected after holding the potential at 0.00 V vs. RHE for 10 minutes
- CVs (10 mV s^{-1}) recorded from 0.00 V to 1.00 V to remove absorbed hydrogen from the sample
- WAXS data collected, holding the potential at 0.50 V vs. RHE
- WAXS data collected after holding the potential at 1.00 V vs. RHE for 10 minutes
- WAXS data collected after holding the potential at 1.00 V vs. RHE for 30 minutes
- CVs (10 mV s^{-1}) recorded from 1.00 V to 0.07 V to remove oxide

- WAXS data collected, holding the potential at 0.50 V vs. RHE for 5 minutes
- WAXS data collected, holding the potential at 0.50 V vs. RHE for 20 minutes

In all cases the potential was moved gradually to the desired value to avoid large increases in the current. Where a hold time is not specified, the cell current was allowed to decay before collecting the data. The samples investigated in this manner were the Pd/C core material, 40 wt% Pt/C, $Pt_{0.5ML}$/Pd/C, Pt_{1ML}/Pd/C, Pt_{2ML}/Pd/C, Pt_{4ML}/Pd/C and the Pt/Pd/C alloy. In addition to this, WAXS data was collected of a carbon electrode, painted from an ink containing the carbon support mixed with the same ratio of Nafion as in the catalyst electrodes, to enable the isolation of the peaks arising from the metal in the samples from those due to the carbon and cell background.

2.2.2 Data Analysis

Before converting the 2D images collected into a 1D radial pattern as a function of intensity, the sample-to-detector distance was refined using the LaB_6 reference file. The data was imported into Fit2D and the calibrant function used to give an accurate distance based on the lattice spacing in LaB_6.[36],[37] This was performed based on the relationship between the sample, X-rays and detector (Figure 2.5), where r is the radius of the Debye-Scherrer ring, n is the number of pixels and d_{pixel} is the diameter of the pixels:

$$D_{sd} = \frac{n \times d_{pixel}}{\tan 2\theta}$$

Equation 2.5

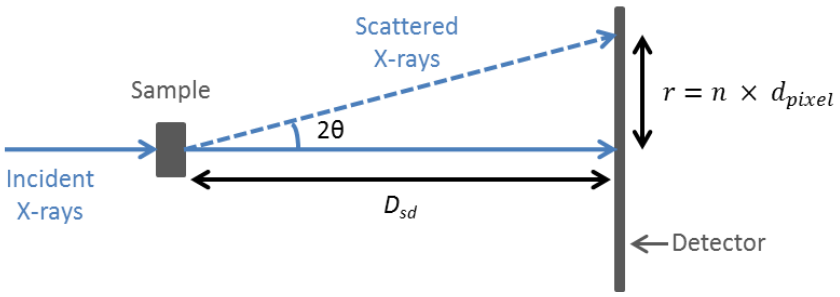

Figure 2.5: Geometrical relationship between the sample, X-rays and detector

The LaB_6 reference sample has a known lattice spacing, d, of 4.157 Å.[38] Combining Equation 2.1 and Equation 2.5 gives the sample-to-detector distance, D_{sd}, as shown in Equation 2.6. For these measurements, a pixel size of 150 µm and a wavelength of 0.9760 Å were used.

$$D_{sd} = \frac{n \times d_{pixel}}{\tan\left(2\sin^{-1}\frac{\lambda}{2d}\right)}$$

Equation 2.6

With the accurate sample-to-detector distance it was then possible to integrate the 2D scans to give an azimuthally-averaged radial 2θ plot as a function of intensity.

The next step of the data analysis was to identify the peaks arising from the metal nanoparticles by comparing the data obtained for the catalyst electrodes with that of the carbon-only electrode. Figure 2.6 shows the data obtained for the carbon-only electrode, also containing all background scattering from the cell, and the Pt/Pd/C alloy.

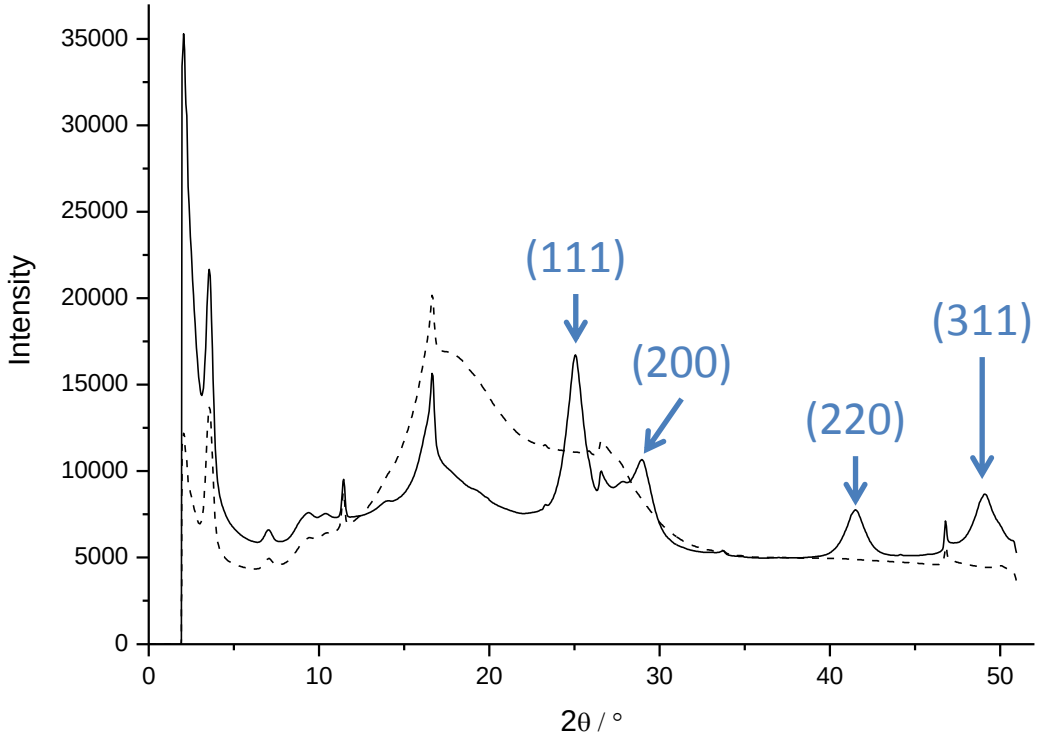

Figure 2.6: WAXS data obtained for a carbon only electrode (dashed line) compared with that of a Pt/Pd/C Alloy electrode (solid line). Data was recorded at 0.50 V vs. RHE in 0.5 M H_2SO_4. The Bragg peaks arising from the alloy are indicated, along with the Miller indices. N.B. Intensities have been scaled to facilitate comparison.

The Bragg peaks from the alloy can be clearly distinguished from the carbon background and are indicated by the blue arrows in Figure 2.6. The assignment of the Miller indices shown was based on the diffraction patterns of Pt and Pd, calculated from Crystallographic Information Files[39] using CrystalDiffract software.

As can be seen in Figure 2.6, there are significant differences in the intensity, despite the data being scaled to aid comparison, between the background scattering from the alloy sample and the scattering of the carbon-only electrode. This was also seen when comparing the carbon background with the scattering profiles of the other catalyst samples. Despite the carbon electrode being prepared from the same carbon used to support the catalysts nanoparticles, there are clearly significant differences in the scattering arising from the carbon. This could be due to changes in the carbon structure during the synthesis of the catalysts and/or differences in the wetting of the electrodes. As the relationship between the intensities of the carbon-only and the alloy electrodes is not scalar, it was not possible to directly subtract the background from the catalyst samples.

To obtain a value for the lattice parameter from the position of the Bragg peaks, it is advisable to average the peak positions obtained from several reflections. However, owing to the variation in the background intensity, it was not possible to fully isolate the (111) and (200) peaks, and the (311) peak was too close to the limit of the detector for accurate determination of the peak position. The (220) peak occurs in a region of 2θ less affected by the background scattering, enabling the isolation of peak and the accurate determination of the peak position. For these reasons, only the (220) peak has been used in the analysis of this data.

A linear background was subtracted from the (220) peak and the 2θ peak position determined by fitting a Gaussian function using OriginLab 8.1. The error in the peak position was estimated from the shift in the sharp diffraction peak arising from the background at $\sim 46°$ 2θ, thus accounting for bowing of the sample, which would result in variations in the sample-to-detector distance, and small variations arising from the background subtraction. The lattice parameter was then obtained for all samples at each potential using Equation 2.3.

Calculation of the crystallite size was not carried out due to the difficulties in complete background subtraction and the need for several peaks to be analysed to separate the contributions of strain and instrumental effects from the size-related peak broadening.

2.3 Results

The subtracted (220) peaks for the Pt/Pd/C samples shown in Figure 2.7, with the peaks of the Pd/C core material and 40 wt% Pt/C shown in Figure 2.8. The corresponding lattice parameters calculated from the position of the (220) peaks at each potential are given for the catalyst samples in Table 2.1.

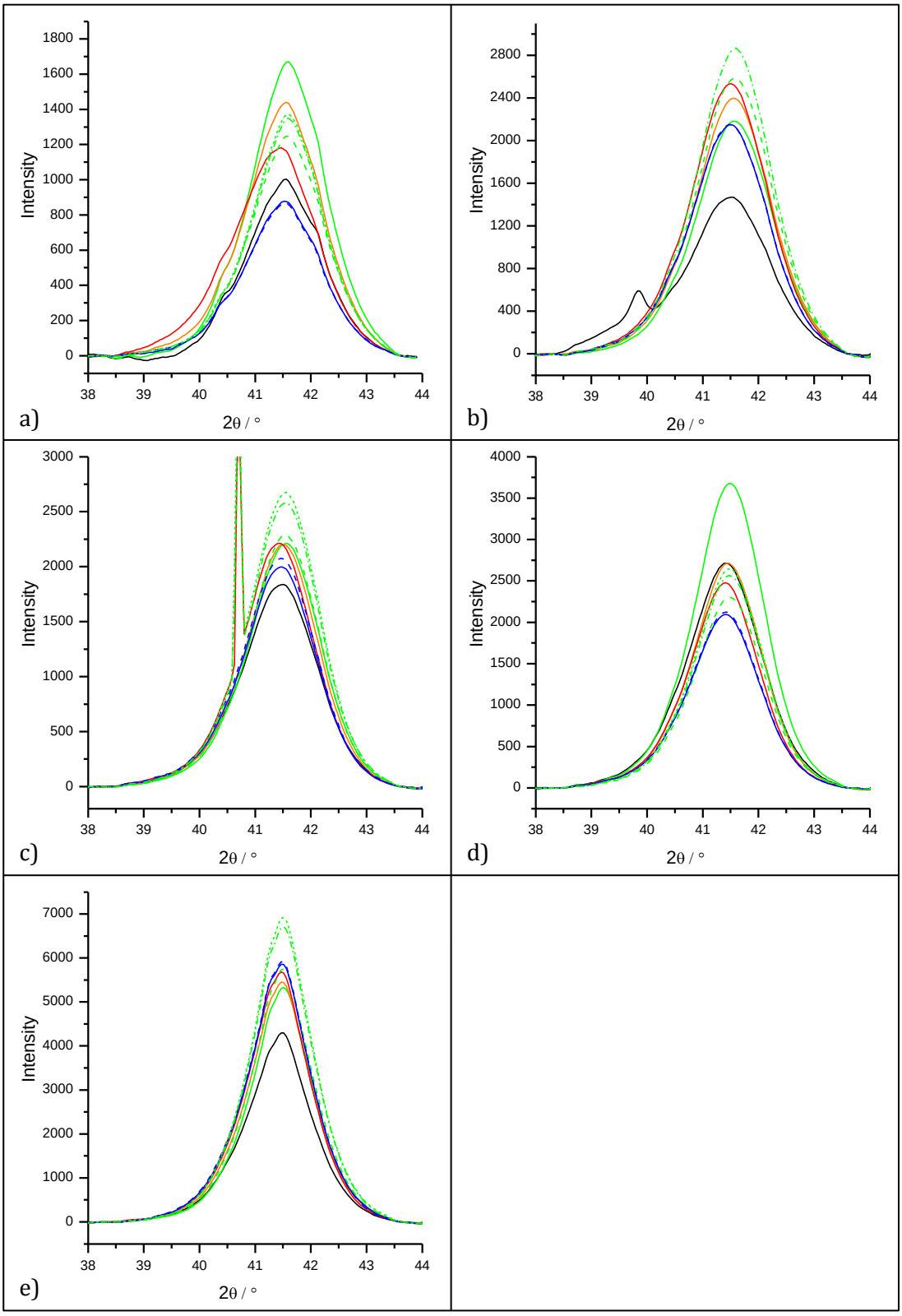

Figure 2.7: (220) peaks of $Pt_{0.5ML}/Pd/C$ (a), $Pt_{1ML}/Pd/C$ (b), $Pt_{2ML}/Pd/C$ (c), $Pt_{4ML}/Pd/C$ (d) and the Pt/Pd/C alloy (e) recorded at OCV (black), 0.50 V (green), 0.07 V (orange), 0.0 V (red) and 1.00 V (blue) vs. RHE in 0.5 M H_2SO_4. The first measurement at each potential is denoted by a solid line. Second, third and fourth measurements (where applicable) are denoted by (---), (-···) and (···) respectively.

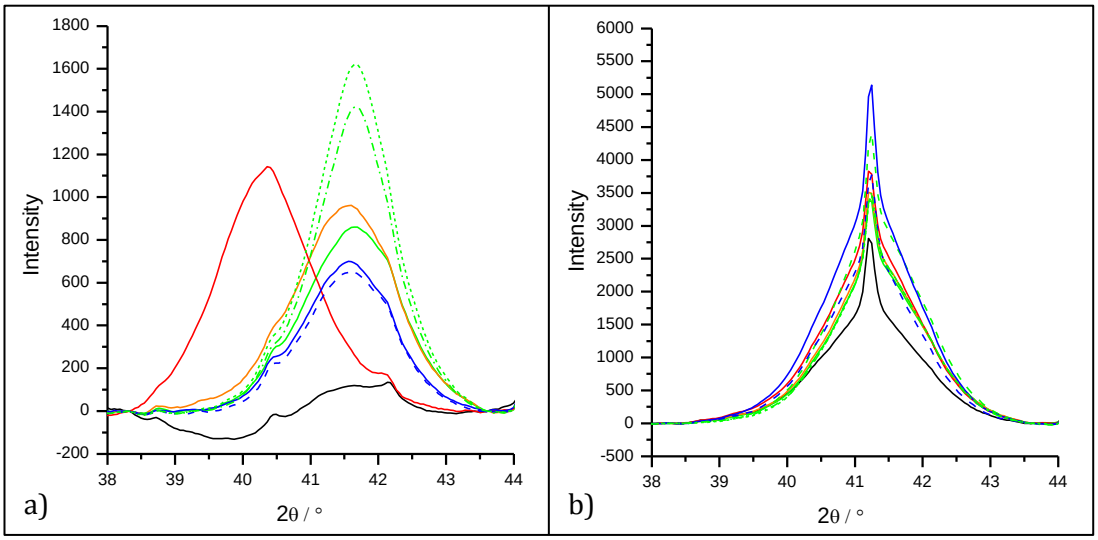

Figure 2.8: (220) peaks of the Pd/C core material (a) and 40 wt% Pt/C (b) recorded at OCV (black), 0.50 V (green), 0.07 V (orange), 0.0 V (red) and 1.00 V (blue) vs. RHE in 0.5 M H_2SO_4. The first measurement at each potential is denoted by a solid line. Second, third and fourth measurements (where applicable) are denoted by (---), (····) and (···) respectively.

Table 2.1: Lattice parameters obtained from fitting the (220) Bragg peaks recorded of the catalyst electrodes under potential control in 0.5 M H_2SO_4. The data is shown in chronological order regarding the potential hold, with the potentials quoted vs. RHE. The error associated with the lattice parameters is ± 0.002 Å.

	a / Å								
Catalyst	OCV	0.50 V	0.07 V	0.00 V	0.50 V	1.00 V	1.00 V	0.50 V	0.50 V
Pd/C Core	-	3.885	3.895	4.002	-	3.892	3.890	3.883	3.884
40 wt% Pt/C	3.920	3.912	3.913	3.918	3.911	3.919	3.919	3.911	3.911
$Pt_{0.5ML}$/Pd/C	3.894	3.888	3.894	3.910	3.890	3.897	3.897	3.889	3.889
Pt_{1ML}/Pd/C	3.897	3.891	3.893	3.898	3.891	3.899	3.899	3.891	-
Pt_{2ML}/Pd/C	3.901	3.894	3.898	3.905	3.895	3.902	3.902	3.895	3.895
Pt_{4ML}/Pd/C	3.906	3.899	3.902	3.907	3.899	3.907	3.907	3.899	3.900
Pt/Pd/C	3.902	3.898	3.901	3.903	3.898	3.902	3.902	3.898	3.898

The most significant effect in the position of the (220) peaks due to applied electrode potential is the large shift to lower 2θ seen in the Pd/C core material at 0.00 V compared to the 2θ positions at all other potentials (Figure 2.8a). This corresponds to an increase in the lattice parameter and is a result of the absorption of hydrogen by Pd, as seen in the EXAFS data shown in Section 1.3.2. At OCV, the (220) peak is barely visible, showing that the Pd/C core material has very limited crystallinity prior to the application of an electrode potential.

In the Pt/Pd/C samples (Figure 2.7), a slight shift is also visible with the reduction in potential from 0.50 V to 0.00 V in the 0.5 ML, 1 ML and 2 ML catalysts (plots a, b and c). Increasing the potential to 1.00 V also results in a shift to lower 2θ, and was observed in all samples. The additional peaks visible at lower 2θ in the 1 ML and 2 ML samples (plots a and c) can be attributed to background scattering effects.

As can be seen from the values in Table 2.1, the repeated measurements at 0.50 V following potential holds at 0.00 V and 1.00 V do not display any variation in the lattice parameter within error. This means that the increase in the lattice parameter in the hydrogen and oxygen regions is reversed following the collection of cyclic voltammograms. The lattice parameter obtained from the repeated measurement at 1.00 V, where WAXS data was collected after holding the potential for 30 minutes, also showed no variation within error from the value calculated from the first data collection. This demonstrates that over these time scales there is no cumulative effect of oxide formation on the crystalline region of the nanoparticles.

Figure 2.9 compares the lattice parameters obtained at each potential for the different catalyst samples, along with the values from the ex situ powder XRD reported in Chapter Two. Only the parameters from the first data collection at 0.50 V and 1.00 V have been included for clarity.

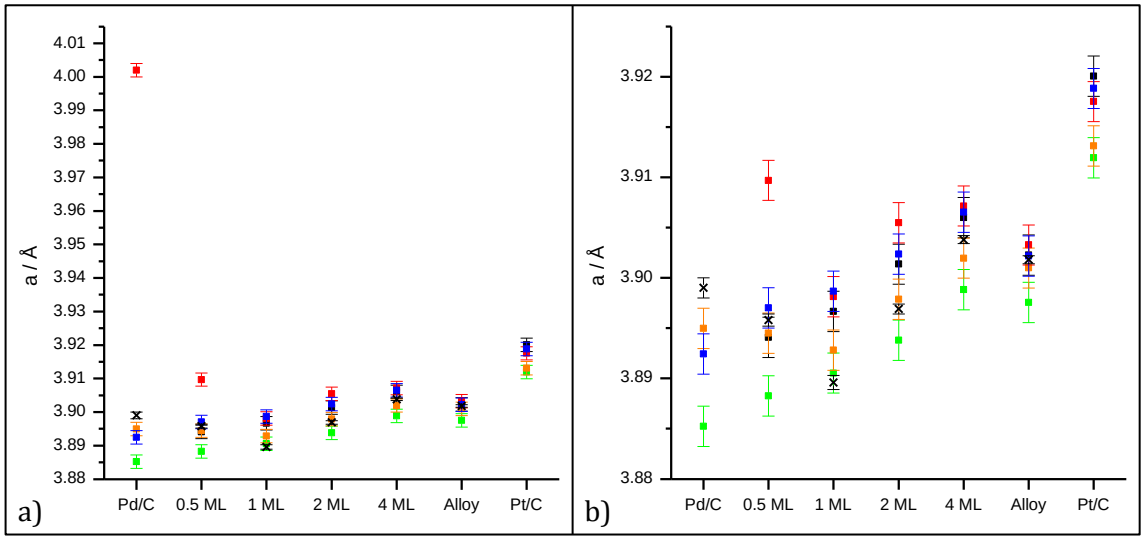

Figure 2.9: Comparison across the samples of the lattice parameters at OCV (black), 0.00 V (red), 0.07 V (orange), 0.50 V (green) and 1.00 V (blue) for the first data collection at each potential. All values are shown in (a), with the value obtained at 0.00 V for the Pd/C core omitted from (b). The values from the ex situ powder XRD reported in Chapter Two are included for reference (✖).

The pronounced effect of hydrogen absorption into the Pd/C core material in comparison with the other catalyst samples can clearly be seen in Figure 2.9 (plot a). There is a general increase in the lattice parameter with changes in the potential from 0.50 V, including at OCV, for all samples. There is also a general trend of increasing lattice parameter with increasing Pt shell thickness, which is in reasonable agreement with the ex situ XRD data, and can be attributed to the increasing presence of Pt and/or Pt-Pd alloy phases within the crystallite.

The effect of hydrogen absorption becomes less pronounced with increasing shell thickness, indicating that either the Pt shell is preventing the absorption or that the peak position is a result of different Pt, Pd and Pt/Pd phases. As seen in the EXAFS data, the Pt lattice parameter is also shifted at 0.00 V.

At OCV and 1.00 V, where oxide species will be present, the increase in the lattice parameter can be attributed either to the presence of metal-oxide phases, or by changes in the composition of the metal phases. As the increase was seen in the monometallic samples as well as in the bimetallics, it is likely that this is due to the presence of oxide phases rather than changes in the metal phase composition.

To be able to distinguish between the different phases present at each potential, full profile fitting and peak deconvolution is required. Owing to the discrepancies between the recorded background sample and the background seen in the WAXS data of the catalyst samples this was beyond the scope of this work.

2.4 Conclusions

This in situ WAXS data has shown

- A clear effect of electrode potential on the lattice parameter of the catalyst samples.
- The increase in the lattice parameter due to hydrogen absorption by Pd is significantly limited by the presence of Pt in the samples, however, an effect is still seen even for the Pt-only catalyst.
- The presence of oxide also causes an increase in the lattice parameter, likely to be due to oxide phases in the crystalline region of the sample.
- Distinguishing between the different phases present in the crystalline region of the nanoparticles by carrying out more detailed analysis was not possible in this work owing to the significant variation in the background scattering.

References

[1] A. E. Russell, B. Tessier, A. Wise, A. Rose, S. W. Price, P. W. Richardson, S. Ball, B. Theobald, D. Thompsett, E. M. Crabb, *ECS Trans.* **2011**, *41*, 55-67.
[2] M. de Broglie, *Comptes Rendus* **1913**, *157*, 924-926.
[3] F. W. Lytle, *J. Synchrotron Radiat.* **1999**, *6*, 123-134.
[4] R. d. L. Kronig, *Z. Phys. A Hadrons and Nuclei* **1932**, *75*, 191-210.
[5] D. E. Sayers, E. A. Stern, F. W. Lytle, *Phys. Rev. Lett.* **1971**, *27*, 1204-&.
[6] J. J. Rehr, R. C. Albers, *Rev.Mod. Phys.* **2000**, *72*, 621-654.
[7] A. E. Russell, A. Rose, *Chem. Rev.* **2004**, *104*, 4613-4635.
[8] G. Bunker, *Introduction to XAFS: A Practical Guide to X-ray Absorption Fine Structure Spectroscopy*, 1 ed., Cambridge University Press, Cambridge, **2010**.
[9] E. A. Stern, *Contemp. Phys.* **1978**, *19*, 289-310.
[10] S. D. Kelly, D. Hesterberg, B. Ravel, in *Methods of soil analysis - Part 5: Mineralogical methods* (Eds.: A. L. Ulery, L. R. Drees), Soil Society of America, Inc., Madison, **2008**, pp. 367-463.
[11] G. G. Li, F. Bridges, C. H. Booth, *Phys. Rev. B* **1995**, *52*, 6332-6348.
[12] J. J. Rehr, R. C. Albers, *Phys. Rev. B* **1990**, *41*, 8139-8149.
[13] http://beamlines.ps.bnl.gov/beamline.aspx?blid=X23A2, **2010**.
[14] http://www.esrf.eu/UsersAndScience/Experiments/CRG/BM26/Beamline Description, **2010**.
[15] https://hasylab.desy.de/facilities/doris_iii/beamlines/x1_roemo_ii/, **2010**.
[16] http://www.diamond.ac.uk/Home/Beamlines/B18.html, **2011**.
[17] K. Q. Lu, E. A. Stern, *Nucl. Instrum. Methods Phys. Res.* **1983**, *212*, 475-478.

[18] W. H. McMaster, N. K. Del Grande, J. H. Mallett, J. H. Hubbell, *Compilation of X-Ray Cross Sections*, Lawrence Livermore National Laboratory Report UCRL-50174 Section II Revision I, **1969**.
[19] B. Ravel, M. Newville, *J. Synchrotron Radiat.* **2005**, *12*, 537-541.
[20] M. Newville, *J. Synchrotron Radiat.* **2001**, *8*, 322-324.
[21] M. Newville, P. Livins, Y. Yacoby, J. J. Rehr, E. A. Stern, *Phys. Rev.B* **1993**, *47*, 14126-14131.
[22] S. Calvin, E. E. Carpenter, B. Ravel, V. G. Harris, S. A. Morrison, *Phys. Rev. B* **2002**, *66*, 224405.
[23] S. W. T. Price, *PhD Thesis: Enhanced Structural Characterisation of Supported Catalysts*, University of Southampton, **2011**.
[24] A. M. Beale, B. M. Weckhuysen, *Phys. Chem. Chem. Phys.* **2010**, *12*, 5562-5574.
[25] F. A. Lewis, *The Palladium Hydrogen System*, Academic Press, London, **1967**.
[26] B. Ravel, S. D. Kelly, *AIP Conf. Proc.* **2007**, *882*, 150-152.
[27] Z. Dauter, *J. Mol. Struct.* **1996**, *374*, 29-35.
[28] L. V. Azároff, *Elements of X-Ray Crystallography*, McGraw-Hill, New York, **1968**.
[29] V. K. Pecharsky, P. Y. Zavalij, *Fundamentals of Powder Diffraction and Structural Characterization of Materials*, Springer, New York, **2003**.
[30] http://pd.chem.ucl.ac.uk/pdnn/diff2/kinemat2.htm, **2012**.
[31] B. D. Cullity, *Elements of X-Ray Diffraction*, Addison-Wesley Publishing Company, Inc., Reading, MA, **1956**.
[32] J. I. Langford, A. J. C. Wilson, *J. Appl. Crystallogr.* **1978**, *11*, 102-113.
[33] P. Whitfield, L. Mitchell, *X-ray diffraction analysis of nanoparticles: Recent developments, potential problems and some solutions, Vol. 3*, World Scientific Publ Co Pte Ltd, Singapore, **2004**.
[34] http://www-ssrl.slac.stanford.edu/beamlines/bl11-3/, **2010**.
[35] A. L. Dragoo, *Powder Diffr.* **1986**, *1*, 294.
[36] A. P. Hammersley, in *ESRF Internal Report*, **1997**.
[37] A. P. Hammersley, S. O. Svensson, M. Hanfland, A. N. Fitch, D. Hausermann, *High Pressure Res.* **1996**, *14*, 235-248.
[38] C. T. Chantler, C. Q. Tran, D. J. Cookson, *Phys. Rev. A* **2004**, *69*, 042101.
[39] G. Bredig, R. Allolio, *Z. Phys. Chem.* **1927**, *126*, 41-71.

CHAPTER FOUR: EXAFS AND WAXS INVESTIGATIONS OF CATALYST STABILITY

Chapter One introduced the importance of catalyst stability on the development of commercially viable PEMFCs. This chapter describes the effect of electrochemical ageing by repeated potential cycling in the oxide region on the Pt/Pd/C electrocatalysts. The results of in situ EXAFS and WAXS data collected of the electrochemically aged Pt/Pd/C electrodes are presented and compared with those obtained for the fresh electrocatalysts reported in Chapter Three.

1 Introduction

As noted in Chapter One, an understanding of the stability of oxygen reduction electrocatalysts and the mechanisms of their degradation are important aspects of the development of PEMFCs. Owing to this, much research has been devoted to investigating the effect of potential cycling and steady state potential holds on the performance of ORR catalysts.[1]

Pt/C and Pt alloy catalysts have been shown to degrade when operating under fuel cell conditions as a result of the acidic environment, the operating temperature of 80 °C and the varying electrode potential of above 0.6 V vs. RHE.[2] This degradation is typically monitored by periodically measuring the electrochemical surface area (ECA), determined from the charge of the H_{ads} and/or the CO oxidation peak as described in Chapter Two, with a larger ECA generally indicating a more active catalyst owing to the greater number of active sites available.[3]

There are several mechanisms by which this loss of area can occur, including the dissolution of the metal and the growth of the particles via agglomeration or coalescence. The terminology of these processes varies in the literature but for the purposes of this study the definitions outlined below will be used. Dissolution of Pt can occur either as direct dissolution of the metal or by formation of a Pt oxide which is then dissolved, resulting in a loss of ECA from the direct loss of the catalyst particles.[4] Agglomeration occurs when the catalyst nanoparticles migrate over the carbon support, forming agglomerates of the particles, with the loss in ECA resulting from the surface area masked by the conjoined particles. Coalescence refers to the growth of the particles via either direct coalescence of the particles as a whole, or by the dissolution and redeposition of

smaller particles by a mechanism known as Ostwald ripening, with the loss in ECA attributed to the larger particle size.[3],[5],[6]

B. Tessier investigated the stability of $Pt_{xML}/Pd/C$ (x = 0.5, 1, 1.5, 2) catalysts analogous to the ones investigated in this study by cycling the potential between 0.6 and 1.0 V vs. RHE at 80 °C in 1 M H_2SO_4, emulating the working conditions of a fuel cell, over 1000 cycles. [7] The evolution of the ECA was monitored by periodically recording cyclic voltammograms (CVs) and CO oxidation voltammograms, and the electrolyte was sampled to determine the rate of dissolution of Pt and Pd using ICP-ES. The catalysts displayed a loss of ECA with increasing number of cycles. The ICP-ES analysis showed a very small amount of Pt dissolution, but significant (up to around 40%) loss of Pd. However, the amount of Pd in the solution varied significantly, as shown in Figure 1.1, thought to be due to redeposition of the Pd onto the working electrode during the potential hold at 0.15 V vs. RHE as part of the collection of CO oxidation CVs.

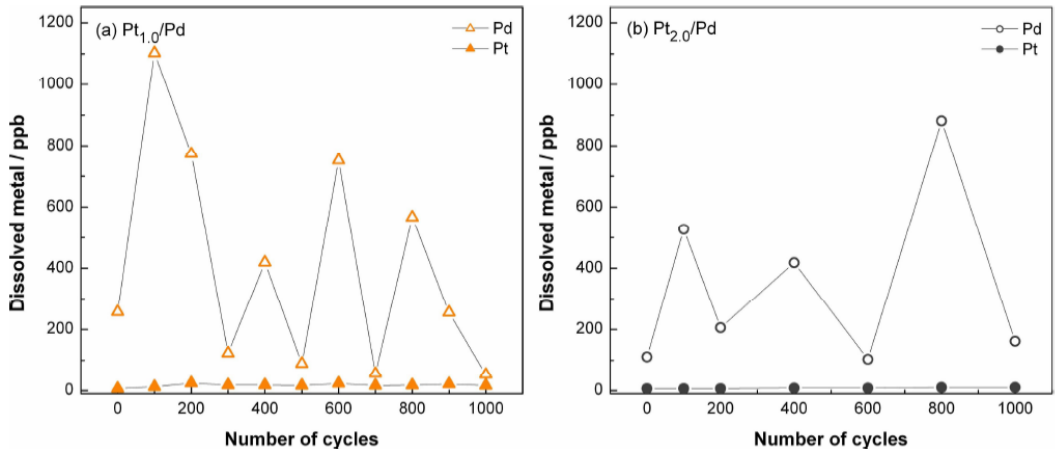

Figure 1.1: Concentration of dissolved metal in the electrolyte measured periodically during cycling between 0.6 and 1.0 V vs RHE at 80 °C in 1 M H_2SO_4 for $Pt_{1.0}/Pd/C$ (a) and $Pt_{2.0}/Pd/C$ as reported by B. Tessier.[7]

Knowing that this electrochemical ageing procedure resulted in a loss of ECA and dissolution of metal, these experiments were repeated for the Pt/Pd/C catalysts used throughout this work. The aim of this was to characterise the structure of the cycled samples to elucidate the mechanisms behind the loss of ECA seen in these materials in terms of dissolution, agglomeration and coalescence. To prevent the re-plating of the Pd, the experimental set-up was modified to use two electrochemical cells, one for cycling the electrodes and a separate cell for recording the CVs and CO oxidation voltammograms.

2 Experimental

2.1 Electrochemical Ageing

Catalyst electrodes were prepared as described in Chapter Two and hydrated by boiling in demineralised water. As mentioned above, the electrochemical ageing was conducted using a two-cell system, swapping the electrodes between the cells as outlined below. The electrodes used for these measurements were a MMS reference electrode, connected via a Luggin capillary, and a Pt gauze counter electrode, with the catalyst electrode suspended in the electrolyte via a Pt wire. A PGSTAT30 potentiostat was used to control the potential. Both cells were filled with 1 M H_2SO_4 (~ 100 mL), which was then purged with N_2 for 20 minutes while heating the jacketed cells to 80 °C using a circulating water bath. The experiment was then carried out as follows:

- Electrodes loaded into cell one
- Three CVs at a scan rate of 10 mV s^{-1} collected between 1.00 V and 0.02 V vs. RHE, starting at 0.15 V.
- CO oxidation voltammetry was recorded by purging the electrolyte with CO for 15 minutes while holding the potential at 0.15 V vs. RHE, followed by purging with N_2 for 15 minutes. The potential was then swept cyclically from 0.15 V to 1.00 V to 0.02 V for three cycles at a scan rate of 10 mV s^{-1}. This measurement, along with the CVs described above, is referred to as '0' in the results section.
- Electrodes swapped to cell two
- 50 cycles run between 0.6 V and 1.0 V vs. RHE at 50 mV s^{-1}
- Electrodes swapped to cell one
- Three CVs collected and CO oxidation voltammetry recorded (referred to as '50')
- Electrodes swapped to cell two
- 50 cycles run between 0.6 V and 1.0 V vs. RHE at 50 mV s^{-1}
- Electrodes swapped to cell one
- Three CVs collected (referred to as '100')
- Electrodes swapped to cell two
- 150 cycles run between 0.6 V and 1.0 V vs. RHE at 50 mV s^{-1}
- Electrodes swapped to cell one
- Three CVs collected and CO oxidation voltammetry recorded (referred to as '250')
- Electrodes swapped to cell two
- 250 cycles run between 0.6 V and 1.0 V vs. RHE at 50 mV s^{-1}

- Electrodes swapped to cell one
- Three CVs collected and CO oxidation voltammetry recorded (referred to as '500')
- Electrodes swapped to cell two
- 250 cycles run between 0.6 V and 1.0 V vs. RHE at 50 mV s^{-1}
- Electrodes swapped to cell one
- Three CVs collected (referred to as '750')
- Electrodes swapped to cell two
- 250 cycles run between 0.6 V and 1.0 V vs. RHE at 50 mV s^{-1}
- Electrodes swapped to cell one
- Three CVs collected and CO oxidation voltammetry recorded (referred to as '1000')

Throughout the experiment N_2 flow was maintained over the surface of the electrolyte, except for when purging with CO. Following the collection of the CVs and CO voltammetry at 1000 cycles, the catalyst electrode was removed from the cell and washed with water before being allowed to dry to facilitate transport to the beamlines. This electrochemical ageing was carried out on several electrodes of each Pt/Pd/C catalyst to provide a sufficient number of aged samples for X-ray characterisation.

2.2 EXAFS

In situ EXAFS data was collected in fluorescence mode at the Pt L_3 and Pd K edges on beamline B18 at Diamond. Further beamline details are given in Chapter Three, Section 1.2. The in situ cell described in Chapter Two was again employed for these measurements and the experimental team were Laura Calvillo Lamana, Peter Richardson, Andrea Russell and Anna Wise. The beamline scientist was Silvia Ramos.

The Pt/Pd/C electrodes subjected to the electrochemical ageing detailed above were re-hydrated by boiling in water then loaded into the in situ cell. The cell was filled with N_2-purged 0.5 M H_2SO_4 and the electrodes, again using a MMS reference electrode, were connected to the μAutolab III potentiostat. Three CVs were collected at a scan rate of 50 mV s^{-1} followed by three CVs at a rate of 10 mV s^{-1}, starting the scans at OCV with potential limits of 1.00 and 0.05 V vs. RHE. EXAFS data (2 -3 scans) was then collected whilst holding the potential at 0.50 V, 0.05 V and 0.00 V at each absorption edge.

2.3 WAXS

WAXS data was collected in situ in the electrochemical cell on beamline 11-3, Stanford Synchrotron Radiation Lightsource. For these measurements the wavelength used was 0.9744 Å and the sample-to-detector distance was ca. 150 mm. A LaB_6 reference was used to calibrate the sample-to-detector distance as described in Chapter Three, Section 2.2. The MAR345 detector used to collect the WAXS data of fresh catalysts was again employed, with a pixel size of 150 μm. The measurements were conducted by Peter Richardson and Anna Wise and the beamline scientist was Stefan Mannsfeld.

The experimental set-up was the same as that for the WAXS measurements of the fresh catalysts; using N_2-purged 0.5 M H_2SO_4, a μAutolab III potentiostat and a MMS reference electrode. The electrochemically aged catalyst electrodes were hydrated before being loaded into the cell. As there was no time-dependent change seen in the WAXS data of the fresh electrocatalysts during the potential hold at 1.00 V, only one collection was made at this potential. Data collection at 0.50 V was repeated following the potential holds at 0.00 V and 1.00 V to check for any irreversible (under these conditions) changes to the crystalline structure.

The experiment for each sample proceeded as follows:

- First WAXS collection at OCV
- Three CVs at 50 mV s^{-1} were recorded between 1.00 V and 0.05 V, starting at OCV, followed by three CVs at 10 mV s^{-1}
- WAXS data collected, holding the potential at 0.50 V vs. RHE
- WAXS data collected, holding the potential at 0.05 V vs. RHE
- WAXS data collected after holding the potential at 0.00 V vs. RHE for 10 minutes
- CVs (10 mV s^{-1}) recorded from 0.00 V to 1.00 V to remove absorbed hydrogen from the sample
- WAXS data collected, holding the potential at 0.50 V vs. RHE
- WAXS data collected after holding the potential at 1.00 V vs. RHE for 10 minutes
- CVs (10 mV s^{-1}) recorded from 1.00 V to 0.05 V to remove oxide
- WAXS data collected, holding the potential at 0.50 V vs. RHE

As before, the potential was moved gradually to the desired value to avoid large increases in the current. Where a hold time is not specified, the cell current was allowed to decay before collecting the data.

3 Results

3.1 Electrochemistry

The cyclic voltammograms and CO oxidation voltammograms recorded following potential cycling in the oxide region in 1 M H_2SO_4 at 80 °C are shown in Figure 3.1 ($Pt_{0.5ML}$/Pd/C, Pt_{1ML}/Pd/C, and Pt_{2ML}/Pd/C) and Figure 3.2 (Pt_{4ML}/Pd/C, Pt/Pd/C alloy, and the 40 wt% Pt/C for comparison).

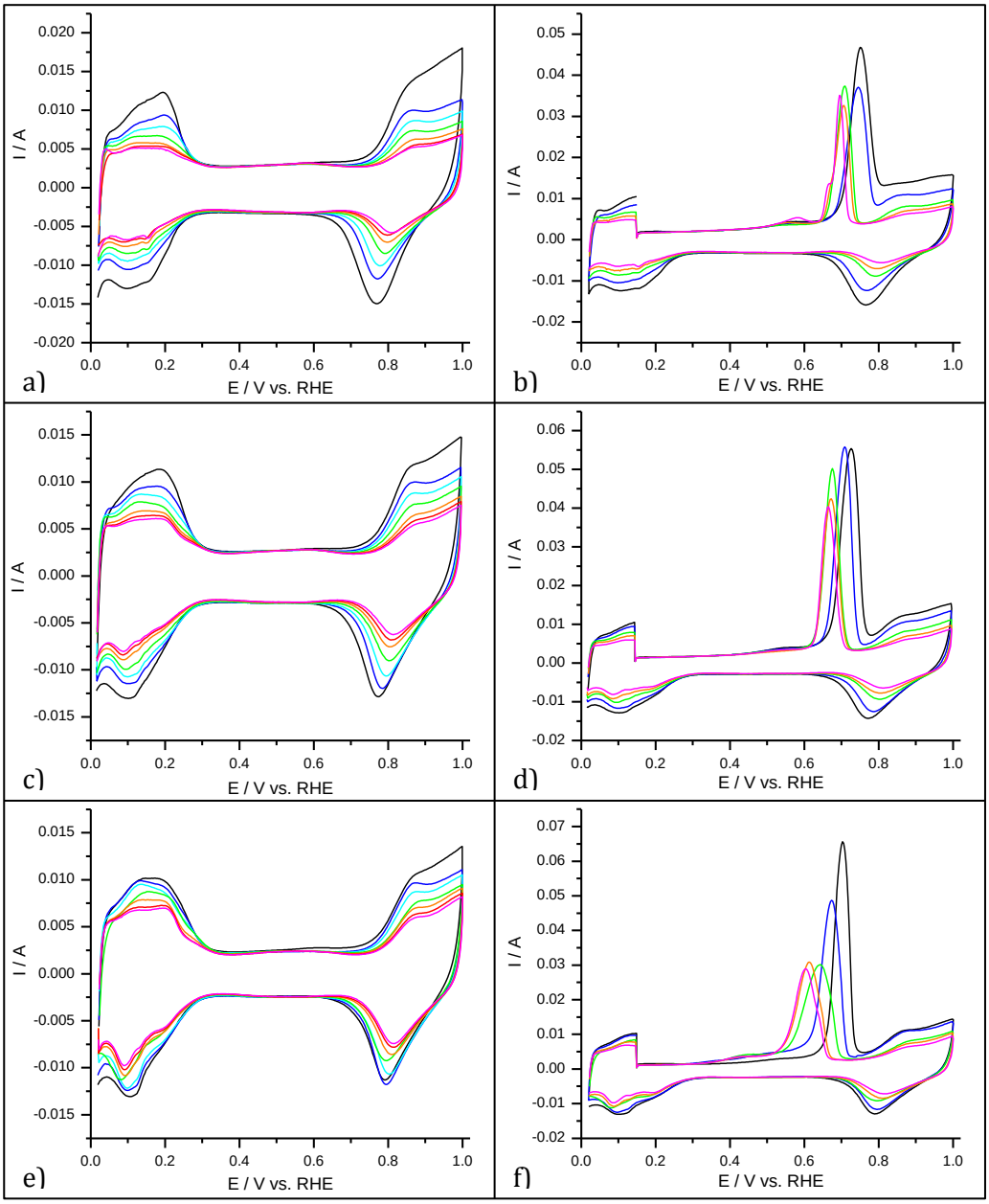

Figure 3.1: Cyclic voltammograms (left) and CO oxidation voltammograms (right) for $Pt_{0.5ML}$/Pd/C (a-b), Pt_{1ML}/Pd/C (c-d) and Pt_{2ML}/Pd/C (e-f) following 0 (black), 50 (blue), 150 (cyan), 250 (green), 500 (orange), 750 (red) and 1000 (pink) cycles between 0.6 V and 1.0 V vs. RHE at 80 °C in 1 M H_2SO_4.

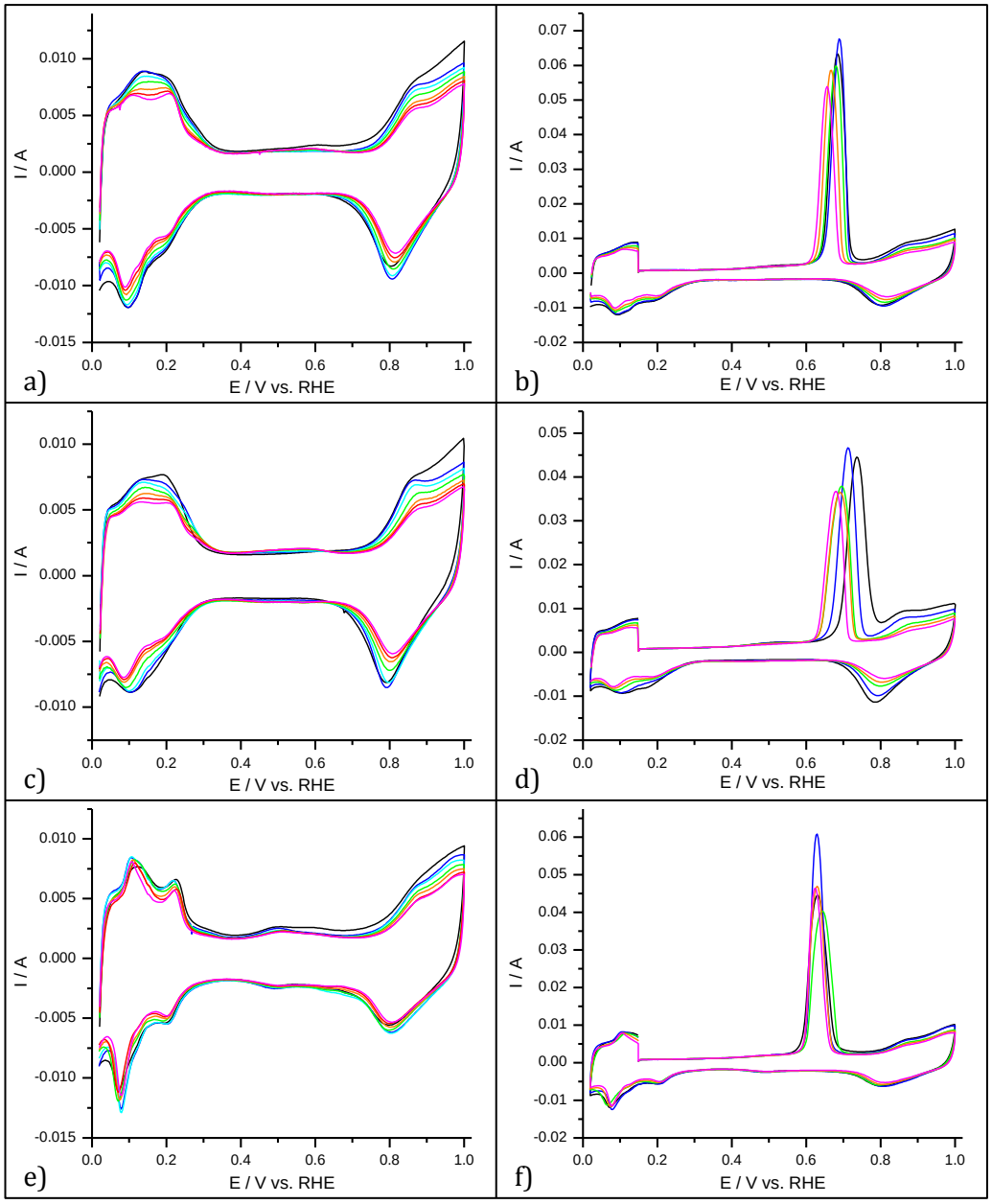

Figure 3.2: Cyclic voltammograms (left) and CO oxidation voltammograms (right) for Pt_{4ML}/Pd/C (a-b), the Pt/Pd/C alloy (c-d) and 40 wt% Pt/C (e-f) following 0 (black), 50 (blue), 150 (cyan), 250 (green), 500 (orange), 750 (red) and 1000 (pink) cycles between 0.6 V and 1.0 V vs. RHE at 80 °C in 1 M H_2SO_4.

The cyclic voltammograms obtained for all samples show a clear decrease in the current in the hydrogen and oxide regions with increasing number of cycles, which correlates to a loss in the electrochemical surface area. The CO oxidation voltammograms show a shift in the CO oxidation peak to lower potentials closer to that of Pt, suggesting that the surface is becoming more Pt-like with cycling, an effect also seen in the shape of the H_{ads} peaks in the CVs. Broadening of the peak is also seen in the 2 ML and alloy samples, which indicates an increase in the variety of CO adsorption sites. The effect of cycling seen in the 4 ML sample

is much smaller than the other Pt/Pd/C samples, and very little change is seen in the Pt-only catalyst.

To quantitatively compare the loss of electrochemical surface area, the ECA was calculated from the H_{ads} and CO oxidation peaks using Equations 4.2 and 4.3 given in Chapter Two. The ECA values obtained in this manner for increasing cycles in the oxide region are shown in Figure 3.3. The data is presented both in terms of the measured ECA values and as the percentage loss in ECA for the Pt/Pd/C core-shell and alloy catalysts, with the 40 wt% Pt/C catalyst also included for comparison.

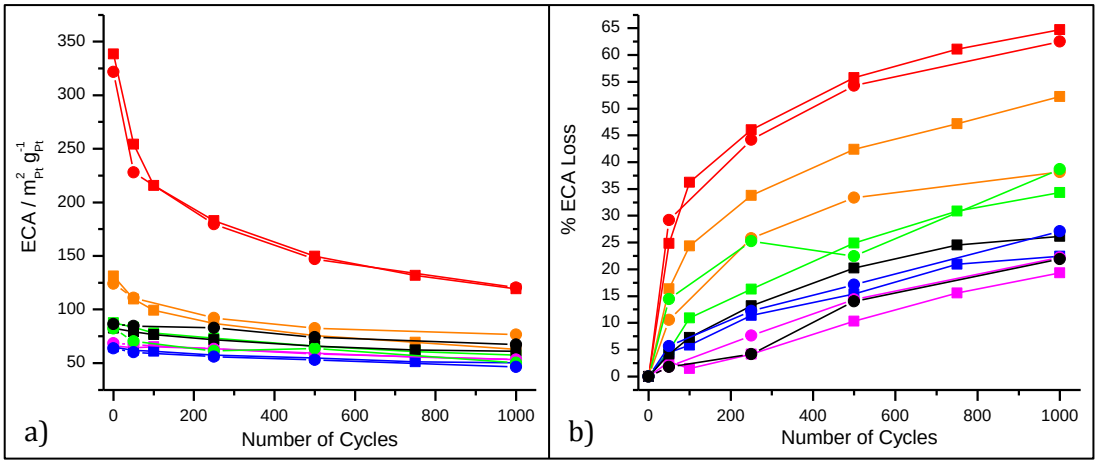

Figure 3.3: Evolution of the electrochemical surface area (ECA) (a) and the % loss of ECA (b) with cycling between 0.6 V and 1.0 V vs. RHE in 1 M H_2SO_4 at 80 °C. ECA values determined from the hydrogen adsorption peaks (■) and CO oxidation peak (●) are shown for $Pt_{0.5ML}$/Pd/C (red), Pt_{1ML}/Pd/C (orange), Pt_{2ML}/Pd/C (green), Pt_{4ML}/Pd/C (blue), the Pt/Pd/C alloy (black) and 40 wt% Pt/C (pink).

The ECA is seen to decrease most rapidly over the first 100 cycles, with the loss of area then slowing with subsequent cycles. Some discrepancies can be seen between the values obtained from the H_{ads} and CO oxidation peaks, in particular for the 1 ML and 2 ML samples, which can arise from variations in the stoichiometry of the CO adsorption at Pt and Pt surfaces.[8]

The most significant change is seen in the $Pt_{0.5ML}$/Pd/C sample, which displayed the highest initial ECA. It is important to note that while the ECA values quoted are normalised with respect to the mass of Pt in the sample, contributions to the area can also arise from H_{ads} and CO_{ads} on the Pd present at the surface which could account, in part, for the significantly higher ECA value determined for the 0.5 ML sample.

The initial ECA values decrease with increasing shell thickness. This can be attributed to the formation of a more Pt-rich, and possibly smoother, structure of the surface, along with the slight increase in particle size reported in Chapter Two. The 4 ML sample displays a very similar initial ECA to the 40 wt% Pt/C, indicating a similar surface structure.

An effect of shell thickness is also seen in the % loss of ECA observed with cycling, with the samples with thicker shells appearing more stable in terms of the calculated area. All of the Pt/Pd/C samples display a greater loss of ECA than the Pt-only catalyst.

The enhanced loss of ECA, along with the changes seen in the CVs and CO oxidation CVs to more Pt-like characteristics, indicates that a significant mechanism of degradation for the Pt/Pd/C catalysts involves the removal of Pd from the surface of the nanoparticle, especially for the materials with thinner Pt coverage. This agrees with the dissolution of Pd seen from the ICP-ES analysis of the electrolyte mentioned in Section 1.

As the dissolution of Pt determined by ICP-ES was seen to be minimal, the loss of surface area seen in the Pt/C points to restructuring of the particles, either by coalescence or agglomeration, which could also be occurring in the Pt/Pd/C samples.

The overestimation of the ECA due to the presence of Pd makes definitive conclusions about changes in the size of the Pt/Pd/C nanoparticles difficult to draw. However, changes in the CVs, CO oxidation CVs and ECA are clearly seen as a result of cycling in the oxide region, which could be a result of dissolution and/or agglomeration and/or coalescence, thus highlighting the need for structural characterisation.

3.2 EXAFS

The EXAFS data and fits are shown in Figure 3.4 - Figure 3.8, with the corresponding fit parameters obtained given in Table 3.1 - Table 3.5. As with the EXAFS data of the fresh electrocatalysts reported in Chapter Three, ΔE_0 was set to be the same for the paths at each absorption edge, and ΔR_{0i} and σ_i^2 were constrained to be the same for the Pd-Pt and Pt-Pd interactions. The S_0^2 values obtained for the data collected on B18 of the fresh catalysts were used to determine the coordination numbers. All fits were carried out using a k range of 3 – 13 $Å^{-1}$ and an R range of 1.4 – 3.2 Å.

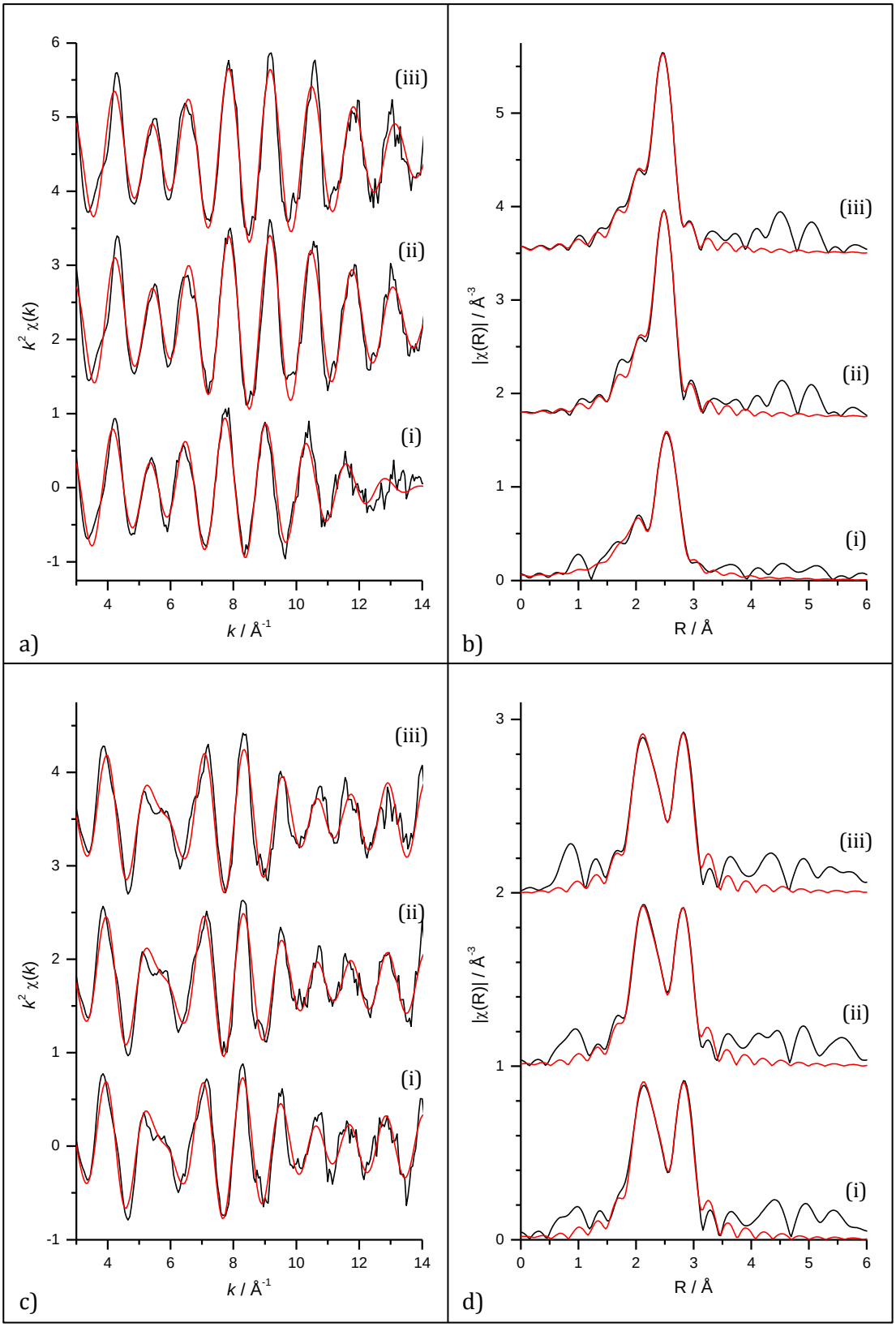

Figure 3.4: k^2 weighted experimental data (black) and fit (red) with the corresponding Fourier transform for electrochemically aged $Pt_{0.5ML}/Pd/C$. Data was recorded in situ at the Pd K (a-b) and Pt L_3 (c-d) edges, holding the potential at 0.00 V (i), 0.05 V (ii) and 0.50 V (iii) vs. RHE in 0.5 M H_2SO_4.

Table 3.1: Structural parameters obtained for electrochemically aged $Pt_{0.5ML}$/Pd/C from fitting in situ EXAFS data acquired under potential control in 0.5 M H_2SO_4. (N.B. first element in the neighbour pair indicates absorption edge of data)

Potential	Neighbour	N	R / Å	σ^2 / Å^2	ΔE_0 / eV	R_f
0.00 V vs. RHE	Pd-Pd	8.45 ± 1.26	2.771 ± 0.006	0.0072 ± 0.0007	-6.64 ± 0.54	0.0071
	Pd-Pt	2.74 ± 0.75	2.747 ± 0.007	0.0049 ± 0.0010		
	Pt-Pd	2.50 ± 0.50			6.04 ± 0.52	
	Pt-Pt	8.07 ± 1.18	2.750 ± 0.005	0.0057 ± 0.0006		
0.05 V vs. RHE	Pd-Pd	8.38 ± 1.21	2.747 ± 0.004	0.0053 ± 0.0005	-5.39 ± 0.46	0.0058
	Pd-Pt	1.76 ± 0.68	2.736 ± 0.011	0.0048 ± 0.0015		
	Pt-Pd	2.41 ± 0.64			5.52 ± 0.75	
	Pt-Pt	8.37 ± 1.38	2.739 ± 0.007	0.0058 ± 0.0009		
0.50 V vs. RHE	Pd-Pd	8.13 ± 1.14	2.737 ± 0.003	0.0051 ± 0.0005	-6.71 ± 0.40	0.0044
	Pd-Pt	2.26 ± 0.61	2.731 ± 0.007	0.0042 ± 0.0009		
	Pt-Pd	2.34 ± 0.45			6.60 ± 0.47	
	Pt-Pt	7.67 ± 1.07	2.736 ± 0.006	0.0051 ± 0.0005		

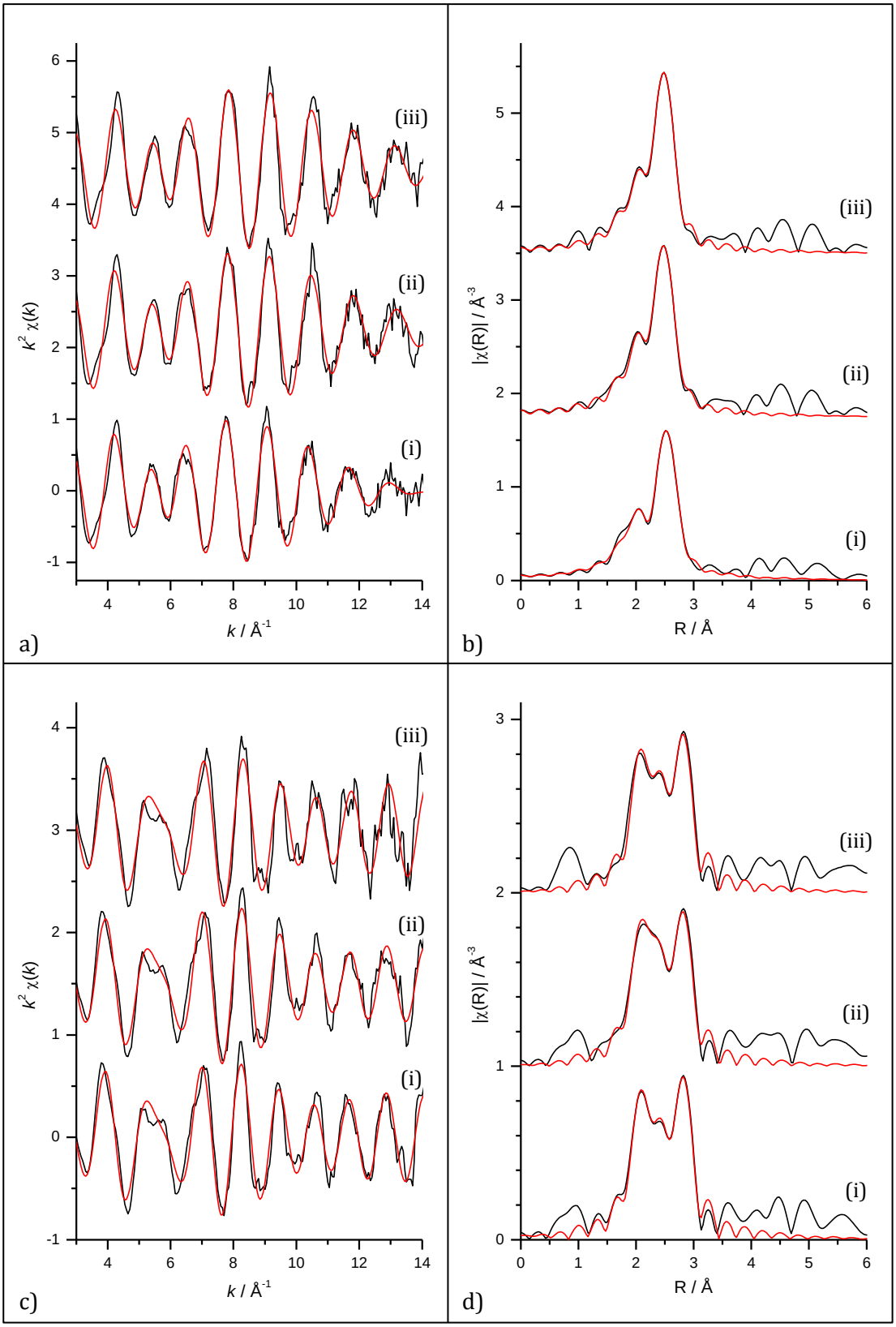

Figure 3.5: k^2 weighted experimental data (black) and fit (red) with the corresponding Fourier transform for electrochemically aged $Pt_{1ML}/Pd/C$. Data was recorded in situ at the Pd K (a-b) and Pt L_3 (c-d) edges, holding the potential at 0.00 V (i), 0.05 V (ii) and 0.50 V (iii) vs. RHE in 0.5 M H_2SO_4.

Table 3.2: Structural parameters obtained for electrochemically aged $Pt_{1ML}/Pd/C$ from fitting in situ EXAFS data acquired under potential control in 0.5 M H_2SO_4. (N.B. first element in the neighbour pair indicates the absorption edge of the data)

Potential	Neighbour	N	R / Å	σ^2 / Å^2	ΔE_0 / eV	R_f
0.00 V vs. RHE	Pd-Pd	7.64 ± 1.15	2.757 ± 0.005	0.0062 ± 0.0006	-6.24 ± 0.50	0.0046
	Pd-Pt	3.58 ± 0.79	2.740 ± 0.006	0.0049 ± 0.0010		
	Pt-Pd	1.73 ± 0.35			5.06 ± 0.40	
	Pt-Pt	8.72 ± 1.17	2.748 ± 0.003	0.0057 ± 0.0004		
0.05 V vs. RHE	Pd-Pd	7.68 ± 1.21	2.741 ± 0.005	0.0051 ± 0.0007	-6.63 ± 0.54	0.0063
	Pd-Pt	2.79 ± 0.77	2.739 ± 0.008	0.0032 ± 0.0011		
	Pt-Pd	1.50 ± 0.35			5.08 ± 0.50	
	Pt-Pt	8.71 ± 1.22	2.744 ± 0.004	0.0057 ± 0.0005		
0.50 V vs. RHE	Pd-Pd	7.66 ± 1.10	2.738 ± 0.004	0.0051 ± 0.0005	-5.70 ± 0.43	0.0070
	Pd-Pt	2.94 ± 0.72	2.728 ± 0.008	0.0046 ± 0.0013		
	Pt-Pd	1.64 ± 0.40			6.25 ± 0.56	
	Pt-Pt	8.05 ± 1.20	2.736 ± 0.005	0.0054 ± 0.0006		

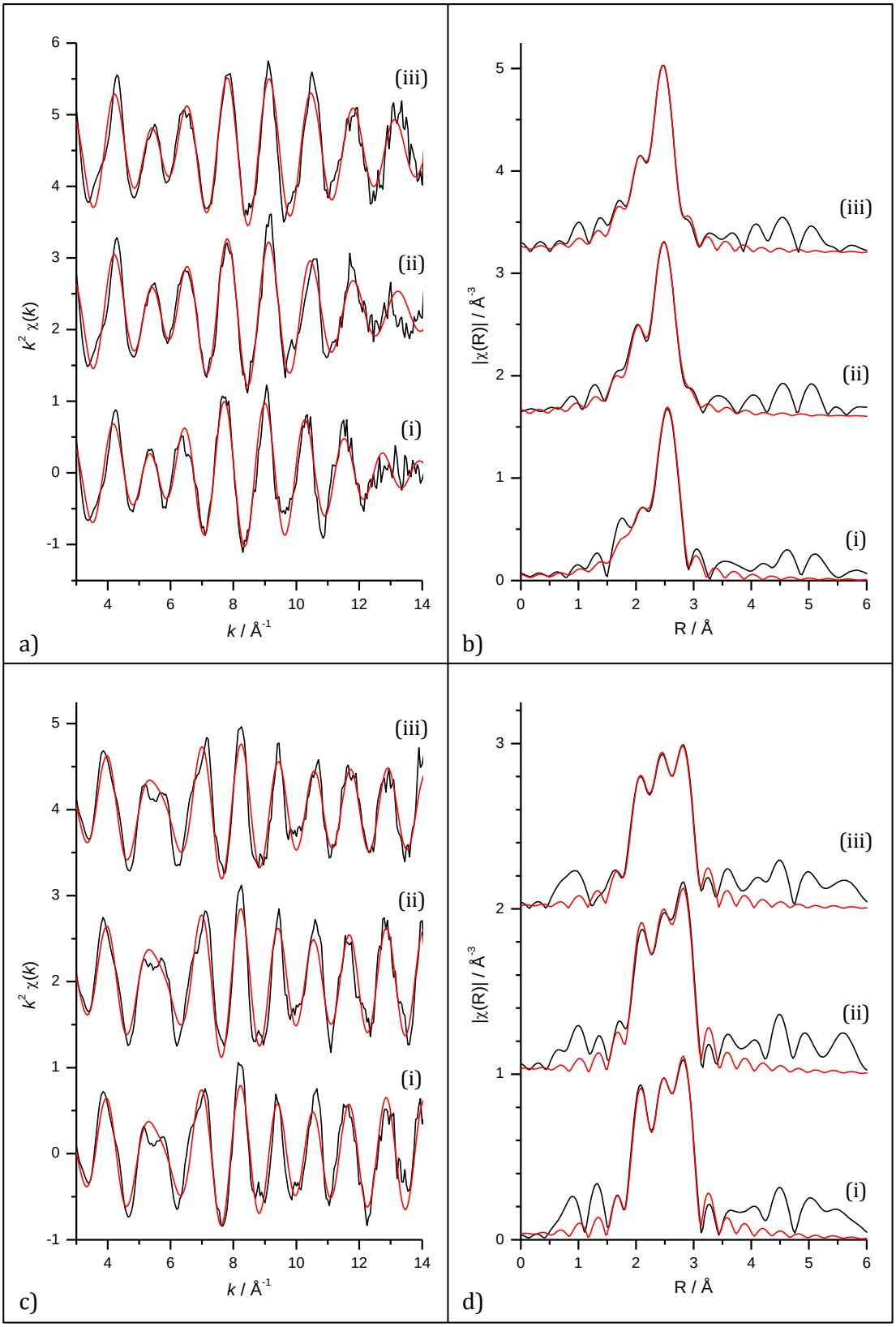

Figure 3.6: k^2 weighted experimental data (black) and fit (red) with the corresponding Fourier transform for electrochemically aged $Pt_{2ML}/Pd/C$. Data was recorded in situ at the Pd K (a-b) and Pt L_3 (c-d) edges, holding the potential at 0.00 V (i), 0.05 V (ii) and 0.50 V (iii) vs. RHE in 0.5 M H_2SO_4.

Table 3.3: Structural parameters obtained for electrochemically aged $Pt_{2ML}/Pd/C$ from fitting in situ EXAFS data acquired under potential control in 0.5 M H_2SO_4. (N.B. first element in the neighbour pair indicates the absorption edge of the data)

Potential	Neighbour	N	R / Å	σ^2 / Å^2	ΔE_0 / eV	R_f
0.00 V vs. RHE	Pd-Pd	6.65 ± 1.23	2.777 ± 0.010	0.0057 ± 0.0010	-5.97 ± 0.90	0.0117
	Pd-Pt	3.22 ± 1.06	2.738 ± 0.012	0.0044 ± 0.0018		
	Pt-Pd	1.19 ± 0.41			6.19 ± 0.61	
	Pt-Pt	9.06 ± 1.33	2.753 ± 0.004	0.0050 ± 0.0006		
0.05 V vs. RHE	Pd-Pd	7.32 ± 1.17	2.745 ± 0.006	0.0050 ± 0.0008	-6.44 ± 0.59	0.0067
	Pd-Pt	2.68 ± 0.81	2.747 ± 0.010	0.0030 ± 0.0014		
	Pt-Pd	1.07 ± 0.32			6.75 ± 0.54	
	Pt-Pt	9.11 ± 1.29	2.754 ± 0.004	0.0049 ± 0.0005		
0.50 V vs. RHE	Pd-Pd	6.84 ± 0.97	2.744 ± 0.004	0.0045 ± 0.0005	-6.38 ± 0.45	0.0045
	Pd-Pt	3.54 ± 0.85	2.748 ± 0.009	0.0051 ± 0.0014		
	Pt-Pd	1.04 ± 0.31			6.47 ± 0.48	
	Pt-Pt	9.28 ± 1.29	2.747 ± 0.004	0.0059 ± 0.0005		

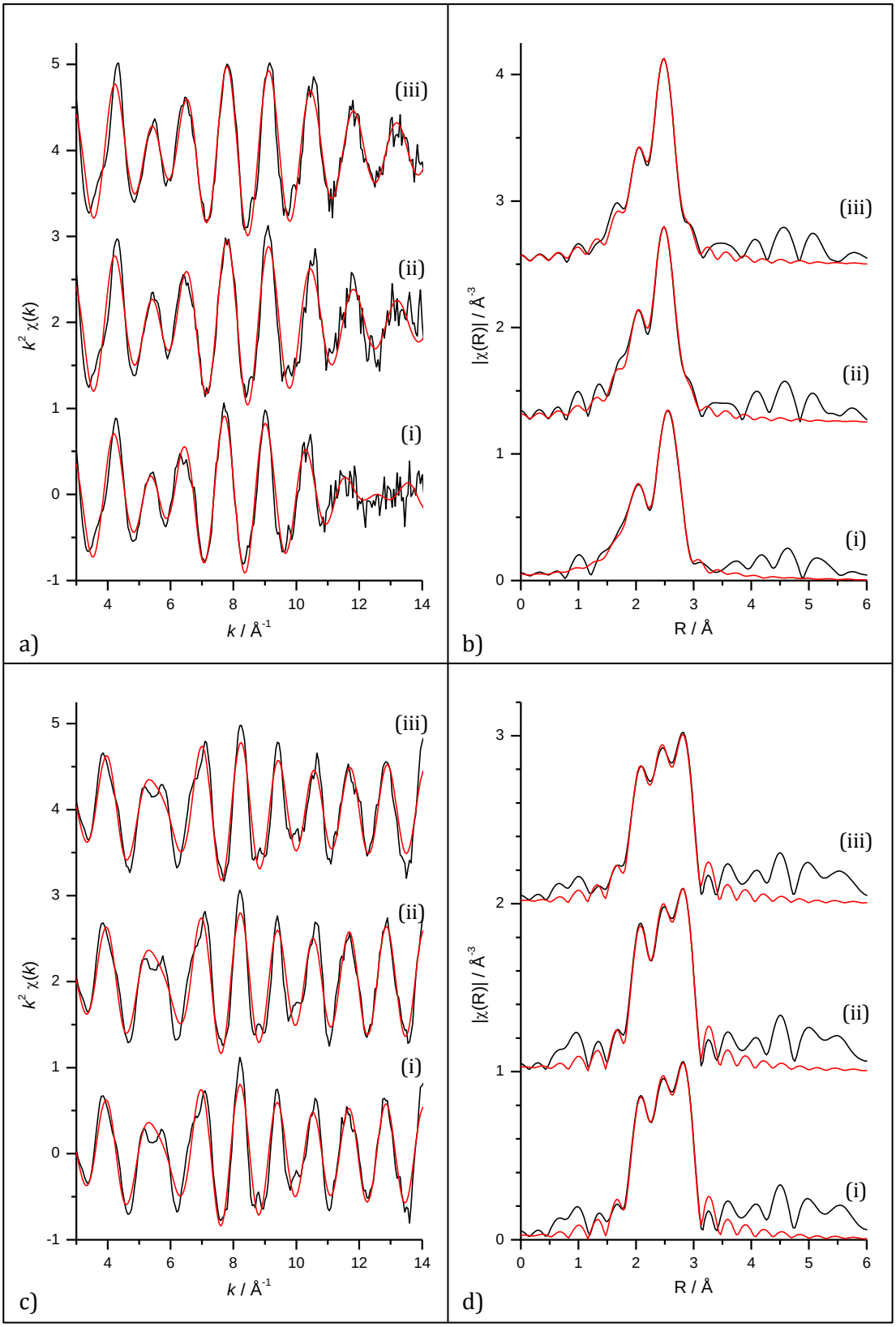

Figure 3.7: k^2 weighted experimental data (black) and fit (red) with the corresponding Fourier transform for electrochemically aged $Pt_{4ML}/Pd/C$. Data was recorded in situ at the Pd K (a-b) and Pt L_3 (c-d) edges, holding the potential at 0.00 V (i), 0.05 V (ii) and 0.50 V (iii) vs. RHE in 0.5 M H_2SO_4.

Table 3.4: Structural parameters obtained for electrochemically aged Pt_{4ML}/Pd/C from fitting in situ EXAFS data acquired under potential control in 0.5 M H_2SO_4. (N.B. first element in the neighbour pair indicates the absorption edge of the data)

Potential	Neighbour	N	R / Å	σ^2 / Å^2	ΔE_0 / eV	R_f
0.00 V vs. RHE	Pd-Pd	6.09 ± 0.99	2.761 ± 0.007	0.0055 ± 0.0008	-6.37 ± 0.60	0.0033
	Pd-Pt	3.97 ± 0.84	2.749 ± 0.007	0.0038 ± 0.0010		
	Pt-Pd	0.99 ± 0.22			6.14 ± 0.34	
	Pt-Pt	9.30 ± 1.21	2.756 ± 0.003	0.0053 ± 0.0003		
0.05 V vs. RHE	Pd-Pd	6.59 ± 1.06	2.742 ± 0.006	0.0050 ± 0.0008	-6.43 ± 0.60	0.0054
	Pd-Pt	3.93 ± 0.97	2.743 ± 0.009	0.0047 ± 0.0013		
	Pt-Pd	1.13 ± 0.29			6.21 ± 0.40	
	Pt-Pt	9.13 ± 1.21	2.753 ± 0.003	0.0051 ± 0.0004		
0.50 V vs. RHE	Pd-Pd	6.50 ± 0.94	2.743 ± 0.004	0.0046 ± 0.0006	-6.12 ± 0.48	0.0046
	Pd-Pt	3.59 ± 0.81	2.746 ± 0.008	0.0043 ± 0.0012		
	Pt-Pd	1.05 ± 0.29			6.32 ± 0.47	
	Pt-Pt	9.22 ± 1.29	2.749 ± 0.004	0.0055 ± 0.0005		

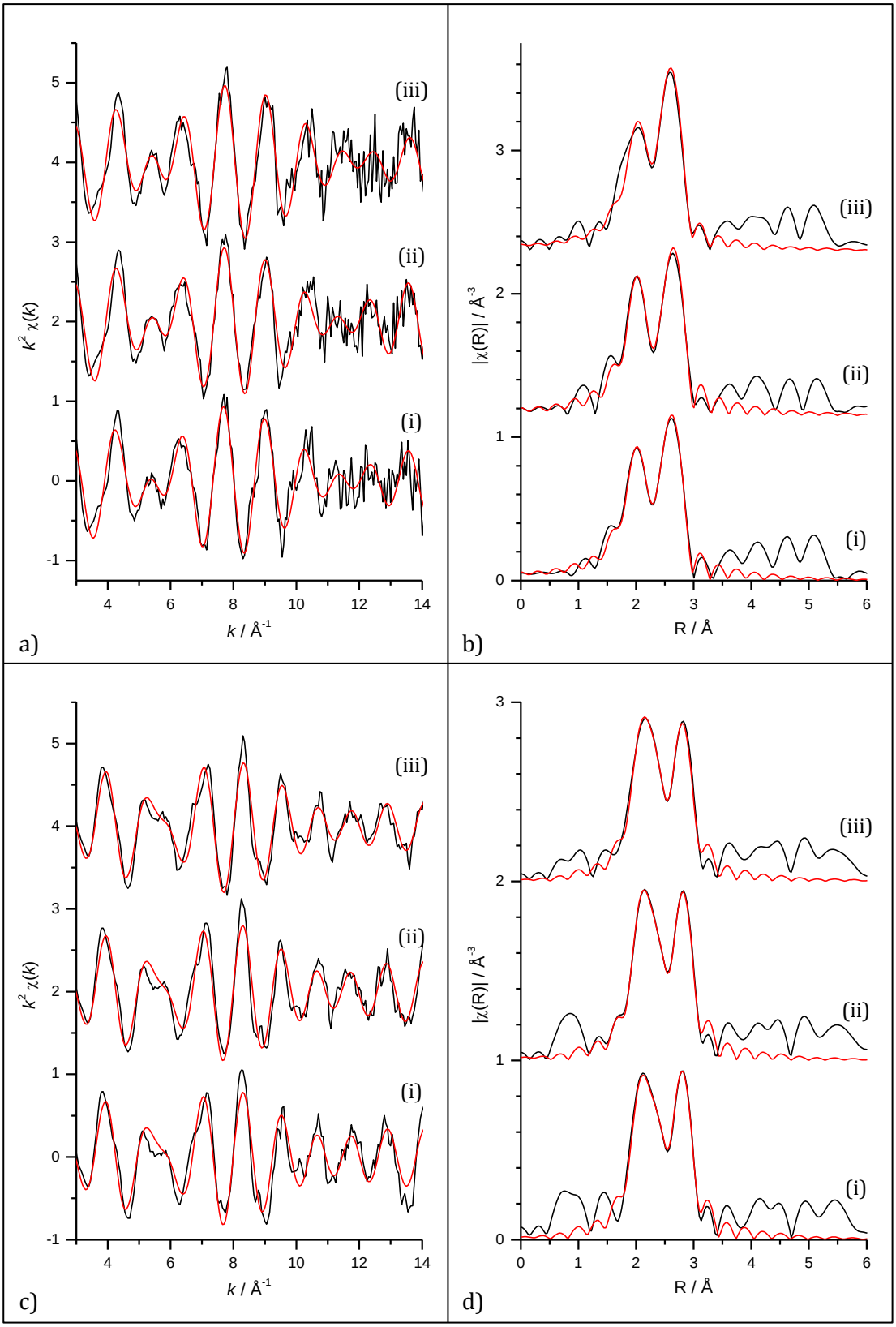

Figure 3.8: k^2 weighted experimental data (black) and fit (red) with the corresponding Fourier transform for the electrochemically aged Pt/Pd/C alloy. Data was recorded in situ at the Pd K (a-b) and Pt L_3 (c-d) edges, holding the potential at 0.00 V (i), 0.05 V (ii) and 0.50 V (iii) vs. RHE in 0.5 M H_2SO_4.

Table 3.5: Structural parameters obtained for the electrochemically aged Pt/Pd/C alloy from fitting in situ EXAFS data acquired under potential control in 0.5 M H_2SO_4. (N.B. first element in the neighbour pair indicates the absorption edge of the data)

Potential	Neighbour	N	R / Å	σ^2 / Å^2	ΔE_0 / eV	R_f
0.00 V vs. RHE	Pd-Pd	3.90 ± 1.08	2.740 ± 0.011	0.0036 ± 0.0017	-7.25 ± 1.01	0.0127
	Pd-Pt	6.52 ± 1.38	2.738 ± 0.008	0.0038 ± 0.0010		
	Pt-Pd	2.08 ± 0.46			5.06 ± 0.62	
	Pt-Pt	8.35 ± 1.29	2.738 ± 0.006	0.0054 ± 0.0007		
0.05 V vs. RHE	Pd-Pd	4.18 ± 0.76	2.741 ± 0.006	0.0037 ± 0.0009	-5.73 ± 0.54	0.0079
	Pd-Pt	6.06 ± 0.95	2.741 ± 0.004	0.0033 ± 0.0005		
	Pt-Pd	2.06 ± 0.32			5.64 ± 0.33	
	Pt-Pt	8.36 ± 1.10	2.744 ± 0.003	0.0053 ± 0.0004		
0.50 V vs. RHE	Pd-Pd	4.45 ± 1.23	2.746 ± 0.011	0.0039 ± 0.0017	-5.66 ± 1.01	0.0157
	Pd-Pt	5.59 ± 1.31	2.737 ± 0.007	0.0035 ± 0.0009		
	Pt-Pd	2.10 ± 0.43			5.46 ± 0.53	
	Pt-Pt	8.05 ± 1.16	2.738 ± 0.005	0.0055 ± 0.0006		

The shapes of the Fourier transforms shown in Figure 3.4 - Figure 3.8 (plots (b) and (d)) are very similar to those seen of the fresh electrocatalysts shown in Chapter Three, with changes with increasing shell thickness visible in the ratios of the peaks, along with a shift in the peak position of the Pd K edge data at 0.00 V. This indicates that the average coordination environment has not been altered dramatically by cycling in the oxide region.

There was again no significant change in the coordination numbers with applied electrode potential, however some differences were seen between the coordination numbers in the fresh and electrochemically aged samples. Figure 3.9 compares the coordination numbers obtained while holding the potential at 0.50 V for the fresh and cycled electrodes.

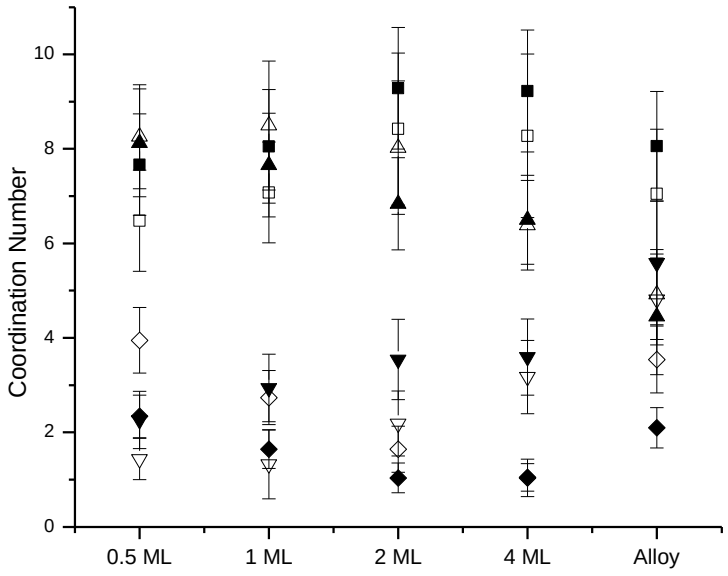

Figure 3.9: Comparison between electrochemically aged (solid symbols) and fresh (empty symbols) catalyst electrodes of the coordination numbers determined for the Pd-Pd (▲,△), Pd-Pt (▼,▽), Pt-Pd (◆,◇) and Pt-Pt (■,□). Data shown was recorded at 0.50 V vs. RHE in 0.5 M H_2SO_4.

Considering first the Pd K edge data, a decrease in Pd-Pd and an increase in Pd-Pt coordination numbers can be seen for all samples. In the Pt L_3 edge data, an increase in the number of Pt-Pt neighbours and a decrease in the number of Pt-Pd neighbours are evident for all samples except for Pt_{4ML}/Pd/C which only displays the increase in the Pt-Pt coordination number. Whilst these differences are within the large error associated with the coordination numbers, the presence of the trend seen across the samples suggests that this is a real effect.

This means that on average each Pd atom is 'seeing' more Pt than in the fresh catalysts, whereas each Pt atom is 'seeing' less Pd. If a greater degree of alloying had occurred following the potential cycling, a decrease in the M_1-M_1 and an increase in the M_1-M_2 coordination numbers at both absorption edges would be expected, however, this is not the case. The decrease in the number of Pd neighbours seen by both Pt and Pd indicates a loss of Pd from the system, which is in agreement with the dissolution of Pd detected by ICP-ES described in Section 1.

Figure 3.10 compares the bond lengths obtained at each potential for the Pd-Pd, Pd-Pt and Pt-Pt interactions, with the values obtained for the fresh samples also shown in plots b - d.

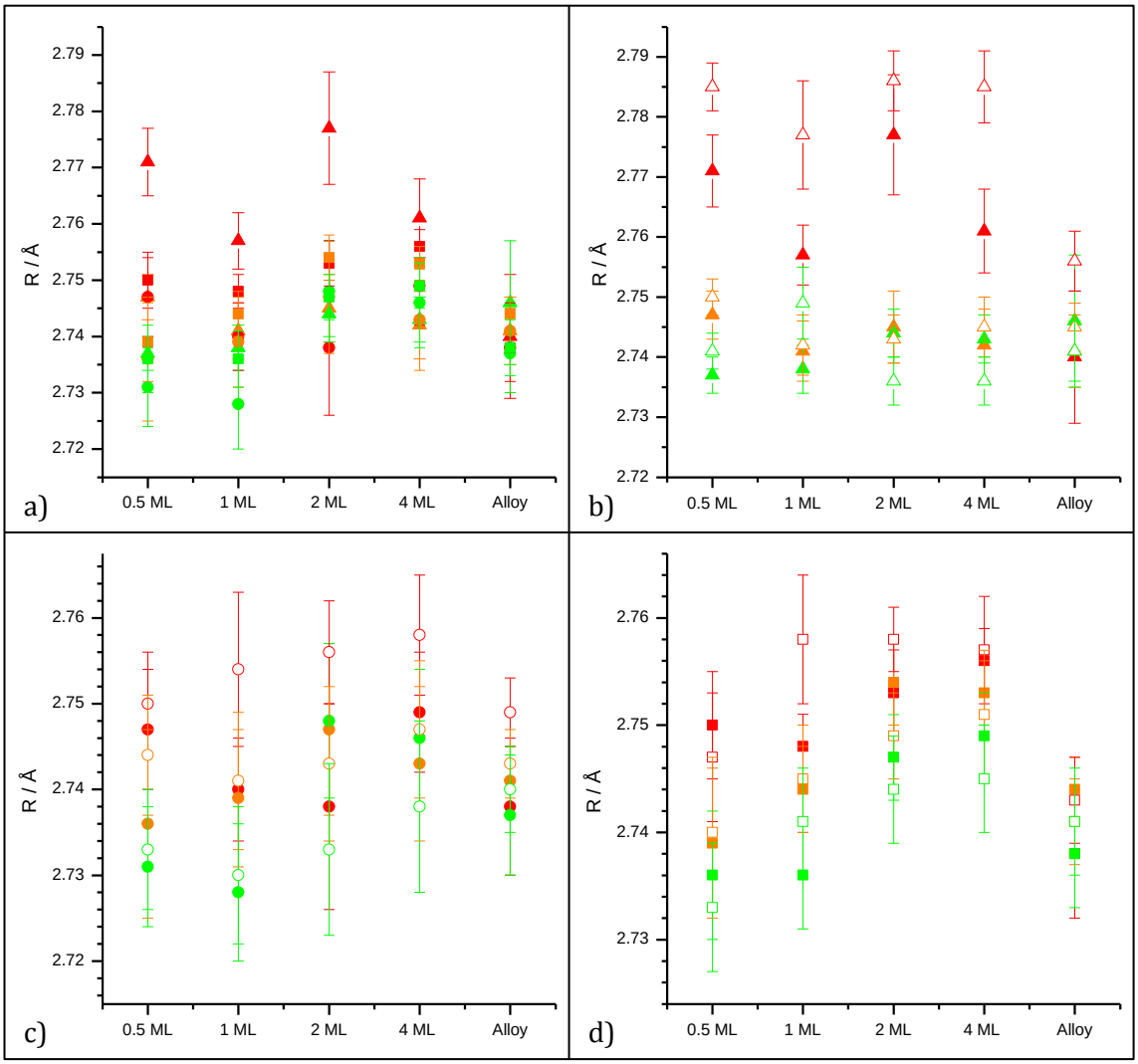

Figure 3.10: Comparison of the bond lengths obtained for the electrochemical aged samples of the Pd-Pd (▲), Pd-Pt (●) and Pt-Pt (■) interactions at 0.00 V (red), 0.05 V (orange) and 0.50 V (green). All interactions are shown in (a), with (b) – (d) focusing on the Pd-Pd, Pd-Pt and Pt-Pt bonds respectively. Data from the fresh catalyst samples is included in plots (b) – (d) for reference, denoted by △, ○ and □ for the Pd-Pd, Pd-Pt and Pt-Pt bonds respectively.

As in the data obtained of the fresh electrocatalysts, a general increase in the bond lengths of all interactions is seen with the reduction in potential, with the most significant effect seen in the Pd-Pd bond length at 0.00 V due to the absorption of hydrogen.

Comparing the bond lengths for all interactions at 0.00 V for the fresh and cycled samples, a general decrease is visible in the cycled samples, most noticeably in the Pd-Pd interaction. For the fresh catalysts, the large increase in the Pd-Pd bond length, caused by the absorption of hydrogen into the core, appeared to result in a perturbation of the bond lengths for the Pd-Pt and Pt-Pt interactions. The reduction of this in the cycled samples shows that the absorption of hydrogen has a smaller effect on the average structure of the sample, which again agrees with the dissolution of Pd.

Aside from the difference seen at 0.00 V, the variation in the bond lengths between fresh and cycled electrodes is within the error of the measurement. This shows that, apart from the loss of Pd indicated by the difference in coordination numbers and the smaller perturbation owing to hydrogen absorption, the per atom average structure has not significantly changed.

3.3 WAXS

The WAXS data was azimuthally averaged using Fit2D to produce a plot of the intensity vs. 2θ.[9],[10] As before, the background scattering from the carbon, electrolyte and cell could not be subtracted directly so the crystallite size was not determined. The (220) Bragg peak was identified and the peak position determined by subtracting a linear background and fitting a Gaussian function, enabling the calculation of the lattice parameter as described in Chapter Three.

Figure 3.11 shows the subtracted (220) peaks for the electrochemically aged samples, with the lattice parameters obtained from the peak positions given in Table 3.6.

The peak profiles are similar to those seen for the fresh catalysts, however without accurate background subtraction and correction for the incident intensity it is not possible to compare them directly. A shift in the peak position to lower 2θ can clearly be seen in the core-shell samples (plots a – d) with the reduction in potential to 0.00 V, again showing an expansion in the lattice due to the absorption of hydrogen.

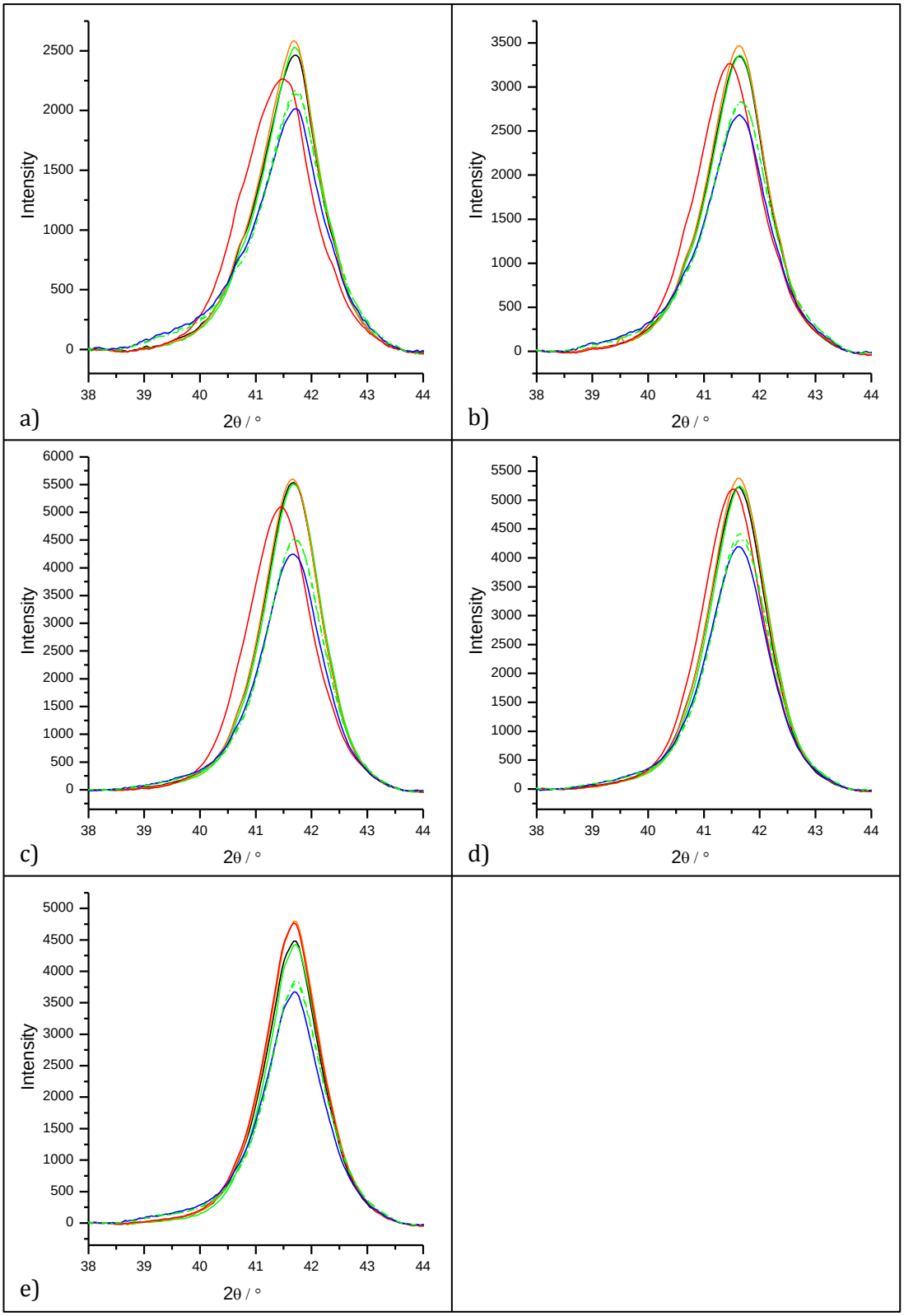

Figure 3.11: (220) peaks of electrochemically aged $Pt_{0.5ML}$/Pd/C (a), Pt_{1ML}/Pd/C (b), Pt_{2ML}/Pd/C (c), Pt_{4ML}/Pd/C (d) and Pt/Pd/C alloy (e) recorded at OCV (black), 0.50 V (green), 0.05 V (orange), 0.00 V (red) and 1.00 V (blue) vs. RHE in 0.5 M H_2SO_4. Second and third measurements at 0.50 V are denoted by (---) and (-···) respectively.

Table 3.6: Lattice parameters obtained from fitting the (220) Bragg peaks recorded of the electrochemically aged catalyst electrodes under potential control in 0.5 M H_2SO_4. The data is shown in chronological order regarding the potential hold, with the potentials quoted vs. RHE. The error associated with the lattice parameters is ± 0.002 Å.

	a / Å						
Catalyst	OCV	0.50 V	0.05 V	0.00 V	0.50 V	1.00 V	0.50 V
$Pt_{0.5ML}$/Pd/C	3.880	3.878	3.880	3.899	3.877	3.880	3.876
Pt_{1ML}/Pd/C	3.882	3.880	3.882	3.895	3.879	3.882	3.878
Pt_{2ML}/Pd/C	3.877	3.875	3.878	3.896	3.874	3.878	3.873
Pt_{4ML}/Pd/C	3.881	3.878	3.880	3.889	3.877	3.881	3.877
Pt/Pd/C	3.875	3.872	3.874	3.876	3.872	3.875	3.871

Figure 3.12 compares the lattice parameters obtained at each potential for the cycled samples. The values obtained for the fresh samples are also shown for reference (plot a).

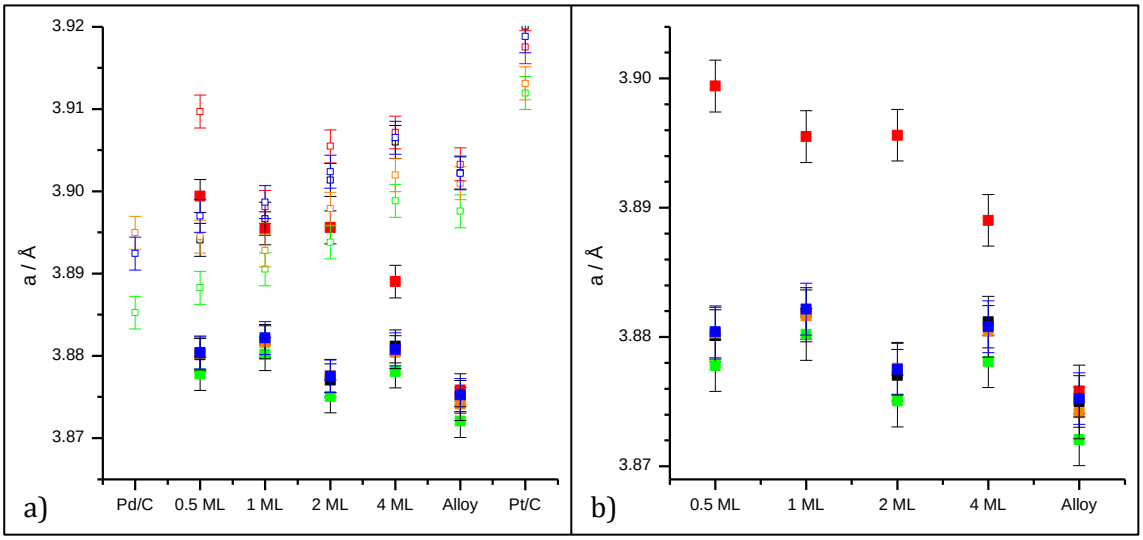

Figure 3.12: Comparison across the samples of the lattice parameters at OCV (black), 0.00 V (red), 0.05 V (orange), 0.50 V (green) and 1.00 V (blue). The electrochemically aged (■) and fresh samples (□) are compared in (a), with (b) showing the lattice parameters of the cycled samples only. N.B. for the fresh samples the data shown in orange corresponds to an applied potential of 0.07 V.

A marked decrease in the lattice parameters is visible for all of the cycled electrodes compared to the fresh catalysts, with the lattice parameters obtained being slightly lower than those of the Pd/C catalyst. The relative expansion of the lattice at 0.00 V is larger for the cycled samples, whereas the change in the lattice parameter at 0.05 V and 1.00 V is smaller. The correlation between lattice parameter and shell thickness has also been lost in the electrochemically aged samples.

The differences between the lattice parameters of the fresh and cycled electrodes, and their response to electrode potential, indicates that the crystalline region of the nanoparticles has been altered significantly with potential cycling. The greater effect of hydrogen absorption on the lattice parameters of the cycled electrodes suggests that a more Pd-like crystalline phase is being detected. This would also partially account for the decrease in the lattice parameters of all of the cycled samples. As the lattice parameters obtained are smaller than that of the Pd core it is also possible that either a decrease in the particle size, or a hollowing of the particle as observed by Sasaki *et al*.,[11] has occurred, resulting in a decrease in the lattice parameter due to increased surface stress.[12]

Without determination of the crystallite size it is not possible to fully account for the decrease in the lattice parameter of the cycled samples. The larger increase owing to hydrogen absorption does indicate that Pd is present in the crystalline phase. This is contrary to the EXAFS data which showed a decrease in the expansion of the Pd-Pd bond due to hydrogen absorption. As EXAFS gives the per atom average, it is possible that Pd is present in an amorphous phase as well as a crystalline phase, which would account for the lower expansion seen with EXAFS.

Conclusions

As in the experiments conducted by B. Tessier described in Section 1, a loss of ECA was seen in all of the catalyst samples subjected to potential cycling in the oxide region. From the electrochemical techniques, EXAFS and WAXS it has been seen that:

- The decrease in ECA is reduced with increasing shell thickness and can be attributed to dissolution of the metal, in particular Pd, and, owing to the decrease in ECA seen in the Pt/C electrocatalyst, an increase in particle size.
- The characteristic features of the CVs and CO oxidation voltammograms become more Pt-like with increasing number of cycles, indicating a loss of Pd from the surface.
- The coordination numbers obtained from the EXAFS suggest a loss of Pd from the system.
- A decrease in the effect of H_{abs} on the Pd-Pd bond length was seen in the EXAFS data, which in combination with the decrease in Pd neighbours, again indicates dissolution of Pd.
- Significant changes in the bond lengths were not seen at 0.05 and 0.50 V compared to the fresh electrocatalysts.

- The WAXS data, however, showed an increase in the lattice expansion at 0.00 V compared to the fresh samples, suggesting the presence of a Pd-rich phase
- A contraction in the lattice parameters of all samples was seen, indicating again a Pd-rich phase and/or the formation of smaller/hollow particles causing a contraction in the lattice due to surface stress.

The dissolution of Pd in acidic solution at the potentials employed in these experiments is well known, [13] and the occurrence of this is supported by the electrochemical data and the EXAFS. The difference seen in the EXAFS and WAXS data at 0.00 V suggests that the system consists of smaller Pd-rich crystalline materials, along with amorphous Pt/Pd particles. No direct evidence was seen of particle growth, suggesting that coalescence has either not occurred or could not be detected using these techniques, and that agglomeration of the particles altered by dissolution was possible. While some conclusions have been drawn, this study illustrates the need for particle size determination using techniques such as TEM and SAXS.

References

[1] M. F. Mathias, R. Makharia, H. A. Gasteiger, J. J. Conley, T. J. Fuller, C. J. Gittleman, S. S. Kocha, D. P. Miller, C. K. Mittelsteadt, T. Xie, S. G. Yan, P. T. Yu, *Electrochem. Soc. Interface* **2005**, *14*, 25-35.
[2] X. Yu, S. Ye, *J. Power Sources* **2007**, *172*, 145-154.
[3] Y. Shao, G. Yin, Y. Gao, *J. Power Sources* **2007**, *171*, 558-566.
[4] R. M. Darling, J. P. Meyers, *J. Electrochem. Soc.* **2003**, *150*, A1523-A1527.
[5] Y. Shao-Horn, W. Sheng, S. Chen, P. Ferreira, E. Holby, D. Morgan, *Top. Catal.* **2007**, *46*, 285-305.
[6] E. Antolini, J. R. C. Salgado, E. R. Gonzalez, *J. Power Sources* **2006**, *160*, 957-968.
[7] B. C. Tessier, *PhD Thesis: Preparation, Characterisation and Evaluation of Core-Shell Electrocatalysts for PEMFCs*, University of Southampton, **2009**.
[8] M. J. Watt-Smith, J. M. Friedrich, S. P. Rigby, T. R. Ralph, F. C. Walsh, *J. Phys. D-Appl. Phys.* **2008**, *41*.
[9] A. P. Hammersley, in *ESRF Internal Report*, **1997**.
[10] A. P. Hammersley, S. O. Svensson, M. Hanfland, A. N. Fitch, D. Hausermann, *High Pressure Res.* **1996**, *14*, 235-248.
[11] K. Sasaki, H. Naohara, Y. Cai, Y. M. Choi, P. Liu, M. B. Vukmirovic, J. X. Wang, R. R. Adzic, *Angew. Chem., Int. Ed.* **2010**, *49*, 8602-8607.
[12] C. Solliard, M. Flueli, *Surf. Sci.* **1985**, *156*, 487-494.
[13] M. Grden, M. Lukaszewski, G. Jerkiewicz, A. Czerwinski, *Electrochim. Acta* **2008**, *53*, 7583-7598.

CHAPTER FIVE: SAXS AND ASAXS STUDIES OF FRESH AND CYCLED CATALYSTS

The characterisation of the fresh and cycled electrodes at the atomic structural level using EXAFS and WAXS was reported in Chapters Three and Four, where it was shown that: (i) the desired core-shell structure had been made and retained in the electrochemical environment (Chapter Three); and (ii) that the effects of cycling were largely explained by loss of Pd from the catalyst particles accompanied by a loss in ECA caused by dissolution and possibly agglomeration of the particles, with no direct evidence of particle growth via coalescence (Chapter Four). This chapter details the use of in situ SAXS and ex situ ASAXS to determine the size and size dispersion of the catalyst nanoparticles, both as a whole and from an element-specific perspective, and how this changes as a result of electrochemical ageing.

1 Introduction

Small-angle and anomalous small-angle X-ray scattering (SAXS and ASAXS) focus on the elastic scattering of X-rays to angles between 0.1° and 10° 2θ, with θ being the angle between the incident beam and the scattered X-rays. As described in Section 2.1 of Chapter Three, the scattered X-rays represent a Fourier transform of the structure of the sample, with smaller angles relating to larger structures. As opposed to wide-angle X-ray scattering, which occurs due to the scattering from the crystal planes of atoms, small-angle X-ray scattering arises from the difference in the electron density between a particle as a whole and the surrounding material, for example the catalyst nanoparticle and the carbon support.

As a result of this, SAXS can be used to determine the size distribution and/or shape of particles within a sample, provided that there is sufficient electron density contrast between the particle of interest and the surrounding matrix. Whilst these parameters are often determined from TEM, the information obtained from SAXS is beneficial as it contains details of the average structure over the whole sample volume investigated, rather than from a relatively small number of particles.[1] In addition, it is also possible to conduct SAXS measurements in situ.

1.1 Theory of SAXS

The scattering of X-rays by atoms was described in Chapter Three in the context of wide-angle scattering. At small angles, the intensity detected is the square of the wave amplitudes of the X-rays scattered elastically by the atoms in the sample, with the number of photons scattered proportional to the electron density contrast between the particle and the matrix. This intensity is typically presented as a function of q, the scattering vector, where:

$$q = \frac{4\pi \sin\theta}{\lambda}$$

Equation 1.1

Relating this to Bragg's Law, which describes the relationship between scattering angle and distance, it can be seen that:

$$q = \frac{2\pi}{D}$$

Equation 1.2

Where D in this context refers to the particle size, thus illustrating the inverse relationship between q and size.

The geometry of a typical transmission SAXS experiment, which is comparable to that of the WAXS experiment described in Chapter Three, is shown in Figure 1.1, highlighting the relationship between q, the sample, and the path of the X-rays.

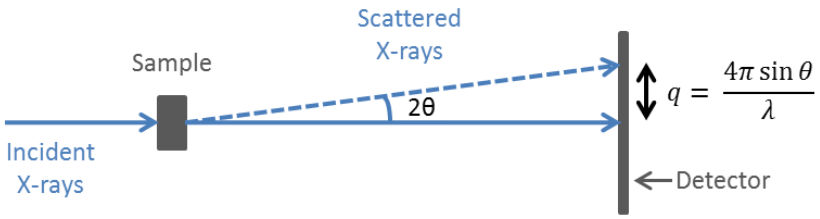

Figure 1.1: Schematic diagram of a transmission SAXS experiment.

The X-rays scattered by a sample of monodisperse particles result in an interference pattern related to the location of the atoms within the particle. This pattern is therefore characteristic of the particle shape and is referred to as the form factor, $P(q)$. To illustrate

this, Figure 1.2 shows the different scattering patterns arising from a variety of particle shapes with the same maximum size.[2]

As can be seen from Figure 1.2, the various shapes result in minima in the scattering profile at different q values. The positions of these minima are also affected by the particle size (Equation 1.2), thus it is important to have some idea of the particle shape if the size is to be determined, and vice versa. For this reason, SAXS measurements are often conducted having previously characterised the sample using microscopy techniques such as TEM.

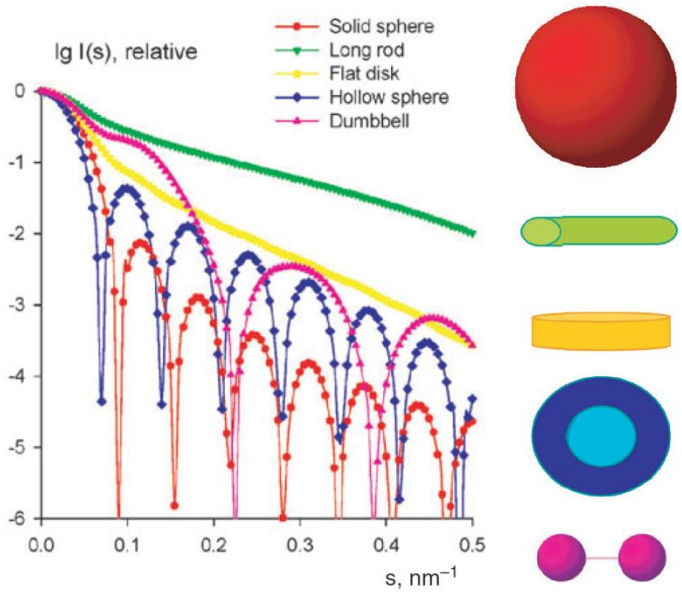

Figure 1.2: Examples of characteristic form factors for different particle shapes with the same maximum size. N.B. Scattering profiles are shown as a function of s, where $s = q$.[2]

The scattering profiles shown in Figure 1.2 have been calculated based on monodisperse particles. When a sample contains a distribution of particle sizes, the features are lost from the profile as a result of the summation of the scattering patterns of the particles of different sizes. This effect is illustrated in Figure 1.3, and presents another reason for having some prior knowledge of the shape and/or size of the sample from another technique before carrying out SAXS measurements, especially if a large size distribution is present.

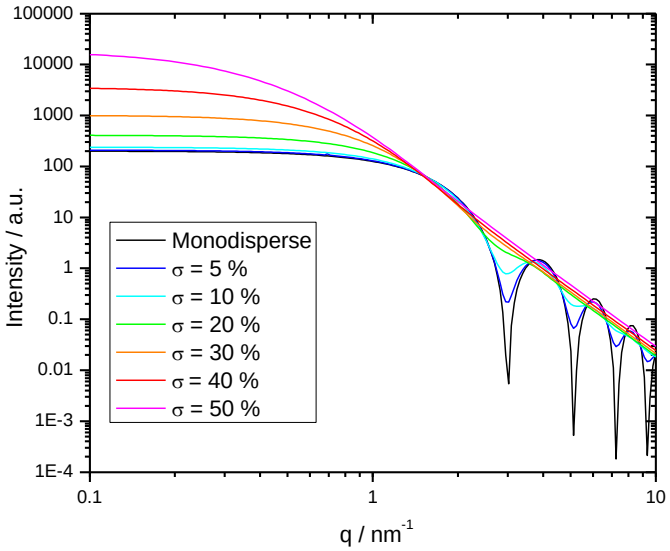

Figure 1.3: Calculated scattering profiles of monodisperse spheres compared to those with a log-normal distribution with a polydispersity of σ. Data was calculated using SASFit.[3]

Another contribution to the scattering profile is the known as the structure factor, $S(q)$, which arises from the interparticle interactions in concentrated samples. In dilute samples, where the distance between the particles is much larger than the wavelength of the radiation used, the structure factor can be assumed to have no effect on the detected signal.[4]

The intensity is proportional to the differential scattering cross section, $d\sigma/d\Omega$, which is the number of scattered photons per unit time relative to the incident flux at a given solid angle of q.[5] For the small-angle X-ray scattering arising from monodisperse spheres, the simplest system which can be considered, $d\sigma/d\Omega$, is given by:

$$\frac{d\sigma}{d\Omega}(q) = N\Delta\rho^2 V^2 P(q) S(q)$$

Equation 1.3

Where:

$$\Delta\rho = \left| d_p f_p - d_m f_m \right|$$

N is the number density of the particles, $\Delta\rho$ is the difference in the scattering length density (related to the electron density multiplied by the radius of an electron) between the particles and the matrix, V is the volume of the particles, $P(q)$ and $S(q)$ are the form and structure factors described above, d_p and d_m are the atomic densities of the particle and the matrix, and f_p and f_m are the atomic scattering factors.[6],[7]

The form factor for a monodisperse sphere with radius *r* is defined as:

$$P(q,r) = \frac{4\pi}{3} r^3 \frac{3[\sin(qr) - qr\cos(qr)]}{(qr)^3}$$

Equation 1.4

The intensity is related to the distribution, $n(r)$, as follows:

$$\frac{d\sigma}{d\Omega}(q) = N\Delta\rho^2 \int_0^\infty n(r)P(q,r)^2 S(qr)dr$$

Equation 1.5

The scattering intensity recorded during a SAXS measurement is then related to the scattering cross section by:

$$I(q) = \phi_0 At(\Delta\Omega)\frac{d\sigma}{d\Omega}(q)$$

Equation 1.6

Where ϕ_0 is the incident flux, A is the area of the sample irradiated by the X-ray beam, t is the sample thickness, and $\Delta\Omega$ is the solid angle subtended by the detector.[8]

The recorded intensity can be converted to an absolute intensity, usually with units of cm^{-1}, which is the scattering cross section normalised by the scattering volume. This is done by careful calibration of the intensity with regards to the detector response and the sample thickness, enabling information about the concentration of the scattering particles to be determined if the form factor and structure factor can be well-defined, however, for many SAXS experiments this is beyond the level of analysis required.

The scattering intensity from the particles is typically isolated by subtracting the SAXS profile of the matrix from the total profile of the matrix and the particles, allowing the analysis of the data to determine the size dispersion. Accurate subtraction of the background is critical for SAXS analysis and, to aid this, the data is typically normalised by the measured transmission of the sample as a whole and of the matrix on its own.

1.2 Theory of ASAXS

Anomalous small-angle X-ray scattering introduces element-specificity to SAXS by utilising the changes in the atomic scattering factors observed near the absorption edge of an element. The atomic scattering factor as a function of q and X-ray energy, $f(q, E)$, is given by:

$$f(q,E) = f_0(q) + f'(q,E) + if''(q,E)$$

Equation 1.7

Where $f_0(q)$ is the Fourier transform of the electron density of the atom, $f'(q, E)$ and $f''(q, E)$ are the real and imaginary parts of the dispersion correction, and i is the imaginary unit.

At the low values of q used in small-angle scattering, the angular dependency of the atomic scattering factor can be neglected and f_0 can be approximated to equal Z, the atomic number of the atom.[9] This results in the following definition of f:

$$f(E) = Z + f'(E) + if''(E)$$

Equation 1.8

At energies near to the absorption edge of an element, the resonance between elastic scattering and absorption causes a variation in the scattering factor by up to 20%, resulting in a decrease in the intensity of the scattering by the atoms of the element in question.[10] This behaviour is given the term anomalous scattering. Figure 1.4 illustrates the change in f' and f'' near the Pt L_3 edge.

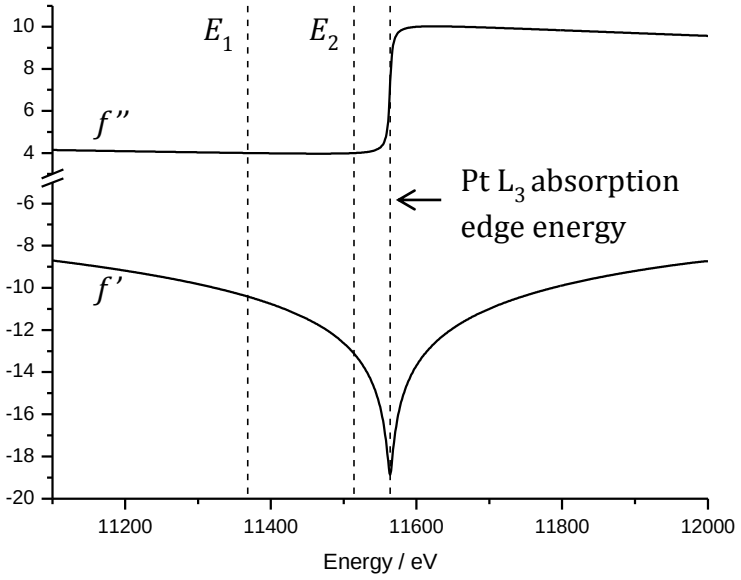

Figure 1.4: Scattering factors (f' and f'') at the Pt L_3 absorption edge, with E_1 and E_2 indicating suitable measurement energies to observe the ASAXS effect.

This variation in the intensity means that the scattering intensity from a given element can be isolated from that caused by the other scatterers in the sample by subtracting the data recorded at energies near the edge (E_2 in Figure 1.4), which will have a reduced contribution from the element of interest, from the data recorded far from the edge (E_1 in Figure 1.4):

$$I_{Pt} = I_{E_1} - I_{E_2}$$

Equation 1.9

ASAXS has been shown to be valuable in studies of Pt/C catalysts as it enables the accurate removal of the scattering from the carbon support and the pores, which can prove difficult in conventional SAXS.[11] For bimetallic catalyst nanoparticles, ASAXS has been used to determine the distribution of the metallic elements within the nanoparticle.[12]

2 Experimental

2.1 In situ SAXS

In situ SAXS data was collected using the electrochemical cell on beamline 1-4, Stanford Synchrotron Radiation Lightsource. Beamline 1-4 is a dedicated SAXS beamline with an energy range of 7.1 – 9.0 keV from a bending magnet source, with the energy controlled using a bent crystal Si(111) monochromator.[13] The incident energy used for these experiments was 8.33 keV, corresponding to a wavelength of 1.4884 Å, with a sample to detector distance of ca. 600 mm. A CCD detector was used to record the SAXS intensity, with a beamstop placed just before the detector to protect it from the intense direct beam. The data was collected by Peter Richardson, Andrea Russell and Anna Wise, with the help of Michael Toney and John Pople from SSRL.

As with WAXS, an accurate sample-to-detector distance is required for the data analysis. To calibrate this, SAXS data was collected of silver behenate (AgBeh) which has a well-defined layered structure with large interlayer spacings (58.4 Å), resulting in Bragg diffraction at small angles.[14] The AgBeh sample was placed in the catalyst electrode position of the electrochemical cell and data recorded prior to measuring any catalyst samples.

The catalyst electrodes were hydrated by boiling in demineralised water and then loaded into the in situ cell. 0.5 M H_2SO_4 was purged with N_2 and fed into the cell using a peristaltic pump. A mercury mercurous sulphate reference electrode was again used, along with the μAutolab III potentiostat. A flight tube filled with He was used between the sample cell and the detector to reduce the further scattering and absorption of the scattered X-rays by air. Figure 2.1 shows the experimental set-up.

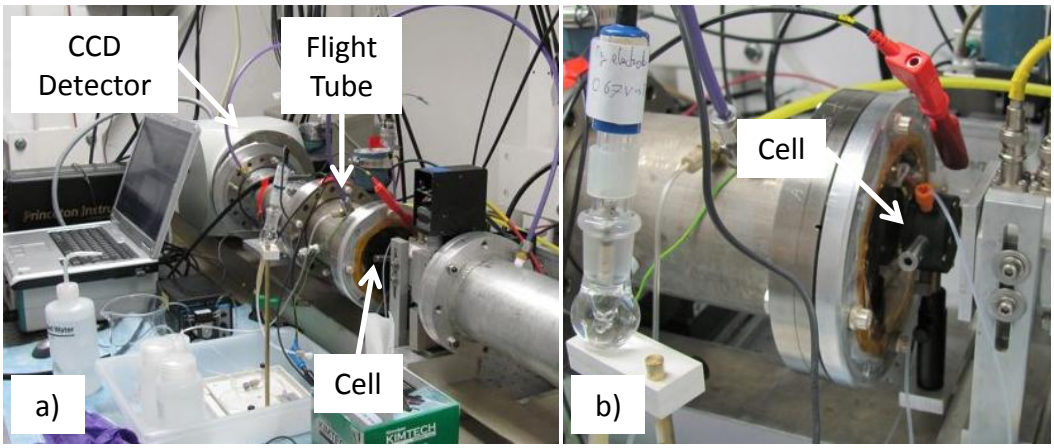

Figure 2.1: Experimental set-up on beamline 1-4, SSRL, with (a) showing the full set-up, and (b) focusing on the in situ cell.

The exposure time required for each sample measurement was determined by running a single exposure test scan to ensure that the scattered intensity was as high as possible without saturating the detector. Several exposures were then recorded for each measurement, giving a total collection time of 5 minutes, with typical single exposure times of 5 s. A dark scan, where there was no incident beam, was recorded using the same exposure time as for the sample before each measurement to enable correction for the time- and temperature-dependent dark counts recorded by the detector. The incident and transmitted intensities of the X-ray beam were also monitored using ion chambers to allow the data to be corrected for absorption by the sample. However, the transmitted intensity was not recorded for all samples and the effect of this will be discussed later in relation to the data analysis.

The measurements for each sample were carried out as follows:

- First SAXS collection at OCV
- Three CVs at 50 mV s^{-1} were recorded between 1.00 V and 0.05 V, starting at OCV, followed by three CVs at 10 mV s^{-1}
- SAXS data collected, holding the potential at 0.50 V vs. RHE
- SAXS data collected, holding the potential at 0.05 V vs. RHE
- SAXS data collected after holding the potential at 0.00 V vs. RHE for 10 minutes
- SAXS data collected after holding the potential at 0.00 V vs. RHE for 30 minutes
- CVs (10 mV s^{-1}) recorded from 0.00 V to 1.00 V to remove absorbed hydrogen from the sample
- SAXS data collected, holding the potential at 0.50 V vs. RHE
- SAXS data collected after holding the potential at 1.00 V vs. RHE for 10 minutes

- SAXS data collected after holding the potential at 1.00 V vs. RHE for 30 minutes
- CVs (10 mV s^{-1}) recorded from 1.00 V to 0.00 V to remove oxide
- SAXS data collected, holding the potential at 0.50 V vs. RHE

As for the previous in situ measurements, the potential was moved gradually to the desired value to avoid large increases in the current, with the cell current being allowed to decay before collecting the data.

Fresh and electrochemically cycled (where the cycling was carried out using the procedure detailed in Chapter Four) catalyst electrodes of $Pt_{0.5ML}$/Pd/C, Pt_{1ML}/Pd/C, Pt_{2ML}/Pd/C, Pt_{4ML}/Pd/C and the Pt/Pd/C alloy were studied using this method. Data was also collected of a fresh Pd/C core electrode. To enable the separation of the SAXS intensity of the catalyst nanoparticles from that of the carbon support, the electrolyte and the cell, data was also collected of an electrode in the filled in situ cell prepared from an ink of the carbon support with the same composition as the catalyst inks.

2.2 Ex situ ASAXS

The ex situ ASAXS data was collected on beamline B1, HASYLAB, which has been optimised for ASAXS measurements.[15] The beamline has a bending magnet source and an energy range of 4.9 – 35 keV controlled by a fixed-exit Si(311) monochromator.[16] Owing to the need to be able to detect the small changes in the intensity resulting from the ASAXS effect, the beamline, including the sample chamber, is operated under vacuum to reduce the background scattering from air. As a result of this, only ex situ measurements could be conducted as the in situ cell was not compatible with the beamline. Operating under vacuum meant that sample-to-detector distances of up to 3635 mm could be used, thus enabling a large *q*-range to be accessed. For these measurements, sample-to-detector distances of 935 and 3635 mm were used to give a *q*-range of 0.1 – 30 nm^{-1}, with the sample-to-detector distance being changed by adding or removing the required number of flight tubes. The detector used for the data collection of the fresh catalysts was a Pilatus 300K, with a Pilatus 1M used for the collection of the cycled catalyst ASAXS. WAXS data was also collected using a Mythen strip detector located in the sample chamber. Figure 2.2 is a schematic diagram of the beamline set-up.

The data was collected by Andrea Russell and Anna Wise, with the help of Ulla Vainio of HASYLAB.

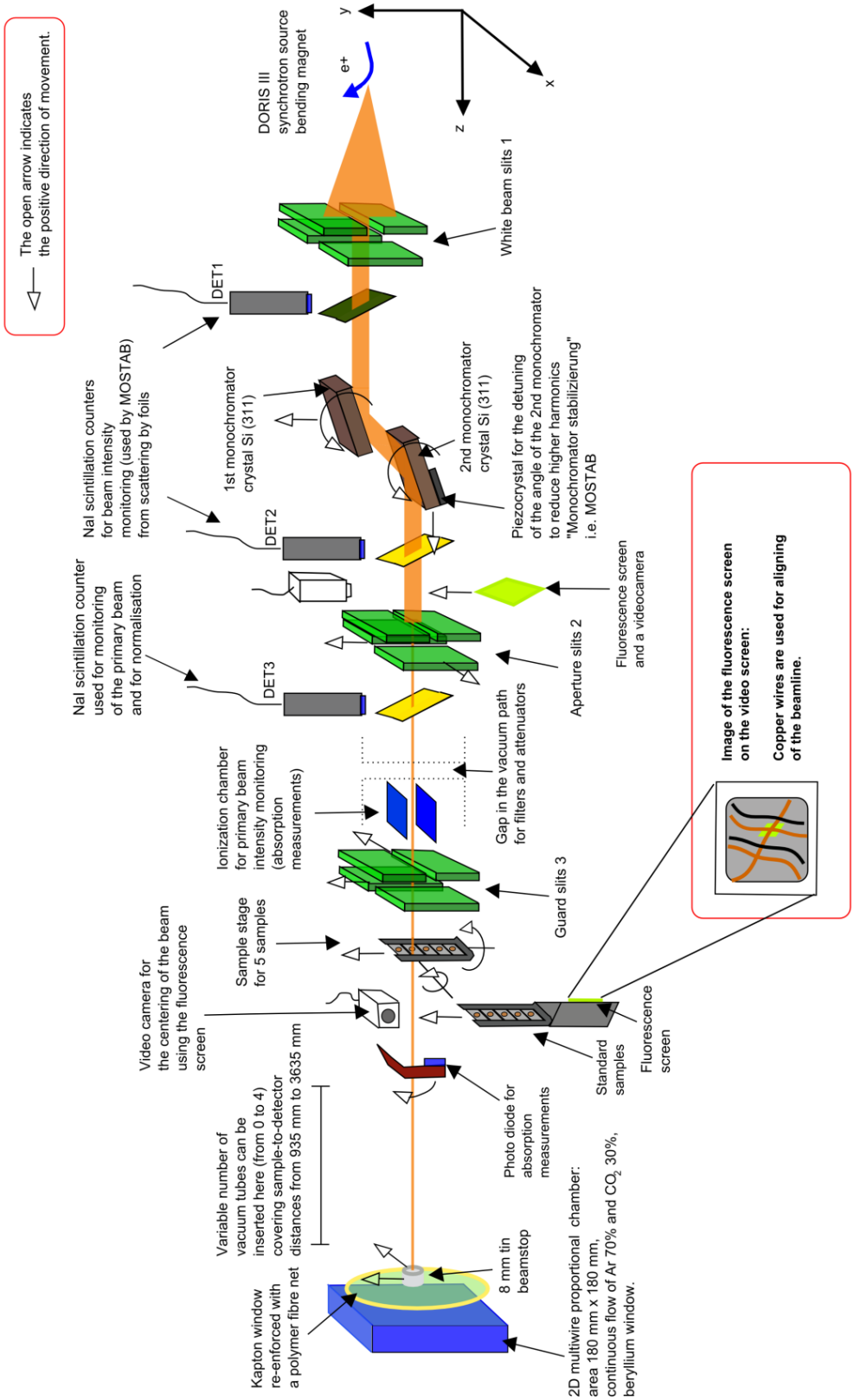

Figure 2.2: Schematic diagram of the set-up of beamline B1, HASYLAB.[16]

Ex situ data was collected at the Pt L_3 and Pd K edges of fresh and cycled catalyst electrodes. The absorption edge energy was calibrated by running XANES scans of Pt and Au foils at the Pt L_3 edge and Pd and Mo foils at the Pd K edge,[17] and the sample-to-detector distance was calibrated using AgBeh for the SAXS and LaB_6 for the WAXS.

The X-ray energies used for the data collection were then chosen to give regular intervals of f' based on the values calculated by Cromer and Liberman.[18] The energies used are given in Table 2.1.

Table 2.1: Energies used for ASAXS data collection with the corresponding f' and f'' values.

	Pt L_3			Pd K		
	Energy / eV	f'	f''	Energy / eV	f'	f''
E_1	11416	-10.97	3.96	24142	-4.02	0.56
E_2	11510	-12.97	3.97	24277	-5.02	0.57
E_3	11544	-14.97	4.12	24324	-6.02	0.63

The thicknesses of the dry catalyst electrodes were measured before being loaded into the standard beamline sample holder (shown in Figure 2.2), which was then fixed inside the sample chamber. The automation of the beamline meant that ASAXS of the five samples in the sample holder could be collected in cycles, with data collected for all of the samples at each energy before moving to the next energy. At the beginning of each of these cycles at every energy, a scan of the empty beam was recorded to measure the scattering from the slits and a glassy carbon reference sample was measured to enable calibration of the data to the absolute intensity scale. The cycles were repeated many times at both sample-to-detector distances to improve the signal-to-noise ratio of the data, with the total collection time for five samples taking several days.

The data was background-subtracted, and normalised for the incident beam intensity and the transmission of the sample. The signal was also corrected for detector, air and window absorption. The intensity was normalised to the absolute intensity scale by correcting for the difference in the recorded intensity for the glassy carbon reference sample and its theoretical intensity. The data was then integrated to obtain the 1D data of intensity as a function of q, and the data recorded at the two sample-to-detector distances was united, along with the WAXS data, to give a scattering curve over the whole q-range. These steps

were all carried out at the beamline using Matlab macros written by U. Vainio, A. Wacha and S. Haas.

2.3 SAXS Data Analysis

Before the SAXS data could be converted from the 2D intensity pattern recorded by the detector to a 1D plot of the intensity vs. q, the sample-to-detector detector distance was determined using the AgBeh calibration file. The data was loaded into Fit2D and the radius of the first Bragg reflection ring was determined in terms of the number of pixels.[19],[20] The sample-to-detector distance was then calculated in the same way as for the WAXS data (Equation 2.1).

$$D_{sd} = \frac{n\ x\ d_{pixel}}{\tan\left(2\sin^{-1}\frac{\lambda}{2d}\right)}$$

Equation 2.1

Where n is the number of pixels, d_{pixel} is the diameter of the pixels, λ is the wavelength of the incident beam, and d is the interlayer spacing of AgBeh.

The CCD detector used for these measurements comprised of a phosphorous screen behind a berylium window which detected the intensity of the X-rays. The measured signal was then transferred via fibres which tapered down to a smaller CCD screen with a pixel size of 24 μm. The taper ratio for this detector was 2.7 which could then be applied to the determined sample-to-detector distance, for example 242 mm, to give the physical sample-to-detector distance; 653 mm in this case. The sample-to-detector distance determined from the calibration and the pixel size of the CCD screen were used for the integration of the data, rather than the values adjusted for the taper ratio, to give an azimuthally-averaged plot of the intensity vs. q.

The dark intensity was subtracted directly from the sample data and the resulting data was normalised for the incident intensity, I_0. As mentioned in Section 1.1, SAXS data is typically normalised for transmission before subtraction of the background intensity arising from the matrix, in this case the carbon support, cell and electrolyte. As the transmitted intensity was not recorded for all samples, the background data normalised for I_0 was scaled according to the difference in the intensity between the catalyst sample and the background. The scaled background intensity was then subtracted from the sample intensity to give the SAXS profile resulting from the catalyst nanoparticles, with

good agreement seen between the data obtained in this manner and that from using the transmitted intensity. Figure 2.3 shows an example of the background subtraction.

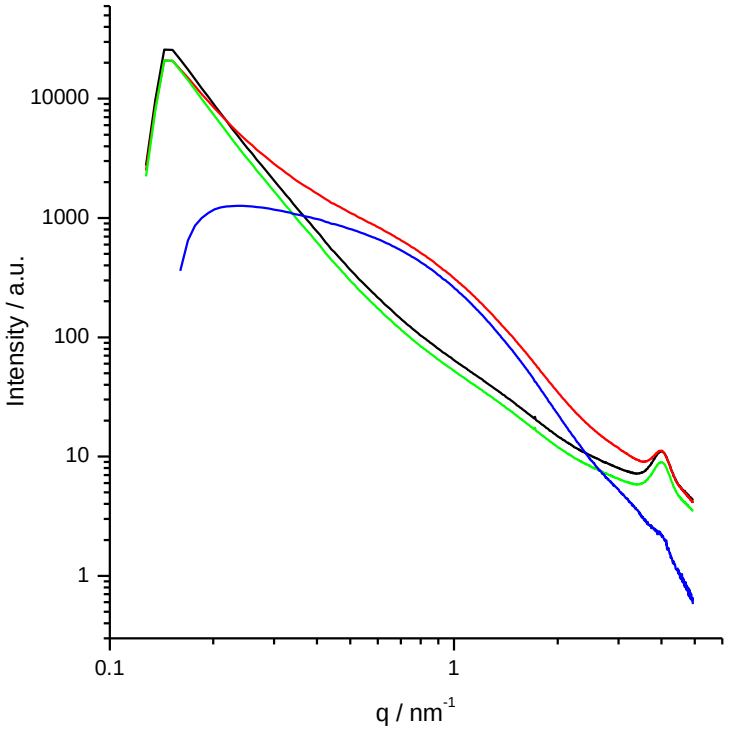

Figure 2.3: SAXS background subtraction of the Pt_{2ML}/Pd/C fresh catalyst (red) recorded at 0.5 V vs. RHE in 0.5 M H_2SO_4. The carbon background is shown as recorded (black) and scaled (green), with the subtracted SAXS intensity from the catalyst nanoparticles shown in blue.

Some artefacts of the background scattering can be seen at high q, which was also noted in the background subtraction carried out by normalising for the transmission, thus illustrating the difficulty of completely removing the contributions from the carbon support, the cell and the electrolyte. However, the intensity in this region is very low and does not represent a significant contribution to the data.

The catalyst SAXS profiles were then analysed to determine the particle size and size dispersion using SAXSFit.[8]

SAXSFit uses the spherical form factor given in Equation 1.4 to fit the particle size distribution in Equation 1.5, including the N and $\Delta\rho^2$ terms in a scaling factor which also accounts for the incident flux, irradiated area, sample thickness and solid angle. The contribution from the structure factor was neglected on the assumption that there were no interparticle interactions contributing to the measured intensity.

The size distribution used was a log-normal distribution given in Equation 2.2, where r_0 is the particle radius, and σ is the dispersion determined during the fitting procedure:

$$n(r) = \exp\left(-\frac{\left[\ln\frac{r}{r_0}\right]^2}{2\sigma^2}\right)\frac{1}{r\sigma\sqrt{2\pi}}$$

Equation 2.2

This distribution has a mean, μ, of:

$$\mu = r_0\exp\left(\frac{\sigma^2}{2}\right)$$

Equation 2.3

And a variance of:

$$r_0^2[\exp(2\sigma^2) - \exp(\sigma^2)]$$

Equation 2.4

The fitting is carried out using a least-squares fitting routine, with the statistical analysis of the fit reported in terms of the reduced χ^2 and R^2 values defined as:

$$\text{Reduced } \chi^2 = \frac{1}{n-p}\sum_i w_i\,(y_i - F(x_i))^2$$

Equation 2.5

$$R^2 = 1 - \frac{\sum_i\left(y_i - F(x_i)\right)^2}{\sum_i\left(y_i - \overline{F(x)}\right)^2}$$

Equation 2.6

Where n is the number of data points, p is the number of free parameters, w_i are the weightings, and y_i and $F(x)$ are the input and calculated $I(q)$ respectively. The data is weighted by $1/y_i$, unless error values are provided in which case the weighting is determined by $1/\sigma_i^2$, where σ_i is the error on the data. The errors on the parameters are calculated based on the weighting of the data using a covariance matrix.

As the q-range of the subtracted data was relatively small, initial fits were performed to determine a suitable value for σ which was then fixed to enable more accurate

determination of r_0. The mean and standard deviation of the radius were then determined from the obtained r_0 value and the fixed σ value.

2.4 ASAXS Data Analysis

Figure 2.4 shows the full scattering curves obtained for the fresh Pt_{2ML}/Pd/C electrode at the Pt L_3 and Pd K edges. As can be seen from this data, the ASAXS effect represents a very small difference in the intensity compared to the background scattering and is not visible on this scale. The data recorded at E_3 was subtracted from the data at E_1 to give the scattering profile of the element at the relevant edge, with the X-ray energies, E, used given in Table 2.1. To check that the change in intensity was due to anomalous scattering, $I(E_1)$ - $I(E_2)$ and $I(E_2)$ – $I(E_3)$ were also plotted and overlaying curves were observed.

The binning of the data resulted in relatively few data points so to enable the analysis using SAXSFit, the data and the error at each point were interpolated using the linear interpolation function in OriginLab. The data was then fitted using the same approach as for the SAXS data, although the weighting for the fits was based on the error provided with the data.

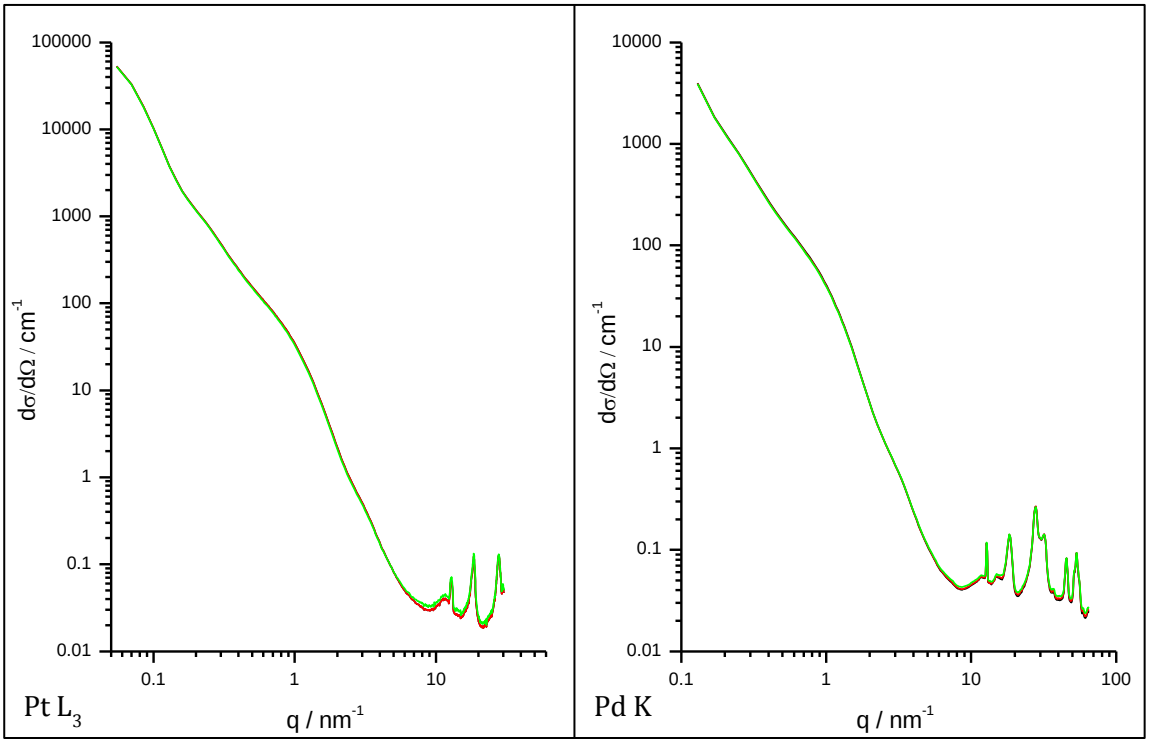

Figure 2.4: Ex situ ASAXS data collected at E_1 (black), E_2 (red) and E_3 (green) at the Pt L_3 (left) and Pd K (right) edges.

3 Results

3.1 In situ SAXS

No distinguishable variation was seen in the SAXS data as a function of applied electrode potential. This shows that SAXS was not sensitive to the relatively small (< 3%) changes in the structure seen in the EXAFS and WAXS data reported in Chapter Three, which is likely to be due, in part, to the polydispersity of the samples. As a result of this, only the data recorded at 0.5 V vs. RHE is reported here.

The subtracted SAXS data showing the small-angle scattering intensity arising from the catalyst nanoparticles is presented in Figure 3.1, along with the fits to the data obtained using SAXSFit. Table 3.1 gives the r_0 values determined by the fit, along with σ which was fixed following preliminary fits to determine a suitable value. These values were then used to obtain the mean particle radius, μ, and its standard deviation, as detailed in Section 2.3, where the standard deviation describes the dispersion of the particle sizes. To aid comparison with the TEM data, μ and the standard deviation have been used to give the mean size and the size dispersion in terms of the particle diameter.

The particle sizes obtained by SAXS for the fresh catalysts are all smaller than the values determined from TEM. This can be accounted for as TEM does not include very small particles, ≤ 1 nm, but realistically ≤ 1.5 nm, whereas SAXS does. SAXS also includes all of the particles in the irradiated volume of the sample, whereas in TEM some particles can be difficult to distinguish and so are omitted from the analysis.[1],[21]

The calculated log-normal distributions are compared to the histograms obtained for the TEM data in Figure 3.2 ($Pt_{0.5ML}$/Pd/C, Pt_{1ML}/Pd/C and Pt_{2ML}/Pd/C) and Figure 3.3 (Pt_{4ML}/Pd/C, Pt/Pd/C alloy and Pd/C core material). The shapes of the distributions obtained are in reasonable agreement, but the SAXS generally has a narrower σ. The SAXS data was obtained at 0.5 V, following the collection of conditioning cyclic voltammograms. However, it is unlikely that this pre-treatment is the origin of the difference between the SAXS and TEM distributions, as the SAXS data recorded at OCV prior to the treatment was indistinguishable from the data presented. Instead, the difference is more likely to be due to the statistical limitations of the TEM data, which uses a relatively small sample set as shown by the number of particles analysed, n_p.

The fits to the SAXS data were carried out, assuming a single size distribution (i.e. not bimodal) and a spherical particle shape, based on the TEM image data obtained previously. As can be seen in Figure 3.1, the fits show good agreement to the data. A shoulder can be seen in the recorded data at high *q*, which can be attributed to an additional distribution of smaller particles. It was not possible to fit this second distribution due to the quality of the data in this region, but it is seen to be more pronounced in the data obtained of the cycled catalysts.

Table 3.1: Parameters obtained from fitting the SAXS data shown in Figure 3.1, along with the particle diameters determined by TEM.

		r_0 / nm	σ_{LN} / nm	R^2	Red. χ^2	μ_r / nm	Diameter / nm	TEM Diameter / nm
$Pt_{0.5ML}/Pd/C$	Fresh	1.173 ± 0.005	0.40	0.999	0.08	1.27 ± 0.53	2.5 ± 1.1	3.70 ± 1.35
	Cycled	1.188 ± 0.006	0.50	0.999	0.40	1.35 ±0.72	2.7 ± 1.4	-
$Pt_{1ML}/Pd/C$	Fresh	1.131 ± 0.007	0.40	0.997	0.17	1.23 ± 0.51	2.5 ± 1.0	3.04 ± 1.57
	Cycled	1.241 ± 0.006	0.50	0.999	0.19	1.41 ± 0.75	2.8 ± 1.5	-
$Pt_{2ML}/Pd/C$	Fresh	1.161 ± 0.004	0.40	0.999	0.13	1.26 ± 0.52	2.5 ± 1.0	3.63 ± 1.37
	Cycled	1.368 ± 0.006	0.45	0.997	0.73	1.51 ± 0.72	3.0 ± 1.4	-
$Pt_{4ML}/Pd/C$	Fresh	1.249 ± 0.004	0.40	0.996	1.33	1.35 ± 0.56	2.7 ± 1.1	4.32 ± 1.32
	Cycled	1.984 ± 0.005	0.35	0.997	1.08	2.11 ± 0.76	4.2 ± 1.5	-
Pt/Pd/C Alloy	Fresh	1.689 ± 0.006	0.35	0.999	0.80	1.80 ± 0.65	3.6 ± 1.3	3.80 ± 1.46
	Cycled	1.987 ± 0.007	0.35	0.999	0.15	2.11 ± 0.76	4.2 ± 1.5	-
Pd/C Core	Fresh	1.126 ± 0.007	0.40	0.998	0.20	1.22 ± 0.51	2.4 ± 1.0	3.80 ± 2.12

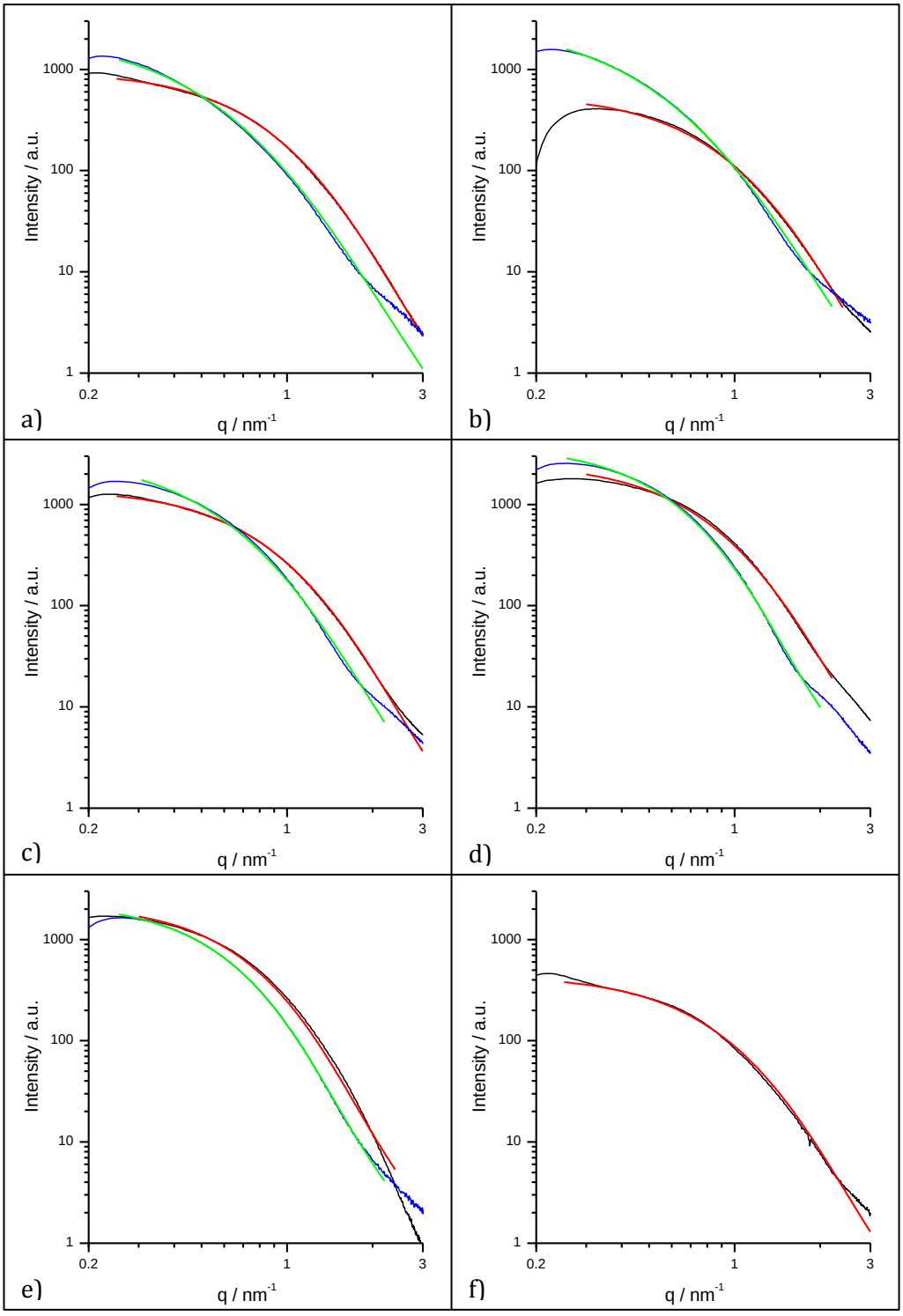

Figure 3.1: In situ SAXS data recorded at 0.5 V vs. RHE in 0.5 M H_2SO_4 of the $Pt_{0.5ML}$/Pd/C (a), Pt_{1ML}/Pd/C (b), Pt_{2ML}/Pd/C (c), Pt_{4ML}/Pd/C (d), Pt/Pd/C alloy (e) and Pd/C (f) catalyst electrodes. The data and fit for the fresh electrodes are shown in black and red, with the data and fit for the cycled electrodes shown in green and blue.

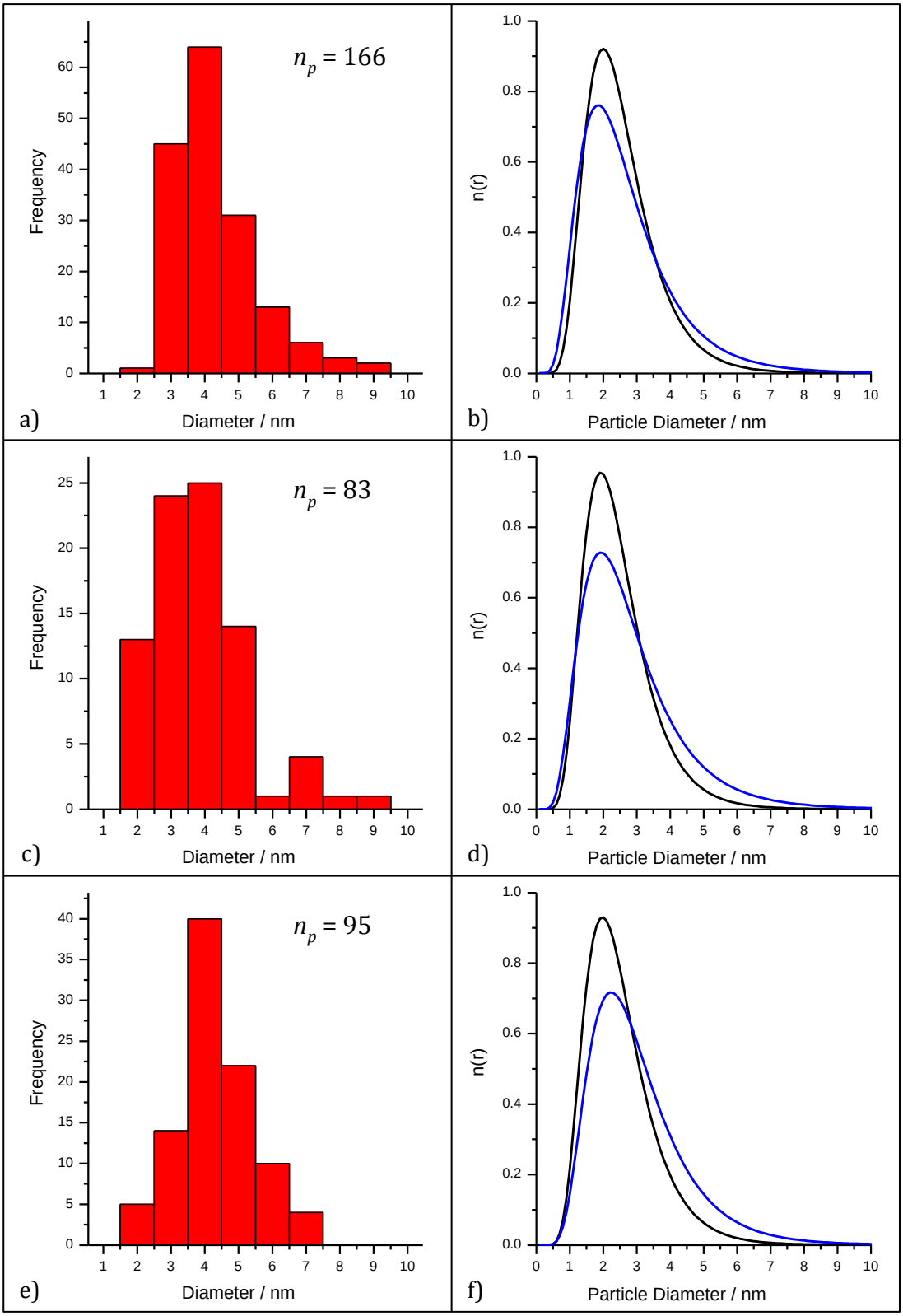

Figure 3.2: Log-normal size distributions (right) for the fresh (black) and cycled (blue) determined from the SAXS data compared to the histograms (left) obtained from TEM of the fresh catalysts for $Pt_{0.5ML}/Pd/C$ (a-b), $Pt_{1ML}/Pd/C$ (c-d) and $Pt_{2ML}/Pd/C$ (e-f).

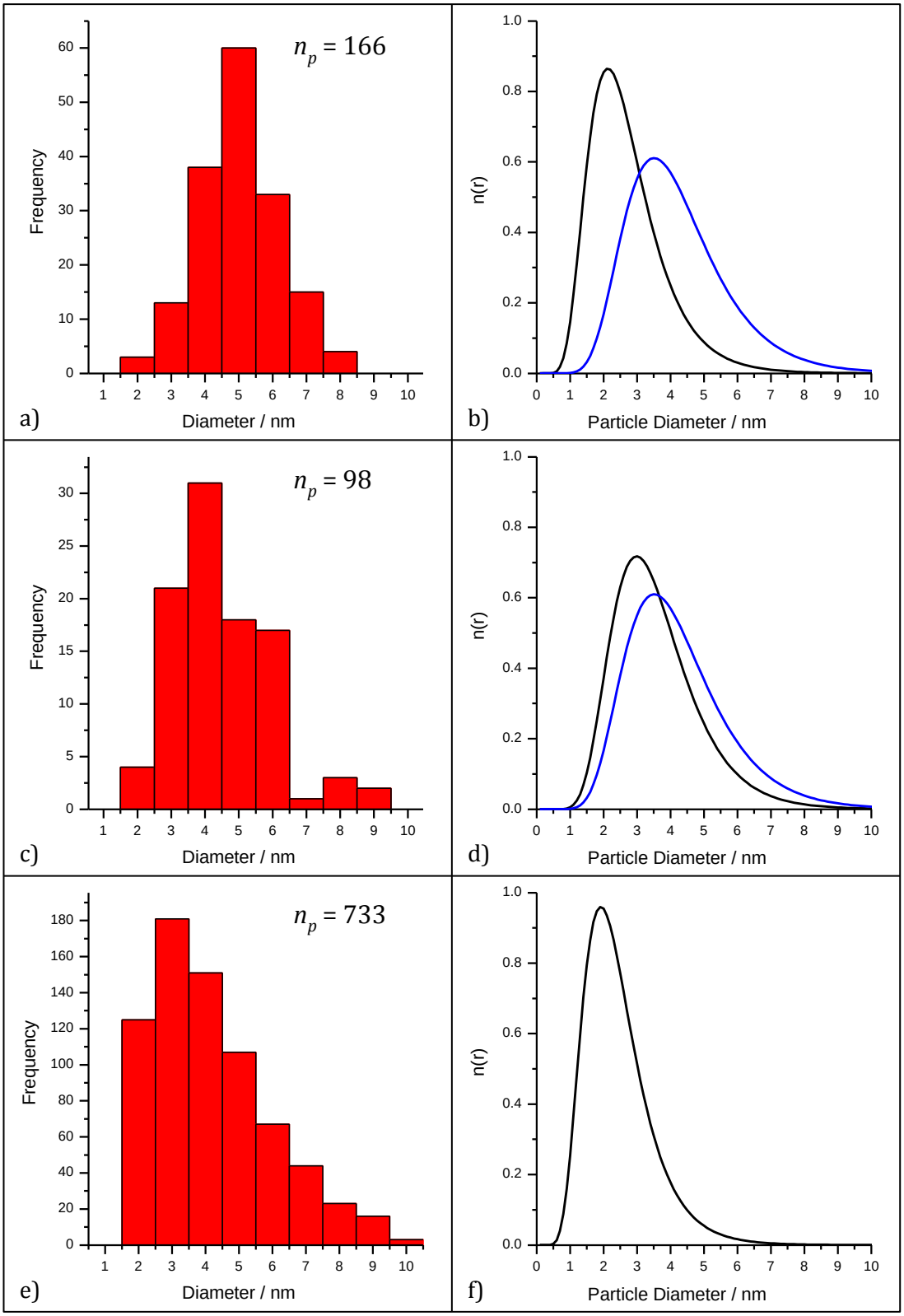

Figure 3.3: Log-normal size distributions (right) for the fresh (black) and cycled (blue) determined from the SAXS data compared to the histograms (left) obtained from TEM of the fresh catalysts for Pt_{4ML}/Pd/C (a-b), Pt/Pd/C alloy (c-d) and the Pd/C core material (e-f).

A general increase in the particle size was seen in the samples subjected to electrochemical cycling, both from the calculated diameter and from the shift in the SAXS profile to lower values of *q*. As described in Chapter Four, a loss of electrochemical surface area (ECA) was observed as a result of the potential cycling in the oxide region, with the possible mechanisms of this loss of area being dissolution and particle growth by agglomeration or coalescence. From the EXAFS and WAXS data, the observed loss was attributed to dissolution and possibly agglomeration of the particles as no direct evidence of particle growth resulting from coalescence was able to be detected. The SAXS data reported here showed a clear increase in the particle size following electrochemical ageing, which can be attributed to coalescence of the particles.

If the loss in ECA for each of the catalysts on cycling was attributed only to an increase in particle size resulting from coalescence, this effect could be estimated by comparing the ratio of the average particle radii before and after cycling. Using this simple approximation, the loss in ECAs were estimated and the results compared to the values obtained from the electrochemically determined areas as shown in Table 3.2.

Table 3.2: Percentage decrease observed in the ECA compared to the percentage increase in the particle size determined from SAXS following potential cycling.

Catalyst	%Δ ECA Electrochemical	%Δ ECA SAXS
$Pt_{0.5ML}/Pd/C$	62 %	7 %
$Pt_{1ML}/Pd/C$	50 %	11 %
$Pt_{2ML}/Pd/C$	32 %	17 %
$Pt_{4ML}/Pd/C$	25 %	36 %
Pt/Pd/C Alloy	14 %	20 %

For the 0.5 ML, 1 ML, and 2 ML samples, the SAXS method significantly underestimates the loss in ECA. Further examination of the SAXS profiles (Figure 3.2) shows that the dispersion for these samples remained largely unchanged following electrochemical cycling. Thus, the true loss in ECA found in the electrochemical measurements can largely be attributed to dissolution of the catalyst particles rather than particle growth. In contrast, the change in ECAs determined electrochemically and using the SAXS data are

more similar for the 4 ML and alloy samples. Comparing the SAXS profiles for the 4 ML sample (Figure 3.3), it can be seen that the width of the peak in the particle size distribution increased, with a shift to larger diameters, at the expense of the smaller particles. A similar, although less significant, difference is observed for the alloy. Thus, the SAXS data supports coalescence via Ostwald ripening or particle growth as the mechanism of ECA loss for these catalysts.

3.2 Ex situ ASAXS

Figure 3.4 and Figure 3.5 show the subtracted ($I(E_1) - I(E_3)$) ASAXS curves of the fresh and cycled catalyst electrodes obtained at the Pd K and Pt L_3 edges respectively. The presence of the scattering profiles over a similar q-range at both edges is indicative of the Pt and Pd being present in particles of a similar size, whereas a significantly different range would show larger or smaller particles of either element. The sharp minima seen in the scattering profiles of the Pd K edge data is indicative of a core-shell structure.[22] A slight shoulder is seen in the ASAXS data at the Pt L_3 edge of the fresh 1 ML and 2 ML samples, due to a second dispersion of smaller particles. Following electrochemical cycling, this becomes more pronounced and is also seen in the data of the 0.5 ML, 4 ML and alloy cycled electrodes.

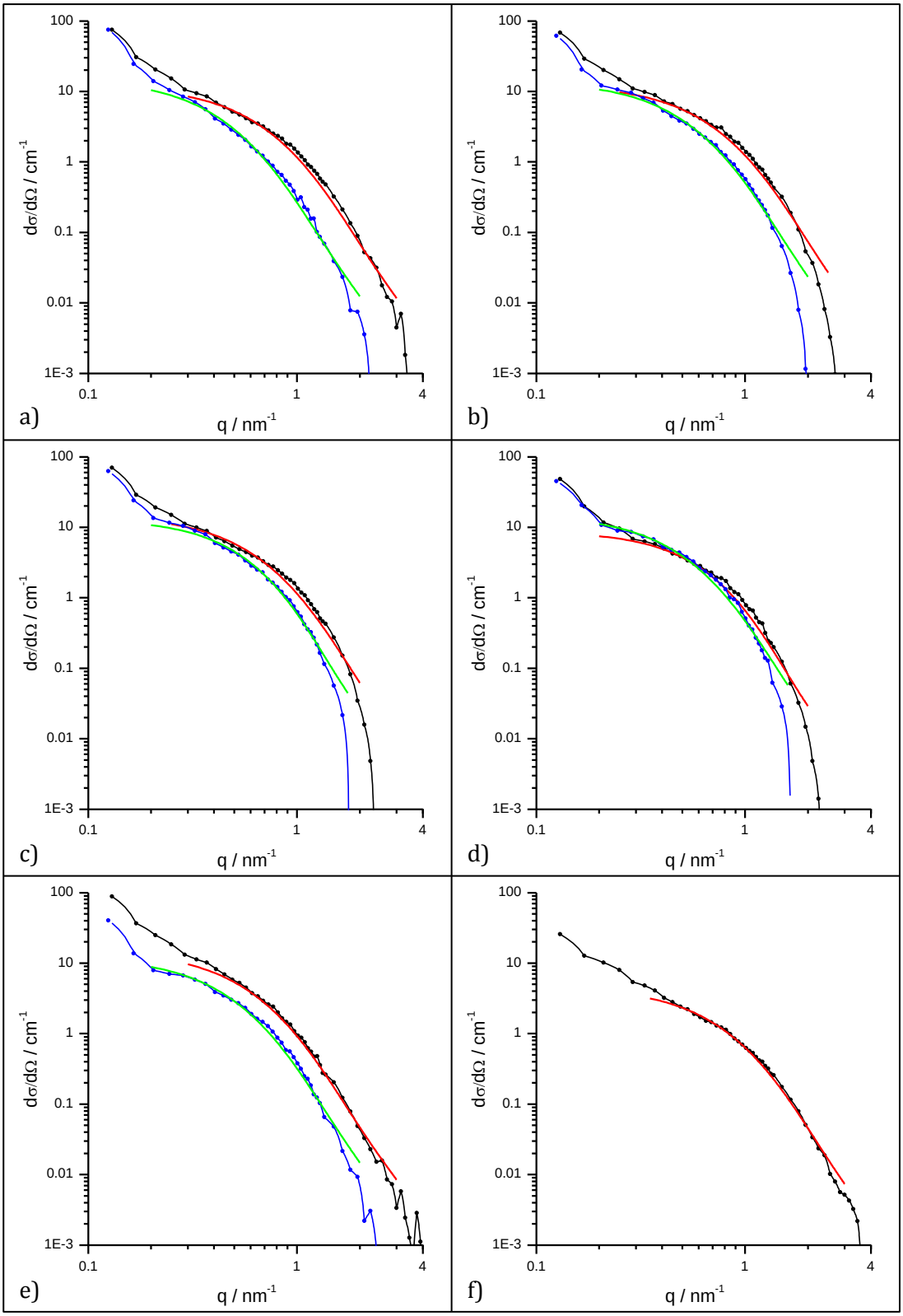

Figure 3.4: Subtracted ASAXS data recorded at the Pd K edge of the fresh (black) and cycled (blue) electrodes, along with the fits obtained shown in red and green respectively. Data is shown for $Pt_{0.5ML}$/Pd/C (a), Pt_{1ML}/Pd/C (b), Pt_{2ML}/Pd/C (c), Pt_{4ML}/Pd/C (d), Pt/Pd/C alloy (e) and the Pd/C core material (f).

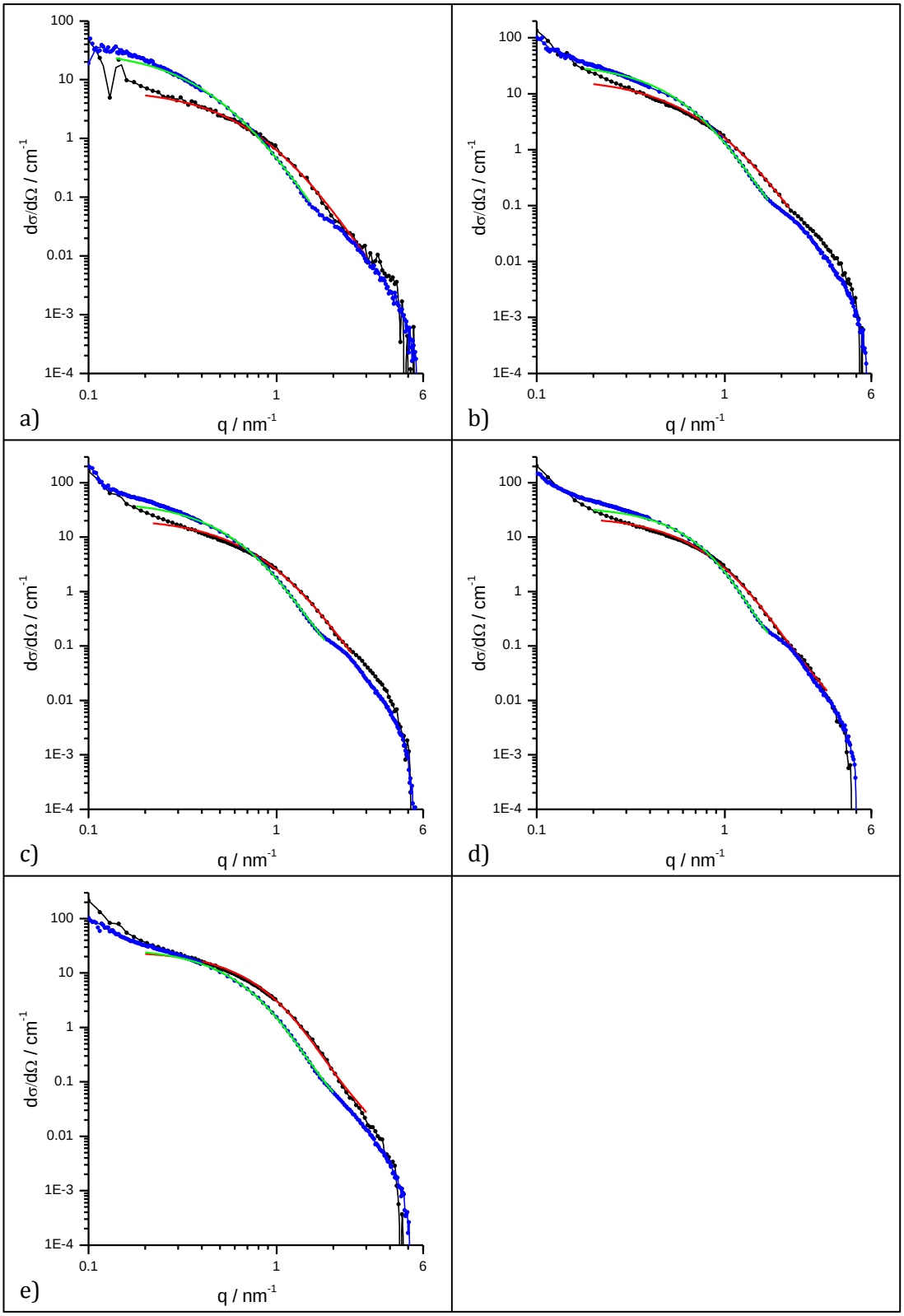

Figure 3.5: Subtracted ASAXS data recorded at the Pt L_3 edge of the fresh (black) and cycled (blue) electrodes, along with the fits obtained shown in red and green respectively. Data is shown for $Pt_{0.5ML}$/Pd/C (a), Pt_{1ML}/Pd/C (b), Pt_{2ML}/Pd/C (c), Pt_{4ML}/Pd/C (d), Pt/Pd/C alloy (e) and the Pd/C core material (f).

Table 3.3: Parameters obtained from fitting the ex situ ASAXS data recorded of the fresh and cycled catalyst electrodes near the Pd K and Pt L_3 absorption edges.

			r_0 / nm	σ_{LN} / nm	R^2	Red. χ^2	μ_r / nm	Diameter / nm
$Pt_{0.5ML}/Pd/C$	Fresh	Pd K	1.453 ± 0.002	0.40	0.989	37.13	1.57 ± 0.66	3.1 ± 1.3
		Pt L_3	0.943 ± 0.002	0.50	0.987	5.35	1.07 ± 0.57	2.1 ± 1.1
	Cycled	Pd K	2.272 ± 0.006	0.40	0.979	13.08	2.46 ± 1.03	4.9 ± 2.1
		Pt L_3	1.640 ± 0.001	0.50	0.971	35.39	1.86 ± 0.99	3.7 ± 2.0
$Pt_{1ML}/Pd/C$	Fresh	Pd K	1.444 ± 0.002	0.40	0.979	31.13	1.56 ± 0.65	3.1 ± 1.3
		Pt L_3	0.973 ± 0.001	0.50	0.959	56.31	1.10 ±0.59	2.2 ± 1.2
	Cycled	Pd K	1.916 ± 0.004	0.40	0.993	29.55	2.08 ± 0.86	4.2 ± 1.7
		Pt L_3	1.897 ± 0.001	0.40	0.984	163.7	2.05 ± 0.86	4.1 ± 1.7
$Pt_{2ML}/Pd/C$	Fresh	Pd K	1.554 ± 0.002	0.40	0.978	31.95	1.68 ± 0.70	3.4 ± 1.4
		Pt L_3	1.117 ± 0.001	0.45	0.974	89.20	1.24 ± 0.59	2.5 ± 1.2
	Cycled	Pd K	2.136 ± 0.004	0.35	0.985	26.65	2.27 ± 0.82	4.5 ± 1.6
		Pt L_3	1.894 ± 0.001	0.40	0.977	124.2	2.05 ± 0.85	4.1 ± 1.7
$Pt_{4ML}/Pd/C$	Fresh	Pd K	1.879 ± 0.004	0.35	0.978	21.57	2.00 ± 0.72	4.0 ± 1.4
		Pt L_3	1.395 ± 0.001	0.40	0.985	108.8	1.51 ± 0.63	3.0 ± 1.3
	Cycled	Pd K	1.980 ± 0.005	0.40	0.995	32.23	2.14 ± 0.89	4.3 ± 1.8
		Pt L_3	2.280 ± 0.001	0.30	0.985	109.4	2.38 ± 0.73	4.8 ± 1.5
Pt/Pd/C Alloy	Fresh	Pd K	1.659 ± 0.003	0.40	0.991	13.19	1.80 ± 0.75	3.6 ± 1.5
		Pt L_3	1.642 ± 0.001	0.35	0.960	163.3	1.75 ± 0.63	3.5 ± 1.3
	Cycled	Pd K	2.063 ± 0.006	0.40	0.997	7.82	2.23 ± 0.93	4.5 ± 1.9
		Pt L_3	2.067 ± 0.001	0.35	0.985	75.23	2.20 ± 0.79	4.4 ± 1.6
Pd/C Core	Fresh	Pd K	1.289 ± 0.002	0.40	0.979	10.83	1.40 ± 0.58	2.8 ± 1.2

The mean particle diameters and size dispersions obtained from fitting the ASAXS data using the same method as for the SAXS are given in Table 3.3, and the values are consistent with those determined by SAXS.

The radii, and thus the diameter, of the particles determined from the Pd K edge data are consistently smaller than those obtained at the Pt L_3 edge, with the exception of the alloy, where they are the same. This is the opposite behaviour to that which would be anticipated for a Pd-core, Pt-shell catalyst, where the size of the Pt particles would be expected to appear larger than the Pd particles, as seen by Yu *et al.* in a study of PtCu-core, Pt-shell electrocatalysts.[12]

In the fitting of this data, the measured intensity was assumed to arise only from the element of the edge being investigated. This is in fact a simplification of the system. The total scattering intensity of the Pt-Pd system, can be described as a sum of three components arising from the partial structure factors:

$$I(q,E) = I_{Pt}(q,E) + I_{PtPd}(q,E) + I_{Pd}(q,E)$$

Equation 3.1

In, for example, the Pt L_3 edge subtracted data, the contribution to the intensity from the Pd, $I_{Pd}(q,E)$, has been removed although the cross-term, $I_{PtPd}(q,E)$, remains. In the fitting procedure used here, the contribution arising from the cross-term was assumed to be zero which is valid in many situations.

In a study by L. Veiga, the partial structure factors (PSFs) for Co-core, Ag-shell nanoparticles were simulated, with the PSFs calculated at the Co K edge shown in Figure 3.6.[23] In this case, P_{11} refers to the Co partial structure factor, P_{22} refers to the Ag PSF, and P_{12} refers to the cross-term. If the contribution to the scattering from the cross-term was assumed to be zero, the subtracted ASAXS curve would be expected to only contain the PSF of the Co-core. However, as can be seen from Figure 3.6, the subtracted scattering profile (plot b) is nearly identical to the profile calculated for P_{12} (plot a), showing that the scattering from the cross-term is dominating the subtracted scattering intensity and therefore can not be neglected in this case.

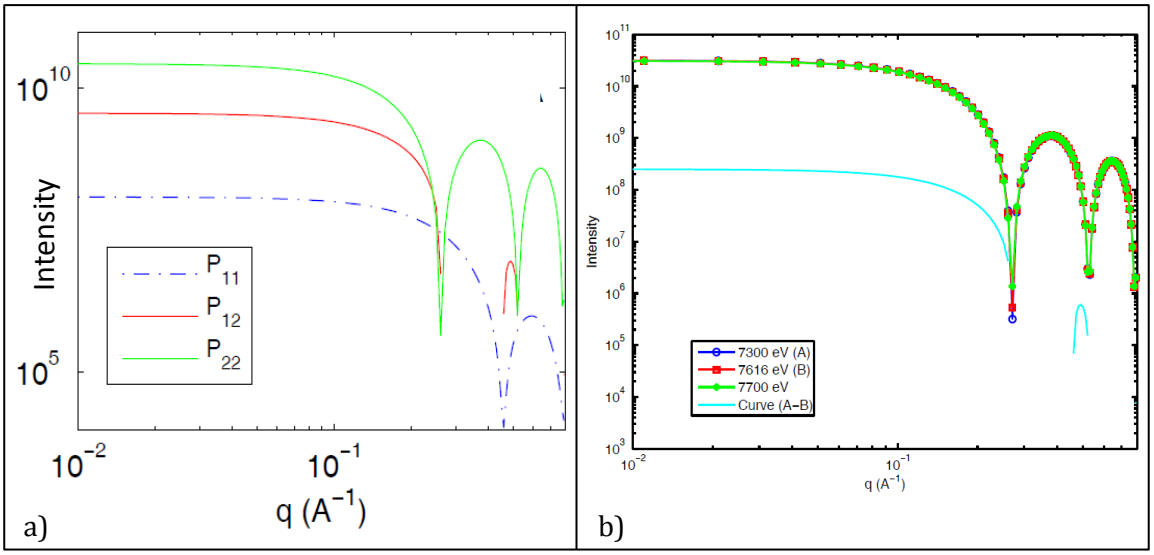

Figure 3.6: a) Simulated PSFs of a Co-core (denoted 1), Ag-shell (denoted 2) at 7616 eV. b) Total scattering intensity simulated at three energies near the Co K edge, along with the subtracted ASAXS intensity.[23]

As the fits to the Pt L_3 and Pd K ASAXS data, neglecting the cross-term, gave particle sizes contradictory to the expected values for a core-shell structure, the presence of which is supported from the evidence of the other techniques discussed in this work, this suggests that the cross-term may have a significant contribution to the subtracted scattering intensity in this system.

Following electrochemical cycling, the Pt and Pd ASAXS curves were again present over the same *q*-range, with similar profiles being observed compared to those of the fresh catalysts, aside from the more pronounced shoulder in the Pt edge data. This indicates general retention of the overall structure of Pt/Pd particles, which is in agreement with the EXAFS data shown in Chapter Four where Pt-Pd and Pd-Pt neighbours were required in the fits.

In agreement with the results of the SAXS, the particle sizes of the cycled catalysts determined from the ASAXS data are larger than those for the fresh catalysts. However, the relative increase as determined from the Pt ASAXS is greater than that of the Pd. In particular, for the 4 ML catalyst, the size determined from the Pt is now larger than that determined from the Pd and is now consistent with that expected for a core-shell structure. This may be interpreted as a decrease in the relative importance of the cross-term. Comparing the relative changes in the intensity of the scattering curves, there is a larger decrease in the Pd ASAXS intensity compared to the Pt, suggesting loss of Pd from

the system. This again agrees with the EXAFS data shown in Chapter Four which showed a decrease in the Pt-Pd, Pd-Pd and Pd-Pt coordination numbers.

Conclusions

The in situ SAXS and ex situ ASAXS data reported in this chapter has shown:

- SAXS data was not sensitive to the small changes in the structure of these samples as a result of the applied electrode potential.
- The particle diameters obtained from the SAXS data for the fresh catalyst electrodes were smaller than those determined by TEM, however, this decrease could be attributed to the different sampling methods of the two techniques, and in general good agreement was seen in the particle size distributions.
- The particle diameters obtained from the ASAXS data showed reasonable agreement to those determined from the SAXS, especially for the Pt/Pd/C alloy and Pd/C electrodes.
- The sizes calculated for the Pt and Pd edge ASAXS data for the core-shell samples gave contradictory values to those expected for the system, with Pd displaying a larger particle diameter than Pt. This effect could be due to a significant contribution to the intensity from the cross-term, which was neglected in the fitting procedure used.
- Following electrochemical cycling, an increase in the particle size was seen in both the SAXS and ASAXS data.
- Comparison of the relative increase in size determined from the SAXS data with the loss of ECA reported in Chapter Four indicated that the loss of electrochemical area seen in the 0.5 ML, 1 ML and 2 ML samples was dominated by dissolution, whereas the loss seen in the 4 ML and alloy was attributed to Ostwald ripening.
- The ASAXS data showed a greater relative increase in the diameters determined from the Pt edge data compared to the Pd edge, which could infer a reduction in the contribution of the cross-term to the scattering intensity.

References

[1] L. C. Gontard, R. E. Dunin-Borkowski, D. Ozkaya, T. Hyde, P. A. Midgley, P. Ash, *J. Phys.: Conf. Ser.* **2006**, *26*, 367.
[2] D. I. Svergun, M. H. J. Koch, *Rep. Prog. Phys.* **2003**, *66*, 1735-1782.
[3] J. Kohlbrecher, I. Bressler, *http://kur.web.psi.ch/sans1/SANSSoft/sasfit.html* **2011**.
[4] H. Schnablegger, Y. Singh, *A Practical Guide to SAXS*, Anton Paar GmbH, Graz, **2006**.

[5] P. Buras, R. Fourme, M. H. J. Koch, in *Handbook on Synchrotron Radiation, Vol. 1* (Ed.: E. E. Koch), North-Holland Publishing Company, Amsterdam, **1983**.
[6] J. S. Pedersen, *Adv. Colloid Interface Sci.* **1997**, *70*, 171-210.
[7] S. Polizzi, P. Riello, G. Goerigk, A. Benedetti, *J. Synchrotron Radiat.* **2002**, *9*, 65-70.
[8] B. Ingham, H. Li, E. L. Allen, M. F. Toney, *arXiv:0901.4782* **2009**.
[9] U. Vainio, *PhD Thesis: Characterisation of Cellulose- and Lignin-Based Materials Using X-Ray Scattering Methods*, University of Helsinki, **2007**.
[10] H. G. Haubold, X. H. Wang, H. Jungbluth, G. Goerigk, W. Schilling, *J. Mol. Struct.* **1996**, *383*, 283-289.
[11] H. G. Haubold, X. H. Wang, G. Goerigk, W. Schilling, *J. Appl. Crystallogr.* **1997**, *30*, 653-658.
[12] C. F. Yu, S. Koh, J. E. Leisch, M. F. Toney, P. Strasser, *Faraday Discuss.* **2008**, *140*, 283-296.
[13] http://www-ssrl.slac.stanford.edu/beamlines/bl1-4/, **2010**.
[14] K. Binnemans, R. Van Deun, B. Thijs, I. Vanwelkenhuysen, I. Geuens, *Chem. Mater.* **2004**, *16*, 2021-2027.
[15] H.-G. Haubold, K. Gruenhagen, M. Wagener, H. Jungbluth, H. Heer, A. Pfeil, H. Rongen, G. Brandenberg, R. Moeller, J. Matzerath, P. Hiller, H. Halling, *Rev. Sci. Instrum.* **1989**, *60*, 1943-1946.
[16] http://hasylab.desy.de/facilities/doris_iii/beamlines/e5707/index_eng.html, **2010**.
[17] S. Kraft, J. Stumpel, P. Becker, U. Kuetgens, *Rev .Sci. Instrum.* **1996**, *67*, 681-687.
[18] D. T. Cromer, D. A. Liberman, *Acta Crystallogr. Sect. A* **1981**, *37*, 267-268.
[19] A. P. Hammersley, in *ESRF Internal Report*, **1997**.
[20] A. P. Hammersley, S. O. Svensson, M. Hanfland, A. N. Fitch, D. Hausermann, *High Pressure Res.* **1996**, *14*, 235-248.
[21] H. Borchert, E. V. Shevehenko, A. Robert, I. Mekis, A. Kornowski, G. Grubel, H. Weller, *Langmuir* **2005**, *21*, 1931-1936.
[22] U. Vainio, *Personal Communication,* HASYLAB, **2010**.
[23] L. Veiga, *DESY Summer School Report: Anomalous Small-Angle X-Ray Scattering of Core-Shell Nanoparticles* **2008**.

CHAPTER SIX: CONCLUSIONS AND FUTURE WORK

1 Summary

The aims of this project were:

- To develop and apply in situ synchrotron X-ray techniques, namely EXAFS, WAXS, SAXS and ASAXS, for the characterisation of core-shell carbon-supported electrocatalysts for the oxygen reduction reaction in proton exchange membrane fuel cells; to provide an understanding of the strengths and weaknesses of each technique in relation to the study of these types of materials, and how the combination of the methods can be used to gain a greater understanding of the catalyst structure.
- To study the effects of shell thickness on the activity of Pd-core, Pt-shell oxygen reduction catalysts and the structural response to electrode potential by applying the techniques developed in the first aim.
- To use the techniques developed in the first aim to understand the mechanism of degradation of the materials as a result of electrochemical ageing.

A key part of the development of the in situ X-ray techniques was the development of the in situ electrochemical cell described in Chapter Two. Compared to the electrochemical cells used previously within the research group, the cell developed in this project had a shorter X-ray path length suitable for small-angle X-ray scattering, better contact to the working electrode, rapid solution changeover, and prevented absorption of oxygen from air into the electrolyte by being fully sealed. The cell has also proved to be very versatile and has been successfully employed to conduct in situ X-ray measurements at several different beamlines, as shown in Chapters Three to Five.

The carbon-supported Pd-core, Pt-shell electrocatalysts with Pt-shell thicknesses of 0.5, 1, 2 and 4 monolayers, along with a Pt/Pd/C alloy, were successfully prepared using the controlled surface reaction,[1] with initial characterisation using TEM, HRTEM and XRD indicative of a core-shell structure. The activity of these electrocatalysts for the ORR was not directly determined as a part of this project, however, activity data was obtained previously using the rotating disk electrode (RDE) on catalysts prepared using the same method with the same Pd-core diameter by B. Tessier.[2] The mass activity normalised for

the mass of Pt and the mass of Pt+Pd at 0.9 V vs. Pd/H reference electrode is shown in Figure for Pd-cores with 0.5, 1, 1.5 and 2 monolayer shell thicknesses.

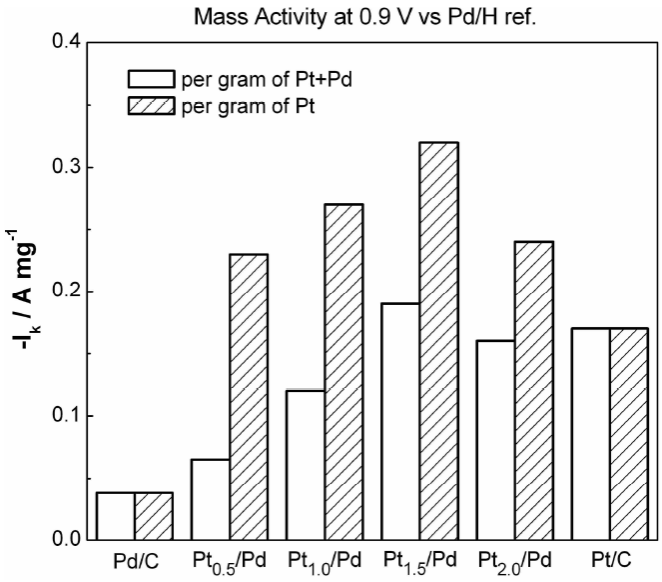

Figure 6.1: Mass activity data obtained by B. Tessier in O_2-saturated 0.1 M $HClO_4$ using the rotating disk electrode.[2]

From the data shown in Figure , it can be seen that the mass activity increases with increasing shell thickness up to 1.5 monolayers of Pt, suggesting that a balance is required between having sufficient coverage of the Pd core and making maximum use of the Pt atoms, with the $Pt_{1.5ML}$/Pd catalyst displaying the highest mass activity, normalised for both Pt and Pt+Pd.

The ORR activity of the catalysts prepared for this thesis was measured using a cavity microelectrode method [3] by Peter Richardson and Oliver White, University of Southampton. The results are summarised in Figure , reported as Pt mass activities which were determined by correcting the specific activities from CO stripping by comparison to the CO areas for painted button electrodes. As can be seen in Figure , the mass activity at 0.9 V, the potential typically used to assess catalyst activity,[4] is highest for the 2 ML sample, indicating that the coverage of the Pd core was not sufficient for the 1 ML sample to achieve the balance mentioned above.

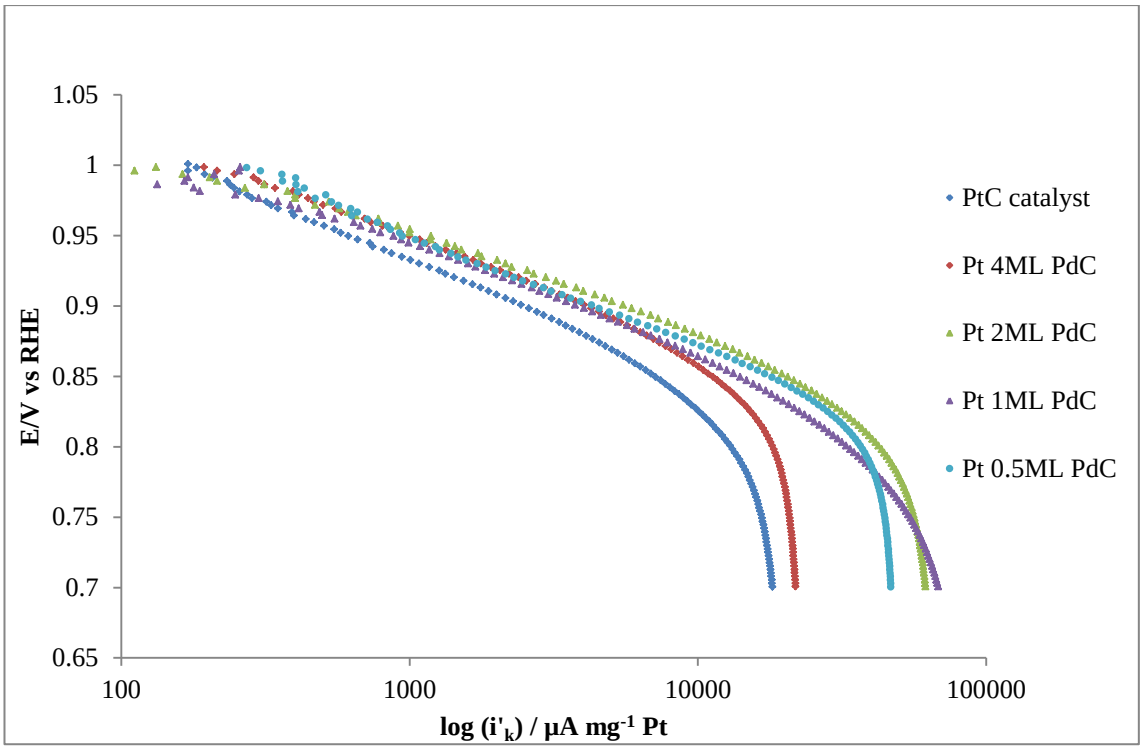

Figure 6.2: Mass activity data obtained in O_2-saturated 0.5 M H_2SO_4 using a cavity microelectrode.[5]

The electrochemical data obtained in the form of cyclic voltammograms and CO stripping voltammograms presented in Chapters Two and Four showed that the surface of the particles became more Pt-like with increasing shell coverage, thus supporting the deposition of the Pt to form a shell on the surface of the Pd core.

The ex situ EXAFS data gave added evidence of the core-shell structure from the segregation in the M_1-M_1 and M_1-M_2 coordination numbers, indicative of two separate elemental regions, for the core-shell samples. The Pt-Pt bond length was seen to increase with increasing shell thickness, with the 2 ML and 4 ML samples displaying a Pt-Pt bond length similar to that of a Pt-only catalyst. Correlated with the ORR activity data shown in Figure , this suggests that the Pt-like bond distance is advantageous for the activity for ORR, although the greater wt% of Pt in the 4 ML sample negates any mass activity benefit.

In terms of the response to electrode potential, the $Pt_{xML}Pd/C$ catalysts all displayed a significant increase in the Pd-Pd bond length when the potential was reduced to 0.0 V, due to the absorption of hydrogen, showing that even with 4 ML coverage of Pt hydrogen was still able to penetrate the Pt-shell. Pd-O neighbours were detected in the data recorded whilst holding the potential at 1.0 V for the 0.5 ML, 1 ML and 2 ML core-shell samples,

showing that Pd was still accessible, however the coordination number decreased with increasing shell thickness indicating higher coverage of the core.

In the WAXS data, the lattice parameter increased with increasing shell thickness, indicating the increasing presence of Pt-Pd or Pt phases in the crystalline region of the nanoparticles. This was supported by the smaller increase in the lattice parameter due to hydrogen absorption at 0.0 V with increasing shell thickness. The lattice parameters obtained for the core-shell samples were significantly lower than those of the Pt-only catalyst, showing that there was the presence of some lattice strain effects which can alter the activity to ORR.[6] The WAXS data analysis was limited by the background scattering of the carbon, meaning that the crystallite size could not be calculated and peak profile fitting was not feasible, thus more specific conclusions about the phases present in the crystal structure could not be drawn.

The particle sizes obtained from the SAXS data agreed with those obtained from the TEM, however, owing to the polydispersity of the samples it was not possible to draw any further conclusions on the structure of the fresh catalysts from the response to electrode potential.

It was hoped that more information regarding the core-shell structure in terms of the level of coverage of the core and the thickness of the shell could be gained from the ex situ ASAXS data. The similar q-range of the data at both edges was indicative of the presence of Pt and Pd in particles of a similar size, which suggested that the Pt was present either as mixed with the Pd or as a shell, rather than as small particles decorating the surface of the core. As discussed in Chapter Five, it is believed that the scattering intensity arising from the cross-term could not be neglected as it was in the fitting model used, thus preventing any further structural information being obtained from the current fitting routine.

The electrochemical ageing procedure used in this study resulted in a decrease in the electrochemical surface area of the catalysts, with a greater loss in area seen in the samples with thinner Pt shell coverage. As described in Chapter Three, the mechanisms of degradation resulting in this loss of area can be described as dissolution, agglomeration and coalescence.

The cyclic voltammograms and CO stipping voltammograms became more Pt-like with increasing number of cycles – an effect more pronounced in the samples with 0.5 and 1 ML

shell thicknesses, indicating a loss of Pd from the surface of the nanoparticles. The EXAFS data showed a decrease in the Pd-Pd, Pd-Pt and Pt-Pd coordination numbers which was again indicative of Pd loss from the system. Aside from this, no significant changes were determined from the EXAFS data between the fresh and cycled electrodes, suggesting that the general structure had been retained.

The lattice parameters determined from the WAXS data were lower than those obtained from the fresh electrodes, suggesting that there may be a larger presence of a Pd-only phase in the crystalline structure. This was accompanied by a greater increase in the lattice parameter as a result of hydrogen absorption, again pointing to a Pd-rich phase. Surface tension effects can also cause a decrease in the lattice parameter, either due to a decrease in the particle size or as a result of hollowing of the particle. However, without determination of the crystallite size and/or peak profile fitting it was not possible to conclude if either of these changes had occurred.

The SAXS data showed an increase in the size of the catalyst following electrochemical cycling. Comparison of the increase in the particle diameter with the loss of the ECA suggested that the decrease in the electrochemical surface area for the samples with lower than 2 ML shell thickness was dominated by dissolution, with particle growth dominating for the 4 ML and alloy samples. The increase in the mean diameter and the dispersion of the 4 ML and alloy catalysts at the expense of the smaller particles suggests that Ostwald ripening may be occurring. Evidence of a second distribution of smaller particles was seen by the shoulder in the scattering profile at high q which could not be fitted using the method used.

The ASAXS data also showed an increase in the particle size following potential cycling. From the shape of the scattering profiles it appeared that the general structure was retained, however the presence of a second distribution of smaller Pt particles could be inferred from the shoulder seen at high q in the Pt L_3 edge data. The relative increase in the particle size was greater for the Pt than the Pd, and the sizes obtained were more typical of those expected for a core-shell structure for the 4 ML sample, indicating that the contribution from the cross-term was reduced following cycling. A decrease in the absolute intensity of the Pd scattering profiles was seen following potential cycling, again showing loss of Pd from the system.

2 Advantages and Limitations of Techniques

The set of core-shell catalysts investigated in this thesis represented an ideal opportunity to enable the assessment of the relative strengths and weaknesses of each of the X-ray techniques used in the determination of the structures of the catalyst particles. From the previously published thesis works of Beatrice Tessier and Peter Wells,[1],[2],[7],[8] and especially the TEM data that they both presented, it was known that the $Pt(acac)_2$ deposition method produced a good core-shell structure. The advantages and limitations of EXAFS, WAXS, SAXS and ASAXS determined from the study of these materials are therefore outlined below:

- The primary strengths of the EXAFS method are that it provides the per atom average coordination environment of each element, thus removing the requirement for the material to have long range order, and the measurements can be conducted in situ. The detailed structural information obtained by fitting the EXAFS data greatly exceeds that from the other techniques. For the series of core-shell catalysts investigated, collection of the data at both the Pt and Pd edges allowed the fits to be refined from both perspectives simultaneously, thereby improving the quality and reliability of the fits. The per atom nature of EXAFS represents a challenge in the interpretation of the results, as the elements are in a variety of coordination environments in the particles. Overall the in situ EXAFS data proved to be one of the most useful methods for determining the effects of increasing the shell thickness and the effects of cycling (accelerated aging tests) on the catalyst structure. The data collection was relatively straightforward and there were few artefacts arising from the nature of the samples. However, the analysis of the EXAFS data was not simple and relied on the design of appropriate models and the errors associated with the parameters determined were significant.

- WAXS is limited by the requirement of long-range order in the sample and as such can only provide information on the crystalline region of a catalyst nanoparticle. Whilst the information from the WAXS measurements can be obtained ex situ using laboratory-based sources, the use of synchrotron radiation allowed the data to be collected in situ so that it could be directly compared to the EXAFS data. This represented the greatest strength of WAXS for the study of these core-shell catalysts as the availability of the WAXS results added weight to the structural models obtained from the EXAFS data. The scattering from the carbon limited the

number of diffraction peaks that could be fully analysed, in the case of the studies presented here to one, and thus the WAXS data was of limited additional value. If the scattering from the carbon could be made more reproducible, perhaps by making the electrode structure and/or the cell window more rigid, then subtraction of the background may have been more complete. Collecting the data to higher angles of 2θ would also be advantageous as the scattering from the carbon is less pronounced in this region.

- Like the EXAFS and WAXS, the SAXS measurements were also conducted in situ. The SAXS provided a means of determining the average particle size and the dispersion, which were not obtained from the other two methods. However, as in the case of the WAXS data, the SAXS also suffered limitations attributable to (i) scattering by the carbon, which was present in the form of the carbon paper current collector and the graphitic carbon support for the catalyst particles and (ii) the polydispersity of the sample. The scattering from the carbon made removal of the background difficult and limited the reliability of the data and its analysis, whilst the polydispersity of the sample washed out any more subtle effects of variation of the applied potential. Nevertheless, when combined with the electrochemical measurements, the SAXS enabled discrimination between the various mechanisms of ECA loss following the accelerated aging tests.

- Finally, the ASAXS data can provide a means of confirming the presence of the core-shell structure and a measurement of the shell thickness, as was previously reported by Yu *et al*.[9] The data presented in this thesis was obtained ex situ, as the beamline at HASYLAB was set up to work under vacuum and could not be modified. Other ASAXS beamlines, such as 7T-MPW-SAXS at BESSY are available and preliminary in situ measurements, not presented in this thesis, were conducted in June 2011. Unfortunately the lengthy data collection for those measurements meant that only a limited number of samples could be studied and data was only obtained for the 2 ML sample at both edges. Additionally, at the Pd edge, the intensity of the beam was very low and most of the beam had to be rejected to remove higher harmonics and to improve the stability of the beam position, which compromised the signal to noise levels of the data.
  The analysis of the ASAXS data presented in this thesis was restricted to a spherical particle model owing to time limitations. Whilst such an analysis worked well for the case of the dealloyed PtCu catalysts reported by Yu *et al*.,[9] the

contribution of the cross-term was more significant in the case of the true core-shell catalysts reported here. Thus, the use of a core-shell model where the data from both edges is fitted simultaneously may prove to be more accurate and such data analysis is planned following on from the work presented here.

3 Concluding Remarks

The extensive structural characterisation provided by combining the various synchrotron based X-ray techniques with laboratory-based XRD and TEM, and the electrochemical measurements such as cyclic voltammetry have enabled the investigation of the effects of the shell thickness on the mass activity and degradation following accelerated aging tests of these Pt-shell, Pd-core catalysts. The work represents the results from 73 days of beam time over 2 years at 6 different synchrotrons. It is perhaps unreasonable to expect this level of access to enable such charactersation of any other set of catalysts. In the opinion of the author, the EXAFS provided the most useful and unique results, followed by the SAXS as this provided information not obtainable from the EXAFS data. The WAXS provided information complementary to the EXAFS and of limited value, but if the effects of the carbon could be removed, or the data collected to higher angles of 2θ, more detailed analysis would be possible. Finally the ASAXS proved to be a very difficult technique both experimentally and in terms of the data analysis and, as such, is unlikely to prove to be as generally applicable as the other methods.

References

[1] B. C. Tessier, A. E. Russell, B. R. Theobald, D. Thompsett, *ECS Trans.* **2009**, *16*, 1-11.
[2] B. C. Tessier, *PhD Thesis: Preparation, Characterisation and Evaluation of Core-Shell Electrocatalysts for PEMFCs*, University of Southampton, **2009**.
[3] E. Guilminot, A. Corcella, M. Chatenet, F. Maillard, *J. Electroanal. Chem.* **2007**, *599*, 111-120.
[4] H. A. Gasteiger, S. S. Kocha, B. Sompalli, F. T. Wagner, *Appl. Catal,. B* **2005**, *56*, 9-35.
[5] O. White, *BSc Dissertation: Investigation into Cavity Microelectrode Studies for the Oxygen Reduction Reaction*, **2012**.
[6] M. Mavrikakis, B. Hammer, J. K. Norskov, *Phys. Rev. Lett.* **1998**, *81*, 2819-2822.
[7] P. P. Wells, E. M. Crabb, C. R. King, R. Wiltshire, B. Billsborrow, D. Thompsett, A. E. Russell, *Phys. Chem. Chem. Phys.* **2009**, *11*, 5773-5781.
[8] P. Wells, *PhD Thesis: Controlled Suface Modification of Supported Platinum Group Metal Catalysts*, **2007**.
[9] C. F. Yu, S. Koh, J. E. Leisch, M. F. Toney, P. Strasser, *Faraday Discuss.* **2008**, *140*, 283-296.